DGK Veröffentlichungen der DGK

Ausschuss Geodäsie der Bayerischen Akademie der Wissenschaften

Reihe C | Dissertationen | Heft Nr. 939

Bobin Cui

GNSS augmentation services for large-area PPP-RTK

München 2024

Bayerische Akademie der Wissenschaften

ISSN 0065-5325 ISBN 978-3-7696-5351-9

Diese Arbeit ist gleichzeitig veröffentlicht in:
DepositOnce – Forschungsdaten und Publikationen der Technischen Universität Berlin
https://doi.org/10.14279/depositonce-19671, Berlin 2023 und
GFZpublic – Publikationsdatenbank Helmholtz-Zentrum Potsdam Deutsches GeoForschungsZentrum GFZ
https://doi.org/10.48440/gfz.b103-24010, Potsdam 2024

DGK Veröffentlichungen der DGK

Ausschuss Geodäsie der Bayerischen Akademie der Wissenschaften

Reihe C Dissertationen Heft Nr. 939

GNSS augmentation services for large-area PPP-RTK

Von der Fakultät VI – Planen Bauen Umwelt
der Technischen Universität Berlin
zur Erlangung des akademischen Grades
Doktor der Ingenieurwissenschaften (Dr.-Ing.)
genehmigte Dissertation

von

Bobin Cui, M.Sc.

München 2024

Bayerische Akademie der Wissenschaften

ISSN 0065-5325 ISBN 978-3-7696-5351-9

Diese Arbeit ist gleichzeitig veröffentlicht in:

DepositOnce – Forschungsdaten und Publikationen der Technischen Universität Berlin
https://doi.org/10.14279/depositonce-19671, Berlin 2023 und
GFZpublic – Publikationsdatenbank Helmholtz-Zentrum Potsdam Deutsches GeoForschungsZentrum GFZ
https://doi.org/10.48440/gfz.b103-24010, Potsdam 2024

Adresse der DGK:

Ausschuss Geodäsie der Bayerischen Akademie der Wissenschaften (DGK)

Alfons-Goppel-Straße 11 ● D – 80 539 München

Telefon +49 - 331 - 6264 1685 ● E-Mail post@dgk.badw.de

http://www.dgk.badw.de

Prüfungskommission:

Vorsitzender: Prof. Dr. Frank Flechtner

Referent: Prof. Dr. Dr. hc Harald Schuh

Korreferenten: Prof. Dr. Maorong Ge
Prof. Dr. Lambert Wanninger (TU Dresden)
Ao. Prof. Dr. Robert Weber (TU Wien)

Tag der mündlichen Prüfung: 15.11.2023

© 2024 Bayerische Akademie der Wissenschaften, München

Alle Rechte vorbehalten. Ohne Genehmigung der Herausgeber ist es auch nicht gestattet,
die Veröffentlichung oder Teile daraus auf photomechanischem Wege (Photokopie, Mikrokopie) zu vervielfältigen

ISSN 0065-5325 ISBN 978-3-7696-5351-9

Acknowledgements

I would like to express my gratitude to all the people who have supported me throughout my academic journey.

My heart overflows with gratitude for my supervisors, Prof. Harald Schuh and Prof. Maorong Ge. Their unwavering support, invaluable guidance, and boundless patience have been the light that has guided me through the challenges of this research. Their profound expertise and insights have been the foundation upon which I built my investigations. Their encouragement has been a wellspring of motivation, constantly urging me to pursue excellence. I am forever grateful for their generosity in providing me with the opportunity to stay at GFZ, to explore freely the scientific depths of my inquiries, and for providing me with all the facilities I needed to conduct my research. Their deep knowledge in space geodesy has been the compass that has steered me through my study, and their encouragement has been the wind in my sails.

I am grateful to Dr. Jungang Wang and Dr. Pan Li for their invaluable guidance in my study. I feel honored to have had them as my partners during my Ph.D. period, given their impressive expertise in successfully implementing ambiguity resolution and atmosphere research.

I want to thank Prof. Lambert Wanninger and Prof. Robert Weber, as outstanding experts in this field, willing to review my thesis, which has contributed significantly to the quality of this work.

I would like to acknowledge the staff at GFZ, who provided invaluable technical support and helped me overcome many of the obstacles that arose during my research.

I am also grateful to my colleagues and friends Wenju Fu, Haibo Ge, Xinyuan Jiang, Xiang Zuo, Weiliang Xie, Xiaoyu Shi, Ning Zhai, Xiao Chang, Kai Zheng, Zhilu Wu, Longjiang Tang, Liangwei Nie, Zhiwei Qin, YuanXin Wang, Shuqiong Liu, Shi Du, Jiaxin Huang, Yun Xiong, and Mimi Peng, for their collaboration, encouragement, and moral support, which have made this journey much more enjoyable and rewarding.

Finally, I would like to thank my family for their love, encouragement, and understanding, which have sustained me through the ups and downs of this challenging endeavor. Without their support, this accomplishment would not have been possible.

My stay at GFZ is financially supported by the China Scholarship Council.

Bobin Cui
May, 2023
GFZ, Berlin

Abstract

With the ongoing deployment of Global Navigation Satellite Systems (GNSS) ground stations and the modernization of satellite signal systems, the utilization of various augmentation technologies enables the realization of Precise Point Positioning (PPP) in real-time. Augmentation technology, which introduces precise atmospheric and signal-related delays, has become an essential component of high-precision real-time services and is attracting growing interest in scientific research, disaster monitoring, autopilot, etc. Previous studies have dedicated significant efforts to enhance the generation and dissemination of augmentation information on the service side and improve real-time positioning algorithms on the user side. The real-time atmosphere augmentation information with sufficient accuracy and proper constraint, and reliable Ambiguity Resolution (AR) for this purpose is the main focus of current GNSS research. However, these efforts have primarily been concentrated on small or medium-sized regions with the capability for transmitting massive data volumes. Alternatively, they have focused on larger areas, but with slow convergence due to the imprecise nature of atmosphere information. To address the challenge posed by the trade-offs among service area size, correction volume, and the precision of represented correction, a new augmentation strategy is proposed. This approach integrates the advantages of atmospheric delay fitting models, unmodeled residuals, and uncertainty information to achieve rapid and high-precision positioning, all while reducing data transmission volume for larger areas. It also allows users to implement different positioning modes depending on their communication capacity. Additionally, all deviations among different types of receivers and satellite signals are calibrated in this study for reliable AR can be achieved on all reference stations. The main contribution of this thesis is summarized as follows.

With the real-time precise orbit, clock, and Uncalibrated Phase Delay (UPD) products, precise atmospheric delay corrections relying on reliable AR can be derived for large-areas augmentation services. To address the challenge of achieving reliable AR across different receiver types and various satellite signals, this thesis proposes a comprehensive method for calibrating receiver-type-related satellite-specific deviations and analyzes the impact of satellite signal bias corrections in data processing. The primary objective is to enhance the reliability of AR, enabling the utilization of all available signals and receiver types in large-area services. Subsequently, new tropospheric and ionospheric delay fitting models applied for large-area are carried out according to the properties of their propagation paths. In addition, the corresponding atmospheric delay uncertainty for large areas is introduced based on the fitting residuals. Finally, a hierarchical mode is developed for augmentation services, leveraging the

advantages of the fitting model and uncertainty grid to reduce data volume and incorporating regional fitting residuals using the interpolation model and ionospheric delay error function, depending on the network capability. Based on hierarchical augmentation, positioning in large areas can not only achieve rapid/instantaneous high-precision convergence but also overcome the conflict among correction volume, represented precision, and coverage size.

In order to derive precise atmospheric delay and accelerate positioning, implementing reliable and robust AR across all types of receivers and satellite signals is essential. It also demonstrates and discusses the advantages of calibrating satellite-signal and receiver-type-related satellite-specific deviations in AR solutions. The deviations related to receivers in terms of UPD products are assessed and calibrated, confirming that a 0.03 cycle consistency in wide lane UPD can be achieved. The effectiveness of the proposed approach is demonstrated using GPS satellite signals, which can improve the AR rate by at least 10% and produce more reliable results. In addition, the impact of different signal settings and corrections on orbit, clock, and UPD generation, as well as positioning and pseudo-range signal systematic and stochastic residuals, is analyzed. These processing strategies provide flexible observation selections, allowing the utilization of all available satellite signals and receiver types, thereby enabling reliable AR and a higher fixing rate. As a result, an AR fixing rate exceeding 95% is achievable across all stations in large-area services.

For precise atmospheric delay modeling over large areas, new models are proposed, including a tropospheric Zenith Wet Delay (ZWD) model and a satellite-wise ionospheric slant delay fitting model. The tropospheric delay model takes the exponential function of water vapor vertical changes into consideration, addressing model anomalies in areas with large altitude differences. The new ionospheric delay fitting model introduces the trigonometric functions to describe differences in slant path delays between the optimal reference propagation path and others, achieving superior modeling performance in large areas. The precision of the fitting model, utilizing a 200 km station-spacing network, demonstrates tropospheric ZWD and ionospheric slant delays of 1.3 cm and 8.9 cm, respectively, with smaller standard deviations. These new fitting models overcome the challenge of handling massive information for providing station-wise corrections and avoid an increase in the number of coefficients. In addition to the function model, the stochastic model, i.e., uncertainty information, is essential for describing the quality of corrections. The atmospheric delay uncertainty for the large-area fitting model is generated based on the fitting residuals and represented in forms of grid-point. Additionally, regional ionosphere unmodeled residual uncertainty is represented by the form of liner function, which is established by the relationship between distance and interpolation precision through inter-satellite cross-verification among all reference stations. The differences between uncertainty value and real delays are 2.5 cm and 0.5 cm for grid and function forms, respectively. For real-

time applications in large areas, the fitting model and grid-based atmosphere uncertainty serve as the essential information, satisfying the requirement of rapid positioning. By further incorporating unmodeled residuals and ionosphere error function, a hierarchical augmentation model is provided.

Based on the fitting model established for large areas, unmodeled residuals are further introduced as optional compensation for specific areas, depending on the magnitude of fitting residuals. This approach results in a 97% reduction in tropospheric delay and a 65% reduction in ionospheric delay transmission volume. Furthermore, leveraging the regional high capability of communication, 85.3% of all solutions can achieve instantaneous convergence at the first epoch with the aid of corresponding regional compensation.

This thesis proposes a large areas augmentation service to overcome the conflict among correction data volume, represented precision, and coverage size. It demonstrates the benefits of an augmentation mode that integrates regional information into large-area services. Under these conditions, a more reliable and rapid AR solution can be easily achieved based on precise atmospheric delay correction and uncertainty in large areas with fewer data volume requirements. This is beneficial for actual real-time services and applications.

Zusammenfassung

Mit der laufenden Bereitstellung von Bodenstationen für globale Navigationssatellitensysteme (GNSS) und der Modernisierung von Satellitensignal-Systemen ermöglicht die Nutzung verschiedener Augmentationstechnologien die Realisierung der Präzisen Punkt-Positionierung (PPP) in Echtzeit. Augmentationstechnologie, die präzise atmosphärische und signalbezogene Verzögerungen einführt, ist zu einem wesentlichen Bestandteil hochpräziser Echtzeitdienste geworden und findet wachsendes Interesse in wissenschaftlicher Forschung, Katastrophenüberwachung, Autopiloten usw. Frühere Studien haben erhebliche Anstrengungen darauf verwendet, die Erzeugung und Verbreitung von Augmentationsinformationen auf der Dienstseite zu verbessern und Echtzeit-Positionierungsalgorithmen auf der Benutzerseite zu optimieren. Die Echtzeit-Atmosphärenaugmentationsinformationen mit ausreichender Genauigkeit und angemessener Einschränkung sowie zuverlässige Ambiguitätsauflösung (AR) für diesen Zweck stehen im Mittelpunkt der aktuellen GNSS-Forschung. Diese Bemühungen konzentrierten sich jedoch hauptsächlich auf kleine oder mittelgroße Regionen mit der Fähigkeit zur Übertragung großer Datenmengen. Alternativ richteten sie sich auf größere Gebiete, jedoch mit langsamer Konvergenz aufgrund der ungenauen Natur der Atmosphäreninformation. Um der Herausforderung durch die Abwägung zwischen Größe des Dienstleistungsgebiets, Korrekturvolumen und Präzision der dargestellten Korrektur zu begegnen, wird eine neue Augmentationsstrategie vorgeschlagen. Dieser Ansatz integriert die Vorteile atmosphärischer Verzögerungsanpassungsmodelle, nicht modellierter Reste und Unsicherheitsinformationen, um eine schnelle und hochpräzise Positionierung zu erreichen, und das bei gleichzeitiger Reduzierung der Datenübertragungsvolumina für größere Gebiete. Es ermöglicht den Benutzern auch, verschiedene Positionierungsmodi je nach ihrer Kommunikationskapazität zu implementieren. Zusätzlich werden in dieser Studie alle Abweichungen zwischen verschiedenen Typen von Empfängern und Satellitensignalen kalibriert, um eine zuverlässige AR an allen Referenzstationen zu erreichen. Die Hauptbeiträge dieser Arbeit werden wie folgt zusammengefasst.

Mit den Echtzeit-Präzbitbahnen, Uhren und Uncalibrated Phase Delay (UPD)-Produkten können präzise atmosphärische Verzögerungskorrekturen für großflächige Augmentationsdienste abgeleitet werden, die auf zuverlässiger AR basieren. Um die Herausforderung zu bewältigen, eine zuverlässige AR über verschiedene Empfängertypen und verschiedene Satellitensignale hinweg zu erreichen, schlägt diese Arbeit eine umfassende Methode zur Kalibrierung von empfängertypbezogenen satellspezifischen Abweichungen vor und analysiert die Auswirkungen von Korrekturen für Satellitensignalverzerrungen in der Datenverarbeitung. Das Hauptziel besteht darin, die Zuverlässigkeit der AR zu verbessern und die Nutzung aller verfügbaren

Signale und Empfängertypen in großflächigen Diensten zu ermöglichen. Anschließend werden neue troposphärische und ionosphärische Verzögerungsanpassungsmodelle für großflächige Anwendungen gemäß den Eigenschaften ihrer Ausbreitungspfade durchgeführt. Darüber hinaus wird die entsprechende atmosphärische Verzögerungsunsicherheit für große Gebiete auf der Grundlage der Anpassungsreste eingeführt. Schließlich wird ein hierarchischer Modus für Augmentationsdienste entwickelt, der die Vorteile des Anpassungsmodells und des Unsicherheitsgitters nutzt, um das Datenvolumen zu reduzieren und regionale Anpassungsreste unter Verwendung des Interpolationsmodells und der ionosphärischen Verzögerungsfehlerfunktion, abhängig von der Netzwerkfähigkeit, zu integrieren. Basierend auf der hierarchischen Augmentation kann die Positionierung in großen Gebieten nicht nur eine schnelle/instantane hochpräzise Konvergenz erreichen, sondern auch den Konflikt zwischen Korrekturvolumen, dargestellter Präzision und Abdeckungsgröße überwinden.

Um präzise atmosphärische Verzögerungen abzuleiten und die Positionierung zu beschleunigen, ist es entscheidend, eine zuverlässige und robuste AR über alle Arten von Empfängern und Satellitensignalen zu implementieren. Es zeigt auch die Vorteile der Kalibrierung von satellitensignal- und empfängertypbezogenen satellspezifischen Abweichungen in AR-Lösungen auf. Die Abweichungen im Zusammenhang mit Empfängern in Bezug auf UPD-Produkte werden bewertet und kalibriert, wobei bestätigt wird, dass eine Konsistenz von 0,03 Zyklen bei Wide-Lane-UPD erreicht werden kann. Die Wirksamkeit des vorgeschlagenen Ansatzes wird unter Verwendung von GPS-Satellitensignalen demonstriert, die die AR-Rate um mindestens 10% verbessern und zu zuverlässigeren Ergebnissen führen können. Darüber hinaus wird der Einfluss unterschiedlicher Signalparameter und Korrekturen auf die Erzeugung von Orbit, Uhr und UPD sowie auf die Positionierung und systematische und stochastische Reste der Pseudo-Range-Signale analysiert. Diese Verarbeitungsstrategien bieten flexible Auswahlmöglichkeiten bei der Beobachtung und ermöglichen die Nutzung aller verfügbaren Satellitensignale und Empfängertypen, wodurch eine zuverlässige AR und eine höhere Fixierungsrate ermöglicht wird. Als Ergebnis ist eine AR-Fixierungsrate von über 95% bei allen Stationen in großflächigen Diensten erreichbar.

Für eine präzise Modellierung atmosphärischer Verzögerungen über großen Gebieten werden neue Modelle vorgeschlagen, darunter ein troposphärisches Zenith Wet Delay (ZWD)-Modell und ein satellitenweises ionosphärisches Schrägverzögerungsanpassungsmodell. Das troposphärische Verzögerungsmodell berücksichtigt die exponentielle Funktion der vertikalen Änderungen des Wasserdampfs und behebt Modellanomalien in Gebieten mit großen Höhendifferenzen. Das neue ionosphärische Verzögerungsanpassungsmodell verwendet trigonometrische Funktionen, um Unterschiede in den Schrägpfadverzögerungen zwischen dem optimalen Referenzausbreitungspfad und anderen zu beschreiben und erreicht so eine

überlegene Modellierungsleistung in großen Gebieten. Die Präzision des Anpassungsmodells, unter Verwendung eines 200 km-Stationen-Netzwerks, zeigt troposphärische ZWD- und ionosphärische Schrägverzögerungen von jeweils 1,3 cm und 8,9 cm mit kleineren Standardabweichungen. Diese neuen Anpassungsmodelle überwinden die Herausforderung, massive Informationen für die Bereitstellung stationsspezifischer Korrekturen zu verarbeiten, und vermeiden eine Zunahme der Anzahl der Koeffizienten. Neben dem Funktionsmodell ist das stochastische Modell, d. h. Unsicherheitsinformationen, entscheidend für die Beschreibung der Qualität der Korrekturen. Die Unsicherheit der atmosphärischen Verzögerung für das großflächige Anpassungsmodell wird auf der Grundlage der Anpassungsreste generiert und in Form von Gitterpunkten dargestellt. Zusätzlich wird die regionale ionosphärische nicht modellierte Restunsicherheit durch die Form einer linearen Funktion repräsentiert, die durch die Beziehung zwischen Entfernung und Interpolationsgenauigkeit durch inter-satellitenkreuz-Verifikation zwischen allen Referenzstationen etabliert wird. Die Unterschiede zwischen Unsicherheitswert und realen Verzögerungen betragen 2,5 cm bzw. 0,5 cm für Gitter- und Funktionsformen. Für Echtzeitanwendungen in großen Gebieten dienen das Anpassungsmodell und die gitterbasierte Atmosphärenunsicherheit als wesentliche Informationen, die die Anforderungen an schnelle Positionierung erfüllen. Durch die weitere Integration von nicht modellierten Resten und Ionosphärenfehlerfunktion wird ein hierarchisches Augmentationsmodell bereitgestellt.

Basierend auf dem für große Gebiete etablierten Anpassungsmodell werden nicht modellierte Reste zusätzlich als optionale Kompensation für spezifische Bereiche eingeführt, abhängig von der Größenordnung der Anpassungsreste. Dieser Ansatz führt zu einer Reduktion von 97% der troposphärischen Verzögerung und einer Reduktion von 65% des ionosphärischen Verzögerungsvolumens. Darüber hinaus können unter Nutzung der regionalen hohen Kommunikationsfähigkeit 85,3% aller Lösungen mit Hilfe entsprechender regionaler Kompensation eine sofortige Konvergenz beim ersten Epochenzeitpunkt erreichen.

Diese Dissertation schlägt einen großflächigen Augmentationsdienst vor, um den Konflikt zwischen Korrekturvolumen, dargestellter Präzision und Abdeckungsgröße zu überwinden. Sie zeigt die Vorteile eines Augmentationsmodus, der regionale Informationen in großflächige Dienste integriert. Unter diesen Bedingungen kann eine zuverlässigere und schnellere AR-Lösung basierend auf präziser atmosphärischer Verzögerungskorrektur und Unsicherheit in großen Gebieten mit geringeren Anforderungen an das Datenvolumen leicht erreicht werden. Dies ist vorteilhaft für tatsächliche Echtzeitdienste und Anwendungen.

List of Related Publications

1. **Cui, B.**, Li, P., Wang, J., Ge, M., Schuh, H. (2021) Calibrating receiver-type-dependent wide-lane uncalibrated phase delay biases for PPP integer ambiguity resolution. Journal of Geodesy 95, 82.
2. **Cui, B.**, Wang, J., Tang, L., Ge, M., Schuh, H. Calibrating differential signal bias of pseudo-range in GNSS data processing. Journal of Geodesy, submitted, August 2022.
3. **Cui, B.**, Wang, J., Li, P., Ge, M., Schuh, H. (2022) Modeling wide-area tropospheric delay corrections for fast PPP ambiguity resolution. GPS Solutions 26, 56.
4. **Cui, B.**, Wang, J., Li, P., Hu, J., Tang, L., Zuo, X. Large-area ionosphere modeling with atmosphere uncertainty generation for real-time positioning. GPS Solutions, submitted, June 2023.
5. Li, P., **Cui, B.***, Hu, J., Liu, X., Zhang., X., Ge, M.; Schuh, H. (2022) PPP-RTK considering the ionosphere uncertainty with cross-validation. Satellite Navigation, 3, 10.
6. **Cui, B.**, Jiang, X., Wang, J., Li, P., Ge, M., Schuh, H. (2023) A new large-area hierarchical PPP-RTK service strategy. GPS Solutions, 27, 134.

The paper 1 and 2 contributed to the Chapter 4; The paper 3, 4, and 5 contributed to the Chapter 5; The paper 6 contributed to the Chapter 6.

List of Contents

1 Introduction and Motivation

1.1 Overview

Global Navigation Satellite Systems (GNSS) are critical for Positioning, Navigation, and Timing (PNT) services, geodesy, geophysical research, and geohazard monitoring and early warning. Each GNSS includes three segments: satellites in space, ground network including a number of monitor and control stations, and the user end. Over the past decades, the GNSS has undergone significant development, achieving the modernization of satellite constellations and the establishment of extensive station networks, enabling the provision of vast amounts of information for global services.

GNSS Precise Point Positioning (PPP) technology gives the absolute coordinate in a global reference frame via the observations simultaneously from at least four satellites, which is determined by the measuring distances to GNSS satellites in combination with precise satellite orbit and clock products. Applications utilizing GNSS signals require accuracy ranging from a few meters for standard navigation and position solutions to centimeter- and millimeter-level accuracy[1]. Generally, the rapid and high-precision positioning relies on the global/large-area/region augmentation information which is generated from ground reference networks and broadcast to users via satellite and the internet communications to enable real-time precise positioning at user-end.

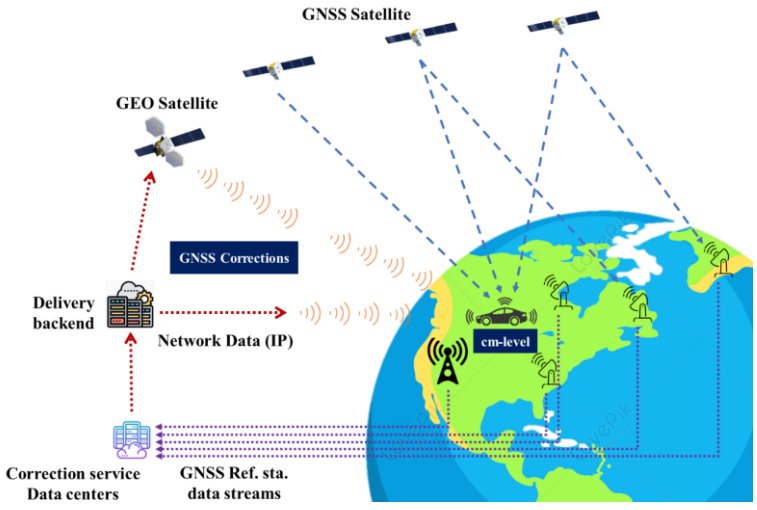

Figure 1-1 GNSS augmentation information service system[2]

[1] https://www.gsc-europa.eu/gnss-market-applications/augmentation-providers-map
[2] https://www.embedded.com/gnss-correction-service-enhances-position-accuracy/

PPP technology has been rapidly improved with the ongoing development of real-time technology (Malys & Jensen 1990; Zumberge et al. 1997; Kouba & Héroux 2001). Relying on precise orbit and clock products, allowing the Ambiguity Resolution (AR) technology achieved in real-time absolute positioning service (Ge et al. 2007). Moreover, the utilization of external atmosphere information from the reference network contributes to the rapid convergence of the positioning.

In principle, a real-time GNSS augmentation system includes data collection, correction information generation, high-frequency correction broadcast, and user realization. Utilizing global observation data, precise orbit, clock, and signal delay products can be obtained. Moreover, regional reference networks can further provide stable and highly accurate tropospheric and ionospheric delays. Additionally, multiple forms can be employed for generating and transmitting correction information for different purposes. Ultimately, users achieve positioning by utilizing the received information.

1.2 Motivation and objective

High-precision augmentation information is typically only available in small regions. However, with the continuous advancements in GNSS ground station network deployment and product generation, it has become possible to extend high-precision augmentation to larger areas. Nevertheless, the expansion of augmentation from regional to large-scale areas still faces challenges such as unreliable AR, imprecise atmospheric delay correction, and the need for handling massive correction information. To address these challenges, numerous studies have been conducted.

1.2.1 Integer ambiguity resolution

In order to achieve precise parameter estimation, the carrier phase measurement, which is significantly more accurate than the pseudo-range, plays a vital role (Blewitt 1989; Dong & Bock 1989). However, in GNSS observation, the receiver can only precisely measure the fractional part of the carrier phase and account for its increase when the signal is tracked continuously, but the integer part could be lost due to the signal transmission impact, e.g., ionospheric and tropospheric delays, etc. Additionally, due to the hardware delay which is not an integer value, and the separation of integer ambiguities in estimation becomes unattainable. As a result, integer AR was exclusively conducted for double-differenced ambiguities, from which hardware delays were eliminated. These hardware delays are also termed as uncalibrated phase delays (UPD). To restore the integer property of ambiguities, only their fractional parts are of

significance. In practice, solely the fractional part is estimated and applied. Therefore, in the context of this study, UPD also denotes the fractional component of UPD.

Based on separating the fractional part delay of satellite and receiver side biases from ambiguities can determine the integer part of the ambiguity (Ge et al. 2007; Collins 2008; Paul 2008; Laurichesse et al. 2009). Once hardware delays are eliminated, constraining ambiguities to integers can significantly improve positioning accuracy (Li et al. 2015, 2016). Generally, the AR is based on Ionosphere-Free (IF) combination to eliminate the first-order ionospheric delays in data processing; however, its ambiguity is separated into Wide-Lane (WL) and Narrow-Lane (NL) for fixing. The WL ambiguity fixing is carried out first by Melbourne-Wübbena (MW) combination as the prerequisite of NL fixing because WL ambiguity can be easily estimated and fixed due to its long wavelength (Melbourne 1985; Wübbena 1985). In contrast, the NL ambiguity fixing needs a lot of effort to improve the performance of IF ambiguity estimates (Ge et al. 2007; Collins 2008; Paul 2008; Laurichesse et al. 2009). While being provided directly to users, the NL UPD can also be implicitly expressed, for example, merged into satellite clock corrections as decoupled or integer clocks (Collins 2008; Laurichesse et al. 2009). These three methods have different expressions but are equivalent in principle.

1.2.2 Pseudo-range biases correction

The resolved integer ambiguities are not always true in the deterministic sense, and wrong integer ambiguities can seriously bias the fixed solution (Verhagen 2004; Verhagen & Teunissen 2012). In AR, the pseudo-range and carrier phase observations are used, and thus, both could impact the UPD estimation and AR. Compared with carrier phase observation with an accuracy of about 3 mm, the pseudo-range only achieves decimeter-level accuracy due to the code length dependent. The biases that existed in the pseudo-range could also jeopardize the ambiguity fixing rate and fixing reliability because the WL UPD and IF ambiguity are sensitive to the biases or noise of pseudo-range observations (Duong et al. 2019; Xiao et al. 2019). Even small contamination could directly affect the integer feature, resulting in incorrect or failed AR (Li et al. 2018). It is demonstrated that signal biases exist in pseudo-ranges due to different channels and tracking methods, which prevents using mixed signal types in data processing (Langley 1998). Nowadays, parallelly used Differential Signal Biases (DSB) and Differential Code Biases (DCB) products are adopted for the pseudo-range biases correction (Li et al. 2012; Wang et al. 2015; Wang et al. 2020), in which DSB provides for all signals and DCB only for P and C/A codes without detailed classification. Additionally, the bias correction values are also different between DCB and DSB products, which could introduce differences in data processing.

In addition, the different pseudo-range observations could also be biased with respect to

different types of receiver realization of manufacturers (Hauschild & Montenbruck 2014; Liu et al. 2016b). With an increasing number of receiver types involved in GNSS data processing, the receiver-related biases are often overlooked or probably such biases are considered to be small and negligible compared to the pseudo-range noise and WL wavelength (Fan & Ma 2014; Seepersad & Bisnath 2014). Even though studies highlight the code biases for pseudo-range corrections, sub-divided signal biases and receiver-type-related satellite-specific deviations in the pseudo-range could further affect the UPD accuracy and AR, which hinders the application of all available signals and receiver types.

1.2.3 Precise atmosphere augmentation

Due to a strong correlation between atmospheric delay, ambiguity, and receiver coordinates, the PPP has to take a long time to separate these parameters and achieve an accurate solution. Therefore, the AR still takes a relatively long time, limited by the initially poor parameter accuracy (Ge et al. 2007). As presented, PPP based on regional networks overcomes these limitations and gives centimeter-accuracy in a few seconds (Teunissen & Khodabandeh 2014) with the help of regional atmospheric delay corrections. Relying on accurate AR implemented on each reference station, the precise tropospheric and ionospheric delays or compacted observation corrections can be precisely derived from the reference stations (Wübbena et al. 2005; Zhang et al. 2011). Consequently, the derived information can be used to separate the estimable parameters, and thus accelerating the AR.

Utilizing the Observation Space Representation (OSR) form offers the advantage of providing more detailed information of all observations at the reference network. However, it comes with the drawback of requiring approximately twice or even more communication volume compared to atmospheric delay State Space Representation (SSR) form, depending on the number of frequencies involved (Fotopoulos & Cannon 2001). In addition, the OSR-based interpolation is limited by the inter-station distance and observation signal selection due to the condition of inter-satellite common-view and interpolation errors (Hirokawa et al. 2021). Therefore, the separation and modeling of the various error sources, including ionospheric and tropospheric delays, improves performance and reduces the bandwidth required for transmission in larger area service (Agency 2019), which is the advantage of the atmosphere-based augmentation mode (Wübbena et al. 2005). It can more accurately describe the error sources characteristics and could be represented by mathematical functions.

Generally, the ionospheric delay can be mitigated by the IF combination using dual-frequency observations or estimated as an epoch-wise parameter for the un-combined solution (Laurichesse et al. 2010). For multi-frequency and multi-GNSS applications, providing external

precise ionospheric delay is beneficial to reduce the convergence time. For global real-time application, Klobuchar and NeQuick models are provided in broadcast ephemeris (Klobuchar 1987; Coïsson et al. 2006; Vuković & Kos 2017; Bilitza 2018; Liu et al. 2021). Moreover, to provide an improved precision model, the Global Ionosphere Map (GIM) with hourly IONEX (The IONosphere Map EXchange) model is supplied with a 2.5°×5° sampled global grid [3]. However, both of these models have a poor precision of about 2.7 TECU (Total Electron Content Unite) (Liu et al. 2021). On the other hand, precise ionospheric delay corrections could be provided via dense station networks in small or medium regions with high network capability (Psychas et al. 2019b; Li et al. 2021). For example, the Quasi-Zenith Satellite System (QZSS) constellation cm-level service is implemented by dense stations via 30 km grid points [4]. Moreover, the ionospheric delay also can be directly achieved by interpolation modes from nearby reference stations or fitting models generated on all coverage reference stations (Li et al. 2019; Liu et al. 2019; Ren et al. 2019; Boisits et al. 2020; Liu et al. 2021; Zhao et al. 2021). However, a conflict is between the model correction data volume and the represented precision of the model. In other words, a high-precision model inherently requires a larger number of parameters and input resources (Banville et al. 2022).

In addition, using the tropospheric delay estimates of a regional GNSS reference network, a correction model can be generated and broadcast to the users within the region, that is, the tropospheric delay augmentation (Takeichi et al. 2009; Fund et al. 2010; Kalinnikov et al. 2012). Compared to the ionospheric delay, the tropospheric delay has slightly moderate variations, and thus, the modeling sophistication is lower. Similar with ionospheric delay, the regional tropospheric delay augmentation model also can be represented in the form of grid point (Rózsa et al. 2020; Li et al. 2021) or the polynomial function model (Shi et al. 2014; Zou et al. 2017; Zhou et al. 2019). To fit the properties of the tropospheric delay, an improved Optimal Fitting Coefficient (OFC) model is further proposed (Shi et al. 2014; Cui et al. 2022). However, it is still only achieved in regional areas (50-500 km), and modeling performance is impacted by altitude changes (de Oliveira et al. 2016).

Furthermore, the external corrections always have differences between the true atmospheric delay and model generated, therefore, a stochastic model is essential to describe the accuracy of corresponding corrections, i.e., atmospheric delay uncertainty (Psychas et al. 2019b; Psychas et al. 2021). The constraint type can be classified into weighted, free, and constant modes (Zha et al. 2021; Banville et al. 2022). When the weight of the constraint is close zero or infinite, it evolves into the free or constant model (Li et al. 2022). The free constraint equals the ionospheric delay estimation with a limited contribution to convergence. In contrast, the constant constraints are

[3] https://cddis.nasa.gov/Data_and_Derived_Products/GNSS/atmospheric_products.html
[4] https://qzss.go.jp/en/

applicable only in small areas (up to 100 km), and medium regions (200 km) under quiet ionosphere periods (Li et al. 2010; Psychas et al. 2019a; Psychas et al. 2019b; Li et al. 2021), which is challenging for applications in large areas. The weighted model introduces a stochastic model to characterize the accuracy of external atmosphere corrections, enabling online adaptation to account for correction inhomogeneity and differences in large-area applications. Some adopting of constraint online methods are also gradually applied to ionospheric delay (Teunissen et al. 2010; Zhang et al. 2011; Nadarajah et al. 2018; Aggrey & Bisnath 2019; Wang et al. 2019). Compared with the constant and free constraint, the weighted constraint can rapidly decorrelate the parameters, and thus, the accurate determination of atmospheric delay uncertainty is also essential for atmosphere information applications (Cherniak et al. 2018; Psychas et al. 2021; Li et al. 2022). Additionally, the majority of studies in the field have primarily focused on the ionosphere, given its significant variation. In contrast, the tropospheric delay has received relatively little attention.

1.2.4 Objective and methodology

In order to achieve high-precision real-time positioning, previous studies have typically been conducted in small regions with massive corrections (Teunissen & Khodabandeh 2014; Psychas & Verhagen 2020; Li et al. 2021; Zha et al. 2021; Banville et al. 2022; Cui et al. 2022). By relying on precise real-time orbit and clock product streams, it becomes possible to achieve accurate atmospheric delay at individual stations and provide accurate models for large areas. When performing positioning in large areas, a conflict arises between correction accuracy and service area size. Striking a balance between modeling precision and communication volume becomes crucial, as high-precision modeling naturally demands a dense network of stations to deliver precise and detailed augmentation data. This implies that the extensive data volume of precise correction information still poses a significant challenge for real-time data transmission in large-area services.

Generally, in small regional augmentation, the same receiver type with consistent signals are achieved in service end for precise correction generation with reliable AR. However, in large-area services, observations of different signals are usually included because receivers of different types and from various manufactures. The existing deviations in the pseudo-range measurements, in turn, jeopardize the reliability of AR and limit the utilization of pseudo-range observations in large-area applications. Furthermore, ensuring reliable AR across all types of receiver and signals is also a prerequisite for achieving precise solutions at the user and server end. Based on reliable AR achieved in all augmentation reference stations, precise tropospheric and ionospheric delays, along with their corresponding uncertainty information, can be modeled

and broadcast to users. However, the current fitting models for tropospheric ZWD in large-area still have restrictions; this is, modeling performance degradation due to altitude differences increasing. Additionally, the requirements of dense stations and massive correction volume pose challenges in term of the service area size. Apart from the models, real-time calculating uncertainty information to describe the specific model precision is also crucial for augmentation applications. Moreover, implementing a suitable data broadcast strategy to enable real-time high-precision positioning is crucial in large-area services.

The primary objective of this thesis is to establish a high-precision real-time augmentation system for large areas. With a focus on minimizing data communication burdens and accommodating various receiver types and signals, the augmentation system aims to achieve accurate signal delay deviations, precise atmospheric delay corrections, and proper uncertainty information. It is essential to identify the characteristics of different pseudo-range signal biases and receiver-type-dependent satellite-specific deviations to ensure unbiased AR in precise orbit, clock, and UPD calculation and the accurate recovery of integer ambiguities. Furthermore, performing accurate analysis and constructing the atmospheric delay model is crucial. This involves considering the properties of atmospheric delays to generate precise corrections and proper uncertainty information for real-time positioning in large-area services. By achieving these objectives, the proposed high-precision real-time augmentation system provides an effective solution for large-area positioning, ensuring reliable and accurate positioning results while optimizing data communication efficiency.

Specifically, the following questions will be discussed in this thesis separately.

- How to calibrate deviations of pseudo-range from different types of signals or receivers used in data processing to improve the ambiguity fixing rate?
  - For the pseudo-range signal biases correction products, i.e., DSB and DCB, what impact existed in data processing by using the different corrections?
  - What impact does the signal selection in data processing affect the product generation and AR?
  - How about these signal systematic and stochastic noises?
  - For the increasing receiver types, how to estimate the biases and classify the receiver types with similar corrections?
  - How to calibrate the deviations in order to improve the estimated UPD reliability and accuracy?
- How does the atmospheric delay modeling and uncertainty information generation in the large area?
  - How to model tropospheric delay in large-area with significant altitude difference use

sparse station-network?

- How to generate a satellite-wise ionospheric delay model in large-area considering properties of slant delay? What is the impact of different types of receiver on ionospheric delay modeling?
- What is the relationship of these models among station-spacing and precision of fitting and interpolation models?
- How to establish ionospheric and tropospheric delays uncertainty information for large-area describing generated corrections to provide proper constraints?
- How to describe the significant variation of ionospheric delay by an index which measures the amplitude of the uncertainty?

- How to achieve accurate and rapid positioning with AR in large-area?
  - What is relationship between large-area model and unmodeled residual corrections and how to integrated them in positioning?
  - How to overcome the conflict among data volume, correction precision, and coverage areas to deal with large-area service communication issues?

In addition to addressing the aforementioned questions, this thesis goes beyond the scope of large areas modeling and deviation calibration by also exploring the regional augmentation. The aim is to investigate the feasibility of integrating regional services, characterized by high precision and a large amount of data, with sparse networks that have lower precision and a smaller amount of data. An integrated system can be established by incorporating regional services into the large-area service framework. This study determines the compatibility and effectiveness of such integration, considering the correlating characteristics of dense regional services and sparse networks.

Based on the GeoForschungsZentrum GFZ real-time GNSS Analysis Center (AC), in this study, the large-area augmentation system is established. The system includes satellite- and receiver-end signal biases calibration, the retrieval of atmospheric delays from real-time PPP-AR at all reference stations, modeling of augmentation information, which includes both atmospheric delay, uncertainty information, and the UPD, and the realization of the real-time augmentation at user stations. The augmentation system takes advantage of the real-time multi-GNSS orbit and clock products at GFZ AC and is validated by the European Permanent GNSS Network stations.

The reliable AR is crucial as it serves as a prerequisite for deriving atmospheric delays and achieving precise positioning. Initially, the satellite signal and receiver type deviation are analyzed and calibrated so that reliable AR can be achieved in all reference stations. The modeling of tropospheric ZWD and ionospheric slant delay is then introduced separately for large areas, taking into account their respective properties. It should be noted that accurate

uncertainty is also essential, and thus, the uncertainty information is calculated for large-area and regional corrections. The integration of regional interpolation into the large-area fitting model demonstrates significant data volume savings and much better performance achieved in regional augmentation. The successful implementation of the large-area model and the incorporation of regional unmodeled biases lay the foundation for integrated systems.

1.3 Outline

The outline of this thesis is as follows:

Chapter 1 introduces the motivation and objective, main contributions, and outline.

Chapter 2 briefly describes the basic theoretical background of GNSS and the PPP function and stochastic models. The error sources in the observations and their correction models and parameterization in GNSS data processing are briefly described. The parameter estimation methods, i.e., least squares and Kalman filtering, are both presented.

Chapter 3 provides a concise summary of the implementation methods of the large-area augmentation system in this study, including the estimation and calibration methods for satellite-signal and receiver-related biases, UPD estimation, atmosphere model generation, calculation of residual unmodeled corrections, and the method for generating atmosphere uncertainties, as well as positioning methods with AR and external atmosphere information applied in users.

Chapter 4 presents the estimation and calibration of satellite signal and receiver-type-related satellite-specific deviations. Ensuring reliable AR across all types of receivers and effectively handling the characteristics of satellite signals and their impact on orbit, clock, and UPD products. The chapter begins by describing the criteria for estimating and correcting signal biases, followed by a comparison of the relationship and differences between the signal and code, along with their respective correction products. The generation and assessment of orbit, clock, and UPD products are performed with different signal settings and correction products applied. Additionally, the analysis and comparison of signal systematic and stochastic noises are conducted. Subsequently, methods for estimating and calibrating receiver-type-related deviations are introduced, which are also applied to the remaining augmentation server end of this thesis. The performance of deviation calibration is demonstrated in AR at the end of this chapter.

Chapter 5 introduces methods for atmospheric delay modeling and uncertainty information calculation in large areas. The tropospheric ZWD model is modified to account for significant

altitude differences in modeling. A new satellite-wise fitting model is proposed to model ionospheric slant delays in large areas, considering the relationship between delay and propagation path length in the ionosphere. Furthermore, the performance of ionospheric delay modeling is analyzed and compared across different receiver types. The uncertainty information for large areas atmospheric delay fitting model is derived by utilizing the fitting residuals and represented in form of grid values. Additionally, the relationship between modeling, interpolation precision, and the reference station distance is analyzed to generate the error function for calculating regional ionospheric delay uncertainty, which is then applied to the hierarchical augmentation positioning system described in Chapter 6.

Chapter 6 demonstrates the advantage of a proposed hierarchical augmentation positioning, which applies atmosphere modeling and deviation calibration methods proposed in previous chapters. In order to achieve rapid/instantaneous convergence and high-precision positioning in large areas, the regional unmodeled errors are integrated with large-area models as optional compensation, which is also determined by the indexes of the large-area uncertainty grids. Relying on regional compensation and interpolation error function, the instantaneous positioning is achievable in large areas with less data transmission volume.

Finally, the major findings and conclusions are summarized in Chapter 7, along with further prospects.

2 Global Navigation Satellite Systems: Theory

In this chapter, the theoretical background of GNSS techniques is introduced. The main GNSS constellation's signals and frequencies are presented in general. The data processing method, including observation model, error correction models, and parameter estimation methods, are then introduced concisely, which serves as the fundamental role for the GNSS implementation in the following chapters. This chapter ends with a summary of the main conclusions.

2.1 Global navigation satellite systems

In this section the basic background about GNSS is described. Four GNSS constellations and their signals are presented.

2.1.1 Multi-GNSS constellations

Since the establishment of the Global Positioning System (GPS), four worldwide navigation systems have provided public services until the present. As of September 2022, the United States GPS, Russia's Global Navigation Satellite System (GLONASS), China's BeiDou Navigation Satellite System (BDS), and the European Union's Galileo are fully operational in providing service to global users. Japan's QZSS and Indian Regional Navigation Satellite System (IRNSS) are regional systems with focus on providing regional augmentation to the global systems.

An overview of the overall GNSS architecture and the four existing global systems is given before detailing the GNSS principle and data processing, followed by a discussion of its signal structure. In this thesis, the four major systems, i.e., GPS, GLONASS, Galileo, and BDS, are used and described. Figure 2-1 shows the distribution of Multi-GNSS satellites.

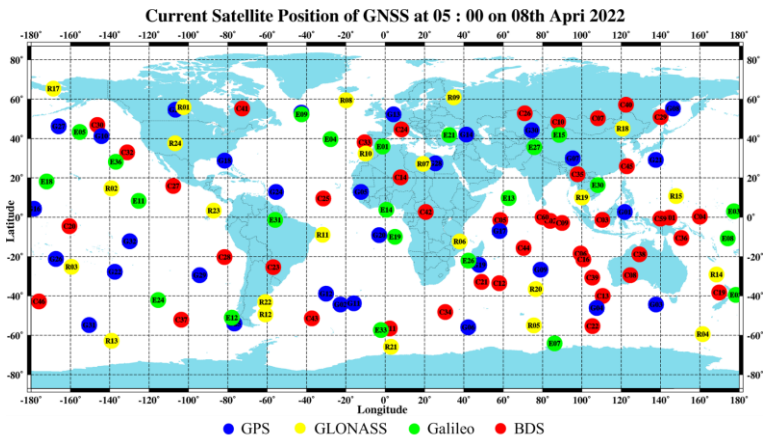

Figure 2-1 Current satellite position of Multi-GNSS at 8th April, 2022

Arranging the satellite with different orbital planes, each including several satellites, can enable at least four satellites available to users anywhere on the planet. The basic constellation information of the four systems are presented in Table 2-1.

Table 2-1 Multi-GNSS satellite time and constellation information

Type		GPS	GLONASS	BDS	Galileo
Time	First Launch	1978	1982	2000	2011
	Fully operational	1995	2011	2020	2023
	Constellation Time Format	Continuous timescale	GLONASS Time	Continuous timescale	Continuous timescale
	starting time	Jan 6, 1980	UTC	Jan 1, 2006	Aug 22, 1999
	Standard Time Format	UTC (USNO)	UTC(SU)	UTC (NTSC)	TAI
	Relation with UTC	$GPST = UTC \pm T_{leap}$	$GLOT = UTC_{SU} \pm 3\ hour$	$BDST = UTC_{NTSC}$	$GALT = UTC - \Delta_{sec}$
MEO	Satellite number	32	24	24	29 (24 designed)
	Orbital altitude	20200 km	19100 km	23222 km	21528 km
	Orbital period	11°58’	11°15’44’’	14°4’45’’	12°53’24’’
	Inclined angle	55°	64.8°	56°	55°
	Orbital planes	6	3	3	3
IGSO	Satellite number	\	\	\	12 (3 designed)
	Orbital altitude				35786 km
	Inclined angle				55°
GEO	Satellite number	\	\	\	8 (3 designed)
	Orbital altitude				35786 km
	Inclined angle				58.75°E, 80°E, 110.5°E, 140°E, 160°E

GPS

GPS satellite system was the earliest global satellite navigation system, from the first satellite launched in 1978, after 16 years to complete the constellation and ground tracking/monitoring network and provide open services. Currently (as of Sept 1st, 2022), there are 32 GPS satellites in orbit, of which 7 are Block IIR satellites, 7 are Block IIR-M satellites, 12 are Block II-F satellites, and 4 are modern GPS III satellites [5]. Among them, 7 Block IIR satellites are legacy satellites, and others are modernized satellites. The current GPS Operational Control Segment (OCS) includes a master control station, an alternate master control station, 11 command and control antennas, and 16 monitoring sites.

[5] https://www.gps.gov/systems/gps/space/

In addition, the GPS time, which starts at 00:00 Coordinated Universal Time (UTC) on January 6th, 1980, is based on a set of atomic clocks at monitor stations and onboard satellites to provide a continuous time scale. Since it is not perturbed by leap seconds, as of June 2022, the GPS is now 18 seconds ahead of UTC.

GLONASS

GLONASS is a global system established by Russia. It started to provide a worldwide service in 1995. Currently, there are 24 satellites on-orbit operating in three orbital planes [6]. The earlier GLONASS and GLONASS-M satellites use Frequency Division Multiple Access (FDMA) signals, while later, the new GLONASS-K1 and GLONASS-K2 satellites adopt Code Division Multiple Access (CDMA) signals.

The GLONASS Central Synchroniser generates GLONASS Time, and the difference between the UTC and GLONASS Time should not exceed one millisecond plus three hours (consider difference between Moscow Time and Greenwich Mean Time) [7]. It's worth mentioning that, unlike GPS, Galileo, or BeiDou, the GLONASS time scale, like UTC, uses leap seconds.

BDS

China BDS, originally called COMPASS, has been incrementally evolved. The BDS constellation is developed from the initial experimental system Beidou-1, through the regional Beidou-2, to the present global Beidou-3 system. Currently, the primary services are provided by the globally BeiDou-3 and regionally BeiDou-2 satellites. The Beidou-2 space segment includes 5 geostationary orbit (GEO), 6 inclined geostationary orbit (IGSO), and 3 medium circular orbit (MEO) satellites (Wickert et al. 2020). The BeiDou-3 satellite space segment includes 24 MEO, 3 IGSO, and 3 GEO satellites [8].

BDS Time (BDT) is a continuous time scale that began at 0h UTC on January 1, 2006, and is synchronized with UTC within 100 ns.

Galileo

Galileo is Europe's GNSS providing improved positioning and timing information with significant positive implications for many European services and users. As of Sept 1st, 2022, 26 satellites are on-orbit, including 4 In-Orbit Validation (IOV) and 22 Full Operational Capability (FOC) satellites

[6] https://www.glonass-iac.ru/
[7] https://gssc.esa.int/navipedia/index.php/Time_References_in_GNSS#cite_note-2
[8] http://en.beidou.gov.cn/SYSTEMS/System/

[9]. The Galileo FOC satellites have the same capabilities as the preceding IOV satellites but with better performance, such as the increased transmit power. Galileo is on track to complete its constellation in 2023.

The Galileo time maintains a continuous-time scale synchronized with International Atomic Time (TAI) with a small offset of fewer than 50 ns. The Galileo time start epoch is defined as 00:00 UT on Sunday, August 22, 1999.

2.1.2 Signal and frequency

Increasingly, with navigation systems modernization, more frequencies are becoming available. GPS and GLONASS satellites begin to provide the third frequency at L5 and G3 bands at May 2010 [10] and February 2011 [11], respectively. The BDS-3 and Galileo satellites provide five frequencies in different bands. The frequency bands and distribution are shown in Figure 2-2.

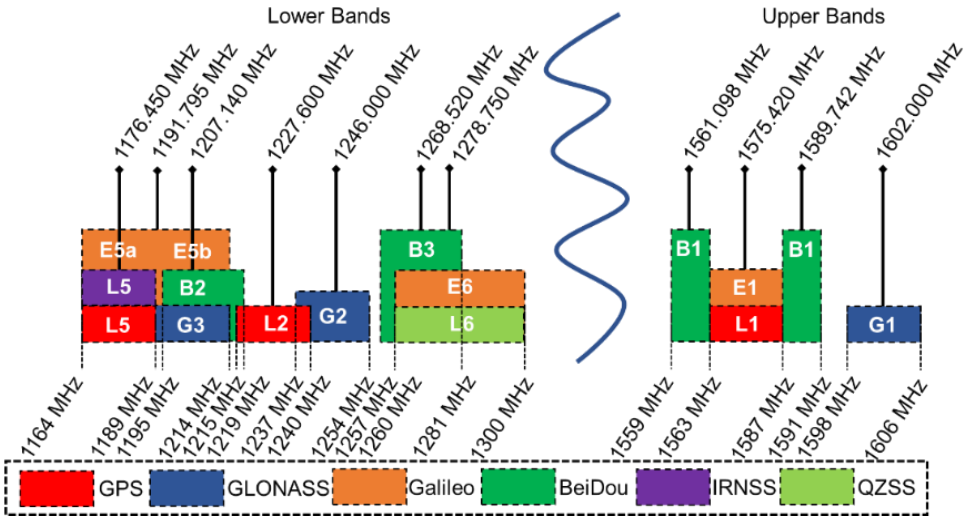

Figure 2-2 Multi-GNSS frequencies bands information

Depending on the receivers' hardware modulation mechanisms of the signal tracking process and channels utilized, different GNSS signals are generated in the same frequency observations. Detailed signal types are distinguished and given separately in the RINEX (Receiver Independent Exchange Format) file. The frequency and signal information of the four constellations are listed in Table 2-2.

[9] https://www.gsc-europa.eu/
[10] https://www.gps.gov/systems/gps/modernization/civilsignals/#L5
[11] https://www.gps.gov/systems/gps/modernization/civilsignals/#L1C

Table 2-2 Multi-GNSS frequency and signal information (Rinex 3.05)

System	Frequency/MHz	Signal
GPS	L1/1575.420	CSLXPWYM
	L2/1227.600	CDSLXPWYM
	L5/1178.450	IQX
GLONASS	G1/1602.000+k×9/16 k=-7,…,+12	CP
	G1a/1600.995	ABX
	G2/1246.000+k×7/16	CP
	G2a/1248.06	ABX
	G3/1202.025	IQX
Galileo	E1/1575.420	ABCXZ
	E5/1176.450 (E5a)	IQX
	E6/1278.750	ABCXZ
	E8/1191.795 (E5)	IQX
	E7/1207.140 (E5b)	IQX
BDS	B1/1575.420 (B1)	IQXA
	B2/1561.098 (B1-2)	IQX
	B5/1176.450 (B2a)	DPX
	B6/1268.520 (B3)	IQXA
	B7/1207.140 (B2b)	IQXDPZ
	B8/1191.795 (B2)	DPX

1 The frequency in brackets is defined in the RINEX document.
2 The frequency presented is observed in the Rinex observation file.

Currently, multi-signal and multi-frequency observations provide more opportunities and more challenges for high-precision data processing. However, not all IGS stations can receive the new signals, and the majority part of receivers can only observe the legacy dual-frequency signals.

2.2 GNSS observable model

GNSS signals are transmitted from the antenna on the satellite side and received by the antenna on the receiver side. Therefore, they are affected by different disturbance sources. Precise data processing must carefully handle these delays to achieve accurate estimates. This section describes the basic principles of the observation model and stochastic model in GNSS data processing.

2.2.1 GNSS observation equation

The raw GNSS observations in the unit of length between station r and satellite s take the form of,

$$\begin{cases} P_{r,f}^{s} = \vec{e}_r^{s}(\vec{x}^{s} - \vec{x}_r) + c(dt_r - dt^{s}) + T_r^{s} + \gamma_f I_{r,1}^{s} + c\left(b_{r,f} + b_f^{s}\right) + \varepsilon_{P,f} \\ L_{r,f}^{s} = \vec{e}_r^{s}(\vec{x}^{s} - \vec{x}_r) + c(dt_r - dt^{s}) + T_r^{s} - \gamma_f I_{r,1}^{s} + \lambda_f N_f + c\left(d_{r,f} + d_f^{s}\right) + \varepsilon_{L,f} \end{cases} \tag{2.1}$$

Where:

s, r, f	satellite, receiver, and frequency band;
$P_{r,f}^{s}, L_{r,f}^{s}$	pseudo-range and carrier phase measurements;
$\vec{e}_r^s$	unit vector from receiver to satellite;
$\vec{x}_r$	receiver coordinates vector;
$\vec{x}^s$	satellite coordinates vector;
c	speed of light;
dt_r, dt^s	receiver and satellite clock offsets;
T_r^s	slant tropospheric delay mapped from the zenith values, including ZHD, ZWD, and gradients;
$I_{r,1}^{s}$	ionospheric delay along the line-of-sight from satellite s to receiver r at the frequency $L1$, and $\gamma_f = f_1^2/f_f^2$;
λ_f	wavelength;
N_f	phase ambiguity;
$d_{r,f}, d_f^s$	carrier phase delays in receiver and satellite-side;
$b_{r,f}, b_f^s$	pseudo-range biases in receiver and satellite-side;
$\varepsilon_{P,f}, \varepsilon_{L,f}$	pseudo-range and carrier phase measurements noise.

A wavelength measurement is usually accurate to within 1%. Pseudo-range observations are limited in accuracy by the very long equivalent wavelength, e.g., around 300 m for GPS C/A-code and 30 m for P-code. On the other hand, the wavelength of the L1 signal is about 19 cm. Therefore, obtaining much more accurate positioning requires the use of carrier phase observations.

It is essential for precise positioning with carrier phase observations to handle all the terms in the observation equations carefully. Some can be corrected with models, but some have to be estimated as unknown parameters.

2.2.2 GNSS stochastic model

In GNSS data analysis, not only the function model but also the stochastic model should be considered. Therefore, before parameter estimation, the stochastic model of the system needs to be determined, which involves the level of accuracy of the observations and the stochastic parameter properties. The commonly used methods of determining stochastic models include the satellite elevation angle, Signal-to-Noise Ratio (SNR), variance component estimation methods, and the signal- or constellation-dependent observed precision.

Stochastic model based on elevation angle

To consider the multi-path effects and modeling errors of atmospheric delays, the low-elevation observations could be down-weighted in different ways, that is, the stochastic model based on elevation angle. Here the following model (Ge et al. 2007) is presented and adopted in this thesis.

$$P(e) = \begin{cases} 1, & e \geq 30 \\ 2\sin(e), & e < 30 \end{cases} \tag{2.2}$$

Stochastic model based on signal-to-noise ratio

To some extent, the receiver SNR can present the observation noise level, reflecting the multi-path effect, antenna gain, internal receiver circuitry, and other data quality elements of the observed data.

The signal strength index I is usually available after the phase data with two digitals in RINEX observation files, and the SNR value can be derived from the signal strength index using the following equation (Wieser & Brunner 2014),

$$S = \begin{cases} 9, & int(I/5) > 9 \\ int(I/5), & other \end{cases} \tag{2.3}$$

where S is the signal-to-noise ratio. Correspondingly, its stochastic model is,

$$\sigma_i^2 = C_i \cdot 10^{\frac{-S}{2}} \tag{2.4}$$

where $C_1 = 0.00224\ m^2Hz$, and $C_2 = 0.00077\ m^2Hz$, i is frequency.

2.3 GNSS observation modelling

The observations are affected by different disruptions, including delays related to GNSS satellites, signal transmission paths, and GNSS receivers, as shown in Figure 2-3.

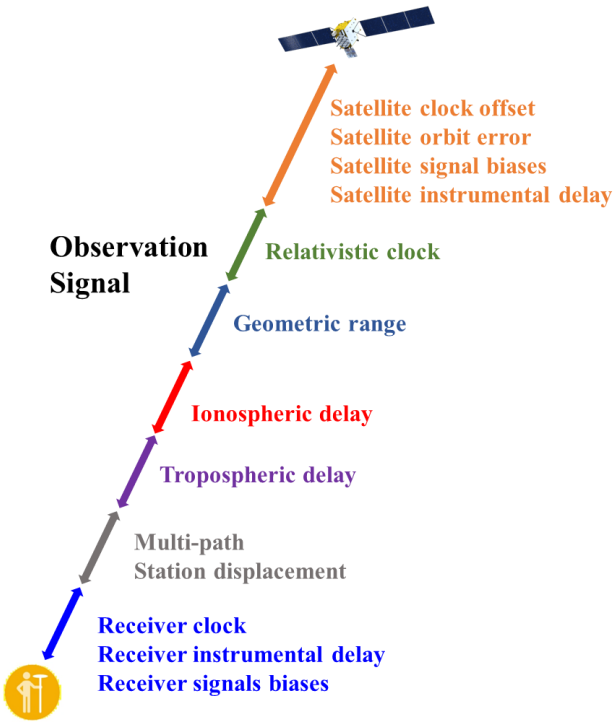

Figure 2-3 Different errors in the GNSS satellite signal transmission

The delays on the satellite side mainly consist of satellite clock offset, orbit, relativistic effects, Sagnac Effect, and hardware bias. The satellite signals travel in space through the atmosphere and suffer considerable delays in the ionosphere and the troposphere. The delays at the receiver side are mainly composed of station displacement, i.e., ocean tide, solid tide, and pole tide, receiver hardware bias, multi-path effect, and receiver clock. In addition, phase wind-up, antenna offsets, and signal biases also impact observations. The details of each disruption and its correction model are illustrated in this section.

2.3.1 GNSS signal delay

GNSS observations from different signals have systematic biases due to various hardware delays or tracking and modulation methods. GNSS signal delays are usually unknown and divided into pseudo-range and carrier phase delays for their observations.

In pseudo-range, the biases are usually divided into two categories, i.e., satellite signal-related biases and receiver-type-related biases. The satellite signal-related biases can be corrected by DSB or DCB product, but the receiver type-related biases in data processing are usually ignored, which have to be pre-estimated and calibrated for AR. In addition, the carrier phase delay is very crucial for undifferenced integer AR. Their fractional part can be estimated from a reference network and provided to user for PPP-AR (Ge et al. 2007; Paul 2008; Laurichesse et al. 2009).

In the UPD estimation, pseudo-ranges are also employed, therefore, the biases in the pseudo-range could jeopardize carrier phase ambiguous integer characteristics and UPD accuracy if the pseudo-range is not calibrated thoroughly. Therefore, it is crucial to calibrate the pseudo-range biases, which could impact the convergence time and AR (Cui et al. 2021).

2.3.2 Satellite orbit and clock biases

Orbit bias refers to the error in the calculated position of a satellite relative to its true position, stemming from uncertainties in the satellite's orbit. The navigation system relies on precise orbit determination techniques to mitigate this bias. Clock bias, on the other hand, pertains to the error in the satellite's onboard atomic clocks when compared to reference time. Precise clock synchronization is vital for accurate positioning. Generally, the real-time satellite orbit and clock offset are provided directly by real-time product stream.

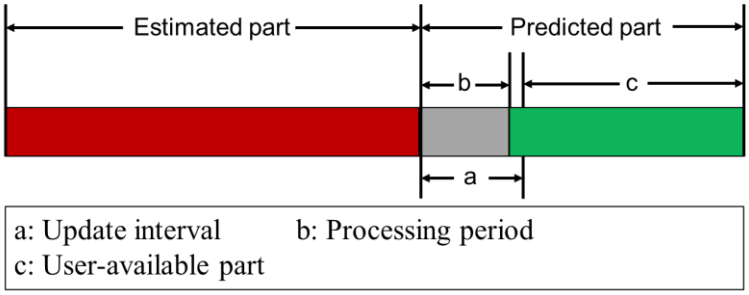

Figure 2-4 Real-time orbit and clock estimation and prediction

In GFZ's real-time product generation process, satellite orbits are estimated every hour, and predictions are generated for three hours. Clock corrections are estimated every five seconds and are broadcast in real-time with a 15-second latency. The update interval for both orbit and clock corrections is set at five seconds.

With continuous improvement, the real-time orbit and clock precision is sufficient for high-precision service. Figure 2-5 shows the Root Mean Square (RMS) values of orbit differences of the GFZ real-time orbit products with respect to the GBM products. The 1-D RMS ($\sqrt{(A^2 + C^2 + R^2)/3}$) of orbit differences between real-time products and GBM products are 38.3, 53.9, 46.8, 60.6, and 86.2 mm for GPS, GLONASS, Galileo, BDS-3, and BDS-2 constellations, respectively. Among them, the GPS satellites have the best precision, followed by the Galileo, GLONASS and the BDS-3 satellites. In contrast, the four BDS-2 MEO satellites show the worst performance.

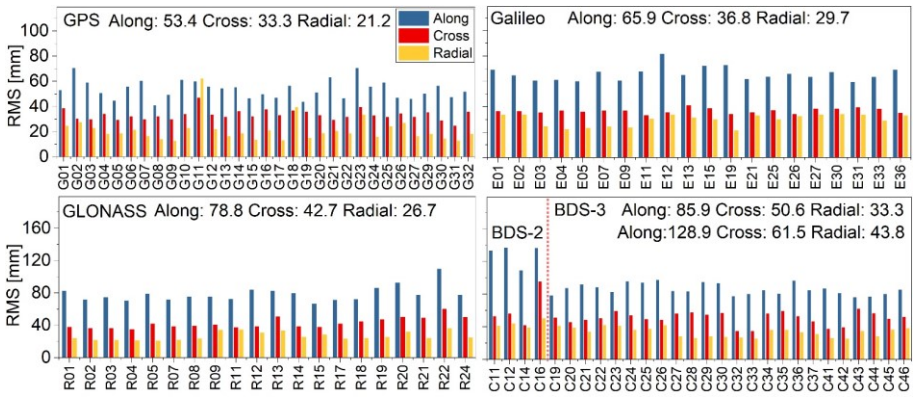

Figure 2-5 RMS comparison of orbit differences between GFZ real-time products and GBM products. (DOY 001-180, 2022)

The precision of multi-GNSS clocks over 180 days in 2022 is presented in Figure 2-6. The GBM clock products are selected as the reference to calculate the differences for all satellites in experiment periods. Due to the datum differences in clock precision calculation, the average satellite clock offsets are set as the reference.

It should be noted that the orbital radial and clock biases exhibit a strong correlation, as both of these biases arise from the direction of signal transmission. Therefore, the radial differences between the real-time orbits and GBM products are calculated first, and then compensated in the clock comparison (Montenbruck et al. 2014b). The Galileo and GPS satellites have comparable accuracy, around 0.08 ns, which is better than the BDS and GLONASS satellites. The GLONASS satellites have the largest STD values compared to other systems, with an average value of 0.14 ns.

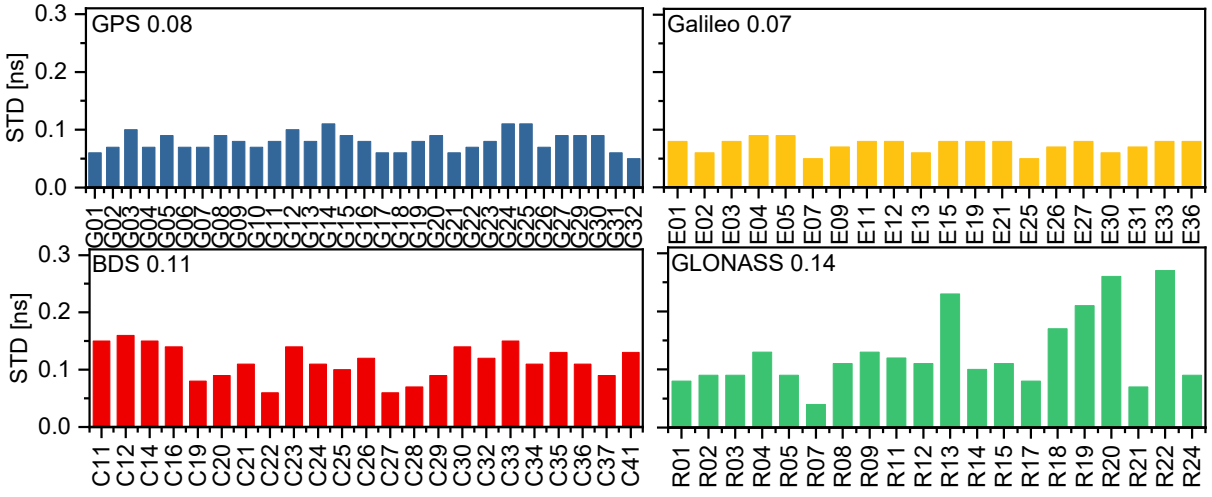

Figure 2-6 STD values of satellite clocks with respect to GBM product.

2.3.3 Tropospheric delay

The Zenith Tropospheric Delay (ZTD) is usually divided into Zenith Hydrostatic Delay (ZHD) and ZWD (Davis et al. 1985). ZHD can be precisely modeled given the surface pressure (Saastamoinen 1972), whereas ZWD is related to the water vapor content, which can hardly be precisely modeled because of its rapid variations in time and space (Bevis et al. 1992; Hadas et al. 2013, 2016).

In GNSS processing, the total slant tropospheric delay at an elevation angle e and azimuth angle α can be written as,

$$T_r(e,z) = mf_h(e) * ZHD + mf_w(e) * ZWD + mf_g(e) * (cos(z) * G_n + sin(z) * G_e) \tag{2.5}$$

where $mf_h(e)$, $mf_w(e)$, and $mf_g(e)$ are mapping functions of ZHD, ZWD, and gradients, respectively; G_n and G_e are the horizontal gradients in the north and east directions, respectively.

In general, the ZHD can be precisely calculated using the Saastamoinen model (Saastamoinen 1972).

$$ZHD_{saas} = \frac{0.0022767 \times P}{1 - 0.00266 \times \cos(2\varphi) - 0.00028 \times h} \tag{2.6}$$

where P is the atmospheric pressure in hPa, φ is ellipsoidal latitude, h is surface height above the ellipsoid.

The atmosphere pressure can be derived for a specific receiver location from the GPT2w (Böhm et al. 2014) model and the mapping function can be calculated by Vienna Mapping Function 1 (VMF1) (Boehm et al. 2006). In addition, ZWD is often estimated as a unknow parameter in data processing because it is hard to model accurately.

2.3.4 Ionospheric delay

The ionospheric delay is frequency-related and satisfies the relation if high-order terms are ignored,

$$\frac{I_{r,j}^s}{I_{r,i}^s} = \frac{f_j^2}{f_i^2} \tag{2.7}$$

Thereafter, the ionospheric delay is usually mitigated by the IF combination of the dual-frequency observations or estimated as a station-satellite-pair parameter in the uncombined

mode (Zumberge et al. 1997; Kouba & Héroux 2001).

Un-Differenced and Un-Combination method

The accurate ionospheric delay are essential to accelerate the PPP convergence and AR. Therefore, at the server end after precise orbit, clock and UPD products are made available in real-time, the Un-Differenced and Un-Combined PPP-AR (UDUC-PPP-AR) mode can be used to derive the ionospheric delay, which is provided for users as external constraints to facilitate a rapid convergence.

Ionosphere-Free combination

Generally, the IF combination can eliminate the first order effect of the ionospheric delay, but the high-order ionospheric delay is still retained in the observations. It is formed by the combination of dual-frequency carrier phase or pseudo-range observations (Blewitt 1989).

$$P_{IF} = \frac{f_i^2 * P_i - f_j^2 * P_j}{f_i^2 - f_j^2}; L_{IF} = \frac{f_i^2 * L_i - f_j^2 * L_j}{f_i^2 - f_j^2} \tag{2.8}$$

where P_{IF} and L_{IF} are IF combination pseudo-range and carrier phase observation, respectively. This thesis uses the IF combination observation in the Precise Orbit Determination (POD), Precise Clock Estimation (PCE), and UPD estimation.

2.3.5 Sagnac effect

The Sagnac effect is a phenomenon caused by the Earth rotation. In most positioning applications, the Earth-fixed coordinate system is used to calculate the position of the receiver and the satellite orbits are also provided in the Earth-fixed system. Since the Earth-fixed coordinate system is not an inertial coordinate system, it rotates and with the Earth rotation. As a result, the Earth-fixed coordinate system corresponding to the moment of satellite signal transmission and the moment of receiver signal reception is different. Therefore, it is essential to consider the Sagnac effect in signal travel time from the satellite to the receiver in the Earth-fixed coordinate system.

The Sagnac effect can be corrected as (Ashby 2004),

$$\delta_\omega = \frac{\omega_E \times r_r \cdot (r_r - r^s)}{c} \tag{2.9}$$

where $r^s = (x^s, y^s, z^s)$ and $r_r = (x_r, y_r, z_r)$ are satellite and receiver coordinates at GPST T_t; $\omega_E = 7.2921151467 \times 10^{-5}\ rad\ s^{-1}$ is the Earth's rotation rate.

2.3.6 Relativistic effect

The relativistic effect is the phenomenon of relative clock offset between the satellite clock and the receiver clock due to the different states of clock operating, e.g., the speed of motion and the gravity potential. The relativistic effects are split into four parts in the GNSS applications (Ashby 2003).

The first two constant rate correction terms have the values.

$$\delta_{rel,con} = \frac{3 \cdot G \cdot M_E}{2 \cdot a \cdot c^2} + \frac{\Phi_0}{c^2} \tag{2.10}$$

where $G \cdot M_E = 3.986004418 \times 10^{14} m^3 s^{-2}$ is the product of Earth's mass times the Newtonian gravitational constant; G is the universal gravitational constant; M_E is the total mass of the Earth; a is the orbit semi-major axis; The Φ_0 includes the scale correction needed in order to use clocks at rest on the earth's surface as references and the value of Φ_0 can be determined at the equator.

$$\frac{\Phi_0}{c^2} = -\frac{G \cdot M_E}{a_1 \cdot c^2} - \frac{G \cdot M_E \cdot J_2}{2 \cdot a_1 \cdot c^2} - \frac{\omega_E^2 \cdot a_1^2}{2 \cdot c^2} = -6.96927 \times 10^{-10} \tag{2.11}$$

where $a_1 = 6.3781370 \times 10^6$ is the earth's equatorial radius; $J_2 = 1.0826300 \times 10^{-3}$ is the Earth's quadrupole moment coefficient.

The result of this equation is a negative value, which means that the standard clock in orbit is beating too faster, primarily because its frequency is gravitationally blueshifted (Ashby 2003). Therefore, the satellite clock frequency is adjusted lower than that on the ground, so that the above relativistic effect is automatically considered in signal generation.

Second, the noncircular orbits of satellites are eccentric, which causes a periodic variation in the satellite clock frequency. The classical periodic satellite clock correction can be described as follows (Kouba & Héroux 2000),

$$\delta_{rel,ecc} = 2\frac{r_I^s(t) \cdot v_I^s(t)}{c} \tag{2.12}$$

where $r_I^s(t)$ and $v_I^s(t)$ are geocentric satellite position and velocity vectors in an inertial

reference frame.

The third term describes the satellite clock traveling through a varying gravitational potential caused by Earth's oblateness. The additional periodic satellite clock correction can be explained by gravitational field expansion,

$$\delta_{rel,J2}(t) = J_2 \cdot \frac{3}{2} \cdot \frac{a_E^2}{c} \cdot \sqrt{\frac{u_E}{a^3}} \cdot sin^2 i \cdot \sin 2u\,(t) \tag{2.13}$$

where a_E is the semi-major axis of the mean Earth; i and u are the orbit inclination and the argument of latitude $u(t) = \omega_E + v(t)$, the sum of the argument of perigee ω and the true anomaly $v(t)$.

Fourth, the Earth's gravitational field causes a propagation delay in the satellite signal, and the space-time curvature can be described as,

$$\delta_{stc} = \frac{2 \cdot \mu_E}{c^2} \cdot \ln\left(\frac{\|r^s\| + \|r_r\| + \rho_r^s}{\|r^s\| + \|r_r\| - \rho_r^s}\right) \tag{2.14}$$

where $\|r^s\|$ is the distance from the satellite to the center of the Earth; $\|r_r\|$ is the distance from the station to the center of the Earth; ρ_r^s is the geometric distance from the station to the satellite.

2.3.7 Ground displacement

Earth's changing varies in time, i.e., gravitational forces and the deformability of the Earth's surface. Therefore, to estimate stable and precise receiver coordinates, the effects of Earth solid tides, pole tides, and ocean loading need to be modeled and corrected. This correction is given by (IERS 2010),

$$disp_r(t) = disp_{r,solid}(t) + disp_{r,ocean}(t) + disp_{r,pole}(t) \tag{2.15}$$

where the components described in IERS,

$disp_{r,soild}(t)$ is solid tide of the Earth, caused by lunar and solar gravitational attraction;

$disp_{r,ocean}(t)$ is ocean tide caused by lunar and solar gravitational attraction;

$disp_{r,pole}(t)$ is pole tides of the Earth based on EOP data and Earth's mean pole;

2.3.8 Antenna offset

The precise orbit products give the coordinates at the satellite mass center and the measurements of the ground receiver are referred to Antenna Phase Center (APC), which is frequency-dependent. Therefore, GNSS Antenna Reference Point (ARP) without frequency-dependent is more suitable as the reference. The differences between the benchmark and antenna phase center should be corrected in the observation modeling. It includes the constant offset, i.e., the constant values between the benchmark and the ARP, the Phase Center Offset (PCO), i.e., frequency-dependent constant between the ARP and the mean phase center, and Phase Center Variation (PCV), i.e., the signal azimuth and zenith angle-dependent correction between phase center and electric phase center (Schmid et al. 2005).

$$\delta r_i(t) = dr_{ARP} + pco_i + pcv_i(a, z) \tag{2.16}$$

where $\delta r_i(t)$ is the carrier phase offset; pco_i is the PCO correction value; and the $pcv_i(a, z)$ is the PCV correction value; dr_{ARP} is the offset between the measurement point and the ARP. The PCO and PCV corrections are usually provided by the (IGS) Antenna Exchange Format (ANTEX) products.

2.3.9 Phase wind-up

The phase wind-up describes the relative change of the orientation of carrier phase wavelength cycles between transmitting and receiving antennas (Wu et al. 1993). The satellite makes the signal transmitting antenna rotate slowly with the satellite's motion to keep the solar sail pointing at the sun, and the receiver antenna of kinematic platforms also rotates.

The phase wind-up correction is modeled as,

$$\delta_{pwu_r^s} = sign(\xi) \cdot \cos^{-1}\left(\frac{\overrightarrow{D^s} \cdot \overrightarrow{D_r}}{\left\|\overrightarrow{D^s}\right\| \cdot \left\|\overrightarrow{D_r}\right\|}\right) \tag{2.17}$$

where ξ is defined as,

$$\xi = \vec{k} \cdot (\overrightarrow{D^s} \cdot \overrightarrow{D_r}) \tag{2.18}$$

where $\vec{k}$ is the unit vector from transmitter to receiver, and $\overrightarrow{D^s}$ is defined as,

$$\overrightarrow{D^s} = x^s - \vec{k} \cdot \left(\vec{k} \cdot x^s\right) - \vec{k} \times y^s \tag{2.19}$$

where x^s and y^s are dipole unit vectors in body-fixed system satellite (x^s, y^s, z^s) effective dipole vector of the transmitting antenna, and $\overrightarrow{D_r}$ is defined as,

$$\overrightarrow{D_r} = x_r - \vec{k} \cdot \left(\vec{k} \cdot x_r\right) - \vec{k} \times y_r \tag{2.20}$$

where x_r and y_r are dipole unit vectors in local reference system receiver (x_r, y_r, z_r) effective dipole vector of the receiving antenna.

Knowing the satellite attitude is necessary to calculate the phase wind-up effect. Therefore, it is necessary to accurately model the attitude of all the navigation satellites when considering the phase wind-up effect in GNSS applications.

It is essential to note that users should use the same navigation satellite attitude model for UPD estimation. Otherwise, the AR on user-side positioning will be biased or irresolvable.

2.3.10 Multipath effect

The multipath effect occurs when the signal direct from a satellites is interfered by indirect signals reflected by the station surroundings, causing biased observations and weakening the signal strength. Severe multipath effects may lead to the loss of locking of satellite signals.

Several strategies could be used to mitigate and reduce the multipath effects, whereas no method can totally remove it. Choosing a suitable site, equipping a diameter suppression plate, or extending the observation time can effectively reduce the multipath effects (Irsigler 2008,2010). Since satellite signals at low elevation angles are more susceptible to multipath effects, setting a proper cut-off elevation angle can reduce the effects (Counselman 1999; Tatarnikov et al. 2016). In addition, the effects of multipath errors on the positioning solutions can also be reduced to some extent by methods such as sidereal day filtering and wavelet analysis (Moradi et al. 2014; Dong et al. 2015).

2.3.11 Receiver clock offset

Most receivers only equip the quartz clock, which has a low stability than the atomic clock and it is hard to model its clock offsets with mathematical models. Therefore, the receiver clock offset of each observed epoch is usually estimated as a white noise.

Currently, the MGEX stations and some regional augmented server stations are equipped with external high-precision Rubidium or Hydrogen atomic clocks to improve the stability and performance.

2.4 Quality control in data processing

The quality of observations directly determines the estimation performance. Outliers and cycle slips in pseudo-range and carrier phases compromise observation accuracy and impact the solution. Detecting outliers in the observations is essential.

Before data processing, the initial step is pre-quality control. Observations with an elevation angle greater than 7 will be excluded due to their increased susceptibility to outliers, cycle slips, and high levels of noise. Subsequent quality controls are performed for pseudo-range, carrier phase, receiver clock, and real-time products.

In addition, for minor outliers, cycle slips, or errors in orbit and clock data, quality control is conducted based on post-processing residuals. Multiple iterations can help identify outliers and reduce the weighting of biased observations or exclude error-prone satellites.

2.4.1 Pseudo-range outlier detection

The essential pseudo-range observation is a measurement of time difference. Outliers are introduced into the observation due to the low precision and stability of the receiver clock, the satellite environment, and the disturbances in the transmission of observations from the satellite to the receiver. Generally, for pseudo-range quality checks, the inter-frequency observations, e.g., P1 and P2, are used to check whether the differences are within thresholds (200 m).

2.4.2 Carrier phase cycle slip detection

During continuous observation, satellite signals are influenced by external factors such as obstructions and interference, leading to temporary signal loss, which interrupts the internal counter of the receiver. As a result, the phase integer cycle exhibits a sudden jump or interruption, and this phenomenon is defined as a cycle slip.

Blewitt (1990) proposed the TurboEdit algorithm for coarse and circumferential hop detection for un-differential observations, which utilizes the combination of MW combinations and Geometry-Free (GF) combinations. The detection threshold value for MW and GF are set as

follow,

$$MW\begin{cases} > 15s & ,2\ cycle \\ 1s-15s & ,1.5\ cycle, \\ < 1s & ,1\ cycle \end{cases} \quad GF\begin{cases} > 15s & ,0.15\ m \\ 1s-15s & ,0.1\ m \\ < 1s & ,0.05\ m \end{cases} \tag{2.21}$$

2.4.3 Receiver clock jump detection

Receivers utilize inexpensive internal oscillators to synchronize their internal clocks with GNSS time to prevent significant clock bias. This synchronization is achieved through periodic clock resets. Although the specific methods used for adjusting the clock in receivers may vary among manufacturers, two common approaches are employed. The first involves steering the oscillator to maintain a near-zero clock bias, resulting in a constant offset within the range of noise and tracking jitter. The second, more frequent method, introduces discrete time jumps in the receiver's time estimation, which will introduce a clock jump into observations.

Relying on analysis, the receiver clock jump can be detected by observing differences between the pseudo-range and carrier phase, pseudo-range and pseudo-range (Guo and Zhang 2014).

2.4.4 Real-time products interruptions

In real-time service, orbit and clock corrections are provided via the product stream. However, unstable internet connections or failed solutions can prevent real-time products from reaching users. Therefore, a prediction model is necessary to ensure temporary product availability for users. For orbit prediction, the Lagrange interpolation method is used to interpolate the orbit based on estimated results. A second-order polynomial fitting model is employed for clock prediction.

2.5 Parameter estimation

In the data processing of this study, the Least-squares adjustment is performed in server-end for generating products, and the Kalman filter is used for user-end positioning.

2.5.1 Least-squares adjustment

The basic principle of GNSS data processing is to solve a system of equations and minimize the sum of post-fit observation residuals formed by the observed values and calculated theoretical

delay (Farebrother 2001). Least-squares adjustment is well known and used extensively for GNSS data processing.

Assuming the observation y is a function of the parameters x,

$$y = F(x) \tag{2.22}$$

In contrast, the calculated observations $\hat{y}$ using the approximate parameters $\hat{x}$ is as,

$$\hat{y} = F(\hat{x}) \tag{2.23}$$

Generally, the observed value y and the calculated value $\hat{y}$ exist difference, i.e., l.

$$l = y - \hat{y} \tag{2.24}$$

where l is the vector of OMC. Considering the noise in observation, the equation can write as,

$$A\Delta x - l = v, \;\; \hat{x} = \tilde{x} + \Delta x \tag{2.25}$$

where v is the vector of observation residuals, A is the design matrix, Δx is the correction of the unknow $\hat{x}$, and $\tilde{x}$ is the approximates values.

$$A = \frac{\partial F}{\partial x}\Big|_{x=\tilde{x}} \tag{2.26}$$

The parameters can be solved accurately with the sum of squares of the residuals minimized for all observations. Since the observable conditions are constantly changing and there is a considerable variation in the quality of the observations, the accuracy of the parameter estimates can be effectively adjusted by adding weights P.

P is a weight-matrix set according to the observation noise or elevation angle. For observation i, the weights are defined as squares of the ratios of a priori sigma value σ_0 and observation noise σ_i. The values $P_{i,i}$ on its diagonal set as,

$$P_{i,i} = (\frac{\sigma_0}{\sigma_i})^2 \tag{2.27}$$

By adding weights P to the observations, the correction of the $\hat{x}$ can be estimated as,

$$\Delta x = (A^T PA)^{-1}(A^T Pl) \tag{2.28}$$

To solve the complexity of high-order matrix inversion and enhance the efficiency of the solution, recursive or sequential least-square methods are usually used instead of least-squares estimation. The least-square method is used to perform POD, PCE and UPD estimation (Liu et al. 1995).

2.5.2 Kalman filter

The Kalman filter is more suitable for dynamic positioning solutions owing to the addition of the state transfer matrix (Kalman 1960; Kalman & Bucy 1961), which uses a recursive algorithm to update state parameters from the a priori information of the parameters and new observations. Generally, it only needs to store the value of the state parameters and their variance-covariance information of the previous epoch without storing all the historical observations simultaneously. Hence, the Kalman filter estimation method has high computational efficiency. The equation is expressed as follows,

$$\begin{cases} X_k = \Phi_{k,k-1} \cdot X_k + w_k \\ L_k = \mathrm{H}_k \cdot X_k + v_k \end{cases} \tag{2.29}$$

where X_k is the state vectors and observations at epoch $t(k)$; $\Phi_{k,k-1}$ is the state transfer matrix from epoch $t(k-1)$ to $t(k)$; w_k is the system noise vector; L_k is the observations at epoch $t(k)$; H_k is the coefficient matrix; v_k is the noise of observation.

$$\begin{cases} E(w_k) = 0, Cov\{w_k, w_j\} = E\left[w_k w_j^T\right] = Q_k \delta_{kj} \\ E(v_k) = 0, Cov\{v_k, v_j\} = E\left[v_k v_j^T\right] = R_k \delta_{kj} \\ Cov\{w_k, v_j\} = E\left[w_k v_j^T\right] = 0 \end{cases} \tag{2.30}$$

where Q_k and R_k are the variance matrix of the system noise sequence (Symmetric Nonnegative Definite Matrix) and the variance matrix of the measurement noise (Symmetric positive definite matrix), respectively. δ_{kj} is Kronecker function,

$$\delta_{kj} = \begin{cases} 1, (k = j) \\ 0, (k \neq j) \end{cases} \tag{2.31}$$

The state parameters that usually need to be estimated in positioning include receiver position, velocity, receiver clock offset, ZWD, slant ionospheric delay at the first frequency, and

ambiguities. Given the initial value of the system state $X_0 = \hat{X}_0$ and variance p_0. The extended Kalman filtering can estimate the state estimate $\hat{X}_k$ at time $t(k)$ by recursive form.

a) Predicted (a priori) state estimate

$$X_{k,k-1} = \Phi_{k,k-1} \cdot \hat{X}_{k-1} \tag{2.32}$$

b) Predicted (a priori) estimate covariance

$$P_{k,k-1} = \Phi_{k,k-1} \cdot P_{k-1} \cdot \Phi_{k,k-1}^T + Q_{k-1} \tag{2.33}$$

c) Filter Gain

$$K_k = P_{k,k-1} \cdot H_k^T \cdot (\mathrm{H}_k \cdot P_{k,k-1} \cdot H_k^T + R_k)^{-1} \tag{2.34}$$

d) Updated (a posteriori) state estimate

$$\hat{X}_k = X_{k,k-1} + K_k \cdot (L_k - H_k \cdot X_{k,k-1}) \tag{2.35}$$

e) Updated (a posteriori) estimate covariance

$$P_k = (I - K_k \cdot H_k) \cdot \mathrm{P}_{k,k-1} \tag{2.36}$$

where I is the unit matrix; $X_{k,k-1}$, $P_{k,k-1}$ are predicted (a priori) state estimates and predicted (a priori) estimates covariance, respectively; K_k is the gain matrix; $\hat{X}_k$ and P_k are values of filter estimates and their variance-covariance matrix, respectively. To reduce the sensitivity of the filter algorithm to computational rounding errors and ensure the symmetric positivity of the P_k in practical calculations. Eq. (2.36) is generally written as follows,

$$P_k = (I - K_k \cdot H_k) \cdot \mathrm{P}_{k,k-1} \cdot (I - K_k \cdot H_k)^T + K_k \cdot H_k \cdot K_k^T \tag{2.37}$$

From the above recursive equations, it is noted that Kalman filtering is a continuous prediction and correction (updating) process, which integrates current observations with past system information to determine the optimal filter value. From the using state information and measurement information sequence, the Kalman filter has two updating processes: time updating and measurement updating.

2.6 Chapter summary

This chapter describes the basic principle and delay modeling in GNSS observation and is summarized as follows.

Section 2.1 describes the concept, background, and signal system of the four major global GNSS constellations, i.e. GPS, GLONASS, Galileo, and BDS. An example of the global MGEX station network is presented, and the each GNSS constellation signals are given.

Section 2.2 illustrates the function model and stochastic models of GNSS observation. The raw observation equation of GNSS is presented. Moreover, the stochastic model of elevation angle and the signal-to-noise ratio are also described.

Section 2.3 details each error source in GNSS observation, including satellite-related, signal transmission-related, and receiver-related.

Section 2.4 describes the quality control of the estimators used in data processing.

Section 2.5 presents the parameter estimation methods on the server-end and user-end.

- The least-square method is used in server-end data processing, including POD, PCE, and UPD estimation.
- The Kalman filter method is used in user-end positioning.

3 GNSS Augmentation Service

The implementation of large areas augmentation system developed in this study is presented in this Chapter. The data processing strategy at the server- and user-end, including biases calibration, UPD estimation, atmospheric delay modeling, and integrated positioning modes, is then introduced.

3.1 System structure

The augmentation system data processing flowchart is shown in Figure 3-1, which is described in the following sections.

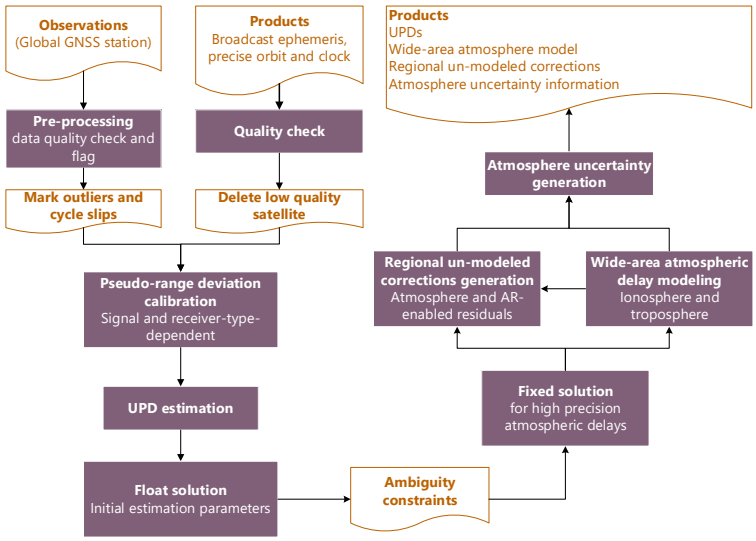

Figure 3-1 Flowchart of large-area augmentation system structure

The augmented system at server end is mainly devided into four parts: deviation calibration, UPD estimation, atmosphere augmentation information generation.

With observations collected from global stations and precise orbit and clock products from the GFZ real-time AC product stream, the data pre-processing and product quality check are performed in advance. Moreover, the satellite signal biases and receiver-related deviations need to be calibrated. Once the UPD has been successfully solved, the UPD and the precise orbit and clock products are provided to all reference stations to estimate precise atmospheric delays through UDUC-PPP-AR methodology. For the atmosphere augmentation modeling in large areas, the tropospheric ZWD can be modeled directly, but the ionospheric delay should be modeled after removing the pseudo-range-related Satellite Plus Receiver (SPR) biases.

Although the fitted model of a low polynomial is not such accurate for all covered areas, it can

shorten the PPP-AR time to three minutes with appropriate constraints. By further providing residual atmospheric delays in case a dense reference network is available and communication capacity is sufficient, instantaneous PPP-AR can be achieved at user-end. In addition, the constraint on the corresponding atmosphere parameter is essential and both should always be used together.

3.2 Pseudo-range bias calibration

Pseudo-range biases are generally categorized as either satellite signal-related and receiver-type-related biases.

For satellite signal biases correction, typically involves the use of products such as DCB, DSB, or Observable-specific Signal Biases (OSB) (Jefferson et al. 2001; Montenbruck et al. 2014a; Wang et al. 2015; Wang et al. 2020). Satellite end products can be estimated and provided as corrections in advance.

For receiver end, these products, i.e., DCB/DSB/OSB, only provide one value for the same signal. However, the satellite-specified characteristics are usually ignored, i.e., for some signals, different satellites have different biases, which in fact, must be properly tackled in precise data processing. Generally, receivers of the same type are equipped in the small region and observe the same signals, which keeps the consistent performance and delays in the received observations. However, in the context of large-area services, various types of receivers are utilized across the service areas. This diversity in receiver types usually leads to variations in observed signals, which, in turn, can introduce deviations and adversely affect the AR. Moreover, these deviations also pose challenges in accurately estimating atmospheric delays. Therefore, receivers of different types may have different satellite-specified range delays at the receiver-end, which have to be handled in advance.

This section provides a description of the methods employed for estimating and correcting pseudo-range biases that are dependent on satellite signals and receiver types.

3.2.1 Signal bias estimation

The GNSS pseudo-range observations obtained from different frequencies and/or bands exhibit biases in their measurements as the result of varying signal modulation modes or hardware differences. In precise data processing, a combination of observations from multiple signal types is typically employed to maximize the utilization of available data. To determine which observations to use, a priority list is established based on factors such as the number of

observed stations and the signal-to-noise ratio (SNR) values. In this thesis, a descending-order priority list is utilized, as presented in Table 3-1. Accordingly, the first signal available in the list is selected for processing. It is important to note that the signals chosen at different frequencies may not necessarily be the same due to differences in their availability. Consequently, these signal discrepancies can introduce biases in the data processing and should be addressed through pre-correction measures.

Table 3-1 The signal priority list for different constellations and frequencies

System	Signal priority list
GPS	L1&L2:PWCSLXYM / L5:IQX
GLONASS	L1&L2:PC / L3:IQX / L4&L6:ABX
Galileo	E1&E6:BCX / E5&E7&E8:IQX
BDS	B1&B2&B6&B7:IQX / B5&B8:DPX

In the estimation, the intra-frequency and inter-frequency biases are estimated separately, which are described in the following sections.

Intra-frequency signal biases

Since the ionospheric delay is frequency-dependent, ionospheric delays for signals of the same frequency are the same. Therefore, intra-frequency signal bias can be determined directly by the difference between pseudo-ranges observations (Jefferson et al. 2001).

$$P_{i,x} - P_{i,y} = \left(DSB^{s}_{i,x-y} + DSB_{r,i,x-y}\right) = \left(b_{r,i,x} - b_{r,i,y}\right) + \left(b^{s}_{i,x} - b^{s}_{i,y}\right) \tag{3.1}$$

where $P_{i,x}$ and $P_{i,y}$ are pseudo-range observations of frequency i on x and y signals, respectively; $DSB^{s}_{i,x-y}$ and $DSB_{r,i,x-y}$ are biases between signals x and y on satellite- and receiver-ends, respectively; $b_{r,i}$ and b^{s}_{i} are receiver- and satellite-ends signal biases, respectively.

Because of the large noise of the pseudo-range observations, more accurate biases can only be obtained by averaging the observations over a long period.

$$SPR_{i,x-y} = \frac{1}{N}\sum_{k=1}^{N}\left(P_{i,x} - P_{i,y}\right) = \frac{1}{N}\sum_{k=1}^{N}\left(DSB^{s}_{i,x-y} + DSB_{r,i,x-y}\right) \tag{3.2}$$

where SPR is the combination of biases on satellite and receiver sides. After obtaining the SPR values at all stations, the biases at the receiver and satellite ends are calculated through a least-squares adjustment. The satellite-related biases are subject to a zero-mean condition to

establish the datum.

Inter-frequency signal biases

Unlike the intra-frequency signal bias, to estimate the inter-frequency signal bias, the ionospheric delay has to be carefully considered. For the inter-frequency signal bias estimation, the ionospheric delay, including SPRs, can be obtained by the "pseudo-range-levelled carrier phase" approach to improve observables accuracy by reducing the noise and multipath effects (Mannucci et al. 1998). Using this method, the SPRs are mixed with ionospheric delays, which is expressed as,

$$\begin{cases} \hat{I}_k = v \times STEC_k + c \times SPR_{i-j,x-y} + \delta \\ SPR_{i-j,x-y} = DSB^s_{i-j,x-y} + DSB_{r,i-j,x-y} \end{cases} \tag{3.3}$$

where $\hat{I}_k$ is the smoothed ionosphere TEC measurement at epoch k; $v = 40.28 \times 10^{16} \times (f_i^{-2} - f_j^{-2})$; f_i and f_j are the frequencies i and j of carrier phase; $STEC$ is the line-of-sight ionosphere TEC along the signal propagation path from satellite to receiver, and δ is the noise of ionosphere measurement. From Eq. (3.3), the estimated ionospheric delay $\hat{I}^s_{r,1}$ also can be expressed as,

$$\hat{I}^s_{r,1} = v \times STEC_k + c \times SPR_{i-j,x-y} = v \times VTEC_r(d\varphi, d\lambda) * M(e) + c \times SPR_{i-j,x-y} \tag{3.4}$$

where $M(e)$ is the mapping function from Vertical TEC (VTEC) to Slant TEC (STEC); $d\varphi$ and $d\lambda$ are the latitude and longitude differences with respect to the reference point.

In order to separate the SPRs and ionospheric delay, the accurate modeling of ionospheric delay is required, which can be individually modeled by the generalized trigonometric series (GTS) function on each station based on a thin-layer approximation (Wang et al. 2015). The model has been demonstrated to describe ionospheric delay variations using single-day data effectively (Li et al. 2012). The single-station-based ionospheric delay model is more flexible and adaptable on each reference station, free of station distribution and number limitations (Li et al. 2012; Li et al. 2014). The single-station VTEC model can be expressed as follow,

$$\begin{cases} VTEC(d\varphi, d\lambda) = \sum_{p=0}^{p_{max}} \sum_{q=0}^{q_{max}} \{E_{pq}(d\varphi)^p \cdot (d\lambda)^q\} + \sum_{k=1}^{k_{max}} \{C_k \cos(k \cdot t) + S_k \sin(k \cdot t)\} \\ M(e) = [1 - sin^2(el)/(R_E/(H_{ion} + R_E))^2]^{-1/2} \\ t = \dfrac{2\pi(t_{cal} - 14)}{T}, \quad (T = 24) \end{cases} \tag{3.5}$$

where p, q, and k are the degrees of polynomial and Fourier series expansions, with the

corresponding maximum degrees p_{max}, q_{max}, and k_{max}, respectively; E_{pq}, C_k, and S_k are the model coefficients to be estimated on each station; t is the local time; H_{ion} is the altitude of the ionosphere single-layer shell as 350 km; and R_E is the mean radius of the earth as 6378 km. In this thesis, the p_{max}, q_{max}, and k_{max} are set as 2, 2, 4, respectively (Wang et al. 2020).

The latitude $d\varphi$ and longitude $d\lambda$ in Eq. (3.5) are calculated as follows,

$$\begin{cases} d\varphi = ds * \cos(\varphi_{dif}), \quad d\lambda = ds * \sin(\varphi_{dif}) \\ ds = (R_E + H_{ion}) * \lambda_{dif} \\ \lambda_{dif} = \arcsin\left(\sin(\lambda - \lambda_0) * cos\varphi / sin\varphi_{dif}\right) \\ \varphi_{dif} = \arccos\left(sin\varphi_0 * sin\varphi + cos\varphi_0 * cos\varphi * \cos\left(\lambda - \lambda_0\right)\right) \end{cases} \tag{3.6}$$

where φ_{dif} and λ_{dif} are latitude and longitude of the Ionosphere Pierce Point (IPP) in spherical cap coordinate system; (φ_0,λ_0) and (φ, λ) are latitude and longitude in geographic coordinates system of station and the IPP, respectively.

After modeling the ionospheric delays for all satellites on each station, a local VTEC model is constructed, allowing the separation of the SPRs X_{spr}^T from the ionospheric delays. The X_{cof}^T is the GTS model fitting coefficients. In signals biases calculation, the least-square adjustment method is introduced to separate the SPRs X_{spr}^T into satellite biases X_{sat}^T and receiver-side biases X_{rec}^T by applying a sum-as-zero constraint of all satellites. For the ionospheric delay model application, we do not need to further separate these into satellite- and receiver-end biases.

$$\begin{cases} \hat{X}_{spr+cof} = \left[\underbrace{X_{spr}^T}_{1*n}, \underbrace{X_{cof}^T}_{1*17}\right] \\ L_{spr} + V = A\hat{X}_{sat+rec} \\ \hat{X}_{sat+rec} = [X_{sat}^T, X_{rec}^T] \end{cases} \tag{3.7}$$

where L_{spr} includes each station all satellites SPRs; subscript sat and rec are satellite and station number, respectively.

Inter-system biases

Inter-system bias (ISB) plays a crucial role in the integrated processing of multi-GNSS constellations (Likasa et al. 2003; Khodabandeh & Teunissen 2016). The ISB represents the hardware delay offset experienced by signals from different constellations within a receiver. It arises from the correlations within the receiver and can range from a few nanoseconds to several hundreds of nanoseconds. It is important to note that ISB exists not only for pseudo-range signals but also for carrier phase signals. The hardware differences in the carrier phase can be compensated by adjusting the phase ambiguities.

Theoretically, an individual receiver clock parameter should be set for each system due to the timing and frequency differences. Given the slight variation in the ISB parameter, it can even be treated as a constant value or estimated with a tight constraint. This allows for the effective introduction of a constant ISB parameter between two systems in the solution. In Eq. (3.24) and Eq. (3.25), the ISB between GPS and BDS and Galileo satellites are simultaneously estimated with other estimable parameters.

3.2.2 Signal biases calibration

Generally, in data processing, intra-frequency signal bias should be corrected first and usually the W signal is selected as the reference to maintain the uniformity of the products.

$$\hat{P}_{CiW} = P_{Cix} - DCB_{Cix-CiW} \tag{3.8}$$

where P_{Cix} denotes the raw pseudo-range observations on signal x of frequency i; $\hat{P}_{CiW}$ is the corresponding W signal pseudo-range converted from the x signal.

After correcting the intra-frequency signal bias, the ranges are aligned to the W signals of each frequency, then the inter-frequency signal bias must be corrected as well.

As IGS has been using IF combination of P1 and P2 (or C1W and C2W) since its beginning, the products are based on the P1 and P2 without range biases correction. In order to keep the consistency of the products, the inter-frequency bias correction is determined not to change its IF observations (Schaer 2012). For IF combination using L1 and L2 frequencies, the bias converted between P_{C1W} and P_{C2W} signals measurements is defined as follows,

$$\begin{cases} b_{C1W} = DSB_{C1W-C2W} * \beta_{IF} \\ b_{C2W} = DSB_{C1W-C2W} * \alpha_{IF} \end{cases} \tag{3.9}$$

$$\begin{cases} \alpha_{IF} = \dfrac{{f_1}^2}{{f_1}^2 - {f_2}^2} \\ \beta_{IF} = \dfrac{{f_2}^2}{{f_1}^2 - {f_2}^2} \end{cases} \tag{3.10}$$

where α_{IF} and β_{IF} are transition coefficients in IF combination. The converted biases are added to the selected signal observations.

$$\begin{cases} \bar{P}_{C1W} = P_{C1x} - DCB_{C1x-C1W} + b_{C1W} \\ \bar{P}_{C2W} = P_{C2x} - DCB_{C2x-C2W} + b_{C2W} \end{cases} \tag{3.11}$$

where $\bar{P}_{C1W}$ and $\bar{P}_{C2W}$ are observations after inter-frequency biases calibration. Calibrated

observations can be used to generate IF combination observations as follow,

$$\begin{aligned} P_{IF} &= \alpha_{IF}\bar{P}_{C1W} - \beta_{IF}\bar{P}_{C2W} \\ L_{IF} &= \alpha_{IF}L_1 - \beta_{IF}L_2 \end{aligned} \tag{3.12}$$

From Eq. (3.8) to Eq. (3.12), the relationship between corrected pseudo-range $\bar{P}^s_{r,j}$ and raw pseudo-range P_{Cix} and their relationship can be expressed as,

$$\begin{bmatrix} \bar{P}^{s,i}_{r,1} \\ \bar{P}^{s,i}_{r,2} \end{bmatrix} = \begin{bmatrix} P_{C1x} & DCB_{C1x-C1W} & DCB_{C1W-C2W} & 0 \\ P_{C2x} & DCB_{C2x-C2W} & 0 & DCB_{C1W-C2W} \end{bmatrix} \cdot \begin{bmatrix} 1 \\ 1 \\ \alpha_{IF} \\ \beta_{IF} \end{bmatrix} \tag{3.13}$$

However, it must be pointed out that the UPD is sensitive to the biases in pseudo-range (Cui et al. 2021). The raw pseudo-range after intra-frequency and inter-frequency signal bias corrections could introduce the deviation in UPD. Additionally, imprecise correction also biased pseudo-range in solution and further impact AR performance. Therefore, the signal biases should be carefully considered to keep the pseudo-range unbiased in UPD estimation and AR. Moreover, the impact of different bias products on the WL UPD, which is analyzed in Chapter 4. Furthermore, the signals marked as the same code in DCB without a clear definition also could introduce the deviation in data processing and AR (Duong et al. 2019; Xiao et al. 2019).

In practice, WL ambiguity is estimated directly from the MW observation, which is a linear combination of the pseudo-range and carrier phase observations (Melbourne 1985; Wübbena 1985), which describes in Eq. (3.18). NL ambiguity is derived from the estimated IF ambiguity and WL integer part, which also introduces the biases into NL UPDs. Eq. (3.14) gives the conversion relationship among UPD, signal biases, and clocks parameters between IF combination and raw observation.

$$\begin{bmatrix} dt^s \\ UPD_{WL} \\ b_{IF} \\ 0 \\ DCB_{C1W-C2W} \end{bmatrix} = \begin{bmatrix} 1 & 0 & 0 & 0 & 0 \\ 0 & \alpha_{WL} & \beta_{WL} & -\alpha_{NL} & -\beta_{NL} \\ 0 & \alpha_{IF} & \beta_{IF} & 0 & 0 \\ 0 & 0 & 0 & \alpha_{IF} & \beta_{IF} \\ 0 & 0 & 0 & 1 & -1 \end{bmatrix} * \begin{bmatrix} dt^s \\ d_1 \\ d_2 \\ b_{C1W} \\ b_{C2W} \end{bmatrix} \tag{3.14}$$

where

$$\begin{cases} \alpha_{WL} = \dfrac{f_1}{f_1 - f_2}, \beta_{WL} = \dfrac{f_2}{f_1 - f_2} \\ \alpha_{NL} = \dfrac{f_1}{f_1 + f_2}, \beta_{NL} = \dfrac{f_2}{f_1 + f_2} \end{cases} \tag{3.15}$$

where from Eq. (3.14), the third line indicates that the satellite IF ambiguity b_{IF}; the fourth line indicates that sum of corrections $b_{C1W} \cdot \alpha_{IF} + b_{C2W} \cdot \beta_{IF} = 0$; UPD_{WL} is the WL UPD; d_1 and d_2

are carrier phase biases on each frequency L1 and L2. Only the C1W-C2W bias after IF combination is zero, while the others are not. It indicates that the inter-frequency signal biases C1W-C2W or P1P2 after the IF combination will have no effect when the observations of the real P_{C1W} and P_{C2W} signals are used.

3.2.3 Receiver biases calibration

The pseudo-ranges obtained from receiver end mainly due to receiver-type-related satellite-specified differences. It is commonly assumed that the UPDs at the receiver side can be eliminated by forming inter-satellite SD measurements, leading to the neglect of their characteristics at the receiver side (Gabor et al. 1999). These inconsistency among all satellites and differences among different receiver types cannot be absorbed by receiver clocks and/or receiver end UPD, but they could impact the satellite UPDs and AR.

In order to address receiver-specific deviations and ensure accurate ambiguity resolution with a high success rate across different types of receivers, a receiver-type-related satellite-specific deviation calibration method is proposed and its details are presented in Section 4.4.

It is important to note that biases in pseudo-range observations from both satellite and receiver ends can influence the MW combination and IF combination observations, which can further impact the NL UPD. Consequently, when WL and NL UPD products are obtained, the related ambiguities can be resolved at a single receiver. However, the presence of biases within the UPDs can lead to incorrect or failed AR. Therefore, it is crucial to carefully calibrate signal biases and receiver-type-related satellite-specific deviations before performing UPD estimation and AR.

3.3 UPD estimation

In data processing, parameters such as ionospheric delay, tropospheric delay, receiver clock, and station coordinates are correlated to ambiguity. Correctly fixing ambiguity is essential to accurately estimate these parameters.

Both the WL and NL UPDs for satellite can be estimated in a single-difference or un-difference model using the corresponding ambiguities. To comprehend the principle of UPD estimation on the server and the utilization of UPDs for AR on both the server and user, the relationship between the IF, L1, L2, WL, and NL ambiguities can be expressed as follows (Ge et al. 2007).

$$\bar{N}_{r,IF}^{s} = \frac{f_1^2}{f_1^2 - f_2^2}\bar{N}_{r,1}^{s} - \frac{f_1 f_2}{f_1^2 - f_2^2}\bar{N}_{r,2}^{s} = \frac{f_1}{f_1 + f_2}\bar{N}_{r,NL}^{s} - \frac{f_1 f_2}{f_1^2 - f_2^2}\bar{N}_{r,WL}^{s} \tag{3.16}$$

with

$$\begin{aligned}\bar{N}^s_{r,WL} &= N^s_{r,WL} + d_{r,WL} - d^s_{WL} \\ \bar{N}^s_{r,NL} &= N^s_{r,NL} + d_{r,NL} - d^s_{NL}\end{aligned} \tag{3.17}$$

where $N^s_{r,WL}$, $\bar{N}^s_{r,WL}$, $N^s_{r,NL}$, and $\bar{N}^s_{r,NL}$ are WL integer and UPDs, and NL integer and float ambiguities, respectively; $d_{r,WL}$, d^s_{WL}, $d_{r,NL}$, and d^s_{NL} are WL and NL UPDs in receiver-side and satellite-side, respectively. Either the estimated IF ambiguity or L1 and L2 ambiguities can be decomposed into the corresponding WL and NL ambiguities.

At epoch i, the MW combination observation of the WL ambiguity can be obtained,

$$N^{s,i}_{r,WL} = \left[(f_1 L^{s,i}_{r,1} - f_2 L^{s,i}_{r,2})/(f_1 - f_2) - (f_1 \bar{P}^{s,i}_{r,1} + f_2 \bar{P}^{s,i}_{r,2})/(f_1 + f_2)\right]/\lambda_{WL} \tag{3.18}$$

where $\bar{P}^s_{r,j}$ is the pseudo-range observation after applied correction of signal biases. λ_{WL} is the wavelength of WL. The estimation is calculated by taking the temporal average of the MW combination observables as,

$$\bar{N}^s_{r,WL} = \langle N^{s,i}_{r,WL} \rangle = N^s_{r,WL} + d_{r,WL} - d^s_{WL} \tag{3.19}$$

With all the float WL ambiguities of a network, the UPDs can be estimated using the iterative procedure by Li et al. (2017), which will be presented later. Assume that satellite-side WL UPDs are already known, the integer $N_{r,WL}$ can be found and introduced to Eq. (3.16) to get the NL float ambiguity,

$$\bar{N}^s_{r,NL} = \left[\lambda_{IF} \bar{N}^s_{r,IF} - c f_2 N^s_{r,WL}/(f_1^2 - f_2^2)\right]/\lambda_{NL} = N^s_{r,NL} + d_{r,NL} - d^s_{NL} \tag{3.20}$$

If the float estimates of all the ambiguities are obtained, the NL UPDs can be estimated.

Each of the float ambiguity can be expressed by the integer ambiguity N^s_r and the related UPDs as shown in Eq. (3.17). Once all WL or NL float ambiguities B^m_n are achieved at all stations, e.g., a network with n stations and m satellites, the receiver and satellite UPDs d_n and d^m can be estimated using Eq. (3.21) (Li et al. 2015; Cui et al. 2021),

$$\begin{bmatrix} B_1^1 \\ \vdots \\ B_1^m \\ B_2^1 \\ \vdots \\ B_2^m \\ \vdots \\ B_n^1 \\ \vdots \\ B_n^m \end{bmatrix} = \begin{bmatrix} I & & & & R_1 & S_1 \\ & I & & 0 & R_2 & S_2 \\ & & \vdots & & & \\ & 0 & & I & & \\ & & & & I \quad R_n & S_n \end{bmatrix} \cdot \begin{bmatrix} N_1 \\ N_2 \\ \vdots \\ N_n \\ d_1 \\ d_2 \\ \vdots \\ d_n \\ d^1 \\ \vdots \\ d^m \end{bmatrix}, \quad Q \tag{3.21}$$

where R_i and S_i are the coefficient matrices for receiver and satellite UPDs, respectively; Q is the co-variance matrix of the un-differenced float ambiguities; matrix R_i has one column with all elements as one and the other columns are zero, matrix S_i each line has one element as negative one and the others are zero. Due to the linear relationship between the receiver-side and satellite-side UPDs in the equation, the matrix is rank-deficient with a rank-deficiency of 1. Consequently, a datum needs to be imposed, such as fixing one UPD as a reference or applying the constraint that the sum of all satellite UPDs is zero, to ensure proper solving of the parameters.

3.4 GNSS augmentation

The accurate estimation of external tropospheric and ionospheric delays is crucial for achieving precise estimation in rapid/instantaneous AR at user-end. Ensuring the reliable AR on all reference stations with different receiver types and signals benefits precise atmospheric delay derivation. This section presents the methods for deriving and modeling atmospheric delays, as well as the generation methods for uncertainty information regarding the atmosphere on the server-side.

3.4.1 Augmentation system structure

The atmosphere augmentation corrections generation is divided into five parts: data preparation, precise atmospheric delay derivation, atmospheric delay fitting model calculation, unmodeled correction generation, and atmosphere uncertainty information calculation, and data processing flowchart is presented in Figure 3-2.

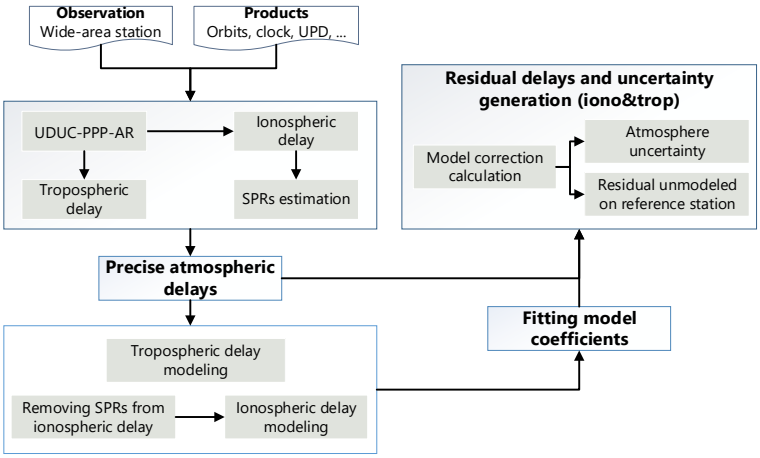

Figure 3-2 Flowchart of atmospheric delay deriving and correction model generation.

In the first step, the observation from reference stations, precise orbits, clocks, and UPD products are prepared for data processing. Subsequently, a quality check is performed on the observation data to identify and mark outliers and cycle slip. After the quality check, the UDUC-PPP-AR is conducted at each reference station to derive accurate atmospheric delays.

Once the precise atmospheric delays are obtained, the atmosphere model can be generate. Tropospheric ZWD from all reference stations can be directly used for modeling. However, when modeling ionospheric delays, it is important to consider receiver-related range biases, which may introduce errors in positioning. These biases need to be removed beforehand. Compared to the legacy vertical TEC model, the slant TEC model provides more precise values for satellite-wise modeling, without compromising the accuracy of slant ionospheric delay.

The estimation of SPRs is based on Eq. (3.5) and Eq. (3.6), using daily slant ionospheric delays from all satellites at each reference station. By removing the biases in the ionospheric delay using the estimated SPRs at each station from the previous day, a "clean" ionospheric delay is ensured for modeling. To maintain a stable and accurate SPR bias, an average value from a seven-day sliding window is introduced.

Finally, residual delay corrections are generated based on the differences between fitting model calculated and PPP-AR derived at each reference station for tropospheric ZWD and ionospheric delays. Depending on the fitted corrections, users can further improve the precision of atmosphere correction by employing the residual delay corrections at reference stations. The selection of three (or more) nearby reference stations is based on the user's location. The further regional unmodeled residuals depend on user positioning requirements and regional internet data transmission capability.

The strategy data processing at the service side is given in the Table 3-2.

Table 3-2 Data processing strategy at the service side in GNSS augmentation system

Items	Models applied
Parameter estimator	Sequential least square for UPD estimation Kalman filter for UDUC-PPP-AR atmospheric delay derivation
Observation	GPS L1&L2, Galileo E1&E5, BDS C2I&C6I, and GLONASS L1&L2
Orbit and clock corrections	From GFZ real-time products stream
Sampling interval	30s for UPD estimation and atmospheric delay extraction
Cut off elevation angle	7º
Relativity effects	IERS 2010
Surface displacements	Solid earth tides, ocean tides, and pole tide
Tropospheric delay	A priori ZHD from Saastamoinen equation with GPT2w meteorological data input, ZWD estimated with random walk process, GPT2w&VMF1 is used as the mapping function
Ambiguity fixed	Round for WL and Lambda for NL
Ionospheric delay	Ionosphere-free combination for UPD estimation Estimated as white noise for ionospheric delay derivation
Code biases	DSB products
Receiver clock offset	Estimated epoch-wisely, with the a priori values obtained from pseudo-range-based positioning
Antenna offset	Satellite/receiver PCO/PCV using igs.atx products
ISB and IFB	Estimated as constant parameters with zero mean constraint

It should be noted that both signal biases and the receiver-type-related deviation are considered to calibrate the deviations before UPD estimation.

3.4.2 Atmospheric delay estimation

By utilizing precise orbits, clocks, and UPDs, UDUC-PPP-AR can be conducted on all reference stations. The raw ambiguities can be converted into fixed WL and NL ambiguities. One advantage of PPP using raw observations over PPP using IF combinations is the ability to estimate ionospheric delay information. To obtain the ionospheric delay with fixed ambiguity, Eq. (2.1) can be re-parameterized as follows,

$$\Delta P_{r,i}^{s} = \overrightarrow{e_r^s} \cdot \Delta x + \hat{d}t_r + T_{r,ZWD} + \gamma_i \cdot \hat{I}_{r,1}^{s} + e_{r,i}^{s} \tag{3.22}$$

$$\Delta L_{r,i}^{s} = \overrightarrow{e_r^s} \cdot \Delta x + \hat{d}t_r + T_{r,ZWD} - \gamma_i \cdot \hat{I}_{r,1}^{s} + \lambda_i \cdot \widehat{N}_{r,i}^{s} + \varepsilon_{r,i}^{s} \tag{3.23}$$

where $\Delta P_{r,i}^{s}$ and $\Delta L_{r,i}^{s}$ are the Observed–Minus–Calculated (O–C) raw pseudo-range and carrier phase observations after linearization, considering all the necessary corrections (tidal effects, antenna PCOs/PCVs, phase wind up, earth rotation, relativistic effects, etc.); $\overrightarrow{e_r^s}$ is the unit vector from satellite s antenna phase center to receiver r phase center corrected by the precise satellite clock and orbit as well as other corrections. Then, all estimable parameters of the reparameterized are described in Table 3-3.

Table 3-3 Estimable parameters of the reparametrized UDUC-PPP

Estimable Parameter	Item
Coordinates	Δx
Tropospheric ZWD	$T_{r,ZWD}$
Receiver clock	$\hat{d}t_r = dt_r + \alpha \cdot b_{r,1} + \beta \cdot b_{r,2}$
Ionospheric slant delay	$\hat{I}^s_{r,1} = I^s_{r,1} + \beta \cdot (D^{12}_{\mathrm{r,DSB}} - D^{s,12}_{\mathrm{DSB}})$
Ambiguity	$\widehat{N}^s_{r,f} = N^s_{r,f} + d_{r,f} - d^s_f - [(\alpha \cdot b_{r,1} + \beta \cdot b_{r,2}) - (\alpha \cdot b^s_1 + \beta \cdot b^s_2) - \gamma_i \cdot \beta (D^{r,12}_{\mathrm{DSB}} - D^{s,12}_{\mathrm{DSB}})]/\lambda_i$

Note: $\alpha = \frac{f_1^2}{f_1^2 - f_2^2}$; $\beta = -\frac{f_2^2}{f_1^2 - f_2^2}$; $D^{s,12}_{\mathrm{DSB}} = b^s_1 - b^s_2$; $D^{s,1i}_{\mathrm{DSB}} = b^s_1 - b^s_i$; $D^{r,12}_{\mathrm{DSB}} = b_{r,1} - b_{r,2}$; $D^{r,1i}_{\mathrm{DSB}} = b_{r,1} - b_{r,i}$

where α and β are the coefficients of IF combination; $D^{r,12}_{\mathrm{DSB}}$ and $D^{s,12}_{\mathrm{DSB}}$ are the differenced signal biases between frequency *L1* and *L2* for receiver and satellite, respectively. $X = [T^s_r, \hat{d}t_{r,IF}, \hat{I}^s_{r,1}, \widehat{N}^s_{r,f}, ISB^{Sys}_r, IFB^{R,s}_r]$ are the parameters to be estimated in UDUC-PPP. Once the AR is successful performed using WL and NL UPDs, the precise atmospheric delay can be derived and modeled.

For multi-GNSS, the ISB and Inter-Frequency Bias (IFB) parameters also need to be considered due to the frequency differences. Considering the correlation of the parameters in Eq. (2.1) and Eq. (3.22) with the stations, satellites, and signal frequencies, Eq. (3.24) and (3.25) can be extended for multi-system as,

$$P^{Sys,s}_{r,IF} = \rho^{Sys,s}_r + T^s_r + c(dt_r - dt^{Sys,s}) + c\left(b_{r,IF} + b^{Sys,s}_{IF}\right) + IFB^{R^s-G}_r + ISB^{Sys-G}_r + \varepsilon^{G,s}_{P,IF} \quad (3.24)$$

$$L^{Sys,s}_{r,IF} = \rho^{Sys,s}_r + T^s_r + c(dt_r - dt^{Sys,s}) + \lambda^s_{IF}\left(N^{Sys,s}_{IF} + d_{r,IF} + d^{Sys,s}_{IF}\right) + IFB^{R^s-G}_r + ISB^{Sys-G}_r + \varepsilon^{Sys,s}_{L,IF} \quad (3.25)$$

where Sys denotes the system of GPS, Galileo, and BDS; $IFB^{R^s-G}_r$ is specific denotes the GLONASS satellite to GPS system.

Since the GLONASS satellites use FDMA technologies, their corresponding receiver side biases are frequency-dependent. Hence, the satellite-specific IFB parameter has only to be added for GLONASS FDMA signals. Moreover, to estimate IFB/ISB parameters, special handling is needed to define the datum, the sum of all receivers as zero as the constraint is used in this study.

3.4.3 Tropospheric delay correction

In GNSS data processing, external precise tropospheric delay products are used as a priori

constraint, e.g., the tropospheric delay from Numerical Weather Model (NWM) (Andrei & Chen 2008; Hobiger et al. 2008; Lu et al. 2017; Wilgan et al. 2017), empirical tropospheric delay models such as Global Pressure and Temperature 2 (GPT2w) and GZTD2 (Böhm et al. 2014; Yao et al. 2016; Chen et al. 2020), in situ instrument measurements such as water vapor radiometer (Ware et al. 1993; Alber et al. 1997), and Raman lidar (Bock et al. 2001; Bosser et al. 2009).

A better way is to generate a correction model using the tropospheric delay estimates of a GNSS reference network. From Eq. (3.22) and Eq. (3.23), the tropospheric ZWD can be derived from the solution at an elevation angle e and azimuth angle α as Eq. (2.5). generally, the tropospheric delay can be devided into ZWD and ZHD as Eq. (3.26), and the ZHD can be precisely modeled. Then, the unmodeled ZHD will go into the ZWD estimates. Hence, only the tropospheric ZWD has to be estimated. In tropospheric delay,

$$T_r^s(e,z) = mf_w(e) * \hat{T}_{r,ZWD} + mf_h(e) * \hat{T}_{r,ZHD} \tag{3.26}$$

where $\hat{T}_{r,ZHD}$ is modeled value, and the $\hat{T}_{r,ZWD}$ is the estimated ZWD value including unmodeled ZHD. In this thesis, consistent ZHD model is used at the server and user sides. Based on the estimated ZWD, a model will be generated for the corresponding region. The model coefficients will be provided for users. For usage of model, the same ZHD correction model, mapping function, and metrological products must be used at reference and user stations.

A modified tropospheric delay fitting model applied in large areas is proposed to consider the altitude differences, which is described in Section 5.1.

3.4.4 Ionospheric delay correction

The ionospheric delay correction is generated for each satellite, i.e., the fitting model uses the slant delays from all stations to the specified satellite. It should be noted that the SPR biases have to be estimated and removed from all satellite station-by-station in advance due to the strong linear relationship between the code biases and ionospheric delay and a consistent benchmark is required for SPRs estimation. The SPR estimation method is mentioned from Eq. (3.3) to Eq. (3.7). Then, the “clean” ionospheric delay can be applied in modeling to eliminate the impact of receiver end biases.

To provide the correction in large areas, a new fitting model for ionospheric slant delay is proposed based on the characteristics of ionospheric delays, which follows the relationship between the length of the propagation path length through ionospheric and the corresponding delay magnitude. The model is described and assessed in Section 5.2.

3.4.5 Unmodeled correction generation

Although the proposed fitting model can effectively capture the majority of atmospheric delays in large areas, residual delays exist at each reference station due to the conflict between the simplified model for communication reasons and rapid temporal and spatial variation of the delays. Particularly in areas with significant meteorological changes or substantial variations in terrain, relying solely on a fitting model may not provide sufficiently precise atmospheric delay corrections.

The unmodeled delays from the nearby stations can afford to compensate further. For each reference station, the residual delay can express as,

$$\begin{aligned} I_{r,j}^{s} - \tilde{I}_{r,m}^{s} &= \hat{l}_{r}^{s} \\ \hat{T}_{r} - \tilde{T}_{r,m} &= \hat{l}_{r}^{t} \end{aligned} \tag{3.27}$$

where $\tilde{T}_{r,m}$ and $\tilde{I}_{r,m}^{s}$ are tropospheric and ionospheric delay fitting model calculated values, respectively; $\hat{l}_{r}^{s}$ and $\hat{l}_{r}^{t}$ are satellite-wise ionospheric and tropospheric delay residuals on station r, respectively. The residual delays can serve as additional atmospheric delays to the fitting models in case appropriate communication capacity is available. At the user-end, the additional corrections can be interpolated from the fitting residuals.

Three nearby reference stations with the Inverse Distance Weighting (IDW) algorithm (Gao 1997) as follows:

$$\hat{l}_{user} = \sum_{i=1}^{3} \hat{l}_{r}^{s}(ref) \cdot w_j \,/ \sum_{i=1}^{3} w_i \tag{3.28}$$

$$w_i = \frac{1}{{d_i}^2} \tag{3.29}$$

where $\hat{l}_{user}$ is the interpolated corrections on the user side; $\hat{l}_{r}^{s}(ref)$ and w_j are the atmospheric corrections and weight of reference station i, respectively; d_i^s is the geometric distance from the user to the reference station i.

3.4.6 Atmosphere uncertainty information

In the context of atmospheric delay augmentation, it is crucial that both the correction and its accuracy are provided, so that the uncertainty of the correction can be properly considered while implementing the delays in user-end positioning.

To address the uncertainty, the atmospheric delay uncertainty grids are introduced, which are

based on ionospheric and tropospheric delay fitting residuals. The atmosphere uncertainty generation and performance are described and analyzed in Section 5.5. Since the ionospheric delay exhibits more significant variations compared to the tropospheric ZWD and demonstrates weaker fitting performance in large areas, a more detailed regional uncertainty function is established specifically for the ionospheric delay, which is described in Section 5.6.

3.5 Positioning solution

Relying on the large areas atmosphere augmentation information and pseudo-range correction products, the rapid/instantaneous ambiguity resolution can be performed in real-time PPP. This section describes the positioning processing strategies, including ambiguity resolution, atmosphere correction applied, and uncertainty information application, in detail.

3.5.1 Positioning processing strategy

Table 3-4 shows the data processing strategy on the user-side.

Table 3-4 User-side PPP processing strategy

Perturbations	Models applied in this study
Observation	GPS, Galileo, BDS, and GLONASS dual-frequency
Sampling interval	30 s interval
Orbit and clock corrections	GFZ real-time corrections stream
Cut off elevation angle	7°
Station displacement	Solid Earth tides, ocean tides, and pole tide displacements (IERS 2010)
Tropospheric delay	A priori delay and mapping function are the same as at the server, but the additional augmentation information, including fitting model, uncertainty grid, and regional unmodeled residuals, is used to provide the a priori ZWD value and the corresponding constraints
Ionospheric delay	Additional augmentation information, including fitting model, uncertainty grid, regional unmodeled residuals, and ionosphere error function, is used to provide the a priori ionospheric delay value and the corresponding constraints
Code biases	DSB products (only correct satellite-side biases)
Sagnac effect	Corrected
Receiver clock offset	Estimated epoch-wisely, with the a priori values obtained from code-based positioning
Antenna offset	Satellite/receiver PCO/PCV using igs.atx products
Coordinates	Estimated
Phase wind-up	Wu et al. (1993)

3.5.2 Ambiguity resolution in positioning

The essential factor in realizing the PPP-AR is to correct or eliminate the fractional cycle biases of the satellite and receiver sides to recover the integer properties of the carrier phase ambiguity.

Ambiguity resolution

In UDUC-PPP-AR, the L1 and L2 frequency ambiguities are usually used, while the estimates are not stable due to their strong correlation with the ionosphere parameters. Therefore, they are converted to IF ambiguities for AR and UPD estimation as in the IF-PPP (Gu et al. 2015), and their usability in UDUC-PPP has been demonstrated by Zhang et al. (2020) and Du et al. (2020).

The positioning with AR is generally performed in three steps. Firstly, the float solution is performed to solve the ambiguity parameter and the corresponding variance-covariance matrix. The next step considers the integer properties of the ambiguity parameters to fix the WL and NL ambiguities in turn. Thanks to its long wavelength properties, the WL ambiguity be fixed by round-up to its nearest integer, while the NL needs the Least-squares Ambiguity Decorrelation Adjustment (LAMBDA) method to search for the best value (Teunissen 1994). Finally, the fixed integer ambiguities are introduced to the estimator to obtain the fixed solution including all the estimates and their covariance matrix.

It should be noted that the UD (with satellite- and receiver-side UPDs) or SD (with satellite-side UPDs with inter-satellite differences) ambiguities are estimable if and only if they are successful in Double-Difference (DD) form and that PPP-AR on single-receiver should be seen as a special case of network DD AR (Khodabandeh & Teunissen 2019). Denoting the reference satellite as s_0, the SD float ambiguity can be expressed as,

$$\Delta\bar{N}_r^{s,s_0} = \bar{N}_r^s - \bar{N}_r^{s_0} = \Delta N_r^{s,s_0} - \Delta d^{s,s_0} \tag{3.30}$$

where $\Delta d^{s,s_0}$ and $\Delta N_r^{s,s_0}$ refers to SD UPD and integer part between satellites, and $\Delta d^{s,s_0}$ is provided in UPD products.

***Ambiguity resolution* verification**

The accuracy of GNSS positioning is very much dependent on the correct integer AR. Incorrect integer ambiguity will lead to decimeter-level or even more significant deviations in the positioning solution, so the AR correctness must be checked and verified (Verhagen & Teunissen 2012; Teunissen & Khodabandeh 2014). Three indicators usually used in the ambiguity

validation process are briefly described below: ambiguity dilution of precision (ADOP), bootstrapping success rate, and ratio-test.

- ***ADOP***

Similar to the Dilution Of Precision (DOP) indicator that describes the effect of receiver-satellite geometric conditions on positioning accuracy, ADOP describes the accuracy characteristics of the ambiguity parameter, which is defined as (Odijk & Teunissen 2008),

$$ADOP = \sqrt{\det\left(Q_{\hat{N}}\right)}^{1/n}, (cycle) \tag{3.31}$$

where $Q_{\hat{N}}$ denotes the variance-covariance matrix of the solution; $\det\left(Q_{\hat{N}}\right)$ denotes the value of its determinant. The ADOP value considers all information of the ambiguity variance-covariance matrix, which is an extremely high degree description of approximation of the average accuracy.

- ***Bootstrapping success rate***

The ambiguity fixing success rate represents the strength of the mathematical model for GNSS data processing and gives quantitative information about the probability of correct fixing (Teunissen 1998; Wang & Feng 2012). The LAMBDA method is based on integer least-squares with the maximum optimal probability of correct integer estimates (Verhagen 2004). Although the success rate of integer least-square is the probability density of float solution in integrals in regular domains, the numerical integration calculation cannot be performed directly. Whereas bootstrapping success rate, as a downside bound on the success rate of integer least squares estimation, is an approximate solution with a very high degree of approximation to the integer least-squares success rate (Teunissen 1998; Wang & Feng 2012). Therefore, the bootstrapping success rate is often used to check the ambiguity fixing in practical applications, and expression as,

$$P = \prod_{i=1}^{n}\left(2 \cdot \Phi \cdot \left(\frac{1}{2 \cdot \sigma_{\hat{N}_{i|I}}}\right) - 1\right) \tag{3.32}$$

where

$$\Phi(x) = \frac{1}{\sqrt{2 \cdot \pi}} \int_{-\infty}^{x} e^{-t^2/2} dt \tag{3.33}$$

where $\hat{N}_{i|I}$ is the abbreviations of $\hat{N}_{i|i-1,2,\ldots,1}$, and it is the conditional estimated value of the i-th ambiguity conditioned on the previous $(i-1)$ fixed ambiguities. σ is the STD value.

The bootstrapping success rate indicator is easy to calculate, promising to check and describe the global quality of the fixed solution (Teunissen & Verhagen 2013). However, the success rate indicator does not directly depend on the actual measurement information. The calculated success rate indicator is unreliable in the presence of undetected bias in the observations. Hence, the success rate indicator is insufficient to guarantee that the accepted fixed solution has a sufficiently high confidence level.

- ***Ratio test***

The ratio test is defined as the ratio of closeness of the optimal and suboptimal integer solutions and is calculated as (Frei & Beutler 1990),

$$R = \frac{\left\|\hat{N} - \breve{N}_2\right\|^2_{Q_{\hat{N}}}}{\left\|\hat{N} - \breve{N}\right\|^2_{Q_{\hat{N}}}} \tag{3.34}$$

where $\breve{N}$ and $\breve{N}_2$ are optimal and suboptimal integer solution, respectively.

A fixed threshold, e.g., from 2 to 3, is usually selected. When the ratio value exceeds the threshold, the ambiguity is considered fixed correctly. The correct ambiguity vector may be excluded if the threshold is over-chosen. Conversely, if the threshold is under-chosen, the wrong ambiguity vector may be accepted, which will lead to a significant error in the fixed solution. Even though the fixed-threshold ratio test is more efficient in practice, for GNSS models with high model strength, the threshold setting of the ratio test is usually too conservative, with a high probability of incorrectly rejecting the correct fixed solution. While for GNSS models with weak strength, the threshold setting is generally too low, resulting in a higher likelihood of accepting incorrect integer solutions (Ji et al. 2010; Teunissen & Verhagen 2013).

Strategy in ambiguity resolution

In order to achieve the correct ambiguity resolution, the ADOP, bootstrapping success rate and ratio test methods are used in ambiguity checking. The fixed solution is accepted only if the ADOP, bootstrapping success rate and the ratio-test test are passed, with the ADOP threshold set as 0.6, success rate threshold set as 0.99, and the ratio-test threshold set as 3.0 for GPS, and 2.5 for GPS+Galileo.

3.5.3 Positioning with augmented information

Once the tropospheric and ionospheric delay are precisely generated on the server, the

correction and corresponding uncertainty are disseminated to users. Moreover, the residual corrections are further provided. Once the augmentation information is received, the PPP-AR can be implemented with the aid of atmospheric delay and corresponding uncertainty information. Given that the external correction values still differ from the real values, the correction is generally set as the virtual observation with a proper constraint. More detail of positioning using augmentation information is presented in Chapter 6.

3.5.4 Positioning performance evaluation

The performance of the proposed augmented positioning is assessed by four indexes: Time To First Fix (TTFF), convergence time, positioning precision, and ambiguity fixing rate (Feng & Wang 2008). The horizontal positioning error is calculated as the root mean squares of the north-south and east-west components.

- TTFF indicates the time when the ambiguity is first successfully fixed continuously in the positioning.
- Convergence time is estimated statistically based on the position differences with respect to their references from a number of positioning experiments. The epoch-wise RMS of the differences degrades along with time and can be a measure of positioning accuracy. Given an accuracy requirement, it can find in the RMS curve the time when the RMS below the given threshold which is defined as the convergence time for the specified accuracy requirement. The threshold for horizontal and vertical are set as 10 cm in this study.
- Positioning accuracy of a individual positioning experiment is the RMS calculated by the differences between the estimated and reference coordinates.
- The ambiguity fixing rate is defined as the ratio of the number of fixed epochs to the number of total epochs.

3.6 Chapter summary

The major content of this chapter is summarized as follows.

Section 3.1 presents the system structure of the augmentation system. From the pseudo-range deviation calibration, ambiguity resolution, and atmospheric corrections generation to user-end.

Section 3.2 focus on the satellite signal and receiver-dependent and satellite-specified biases estimation and calibration methods.

- Estimating and correction methods for satellite signal biases are described.
- The receiver-dependent pseudo-range deviations should be derived first from the UPD

estimation and calibrated for user end positioning.

Section 3.3 presents the UPD estimation methods in detail.

Section 3.4 describes the real-time augmented system in server-side briefly. Relying on the real-time precise orbit and clock information, the real-time precise atmospheric delay estimation, and modeling for large-area, residual delay correction model, and generation of uncertainty information are described.

Section 3.5 presents the positioning and ambiguity resolution methods on the user-side. The application of external corrections in positioning is presented. Finally, the ambiguity resolution and positioning performance evaluation criteria are addressed.

4 Bias Calibration For Ambiguity Resolution

In GNSS data processing, the pseudo-range serves as the basic observation obtained by measuring the signal transmitting time from the satellite antenna to the receiver antenna. However, variations can arise in the pseudo-range observations obtained from different signals, frequencies, or receivers due to diverse tracking and modulation modes or hardware discrepancies. Inconsistent pseudo-range biases can introduce adverse effects on precise data processing and compromise AR.

Typically, pseudo-range biases fall into three categories: intra-frequency signal bias, inter-frequency signal bias, and receiver-related satellite-specified biases. Intra-frequency and inter-frequency signal biases, collectively known as signal (code) biases for both receiver- and satellite-side, can be estimated and provided as (IGS) products such as DCB or DSB for user-end calibration. Although DCB and DSB products are used in parallel, they differ in signal classification and values, and their impact on data processing remains unclear. Conversely, receiver-dependent biases have not yet been considered in data processing.

Given that reliable AR is critical and serves as a prerequisite for high-precision processing, this Chapter analyzes the influence of different signals on orbits, clocks, and UPD estimation, as well as their associated stochastic noise. Furthermore, the impact on positioning AR is investigated. Additionally, a method of receiver-type-related satellite-specific deviation calibration is proposed to keep all types of receiver with reliable AR. In this Chapter, all available signals and receiver types are enabled in large-area service with reliable AR to provide precise atmospheric delay.

4.1 Signal bias estimation and correction

Due to the impact of range biases among different range types on precise GNSS data processing, the IGS has made great efforts to estimate these range biases to minimize their inconsistency. Two products, namely DCB and DSB, are provided respectively by the CODE and the CAS Acs, respectively. Since these products are used in parallel nowadays, the details on them will be given and investigated their agreement.

4.1.1 Relationship between code and signal

To handle systematic biases in pseudo-range observations, the CODE AC provides the DCB (Jefferson et al. 2001; Feltens 2003) products, namely COD DCB (Arikan et al. 2008; Keshin 2012;

Mylnikova et al. 2015). As its name suggests that only range bias differences between different code types instead of signal types are considered. Therefore, the COD DCB product only provides DCB of P1P2, P1C1 and P2C2 of GPS, and that of P1P2 of GLONASS. With the rapid development of multi-frequency and different signal modulation modes, more signals are available as shown in Figure 4-1.

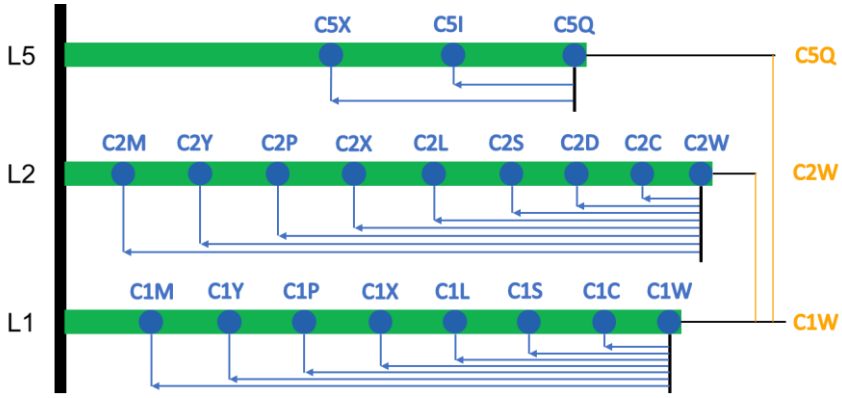

Figure 4-1 Classification of signals and their reference signal for each frequency (Wang et al. 2020)

Moreover, there could be several signals based on the same code and these signals may have different range biases. One of the reason is that the signal differences was not yet revealed that time and in the earlier RINEX version range observation of different code types are valid. The relationship between signals and codes for GPS is illustrated in Table 4-1.

Table 4-1 Current and planned GPS signals (Parkinson et al. 2020)

Center frequency	Signal description	Civil (C) or protected (P)	Signal	First broadcast
1575.42 MHz	L1 C/A: first civil signal	C	C	1978
	L1 P (Y): original military	P	P	1978
	L1 M: new military	P	M	2005
	L1C: new international GNSS (Block III)	C	S/L/X	2019
1227.60 MHz	L2 P(Y): original military	P	P	1978
	L2M: new military	P	M	2005
	L2 CM: civil data channel	C	S	2005
	L2 CL: civil pilot channel	C	L	2005
1176.45 MHz	L5 I: new civil safety-of-life data channel	C	I	2010
	L5 Q: new civil safety-of-life pilot channel	C	Q	2010

From Table 4-1, C/A-code could correspond to C, S, L, and X signals even if between these signals exist biases (Schaer 2012; Montenbruck et al. 2014a). Moreover, P-code could correspond to P and W signals. In some programs, e.g., GFZRNX, the S, X, C, and L signals are marked as C code, and W and P signals are marked as P-code while transforming Rinex-3 and Rinex-4 to Rinex-2,

though biases between these signals (Nischan 2016).

With the modernization of GPS satellites, new frequencies and signals became available. Block IIR satellite provides C/A code on L1 and P(Y) code on L1 and L2 frequencies. Block IIR-M satellite provides the second civil signal on L2 frequency, namely L2C. Block IIF satellite provides a new frequency on L5 band. GPS III/IIIF satellite provides the fourth civil signal on L1 frequency, namely L1C. Figure 4-2 gives the statistics of the tracking status of each signal of the 350 MGEX stations, where the number of stations that tracked signals are calculated for each GPS satellite.

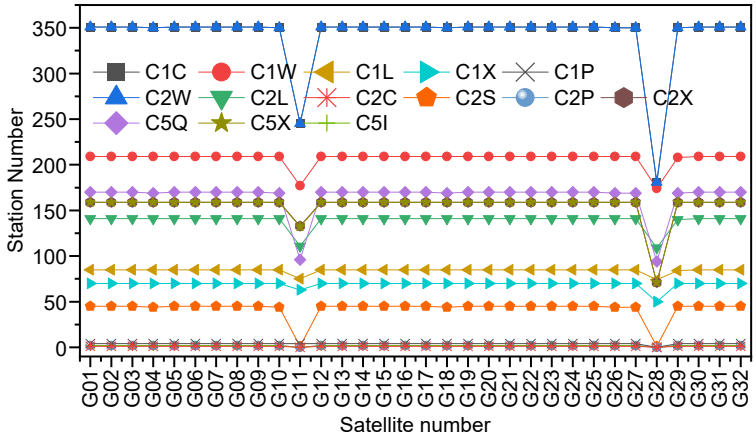

Figure 4-2 Station number observing individual signals among the 350 MGEX stations analyze for each GPS satellite. All data types information are collected from their observation files.

A total of 14 signals are monitored, with all stations tracking the C1C and C2W signals. The C1W, C2X, C2L, and C2S signals also have good tracking statistics, tracked by half of the stations. For L5 frequency, C5Q, C5X, and C5I bands are tracked by 170, 159, and 2 of the stations, respectively. However, a few signals, including C1P, C2C, C2P, and C5I, are tracked by less than 5 of the 350 MGEX stations. Among them, the C2C, C2P, and C5I signals from G11, and the C1P, C2C, C2P, and C5I signals from G28 cannot be tracked by any receivers. Note that some signals are not showed up in any of the observations file, such as C1S, C1Y, C1M, and C2M, and thus they are not presented in Figure 4-2.

However, C and W signals are the dominant signal types received by most receivers. In the case of using DCB, DCB among C- and P-code corrections are applied by ignoring the signal types. From the Table 4-1, the code is not corresponding to the specific signal, but it could include several different signals (Montenbruck et al. 2014a; Wang & Yuan 2016; Wang et al. 2020; Liu & Zhang 2021).

4.1.2 Signal bias estimation

The inter-frequency and intra-frequency signal biases can be estimated using the Eq. (3.2) and Eq. (3.7). Generally, the intra-frequency signal biases are very stable because the bias is calculated by averaging the long-term differences between the signals on the same frequency. In contrast, the inter-frequency bias stability is lower than that of intra-frequency due to the frequency-dependent ionospheric delay. In order to estimate accurate biases, the precise SPRs estimation is essential. Meanwhile, the performance of the SPRs is also crucial for large-area ionospheric delay modeling, as the receiver-side pseudo-range bias could cause the datum difference. Hence, a stable SPRs solution not only supports a precise biases value but also protects the ionospheric delay modeling unbiased.

The ZIM3 station inter-frequency SPR values from DOY 270, 2021 to DOY 300, 2021 (30 days) are presented in Figure 4-3 as an example. The SPR values show very stable performance and the fluctuations are within 5 cm.

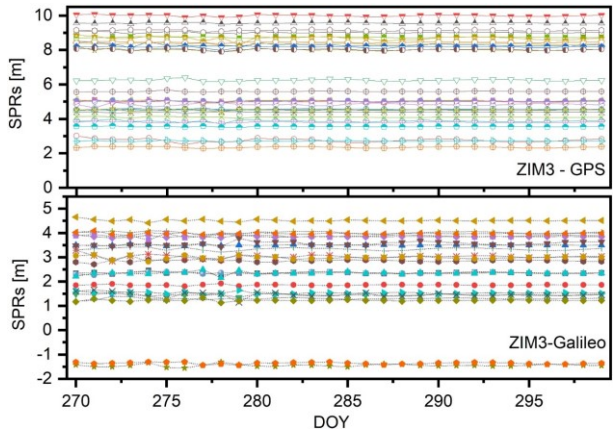

Figure 4-3 The inter-frequency SPRs values on ZIM3 station during 30 days. The top panel is the difference between C1W and C2W signals on GPS satellites, and the bottom panel is the differences between C1X and C5X signals on Galileo satellites. Different colors denote different satellites.

4.1.3 Signal bias correction

A first illustration of the impact of signal bias corrections on raw observations is given in Figure 4-4, where the differences of raw observations between different signals on the same frequency are given.

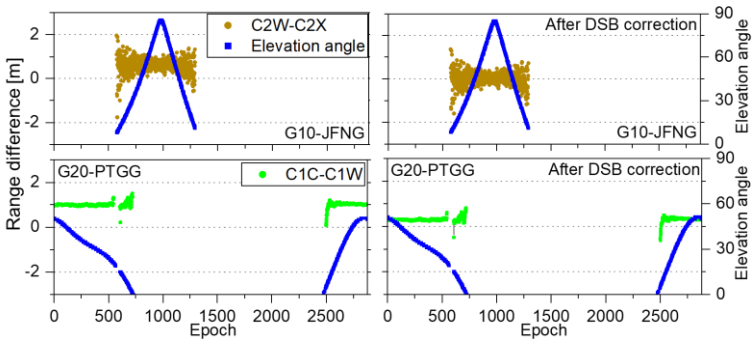

Figure 4-4 The difference between C2W and C2X of G10 (BLOCK III) in the top panels, and that between C1C and C1W signals of G20 (BLOCK IIF) satellites in the bottom panels. Left: before applying IGS CAS provided DSB correction, right: after applying DSB corrections. The PTGG and JFNG stations on DOY 285, 2021 are presented.

As shown in Figure 4-4, the raw observations show systematic biases among different signals, with values reaching up to 1 m. However, after applying the bias corrections, these systematic biases are mitigated largely. It should be noted that despite calibration, residual biases still persist in the pseudo-range differences due to the biases at the receiver side. Notably, the biases between C1C and C1W measurements demonstrate high stability, while C2X and C2W signal measurements exhibit noise characteristics related to the elevation angle. The results clearly indicate the significant impact of these signal biases. The fluctuation observed during the start and end periods of each arc is attributed to the influence of multipath effects and/or observation noise, which are dependent on the satellite's elevation angle.

4.1.4 Comparison of different correction products

Currently, three IGS ACs provide bias products, including DLR (DSB) and CODE (DCB) with a monthly release rate and CAS (DSB) with a daily release rate. Note that the product sampling rate of both DLR and CAS product is one day, but DLR update monthly with one-month daily information. In this part, the bias products from CODE and CAS are compared.

The differences between DCB and DSB products are presented in Figure 4-5, where only the same signals are compared. As we can see, large biases up to 0.6 ns exist, e.g., the C1C&C1W signals (P1C1 in DCB products) G03 and G29 satellites. The differences in the C2C&C2W signals (P2C2 in DCB products) are smaller than others, but still reach up to 0.2 ns. Such a large difference indicates that the DCB products are not precise enough and could cause large biases in the data processing, as presented before.

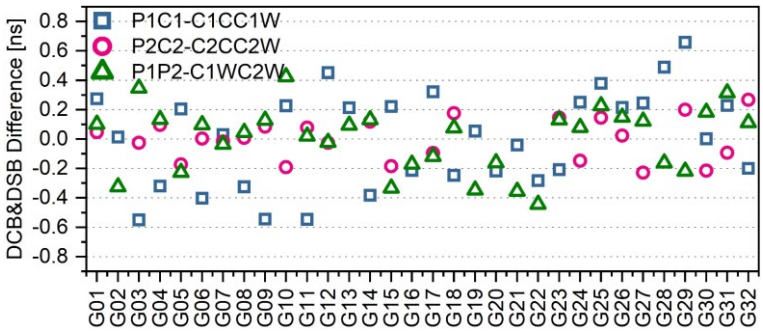

Figure 4-5 Satellite-specified averaged differences between DCB and DSB products for the same signals during the 30 days.

Due to the differences between the DCB and DSB corrections, the impact on POD, PCE, UPD estimation, and positioning performance using different signal settings should be investigated. In addition, more detailed signal biases are only presented in DSB products, and DCB with only code bias ignores signal type.

4.2 Impact of signal biases in product generation

This section investigates and compares the impact of DSB and DCB products and different signal settings on GPS satellite data processing.

4.2.1 Data set

This experimental validation involves 350 globally dispersed reference stations from the MGEX between Day of Year (DOY) 270 and 300. Figure 4-6 provides the distribution of these stations, including 161 stations (blue dot) for the products generation and 189 stations (red triangle) for positioning validation.

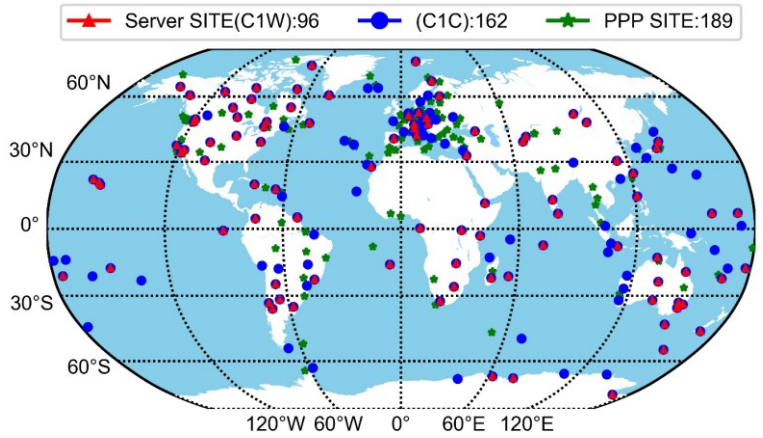

Figure 4-6 The selection of 350 MGEX stations for the experimental validation. Blue dot denotes the stations for POD, PCE, and UPD estimation; green star denotes the stations for positioning verification.

In the product generation, the mixed signals could be used to ensure the maximum observation data utilization. Considering the number of observed stations and the observations SNR characteristics, a signal priority list is set to automatically select the observations (refer to Table 3-1).

Moreover, even if the same bias product is used, different signal selections could also cause deviations. The signals selected at different frequencies are not necessarily the same because the observed signals are different. From Figure 4-2, all stations have C1C and C2W signals on frequencies L1 and L2, respectively. Two sets signal-setting are used to compare the different bias products correction performance.

Table 4-2 Signals setting and products used in data processing

Type	Scheme	Bias correction products used in solution
Signal setting	Mixed-signal	According to signal priority list (Table 3-1)
	Fixed-signal	L1 use C1C and L2 use C2W signals
Correction using	DSB	Using DSB products correct biases
	DCB	Using DCB products correct biases

4.2.2 Analysis of precise orbit determination

As one of the basic observations used in POD, the impact of their biases caused by using DCB and DSB products and different signal-setting on POD are investigated.

Orbit and clock estimation strategies

In POD processing, the initial orbits and clocks are taken from the corresponding broadcast ephemeris. By iteratively adjustment and data cleaning, the accuracy of the satellite orbit parameters can be continuously improved. The parameter settings used for the POD and PCE in this thesis are presented in Table 4-3.

Table 4-3 Data processing strategies in satellite orbits and clocks

Items	Description
Arc length	24-hour
Station coordinates	Estimated as daily constant, no-net-rotation constraints on the datum stations to IGS14
Weighting	0.015 cycle and 1.0 m for raw phase and code, respectively, elevation (E)-dependent, 1 for E>30º

	otherwise 2sin(E)
Solar radiation	GPS: ECOM1
Receiver and satellite clock	estimated as epoch-wise white noise
Earth radiation	Applied (Rodriguez-Solano et al. 2012)
Transmitter thrust	Applied (Steigenberger et al. 2017)
Earth gravity	EIGEN6C (Förste et al. 2011) up to 12×12
Tropospheric delay	GPT2w for the a priori zenith delay, residual zenith wet delay estimated as 2-h piece wise constant, north and east gradients estimated as daily constant Mapping functions: GMF (Liu et al. 2016a) for zenith delays and Chen-Herring (Chen & Herring 1997) for horizontal gradients
Ambiguity fixing	Double-differenced ambiguity resolution (Ge et al. 2005; Ge et al. 2006)
Earth rotation parameters	A priori value: IERS finals 2000A product Polar motion components estimated as daily offset and rate, and only daily rate (LoD) for UT1-UTC. The sub-daily variations of ERP are modeled according to IERS 2010 Conventions

The coordinates, velocities, and solar radiation pressure model parameters of ECOM at reference epoch for each satellite are estimated, and ground station coordinates are estimated as daily constant. The solution is tightly constrained to the IGB14 solution by the no-net-rotation constraint on all the IGS14 core stations. Earth Rotation Parameters (ERP) are estimated as daily offset and drift for polar motion, and Length of Day (LOD) is estimated one offset per day. Double differenced ambiguity fixing is performed in POD and PCE.

Orbit accuracy evaluated

The orbit accuracy of different scheme is firstly evaluated by comparison with the reference product. Figure 4-7 and Figure 4-8 show the average RMS values of orbit differences, calculated as,

$$RMS_j = \sqrt{\sum_{i=1}^{n} res_{i,j}^2/n} \quad , \quad j = a, c, r \tag{4.1}$$

$$RMS_{3D} = \sqrt{\sum_{i=1}^{n} (res_a^2 + res_c^2 + res_r^2)/3n} \tag{4.2}$$

where $res_{i,j}$ is the orbital residual of the j component, including along-track, cross-track and radial components, at i epoch, n is the total number of epochs of the orbit differences.

Analysis of orbit quality

Figure 4-7 presents the orbit differences between the four solutions using DCB or DSB product combined with using mixed-signal or fixed-signal settings, respectively, for the float solution (top) and fixed solution (bottom). For each daily POD, the RMS of the orbit differences between the solutions per satellite is calculated, and the average value over 30 days are presented in the figure.

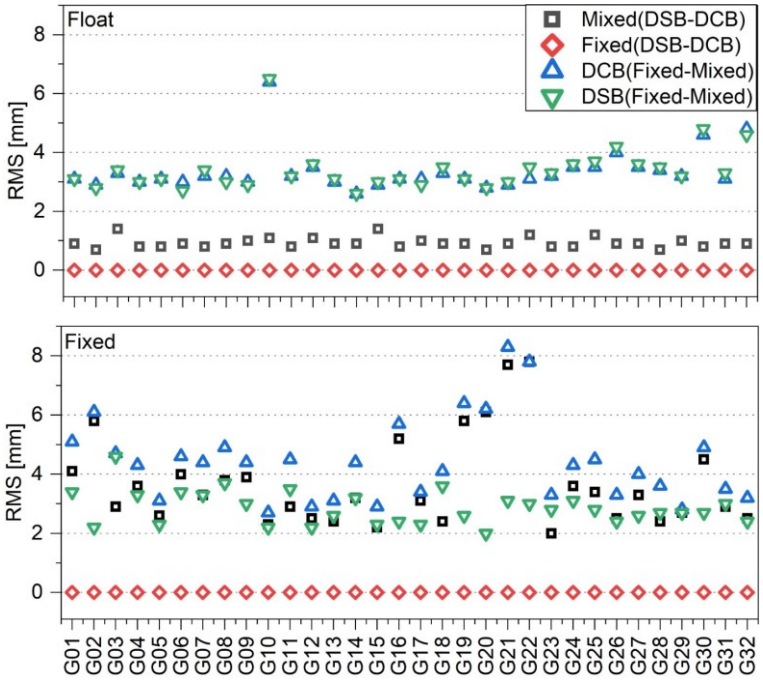

Figure 4-7 GPS satellite orbit difference between using DCB and DSB products and using mixed-signal and fixed-signal settings, average value during 30 days, without (upper panel) and with (lower panel) double-differenced ambiguity fixing.

Figure 4-7 illustrates the slight differences between DSB and DCB when using fixed-signal setting, regardless of whether ambiguity fixing is applied. In contrast, the differences between DCB and DSB using mixed-signal setting can reach up to 1.6 and 7.7 mm in float and fixed solutions, respectively. In fixed-signal setting, the difference is avoided because all 162 stations can receive the C1C signal, but in the mixed-signal scheme, 96 and 66 stations are tracking C1W and C1C signals, respectively. This discrepancy arises from the fact that DCB products only provide the P2C2 bias, while DSB products offer detailed biases for C, X, S, and L signals. Additionally, for fixed-signal, the differences between DCB and DSB is the difference between P1C1+P1P2 and C1C-C1W+C1W-C2W, which is a constant value for all the stations, which is

constant differences can be absorbed by clocks and has no effect on AR. For mixed-signal, 96 stations, receiving C1W and C2W, have the biases of P1P2 with C1W-C2W, and remining 66 stations, receiving C1C and C2W, have the biases of P1C1+P1P2 and C1C-C1W+C1W-C2W. If P1C1-C1C&C1W is also not zero, the two signal sets will have their own constant biases. The differences in these corrections between DSB and DCB on the same signal can reach up to 0.6 ns, and the P2C2 with respect to other DSB detailed corrections are up to 0.2 ns, which could impact the AR solution. Moreover, some stations and epochs could use other signals, e.g., X, S, and L signals, which also introduce the biases between DCB P1C1 and P2C2 and DSB detailed corrections. But their number is rather smaller than that of C and W signals, and thus, the impact should not be such large. Consequently, the fixed-signal scheme performs better and exhibits smaller differences between DCB and DSB solutions. When employing DCB and DSB products with mixed signals for orbit estimates with ambiguity fixing, the discrepancy increases to an average of 2-4 mm, and a few satellites, such as G02, G19, G20, G21, and G22, display considerable differences of up to 10 mm in RMS. This is obviously the impact of wrong fixings caused by inconsistent pseudo-range biases.

When comparing the solutions using mixed-signal and fixed-signal with the same bias products, the DSB scheme shows smaller differences than the DCB scheme. From the top panels of Figure 4-7, which represents the float solutions, the mean RMS of orbit differences between mixed-signal and fixed-signal are 2.7 and 3.1 mm for DSB and DCB solutions, respectively. Although the difference is only 0.4 mm, the use of DCB products results in a larger RMS compared to DSB products, indicating that the latter has better correction capability. Furthermore, it can be easily observed that the utilization of multiple signals has a negligible effect on the quality of the orbit since carrier phase observations carry significantly more weight than pseudo-range observations. However, in the ambiguity-fixed solution, more noticeable disparities are displayed as illustrated in the bottom panel of Figure 4-7, mainly because pseudo-range biases affect AR. The RMS of orbit differences between the mixed-signal and fixed-signal solutions using DSB and DCB products increases to 2.7 and 4.2 mm, respectively. In the DCB solution, the G02, G19, G20, G21, and G22 satellites exhibit larger disparities compared to others, as the large differences are presented between DCB and DSB on P1C1 and C1W-C2W corrections. The same significant discrepancies between the DCB and DSB schemes using mixed-signal with AR are also evident in these satellites. However, the differences between mixed-signal and fixed-signal with DSB corrections are minor compared to the DCB scenario, demonstrating that DSB can better correct the biases between each signal even under mixed-signal settings.

Figure 4-8 presents the mixed-signal orbit solution precision concerning the IGS final products. The average orbit precision is around 11 mm and matches well with the IGS final product. Comparing the orbits using DCB products and those using DSB products, it is clear that the

former agrees better with the IGS combined orbit by around 0.5 mm, which can be expected as most IGS ACs still use DCB products. The unsuitable orbit modeling gives some satellites, e.g., G11 and G18, a relatively large RMS value. They are the newly launched GPS BLOCK III satellites, and the orbit modeling is not precise yet.

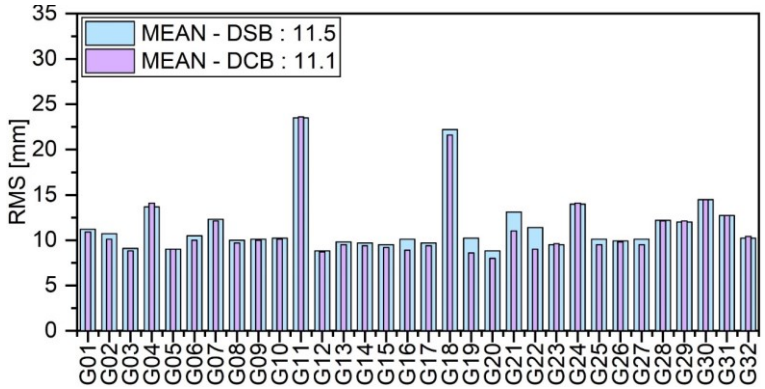

Figure 4-8 The orbit agreement of the solutions using DCB (blue) and DSB (purple) products with respect to the IGS final orbit product.

4.2.3 Satellite clock estimation

As the clock is directly related to the pseudo-range observations, the impact of using DCB and DSB products and selecting different signals on satellite clock estimates is further investigated.

Clock accuracy evaluated

Because the selection of reference satellite will impact all satellites RMS, the average clock among all satellites is used in each product to calculate the clock differences. RMS_{isat} and STD are the clock RMS value in Eq. (4.3) and STD value in Eq. (4.4) after shift with the average clock datum, respectively. After calculating the average difference, only the datum is altered, but their relative differences will not change, calculated as,

$$dif_{isat,iepo} = clk^1_{isat,iepo} - clk^2_{isat,iepo}$$

$$rms_{isat} = \sqrt{\sum_{iepo=1}^{n} (dif_{isat,iepo} - dif_{ref,iepo})^2 / n} \tag{4.3}$$

$$mean_{isat} = \sum_{iepo=1}^{n} (dif_{isat,iepo} - dif_{ref,iepo}) / n \tag{4.4}$$

$$STD=\sqrt{\sum_{iepo=1}^{n}(dif_{isat,iepo}-dif_{ref,iepo}-mean_{isat})^2/n}$$

where rms_{isat} is the RMS of the differences between the two clock products for the satellite, $dif_{isat,iepo}$ is epoch-wise clock difference between evaluated satellite with respect to the reference satellite, $mean_{isat}$ is the average clock among all n epochs, STD is the standard deviation of evaluated satellite clocks.

Analysis of clock biases

From Figure 4-9, four pairs of comparison show that the fixed solutions have the same results as the float solutions. For each satellite, the 30 days average clock difference is calculated and presented. The most significant differences are shown in the scheme of fixed-signal between DSB and DCB products, varying between 1.4 ns (G03) and -1.7 ns (G29). The large differences of up to 0.6 ns in intra-frequency correction between DCB and DSB could introduce biases and impact the clock RMS. However, when mixed-signal processing is employed with more W signals enabled, intra-frequency bias impact is reduced.

Comparing the clock differences between the solutions of mixed-signal and those of fixed-signal, using the DSB products (green) vastly reduces the value more than using the DCB products (blue). The differences between fixed-signal and mixed-signal using the DSB scheme are minor, and all satellites are within 0.15 ns. In contrast, in DCB schemes, such as G03, G11, and G29 satellites, the difference is up to 1 ns.

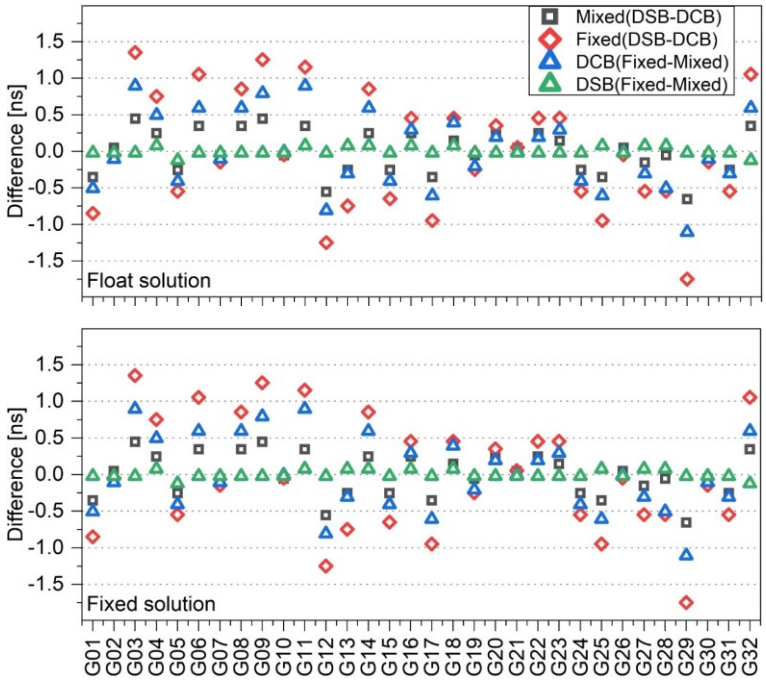

Figure 4-9 Clock differences between solutions using DCB and that using DSB products, with

mixed-signal (black) and fixed-signal (red), and the differences between solution using mixed-signal and that using fixed-signal, with DCB products (blue) and DSB products (green).

Additionally, as inter-frequency signal biases adhere to the characteristic of zero following the IF combination (as shown in Eq. (3.14)) there won't be any difference when stations have observations on C1W and C2W signals in all float solutions. However, not all stations can observe the W signal in all epochs. When the other signals are used to calibrate the intra-frequency signal bias as the W signals, the bias will exist in the float solution after the IF combination. Therefore, the mixed-signal causes systematic bias in pseudo-range observations and clock biases because of the intra-frequency signal biases in IF combination.

The comparisons of ambiguity-fixed solutions show a similar conclusion to those of the float solutions. In addition, the STD values of the clock differences in each daily solution are also calculated, and the values of all comparisons, i.e., between using DCB and DSB products, and between using mixed-signal and fixed-signal, are all close to zero. As the RMS is mainly determined by pseudo-range observations, the STD of satellite clock is primarily affected by phase observations. Comparing different solutions, the difference in the fixing rate is only about 1%, even when the difference in orbit is as much as 10 mm. This results in a corresponding clock difference of about 0.03 ns, which only has an insignificant impact on clock precision.

4.2.4 UPD estimation

Since the UPD estimation is sensitive to pseudo-range biases, the absence of accurate correction for these biases could significantly impact the UPD estimation. As indicated in Eq. (3.14), despite the fact that P1P2 and C1W-C2W corrections satisfy the condition of the IF combination as zero, they still result in discrepancies in WL UPDs because the WL combination is not the same. Moreover, imprecise intra-frequency biases could damage the consistency of both IF and WL combinations due to the different corrections given in DCB and DSB products. The NL UPD could be changed by the WL shifted and imprecise corrected in IF combination observations. Consequently, the WL and NL UPDs are analyzed and evaluated sequentially.

Fractional part of WL UPD differences

Figure 4-10 shows the fractional part differences of WL UPDs between using DCB and DSB products on mixed-signal and fixed-signal setting, and Figure 4-11 gives the differences of WL UPDs between using fixed-signal and mixed-signal settings with DSB and DCB products. All the results are the statistical distribution during 30 days. For each satellite, the range of 50% and 90% data set distributions are within the box and upper and bottom lines, respectively. The blue

markers show those with a bias larger than 0.2 cycles. The orange dots are max and min values. The green symbols denote those within 0.2 cycles.

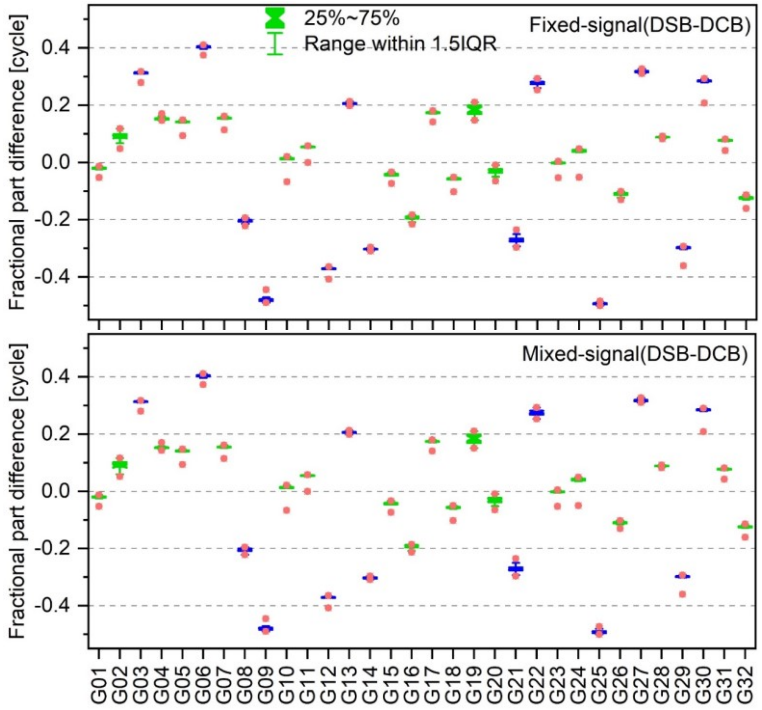

Figure 4-10 WL UPD differences between using DCB and DSB products on Fixed-signal (top) and Mixed-signal (bottom).

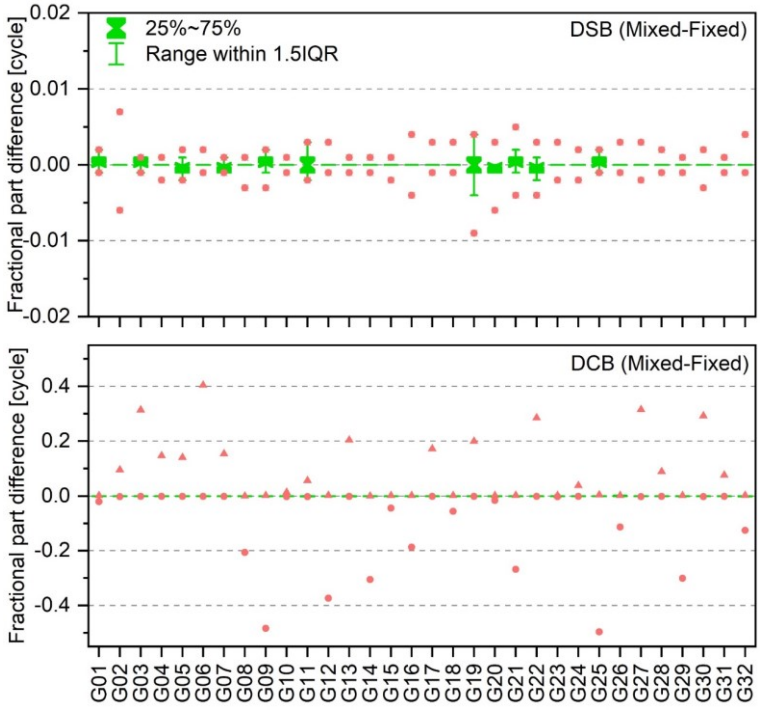

Figure 4-11 WL UPD differences between Mixed-signal and Fixed-signal using DSB (top) and DCB (bottom) products in a period of DOY 270-300, 2021. The dots are the max and min for each stations differences.

As shown in Figure 4-10 and Figure 4-11, WL UPD biases exist between DCB and DSB solutions and mixed-signal and fixed-signal, which are quite stable over a period of one month. Between Figure 4-10 DSB and DCB schemes, mixed-signal and fixed-signal solutions show the same deviations on each satellite, which can be explained by the differences in using DSB products shown in Figure 4-11. Between DSB and DCB results, 13 satellites have differences greater than 0.2 cycle. The biases on G09 and G25 satellites reach 0.47 cycle. However, using DSB product, the 90% differences between fixed-signal and mixed-signal results are within ±0.005 cycle. The largest difference is also within the ±0.01 cycle, demonstrating that the DSB product could accurately calibrate the signal biases. In contrast, using DCB products, 90% differences can be within 0.02 cycle while the largest difference can be up to 0.48 cycle. It is further shown that the DCB products cannot accurately calibrate the biases on each signal.

Integer part of WL UPD differences

Signal bias leads to deviations in the fractional part of the WL UPD, while its integer part may also differ due to some larger biases. Figure 4-12 presents the WL UPD integer part differences between different solutions, i.e., between solution using DCB products and that using DSB products with mixed-signal (black) and fixed-signal (red), and between solutions of mixed-signal and fixed-signal using DCB products (blue) and DSB products (green).

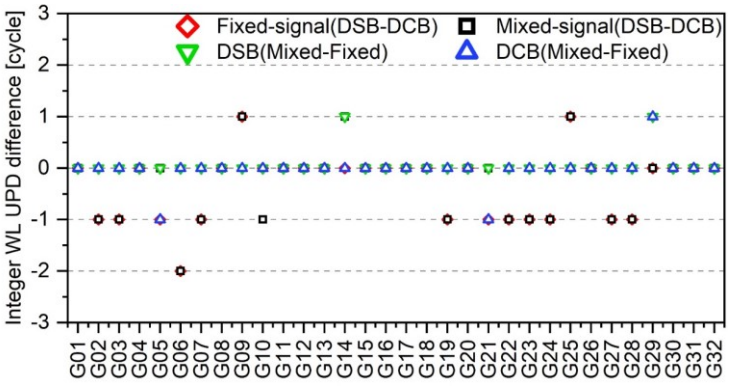

Figure 4-12 WL UPD differences between using DCB and DSB products and mixed-signal and fixed-signal on DOY 298, 2021.

As shown in Figure 4-12, i.e., integer part, there is the largest biases up to two cycles shown between DSB and DCB using mixed-signal or fixed-signal. Between DSB and DCB using the mixed-signal scheme, 13 satellites show one cycle biases while the G06 satellite is up to two cycles. Between DSB and DCB using the fixed-signal scheme, 12 satellites show one cycle biases while the G06 satellite also has the largest bias up to two cycles. In contrast, the differences between mixed-signal and fixed-signal using DSB or DCB products have fewer biases than former schemes. When DSB and DCB products are used between mixed-signal and fixed-signal,

one and three satellites show one cycle biases, respectively. Therefore, the DCB products cannot properly correct the pseudo-range biases for some certain types of signals.

Fractional part of NL UPD differences

The successful and correct AR depends not only on the WL but also on the NL. Furthermore, the difference of NL UPDs using DCB or DSB products on fixed-signal or mixed-signal are also shown in Figure 4-13.

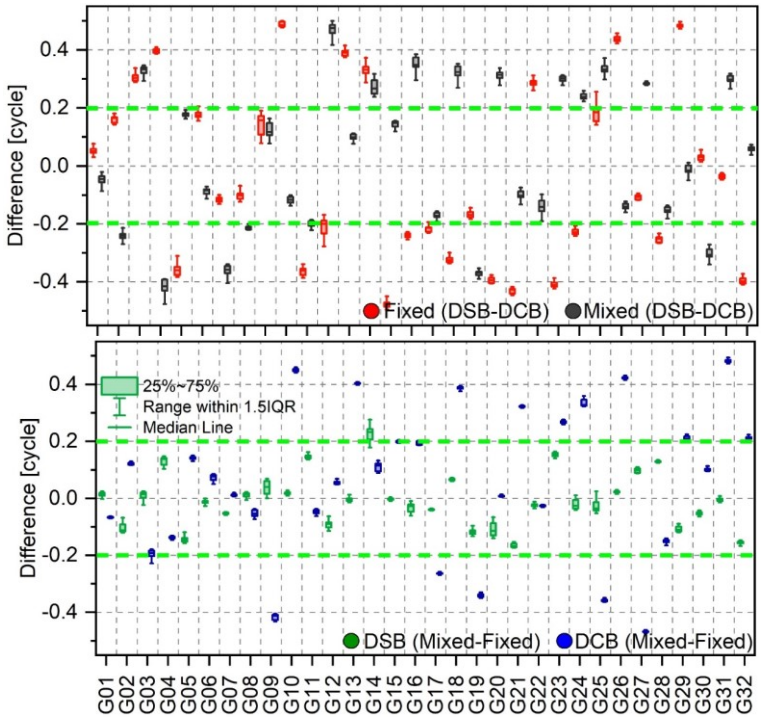

Figure 4-13 The NL UPD differences between solutions using DCB and that using DSB products, with either mixed-signal or fixed-signal on the top panel, and the difference between solutions of mixed-signal and that of fixed-signal, using either DCB or DSB products in the bottom panel at DOY 298, 2021.

As shown in Figure 4-13, the NL UPD of different solutions all have stable performance, with the 5%-95% confidence level of 0.07 cycle. The top panel illustrates that the NL UPD differences between using DCB and DSB products are quite significant in the mixed-signal and fixed-signal solutions, with more than half of the satellites greater than 0.2 cycle. The different bias values provided in the DCB and DSB products are responsible for the differences in the fixed-signal solution, and the differences in the mixed-signal solution are also caused by the fact that the bias values of some signals are not clearly provided in the DCB products. Differences of up to 0.49 cycles in IF combinations and 1-2 cycles in WL UPDs further impact the estimated NL UPDs. The intra-frequency correction on IF combinations and inter- and intra-frequency corrections on WL can affect the NL UPDs if the imprecise correction or different corrections from DCB or DSB

products.

The values of the solution using DSB products are significantly lower than those using DCB products in the NL UPD differences between the mixed-signal and fixed-signal solutions displayed in the bottom panel. The number of satellites with NL UPD difference larger than 0.2 cycle is one when DSB products are applied, i.e., G14, whereas the number is 14 when DCB products are applied. Due to the poor performance and uncategorized DCB product correction values, the relatively large NL UPD differences are presented. It is mainly caused by inconsistent pseudo-range bias corrections but is actually reflected in the WL UPD integer shifts and the estimates of IF ambiguities.

It is worth noting that when the positioning and UPD estimation use the same bias products with selected signal setting, i.e., C1C and C2W, the differences in the UPD will not be important anymore. Otherwise, the imprecise correction for mixed-signal or fixed-signal with inconsistent corrections could introduce biases and further impact the results.

4.3 Impact of signal bias in positioning

The bias of the pseudo-range not only affects AR and convergence time but also the positioning. In this section, the calibration performance of DCB and DSB products is investigated on each signal to analyze and compare the influence in positioning using two sets of products (this is, orbits, clock, and UPDs) generated with DCB and DSB, respectively.

4.3.1 Signal setting in positioning

Since the accuracy of orbits and clocks in the fixed-signal is comparable to that in the mixed-signal, the latter products are used for the following positioning investigation to ensure that more observations are used on the server-side.

The IGS weekly solution is used as a reference for evaluating the positioning precision. The PPP-AR solution is performed using two sets of products, namely DCB and DSB, in the product generation, both with mixed-signal. In kinematic PPP-AR solutions, the correction performance of DCB and DSB products is investigated for each signal set following four scenarios, as illustrated in Table 4-4.

Table 4-4 Scenarios for PPP-AR with different products and different bias corrections applied. “DCB/DSBoc” is short for “orbit and clock”, which indicates where code bias product is used in POD, PCE, and UPD derivation, and DCB/DSB is short for “positioning” applied.

Solution	Bias used for orbit, clock, and UPD	Bias for PPP-AR

	derivation	
DCB-DCBoc	DCB	DCB
DSB-DCBoc	DCB	DSB
DCB-DSBoc	DSB	DCB
DSB-DSBoc	DSB	DSB

The station numbers of specific signals in PPP-AR is further collected and shown in Table 4-5.

Table 4-5 The station number of selected signals in positioning evaluation.

Type	ALL	C1W&C2W	C1C&C2W	C1C&C2L	C1C&C2S	C1C&C2X
Station Number	189	128	189	132	31	144

From Table 4-5, all selected signals used in positioning have correction values in the DSB products. Whereas the GPS L1 frequency only provides C1C-C1W, the L2 frequency provides C2W-C2S, C2W-C2L, and C2W-C2X. From Table 4-1, S, L, X, and C signals should be classified as C-code in DCB, even though biases between these signals still exist. Because the DCB product only provides P2C2 correction without distinction of signals, the performance of DCB P2C2 correction for these signals is also investigated.

4.3.2 Observation residuals

The DCB or DSB products and the C1C&C2W, C1C&C2L, C1C&C2X, C1C&C2S, and C1W&C2W signals are used for positioning and to present the pseudo-range observation residuals.

Residuals calculation

To calculate the residuals in each solution, the mean residuals ave_{isgl}^{isat} and their STD std_{sgl}^{isat} for each satellite of all epochs are calculated firstly.

$$ave_{isgl}^{isat} = \frac{\sum_{iepo=1}^{nepo} res_{iepo}}{nepo}, \qquad std_{isgl}^{isat} = \sqrt{\frac{\sum_{iepo=1}^{nepo}(res_{iepo} - ave_{islg}^{isat})^2}{nepo - 1}} \tag{4.5}$$

where superscript $isat$ and $iepo$ denote satellite and epoch, respectively; subscript $isgl$ denotes signal type; $nsat$ and $nepo$ are satellite and epoch numbers, respectively.

Secondly, the average values of ave_{isgl} and standard deviation of std_{isgl} for all satellites are calculated, and these two values can indicate the systematic and stochastic noise level, respectively.

$$ave_{isgl} = \frac{\sum_{isat=1}^{nsat} ave_{isgl}^{isat}}{nsat}, \qquad std_{isgl} = \frac{\sum_{isat=1}^{nsat} std_{isgl}^{isat}}{nsat} \tag{4.6}$$

Finally, the overall standard deviations std_{isgl}^{bias} and std_{isgl}^{noise} are calculated, and these values can indicate the pseudo-range systematic errors after correction and the consistent performance among each satellite signal noise, respectively.

$$std_{isgl}^{bias} = \sqrt{\frac{\sum_{isat=1}^{nsat}(ave_{isgl} - ave_{islg}^{isat})^2}{nsat-1}}, std_{isgl}^{noise} = \sqrt{\frac{\sum_{i=}^{nsat}(std_{isgl} - std_{isgl}^{isat})^2}{nsat-1}} \tag{4.7}$$

These indicators are used to analyze the residuals in each group's signal positioning.

Analysis pseudorange residuals

The average value of selected signals under four scenarios are shown in Figure 4-14 and Figure 4-15.

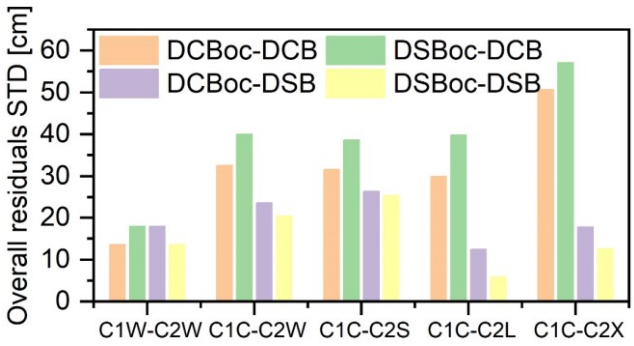

Figure 4-14 Overall STD std_{isgl}^{bias}.of satellite-specified mean of pseudo-range residuals

From Figure 4-14, it can be observed that the DSB-DSBoc solution consistently exhibits the minimum systematic biases, indicated by the STD of satellite-specified mean of pseudo-range residuals std_{isgl}^{bias}, among the four scenarios. In contrast, the DSBoc-DCB solution consistently performs the worst. For C1C&C2W, C1C&C2S, and C1C&C2L signals in the DSBoc-DCB solutions, the STD values are similar about 39 cm. Conversely, the STD values for the same signals in the DCBoc-DCB scenarios are slightly smaller, at 31 cm, respectively. This suggests that the DSB correction values for each signal are more accurate than those provided by DCB with only P and C codes. Notably, the least overall STD in the DSBoc-DSB scenario for C1C&C2L signals is only 5.7 cm, which demonstrates the high accuracy of the DSB in correcting the bias for these signals. On the other hand, the DCBoc-DCB overall bias is 49.5 cm, indicating the low accuracy of the correction values provided by DCB in C1C&C2X signals. Interestingly, the overall STD between DCB and DSB for the C1C&C2L scenario exhibits insignificant differences, suggesting that the correction performance of the DCB for the C2L signal is better than that for the C2S and C2X

signals.

When using DSB products in positioning, the residuals can be reduced largerly than using DCB products regardless of the generated products used. As a result, the differences in the products have a much lower impact on the positioning results than the DSB corrections at the user stations. As DSB is better than DCB for almost all signals, using DSB has the smallest range of residuals. Among all solutions, DSB and DCB have similar performance on W-signals. However, for C1C&C2W, C1C&C2L, C1C&C2S, and C1C&C2X signals using DSB products, pseudo-range residuals are reduced by 15%, 71%, 25%, 71% compared with that using DCB, respectively. To sum up, pseudo-range residuals show that the DSB corrections are accurate for all the signals.

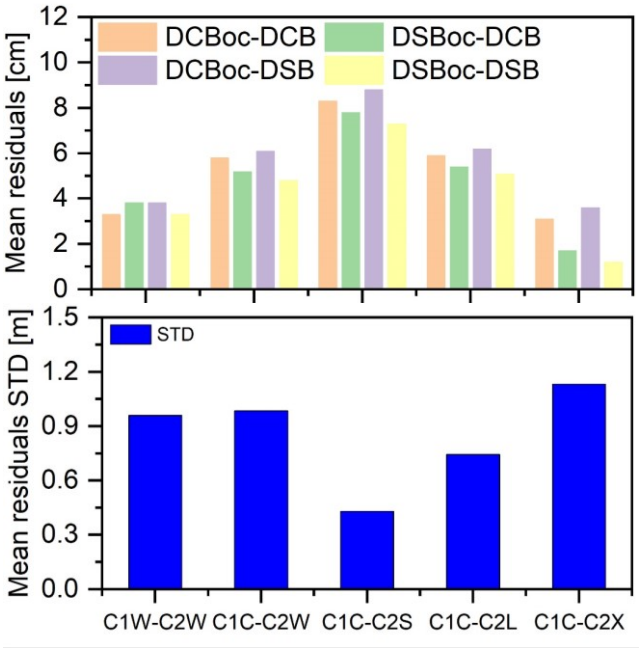

Figure 4-15 Satellite-specified mean noise ave_{isgl} (top) and noise STD std_{isgl} (bottom) of pseudo-range residual statistics in different positioning schemes.

In Figure 4-15, the mean signal noise level can be reflected through the mean value of satellite-specified average residuals ave_{isgl} and their standard deviation std_{isgl}. Different biases and mixed-signal generated products are utilized for positioning, but they do not affect the signal noise level. Among the five types, the C1C&C2X scenarios exhibit the lowest mean noise at 1.2 cm. Meanwhile, the C1C&C2W and C1W&C2W scenarios demonstrate comparable performance, with the mean of all satellites stochastic residuals of 5.3 cm and 3.5 cm, respectively. However, the residuals standard deviation for C1C&C2W (about 98.6 cm) is smaller than that of C1W&C2W (about 96.1 cm), indicating that these two combination has a larger residual differences between each satellite. The C2S signal has a higher mean residual than C2L, but the lower standard deviation is reversed. In addition, the C1C&C2S combination has the lowest noise standard deviation of 42.9 cm, implying that the noise levels of each satellite are

comparable. The noise standard deviation for C1C&C2X is 113.2 cm, and the mean noise level is 2.7 cm, indicating that these signals exhibit a significant difference. Overall, the noise levels of the signals are in ascending order as X, W, C, L, and S, while the noise difference among all satellites in the same signal follows the order of S, L, W, C, and X in ascending order.

4.3.3 Convergence time

The differences between estimated and reference coordinate absolute values are calculated, and the result of all solutions are sorted from largest to smallest epoch by epoch. The 68th percentile denotes the data at each epoch's 68th percentile of the sorted data. In addition, the 68th, 90th, and 95th percentile positioning results convergence time are given in Table 4-6.

Table 4-6 Average time of convergence to 10 cm with 1-sigma and 2-sigma percentile results during 30 days. Unit is min.

Signal	Bias-type	68th	95th
C1W-C2W	DCBoc-DCB	10.2	53.0
	DSBoc-DCB	11.2	53.7
	DCBoc-DSB	10.9	53.2
	DSBoc-DSB	10.0	52.1
C1C-C2W	DCBoc-DCB	13.7	65.1
	DSBoc-DCB	14.2	65.6
	DCBoc-DSB	12.9	64.3
	DSBoc-DSB	12.2	63.7
C1C-C2L	DCBoc-DCB	32.1	110.3
	DSBoc-DCB	33.2	117.6
	DCBoc-DSB	26.1	96.0
	DSBoc-DSB	24.3	92.2
C1C-C2X	DCBoc-DCB	42.9	-
	DSBoc-DCB	43.6	-
	DCBoc-DSB	42.2	-
	DSBoc-DSB	40.7	-
C1C-C2S	DCBoc-DCB	34.0	106.4
	DSBoc-DCB	36.1	115.5
	DCBoc-DSB	31.2	95.7
	DSBoc-DSB	28.1	91.2

The C1W-C2W signals exhibit the shortest convergence time among all the results. After applying DSB products, the convergence time using the C1C-C2L signals is improved by 24.4% and 16.4% for 1-sigma and 2-sigma, respectively. Similarly, for the C1C-C2S signal, the improvements are 16.4% and 14.3% for 1-sigma and 2-sigma, respectively. Because of the generated orbit and clock still use the C1W, C2W, and C1C signals. In addition, all satellites can provide C1C, C1W and C2W signals, but only 24 satellites can provide C2L, C2S, and C2X signals,

which significantly effect the precision and convergence time. Even if S and L have low stochastic and systematic noises, the C and W signals still have the best performance. As for the C1C-C2W signal, the improvements are 10.9% and 2.2% for 1-sigma and 2-sigma, respectively. On the other hand, the correction using DSB and DCB for the C1C-C2X signal shows only small differences, around 4.6% and 2.5%, respectively. In the case of the C1W-C2W signals, the use of DSB products leads to improvements of approximately 8.6% and 1.7% compared to DCB for 1-sigma and 2-sigma, respectively.

Among all results, the DSB-DSBoc has the shortest convergence time, but DCB-DSBoc has the longest time. Because the W and C signals are mainly selected in the products generated, most biases between signals are corrected. The results of DSB-DCBoc are close to those of DSB-DSBoc, indicating that using DSB products in positioning can bring better convergence performance. There are no significant differences in C1W&C2W signals between DCB and DSB results, which is also consistent with the residuals of this signal in Figure 4-14 and Figure 4-15.

4.3.4 Ambiguity fixing rate analysis

The number of epochs that have successful ambiguity fixing is kept track and presented in Figure 4-16.

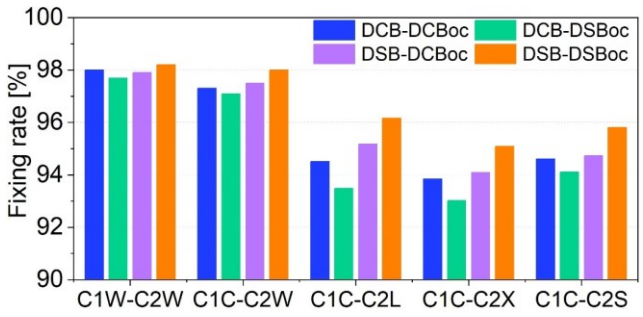

Figure 4-16 The ambiguity fixing rate in each type of signals. Note that the vertical axis starts from 90% for better visualization.

In the mixed-signal setting, the W and C signals account for the majority of observations, approximately 99%. Consequently, the fixing rate of the S, L, and X signals. On the one hand, the products are generated by the C and W signals, which intra-frequency biases could impact the UPD and be inconsistent with the S, L, and X signal corrections. On the other hand, the less satellite can provide C2S, C2L, and C2X signals. While the C1W&C2W and C1C&C2W signals exhibit similar fixing rates, the other signal types show a 3% lower fixing rate. Among all the results, the DSBoc-DSB combination demonstrates the highest fixing rate, whereas DSBoc-DCB yields the lowest. The results obtained with DCBoc-DSB are comparable to those of DSBoc-DSB-,

indicating that using DSB products in positioning can significantly improve biases and expedite convergence. Overall, the generated products have a minor impact on positioning.

DSB products have been shown to enhance positioning convergence and fixing rates when utilizing C, L, S, and X signals, compared to DCB solutions. This observation aligns with the fact that, despite being labelled as C-code, there are deviations among these signals, which in turn affect ambiguity fixing rate and convergence time. This finding is also consistent with the positioning results and pseudo-range residuals. As the bias products used in positioning may differ from that employed in product generation, this discrepancy can influence the ambiguity fixing rate on the positioning, which could impact the precise atmospheric delay derivation over large-area.

4.4 Handling satellite-specified range bias at receiver-end

While DCB/DSB products are employed to correct pseudo-range biases associated with satellite signals, deviations at the receiver end are frequently overlooked. This is because receive-end range biases are typically assumed to be uniform for all satellites and signals, and can be eliminated by taking the difference between two satellites. Currently, multiple manufacturers and model receivers distribute worldwide/large-area to provide GNSS technology development and industry application services. Different manufacturers or brands of receivers also could cause a satellite-specific deviations in the pseudo-range observations. Hence, achieving reliable ambiguity resolution across all receiver types necessitates consistent pseudo-range and precise UPD products, as the pseudo-range biases are sensitive to WL UPD. This section introduces the method for estimating WL UPD deviations related to satellite-specified range biases at the receiver-end.

4.4.1 Receiver bias calibration

For the receiver-end range biases, it is obvious that they can be cancelled by forming difference between satellites if the biases are the same for satellites. Moreover, if the receiver-end biases are the same among different types of receiver, the inconsistent satellite-specified biases can also be absorbed by the satellite-end UPDs. Unfortunately, the receiver-end biases could be different among satellites and receiver-types as well. Based on above discussion, only the inconsistency of satellite-specified pseudo-range biases between different receiver types will bias WL ambiguities differently and thus contaminate UPD estimates. These inconsistent biases can be revealed in the DD fractional part of the float ambiguities (FPAs) or UPDs where common impacts at both receiver- and satellite- sides are already removed (Hauschild & Montenbruck

2014) as follows,

$$d_{r,q}^{s,p} = d_r^{s,p} - d_q^{s,p} = (d_r^s - d_r^p) - (d_q^s - d_q^p) \tag{4.8}$$

where $d_{r,q}^{s,p}$ refers to the DD of UPDs between satellite s and p and receivers r and q. The DD UPDs should be very close to zero if the UPDs estimated from different receivers are consistent with each other. Under the normal distribution assumption for UPD uncertainty, a significant inconsistency can be detected as outliers under the three times σ principle.

As soon as a large set of UPD samples is available, they can be classified into clusters based on their agreement, i.e., groups with locally higher sample density compared to other regions (Krishna & Narasimha Murty 1999). Significant differences between different groups would suggest that they possess inconsistent UPDs.

The K-Means algorithm is used to choose the best clusters to minimize the sum-square-error of the distances between a sample and its cluster centroid. It can be expressed mathematically as (Likas et al. 2003; Hansen et al. 2005),

$$P(S\{S_1, \cdots, S_k\}) = min \sum_{i=1}^{k} \sum_{j=1}^{n_{S_i}} \|w_{ij} - \overline{w}_i\| \tag{4.9}$$

where S is the set of total samples to be classified, $\{S_1, \cdots, S_k\}$ are the k clusters found which minimization criteria. For each cluster S_i there are n_{S_i} samples, w_{ij} is the j th sample of the i th cluster, and $\overline{w}_i$ is the centroid of the i th cluster which is defined as,

$$\overline{w}_i = \frac{1}{n_{S_i}} \sum_{j=1}^{n_{S_i}} w_{ij}\,, \quad i = 1, \cdots, k \tag{4.10}$$

The algorithm of clustering consists of looping of the following steps.

- **Step 1.** Select the data as initial partition of the whole dataset (Pena et al. 1999) for the groups $\{S_1, \cdots, S_k\}$. In this thesis, the clustering is applied on a satellite base. The initial groups are set according to the receiver types and sort the corresponding FPAs into the groups.
- **Step 2.** For each group, calculate its centroids $\overline{w}_i$ from all members $w_{i,j}$ by Eq. (4.10) and the STD of the residuals, take three-time averaged group STD as the threshold for testing

the group significance. Two groups are merged if their distance is shorter than the threshold. This will be repeated until no further groups can be merged.

- **Step 3.** for each member $w_{i,u}$ in group S_u reassign it to the closest group S_v if $\left\|w_{i,u} - \overline{w_v}\right\| \leq \left\|w_{i,u} - \overline{w_t}\right\|$ for all $t = 1, \cdots, k$.
- **Step 4.** Recalculate centroids for all the clusters after all the member in S_u are checked and then repeat Step 3 for all the groups
- **Step 5.** If there is no new group reassignment in Step 3 and 4, the processing stops. Otherwise, repeat Step 2 to 5.

As described in the preceding steps, the K-Means algorithm provides an initially partitions of the deviation and computes the average value of the resulting groups. Subsequently, the algorithm relocates database instances to the nearest centroid group, aiming to minimize the sum-square-error. Whenever an instance changes its group membership during relocation, the centroids of the groups and the sum-square-error are recomputed. The aforementioned process is iteratively repeated until convergence, which is achieved when the sum-square-error cannot be further reduced, indicating that no instance changes its group membership.

It should be noted that MW combination can be influenced by biases in pseudo-range observations from satellite- and receiver ends. The biased pseudo-range affect of the WL and IF combinations could further jeopardize the NL UPD. Correspondingly, with achieved WL and NL UPD products, the related ambiguities can be fixed at a single receiver. The existence of bias within the UPD makes the PPP-AR incorrect or failed. Therefore, consistent signals biases have to be carefully calibrated before server-side UPD estimation and user-side positioning with ambiguity resolution.

4.4.2 Data processing

1560 regionally-distributed reference stations from the National Geodetic Survey (NGS) of the USA permanent network are selected for a period of 30-day in January 2019. To ensure the stability and accuracy of UPD estimation, only the type of receivers with more than 40 stations are selected to perform UPD estimation (Wang et al. 2018). The distributions of stations are shown in Figure 4-17 and Figure 4-18, with the different colors representing different receiver hardware and firmware versions and the number of stations for each types of receiver are summarized in Table 4-7.

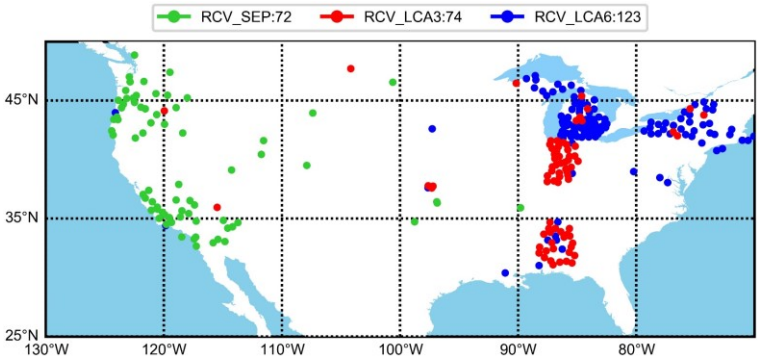

Figure 4-17 Distribution of GNSS stations of the USA NGS GNSS network (as of January 2019). Green dots denote the RCV_SEP, red dots denote the RCV_LCA3, blue dots denote the RCV_LCA6.

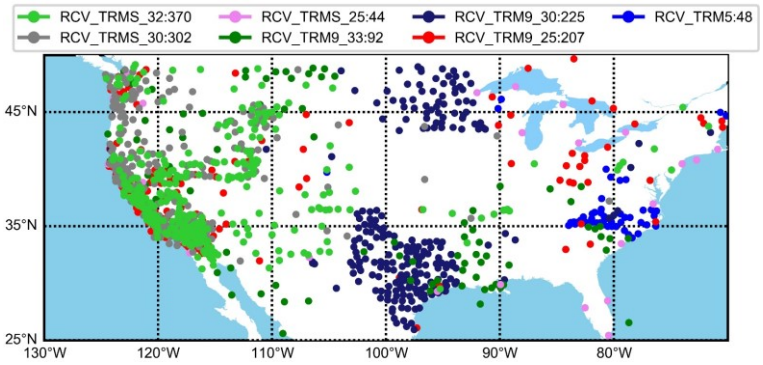

Figure 4-18 Distribution of different types of Trimble receivers in the USA NGS network (as of January 2019).

As shown in Figure 4-17 and Figure 4-18, each type of receiver have enough stations to estimate UPD. During the test period, all GPS satellites are in good condition except the satellite G04, which is unusable for most days, therefore is excluded in the processing.

Table 4-7 Receiver types and the corresponding number

Receiver	Type	Version	Num
Trimble (RCV_TRM)	NETRS (RCV_TRMS)	1.3-2 (RCV_TRMS_32)	370
		1.3-0 (RCV_TRMS_30)	302
		1.2-5 (RCV_TRMS_25)	44
	NET9 (RCV_TRM9)	5.33 (RCV_TRM9_33)	92
		5.30 (RCV_TRM9_30)	225
		5.22 (RCV_TRM9_22)	207
	NETR5 (RCV_TRM5)	48.01	48
SEPT (RCV_SEP)	POLARX5	5.1.0	72
LEICA (RCV_LCA)	GRX1200GGPRO (RCV_LCA3)	9.20/3.	74
	GRX1200+GNSS (RCV_LCA6)	9.20/6.	123

4.4.3 FPAs data statistics

The number of ambiguities contributing to estimating a single satellite's UPD is equal to the number of all continuously observed data arcs of the satellite, which is a measure of observation redundancy. As outliers should be excluded in the UPD estimation, the data usage rate, i.e., the percentage of the ambiguities used, must also be considered for quality control. For a direct illustration, the statistics of the number of ambiguities and the usage rate in UPD estimation over the test periods (30 days) are shown in Figure 4-19 for RCV_TRM9_22 and RCV_TRM9_30, respectively.

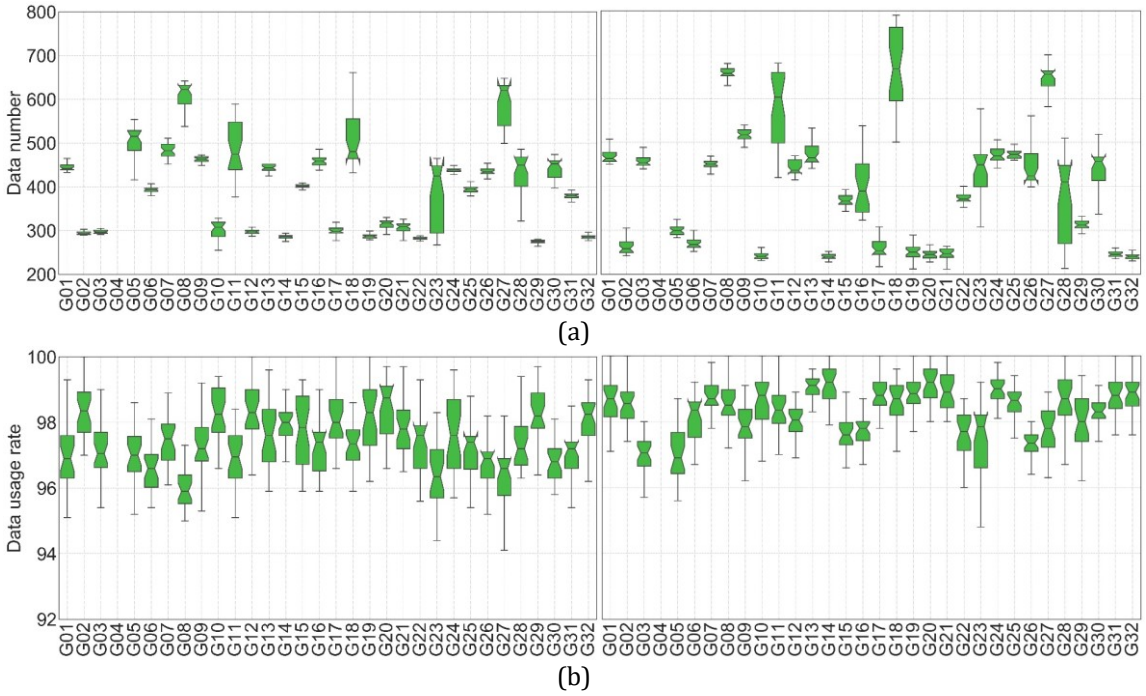

Figure 4-19 The statistics of the observation number (a) and the usage rate (b) over the 30 days test period for receiver type RCV_TRM9_22 (left) and RCV_TRM9_30 (right)

In Figure 4-19 the boxplot is used to show the statistics where the box contains a 50% confidence interval, while the top and bottom lines contain a 90% confidence interval; the line in the box is the median value. For all the satellites the number of data arcs is more than 200, and the data usage rate is above 95%, which means they have a large number of input observations for parameter estimation. For the G11, G18, and G23 satellites, the observation number fluctuation is large than others because some of the poor quality data are eliminated during the data pre-processing.

4.5 Receiver-dependent bias calibration

In this section, the estimated FPAs are used to investigate the consistency among different receivers. Moreover, the estimated satellite WL UPDs are compared for their receiver-type-dependent inconsistency. The deviations of daily WL FPAs from all stations and the deviations in

the estimated UPDs for each type of receiver are calibrated.

4.5.1 UPD clustering

FPAs calculation

As the WL float ambiguities are determined by the observations without any modeling, they are therefore highly correlated with the receiver's hardware characteristics. Each ambiguity or its FPA can be considered as an observation of the corresponding receiver and satellite UPDs, so FPAs can be applied to investigate the UPD consistency among receivers and receiver types as well.

After the statistical analysis of the observations used, the temporal stability of the WL FPAs of all stations of the 30 daily solutions is first demonstrated. For a station-satellite pair, there may be several ambiguities in a daily solution, their FPAs should agree with each other very well if the continuous observations are long enough (at least 30 minutes). In principle, the daily FPAs are very stable as reported (Li et al. 2016; Li et al. 2017). Three typical examples of FPA with the good, moderate, and poor agreement are shown in Figure 4-20.

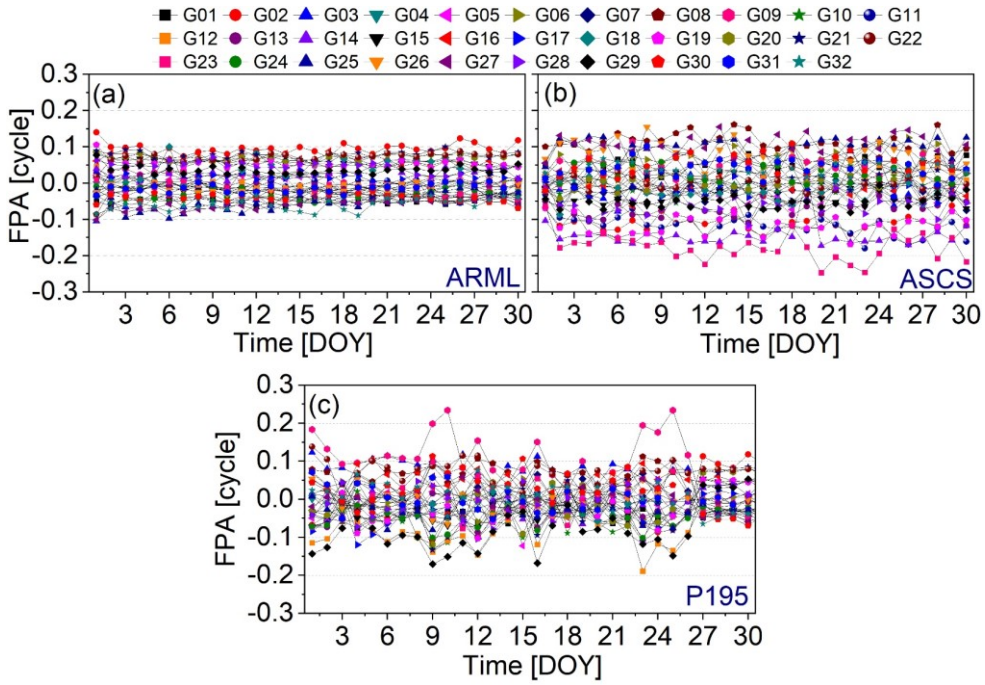

Figure 4-20 Daily FPA estimates for all GPS satellites at three stations: (a) ARML with good stability, (b) ASCS with moderate stability, and (c) P195 with poor stability. The x-axis is the DOY in 2019.

As shown in Figure 4-20c, at the station P195 with a poor stability, there are few satellites with

large fluctuation in the daily FPAs, e.g., G09, G13. The other satellites, however, all have stable performance during the 30-day period. All the satellites at the stations with the good (ARML) and moderate (ASCS) agreement have very stable variation, with the biases smaller than 0.05 cycle. Therefore, the averaged FPAs over 30 days can be applied for the investigation of receiver-type dependent UPD biases.

For each station-satellite pair, there is only one averaged FPA over the test period, and for each satellite, the total number is the number of stations that have enough observations to this satellite. For each satellite, the distribution of the FPAs of one type of receivers gives a measure of their agreement. Stacking the distributions of all receiver types further depicts the agreement among different receiver types. Figure 4-21 shows three typical cases with almost no, small, and significant differences among different receiver types. It should be noted that the G01 satellite is selected as the reference to remove the receiver UPDs which could vary in each daily solution.

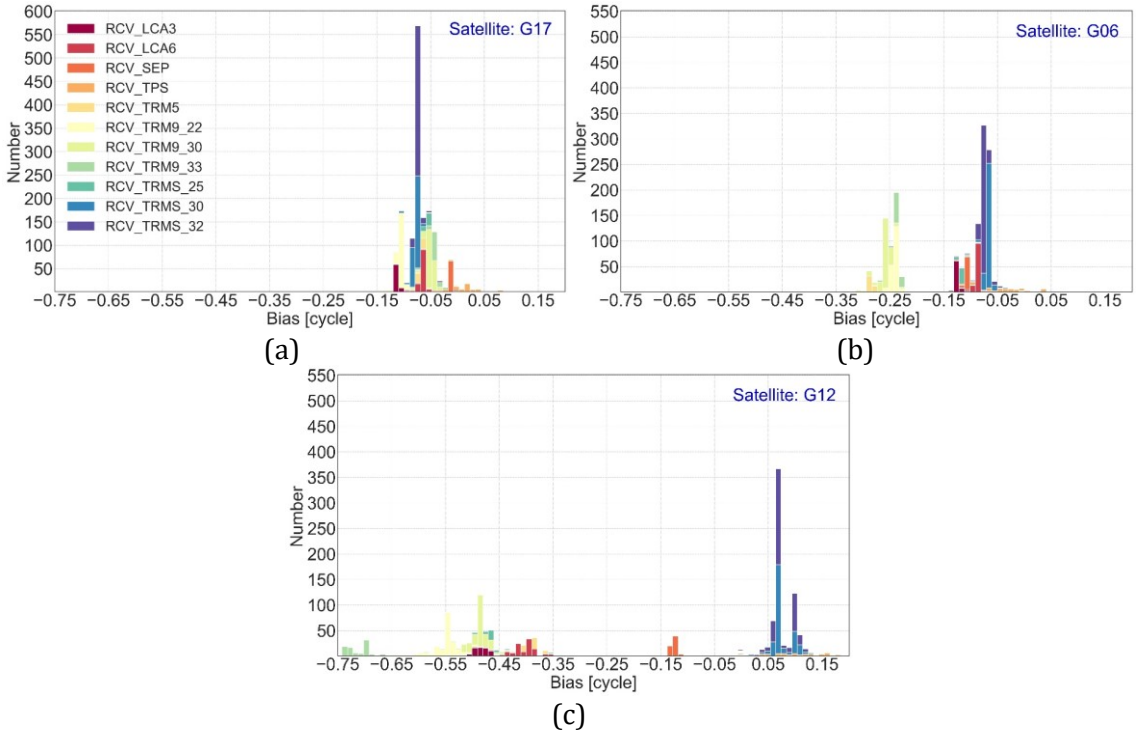

Figure 4-21 Distribution of satellite WL FPAs of receiver types with almost no (a), small (b), and significant (c) differences among different receiver types.

The histogram of each receiver type is in a different colors. The centralization of each histogram represents the agreement of FPA of this receiver type and the distance between the histogram of different colors shows bias among receiver-types. From Figure 4-21a, for G17 satellite all the FPAs agree with each other within ± 0.05 cycle, i.e. the various types of receivers show high consistency. While for G06 satellite, RCV_TRMS_33, RCV_TRMS_30 and RCV_TRM9_22 have a deviation of -0.20 cycle from the others, the G12 satellite shows a rather large difference in six groups.

Clustering and classification of WL FPAs

In general, the differences in FPA among different receiver types are very significant and vary from satellite to satellite. Hence, the automatic classification algorithm K-Means described in section 4.4.1 is applied to obtain the estimates of the differences in a rather convenient way. To remove outliers in the FPAs, a threshold of three times of STD of corresponding FPAs is applied. However, if the STD is too small, this threshold may result in wrong outlier detection. To avoid such mistakes, a 0.05 cycle is set as the smallest threshold, i.e., if the three-time STD is smaller than 0.05 then 0.05 is used. This value is chosen according to the WL wavelength and observation noise. The result is shown in Table 4-8 with the classified groups and their FPA differences referring to the receiver type of RCV_TRMS_32 (f).

Table 4-8 Result of K-Means automatic classification of fractional parts of WL ambiguities of receiver types. The estimated group difference is shown in the parentheses in the unit of WL cycle. The receiver types and label names are RCV_TRM9_22(a), RCV_TRM9_30(b), RCV_TRM9_33(c), RCV_TRMS_25(d), RCV_TRMS_30(e), RCV_TRMS_32(f), RCV_TRM5(g), RCV_LCA3(h), RCV_LCA6(i), and RCV_SEP(j).

Type	Sat	Clustering Group (cycle)				
		Cluster 1	Cluster 2	Cluster 3	Cluster 4	Cluster 5
IIR	G02	b,c,d,e,f,g,h,i	a (-0.09)	j (0.10)		
IIF	G03	e,f,g,h,i,j	a,c (-0.16)	d (0.08)	b (0.13)	
IIR-M	G05	e,f,g	c (-0.39)	d,j (-0.28)	a,b,h,i (-0.22)	
IIF	G06	d,e,f,h,i,j	a,b,c,g (-0.16)			
IIR-M	G07	a,b,c,d,e,f,g,h,i				
IIF	G08	d,e,f,g,h,j,i	a,c (-0.12)	b (0.11)		
IIF	G09	h,i,j,d,e,f	a,c (-0.21)	b,g (0.05)		
IIF	G10	a,b,c,d,e,f,g,h,i,j				
IIR	G11	a,e,f,h,i,j	b,d (-0.50)	c,g (-0.39)		
IIR-M	G12	e,f,j	c (-0.75)	a,b,d,h,g (-0.51)	i(-0.13)	
IIR	G13	e,f,g,h,i	a,b,c,d,j (0.09)			
IIR	G14	c,d,e,g,f,j	h (-0.10)	a,b,i (0.07)		
IIR-M	G15	a,e,f,h,j	d (-0.49)	i,g (-0.42)	c,b (-0.29)	
IIR	G16	b,c,d,e,f,i	a,g,h (-0.08)	j (0.10)		
IIR-M	G17	b,c,d,e,f,g,i	a,h (-0.05)	j (0.06)		
IIR	G18	a,c,e,f,g,i	b (-0.29)	d,h,j (-0.20)		
IIR	G19	a,e,f,h,i	b,d (0.08)	g,c,j (0.13)		
IIR	G20	a,c,e,f	d,j (0.11)	b,g,h,i (0.31)		
IIR	G21	a,b,c,d,e,f,h,i	g (0.09)	j (0.10)		
IIR	G22	b,e,f	a,c,d,g,h,i (-0.08)	j(0.08)		
IIR	G23	a,c,d,e,f,g,h,i,j	b (0.10)			
IIF	G24	a,c,d,e,f,h,j	g,i (0.14)	b (0.29)		
IIF	G25	a,b,c,d,e,f,g,h,i,j				
IIF	G26	a,c,d,e,f,j	b,g,h,i (0.18)			
IIF	G27	c,d,e,f,h,j	g (-0.07)	a,b,i (0.09)		
IIR	G28	e,f	a,b,j,d (-0.71)	c,g,h,i (-0.48)		
IIR-M	G29	a,c,e,f,g,h	b,d,i (0.08)	j (0.12)		
IIF	G30	a,b,c,d,e,f,j	g,h,i (-0.09)			

IIR-M	G31	a,b,c,d,e,f,g,i,j	h (-0.06)			
IIF	G32	e,f,j	d (-0.72)	c,h,i (-0.51)	b,g (-0.37)	a (-0.20)

Table 4-8 shows that most of the receiver types have very good agreement with each other with few exceptions. For the G07, G10, and G25 satellites, all receiver types demonstrate highly consistent characteristics. Conversely, with respect to the G03, G05, G12, G15, and G32 satellites, certain receiver types exhibit significant deviation from the reference type RCV_TRMS_32(f). The observations and estimation procedures for these satellites have been reviewed and no anomalies have been identified relative to other satellites. Furthermore, classification results indicate that RCV_TRMS_30(e) and RCV_TRMS_32(f) are grouped together for all satellites, signifying that these two receiver types possess highly similar WL FPA performance. However, RCV_TRM9_22(a) and RCV_TRM9_30(b) display the greatest disparity relative to the reference type RCV_TRMS_32(f).

4.5.2 Satellite WL UPD deviation

The RCV_TRMS_32 is selected as the reference type because it is the reference type in FPA clustering and compare its UPDs estimates with the other six types of Trimble receivers. The daily UPDs of each receiver type are estimated, i.e. 30 UPD solutions in total. The characteristics of the satellite UPD differences of the six receiver types with respect to the reference are shown in the box-plot in Figure 4-22 with the average and the STD.

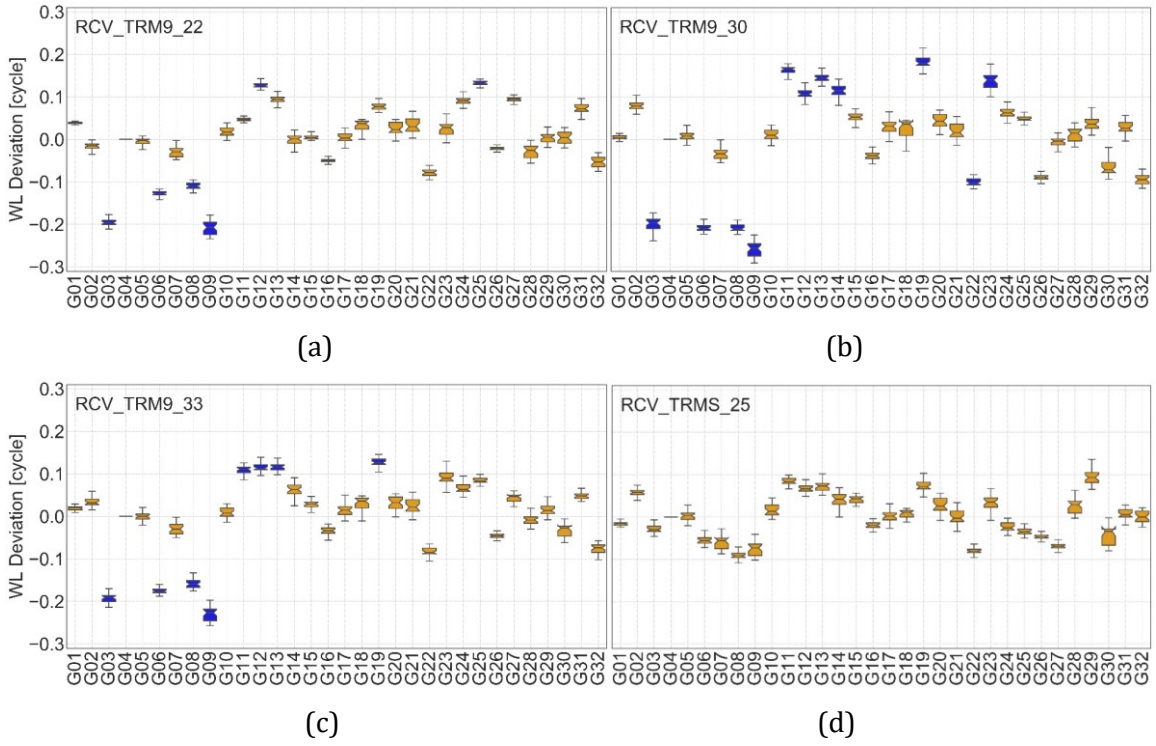

(a) (b)

(c) (d)

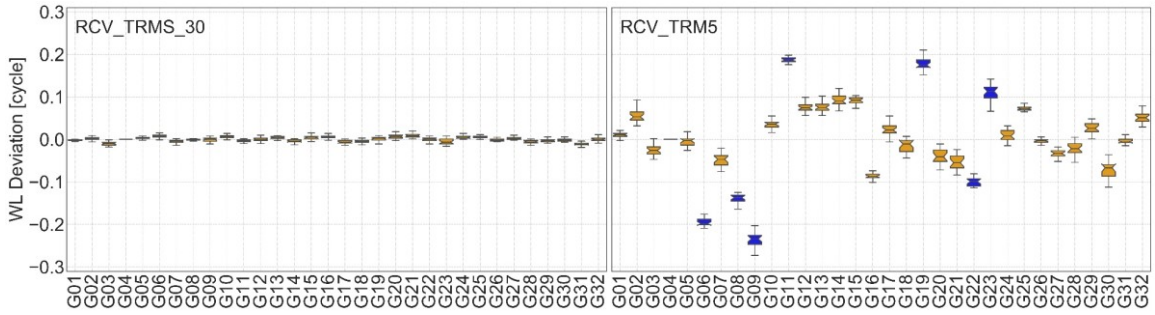

(e) (f)

Figure 4-22 WL UPD differences of different receiver types with respect to the RCV_TERMS_32 type, (a) RCV_TRM9_22, (b) RCV_TRMS_30 (c) RCV_TRM9_33 (d) RCV_TRMS_25 (e) RCV_TRMS_30 (f) RCV_TRM5. For each satellite, the 5% and 95% are within the box and upper and bottom lines, respectively. The blue markers show those with a bias larger than 0.1 cycle.

As depicted in Figure 4-22, RCV_TRMS_30 exhibits the highest degree of similarity with the reference receiver RCV_TRMS_32, with a bias of ±0.03 cycle observed across all satellites. Conversely, some satellites within the other three RCV_TRM9 series and RCV_TRM5 series exhibit substantial UPD deviations. With respect to RCV_TRM9, deviations larger than 0.1 cycle are observed for GPS Block IIF (G03, G06, G08, G09, G25) and Block IIR (G11, G12, G13, G14, G19, and G23) satellites, while for RCV_TRM5, large biases of up to 0.2 cycle are observed for Block IIF (G06, G08, G09) and Block IIR (G11, G19) satellites. These results suggest the presence of significant biases among different versions of receivers from the same brand. For RCV_TRMS_25 UPDs, IIR type satellites G11, G13, G19, and G29 exhibit values close to 0.1 cycle. RCV_TRM9_30 demonstrates the poorest performance, with eleven satellites exhibiting STDs larger than 0.1 cycle, and among them, the STDs of G03, G06, G08, and G09 satellites are even greater than 0.2 cycle. Nevertheless, the WL UPD deviations between RCV_TRMS_32 and each Trimble type, including G01, G05, G07, G10, G17, G18, G28, and G31 satellites, remain within ±0.1 cycle.

A similar phenomenon is also reported in the investigation of FPA characteristics in Section 4.5.1. For example, RCV_TRMS_30 and RCV_TRMS_32 agree very well and the FPA deviation of G09 satellite reaches 0.25 cycle for the RCV_TRM9 types. The UPD differences of the receiver types from other manufacturers are also calculated in the same way with respect to RCV_TRMS_32, as illustrated in Figure 4-23. RCV_ALL means UPD estimated using all types of receiver despite the receiver-type dependent biases, which is generally chosen in the data processing.

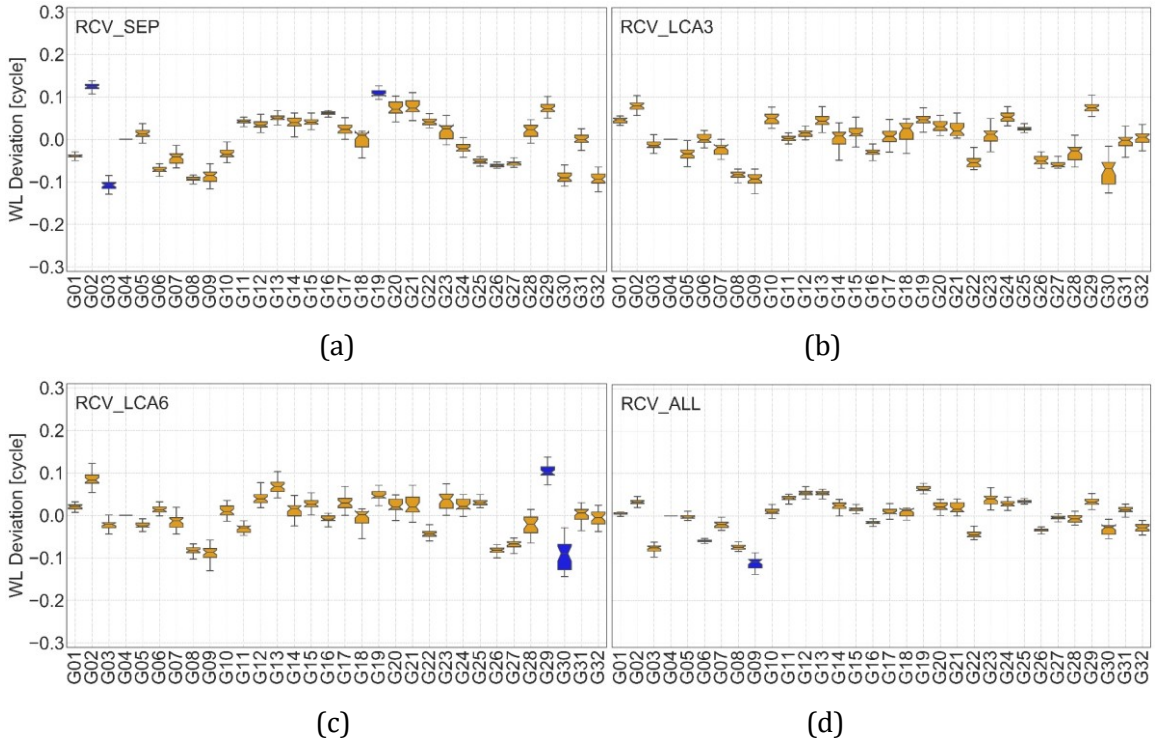

Figure 4-23 UPD deviation of four no-Trimble receiver types with respect to RCV_TRMS_32. (a) RCV_SEP (b) RCV_LCA3 (c) RCV_LCA6 (d) RCV_ALL

The G02, G03, and G19 satellites of RCV_SEP have the largest deviation but only slightly larger than 0.1 cycle. While, for RCV_LCA, these two types (RCV_LCA3 and RCV_LCA6) show a similar distribution. The satellite deviations of WL UPDs show the same features with FPAs distribution shown in Table 4-8. In the type of RCV_LCA6, only G29 and G30 satellites have the deviations of about 0.1 and -0.1 cycle in UPDs and the same approximate 0.08 and -0.09 cycle in FPAs, respectively. Besides, the three types of RCV_TRM9 receivers all have similar large deviations in FPAs and UPDs. This is clearly because UPDs are estimated based on the FPAs. When all types of receiver are implemented, the deviation becomes small because deviation among different types is reduced.

When a mixture of different receiver types is included, the satellite UPDs could be contaminated. More importantly, PPP-AR will be degraded if the UPDs are estimated from different types of receivers with significant UPD deviations. To summarize, the deviations of the WL FPAs among different types of receivers will have negative impact on not only the estimation of satellite UPDs but also PPP-AR.

4.5.3 Calibration of the WL UPD deviation

To uniformly compensate the WL UPD deviations among different types of receivers for both UPD estimation and for PPP-AR, the satellite-specified WL UPD deviations can be estimated by

the classification algorithm or by simply taking the average of the 30 daily UPD estimates depicted in Figure 4-24.

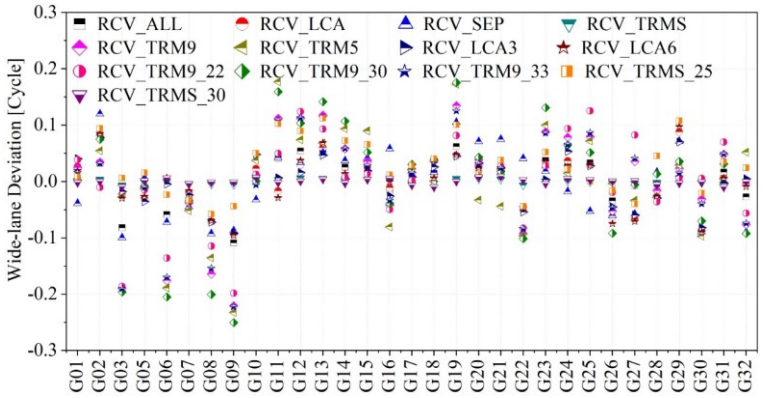

Figure 4-24 Receiver-type dependent WL UPD biases with respect to RCV_TRMS_32 by taking an average of 30 daily UPD estimates

RCV_TRM9_30 has the largest deviation of ±0.26 cycle, while RCV_TRMS has the smallest deviation of ± 0.04 cycles. Besides, for satellite G03, G06, G08, G09, and G19, the UPD deviations among different receiver types could reach 0.2 cycles.

Since it is hard to find out the mechanism of such differences and to precisely characterize receiver WL UPD deviation by a model, therefore, the deviations among different receiver types are calculated and compensated to avoid the trouble caused by inconsistent UPDs at the server- and user-end. The WL deviations is calibrated using the proposed model that classifies according to FPAs. To verify the effectiveness of the calibration after classification, the UPD residuals are calculated for each receiver type, and that of RCV_TRM9_22 and RCV_SEP types are shown as examples in Figure 4-25.

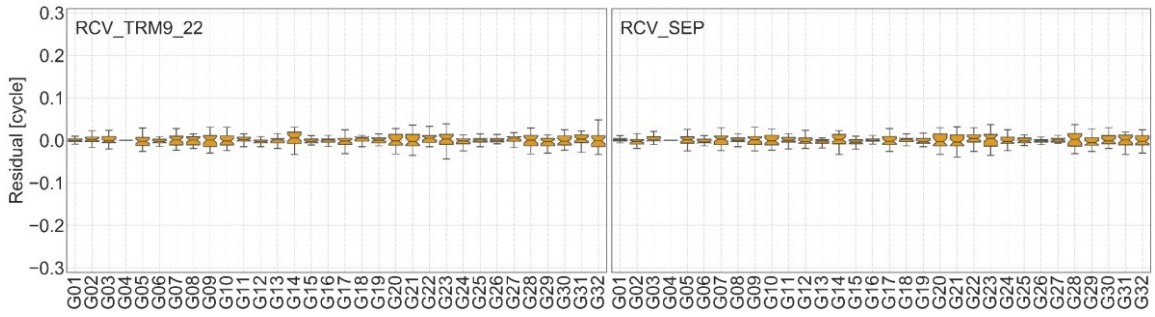

Figure 4-25 WL UPD residuals after the calibration of receiver-type dependent biases

Compared to the subplots in Figure 4-25 with the corresponding subplot for RCV_TRM9_22 in Figure 4-22 and RCV_SEP in Figure 4-23, the deviations after compensation are reduced to within ± 0.03 cycles, very close to zero and its STDs have similar fluctuations as before. Besides, comparing the box diagram in Figure 4-25 with Figure 4-22 and Figure 4-23, the 30-day

residuals of all satellites are reduced and kept very close to 0 without deviations.

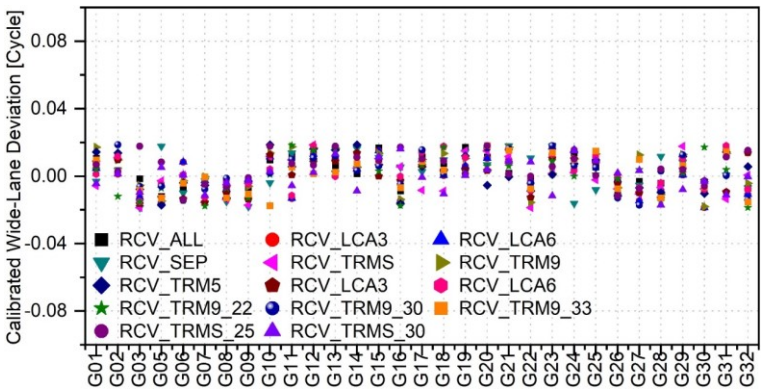

Figure 4-26 The WL UPD deviations after being calibrated

After applying the calibration in Table 4-8, the WL UPDs of all the receiver types can agree within ± 0.03 cycles. It is obvious that the remaining receiver-type dependent WL UPD bias can be ignored for WL ambiguity-fixing. As the corrections are derived with respect to a common receiver type, the corrected UPDs, therefore, refer to a unique reference no matter whether the reference receiver type is involved in the processing or not. Of course, corresponding corrections have to be applied to the user-side to use the corrected WL UPDs.

4.6 Application of the WL UPD deviation correction in positioning

In this section, the estimation of receiver-type-dependent WL UPD biases and their application as corrections to user stations are studied to reduce their impact on ambiguity resolution.

4.6.1 Positioning setting

To validate the reliability and accuracy of the corrected WL UPDs, the performance of PPP-AR using calibrated and uncalibrated UPDs are compared. The processing strategies of PPP-AR are listed in Table 3-2. The average of station coordinates of daily PPP static solution is used as a reference.

4.6.2 Analysis positioning result

All ten types of UPDs are utilized for kinematic PPP-AR for the test stations to statistically assess the impact of WL UPD biases on the PPP-AR performance. The ambiguity fixing rate and positioning accuracy are calculated and shown in Table 4-9 for PPP-AR using receiver-types without UPD differences, or with rather small UPD differences for a few satellites, and in Table 4-10 with large UPD deviations for a few satellites.

Table 4-9 PPP-AR result using receiver types without or with small WL UPD deviation. Positioning accuracy in cm for Horizontal (H) and Vertical (V) and Fixing rate (F) in percentage.

Receiver Type	UPD Type											
	RCV_TRMS_30			RCV_TRM9_32			RCV_LCA3			RCV_LCA6		
	H	V	F/%	H	V	F/%	H	V	F/%	H	V	F/%
RCV_TRMS_30	1.1	3.1	98.8	1.2	3.1	98.6	1.4	3.3	96.9	1.4	3.3	96.9
RCV_TRM9_32	1.2	3.0	97.7	1.2	3.0	97.9	1.5	3.3	96.6	1.5	3.3	96.7
RCV_LCA3	1.5	3.3	97.0	1.5	3.3	97.1	1.2	3.0	98.0	1.2	3.1	97.8
RCV_LCA6	1.6	3.4	97.3	1.6	3.4	97.0	1.2	3.1	98.0	1.2	3.0	98.0

Table 4-10 PPP-AR result using receiver types with large deviation for a few satellites. Positioning accuracy in cm for Horizontal (H) and Vertical (V) and Fixing rate (F) in percentage.

Receiver Type	UPD Types											
	RCV_TRM9_22			RCV_TRM9_30			RCV_TRMS_25			RCV_LCA6		
	H	V	F/%	H	V	F/%	H	V	F/%	H	V	F/%
RCV_TRM9_22	1.4	3.2	97.6	1.7	3.8	92.6	1.8	3.7	97.6	1.6	3.9	90.4
RCV_TRM9_30	1.5	3.7	95.0	1.4	3.1	98.8	1.6	4.2	92.6	1.8	3.5	91.8
RCV_TRMS_25	1.5	4.1	94.2	1.6	4.3	91.5	1.3	3.5	97.3	1.5	3.9	90.5
RCV_LCA6	1.6	4.1	95.3	1.8	4.2	93.7	1.9	4.0	90.6	1.3	3.3	96.9

As shown in Table 4-9, the results of those four types of receivers do not show any significant differences, between the solutions using the WL UPD from the same receiver-types and the others, because of the rather small biases in UPDs as discussed above. However, in Table 4-10, the difference between the solutions using UPD from the same receiver-type and that mixed is relatively obvious, for example, the fixing rate for the former one is about 97% and about 92% for the latter one, similar with the positioning accuracy. This is clearly the effect of the deviations in WL UPDs for different satellites which leads to poor ambiguity fixing.

Despite the majority of stations have similar positioning performance, as we can see from Table 4-9 and even Table 4-10, when PPP uses the UPD estimated from the same receiver-types or the types with small deviation, or for fewer satellites with slightly large deviations, the result of positioning does not show any significant difference. However, there are still some test stations that suffer from significant degradation in positioning performance because of using mismatched UPDs. A set of stations equipped with RCV_TRMS_32 receiver is chosen to compare and analyze the performance using the other five types of UPDs with large deviations and their calibrated ones. Among the result of five types of UPD, the UPD named calibrated indicates that the calibration is used and the result of RCV_TRMS_32 are used as the reference uniformly. The number of fixing epochs is counted and summarized in Table 4-11.

Table 4-11 Statistics of the PPP AR results using UPDs with large deviations

Receiver	UPD	N/cm	E/cm	U/cm	Fixing rate/%	TTFF/ min
	RCV_TRM9_22	4.9	7.9	10.1	82.95	16.5
	Calibrated	1.5	1.6	3.9	94.61	16.0
	RCV_TRM9_30	4.7	8.1	10.7	74.30	16.5
	Calibrated	1.5	1.6	3.7	96.52	16.0
	RCV_TRM9_33	4.2	7.3	10.0	79.62	19.0
RCV_TRMS_32	Calibrated	1.6	1.6	3.5	97.64	18.5
	RCV_TRM5	4.5	6.1	9.5	77.19	17.0
	Calibrated	1.5	1.4	3.9	96.49	16.0
	RCV_SEP	3.8	5.2	8.7	75.83	18.5
	Calibrated	1.4	1.4	3.5	96.15	17.0
	RCV_TRMS_32	1.1	1.0	3.1	98.70	15.0

In Table 4-11, using RCV_TRM9_22 UPDs for positioning, there are significant low fixing rates and precision divergence, but these positioning results show normal after calibration on WL UPDs. Using the calibrated RCV_TRM9_22 UPD, the accuracy of N, E, and U are improved from 4.9, 7.9, and 10.1 cm to 1.5, 1.6, and 4.0 cm, while those of the RCV_SEP are improved from 3.8, 5.2, and 8.7 cm to 1.4, 1.7, and 3.5 cm, respectively. In these two receiver types, more than 13 satellites were calibrated with an average deviation of about 0.2 cycles. The accuracy and fixing percentage of RCV_TRM9_30, RCV_TRM9_33, and RCV_TRM5 is also improved by about 50%. It is indicated the deviation in WL UPD makes the ambiguity fixing abnormal, and affects the convergence time and fixing rate and finally results into large positioning errors. However, after calibrating the WL UPD deviations, the fixing rate and TTFF and the accuracy of the PPP-AR have been improved to the same level of that using the UPDs of the same receiver type.

Table 4-11 shows two stations with obvious impact as examples for discussion, namely CSST and BSRY both equipped with the RCV_TRMS_32 receiver. The positioning differences with respect to the ground true on DOY 6 2019 are shown in Figure 4-27, where three PPP-AR solutions using UPDs corresponding to RCV_TRM9_30, RCV_TRM9_30 calibrated, and RCV_TRMS_32, respectively.

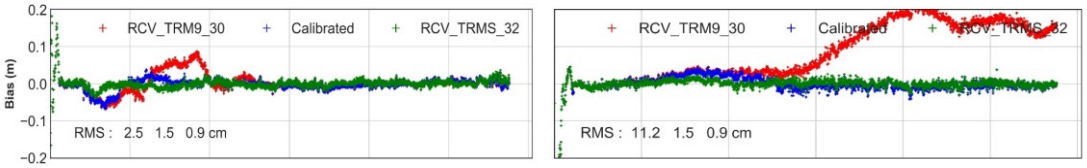

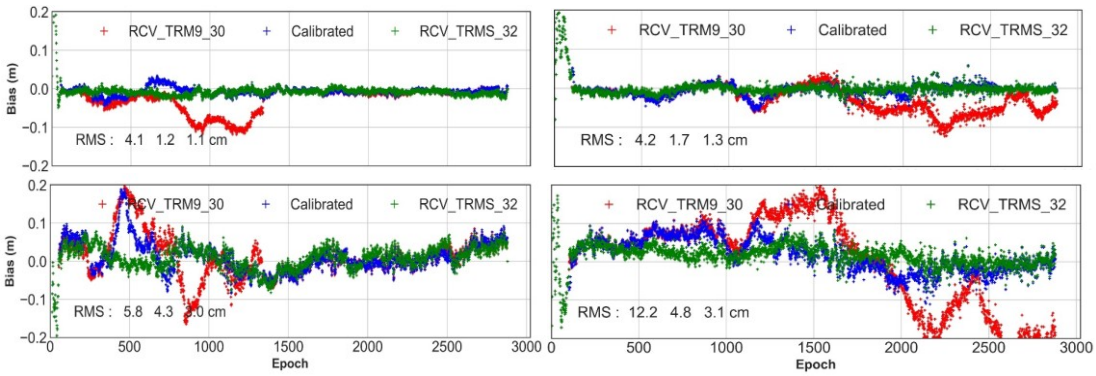

Figure 4-27 Positioning biases of PPP-AR solutions at stations CSST (left) and BSRY (right), from top to bottom is N, E, U, respectively. Both stations equipped with RCV_TRMS_32 receiver using UPDs of RCV_TRM9_30 (red) and RCV_TRM9_30 calibrated (blue) and, RCV_TRMS_32 as reference (green)

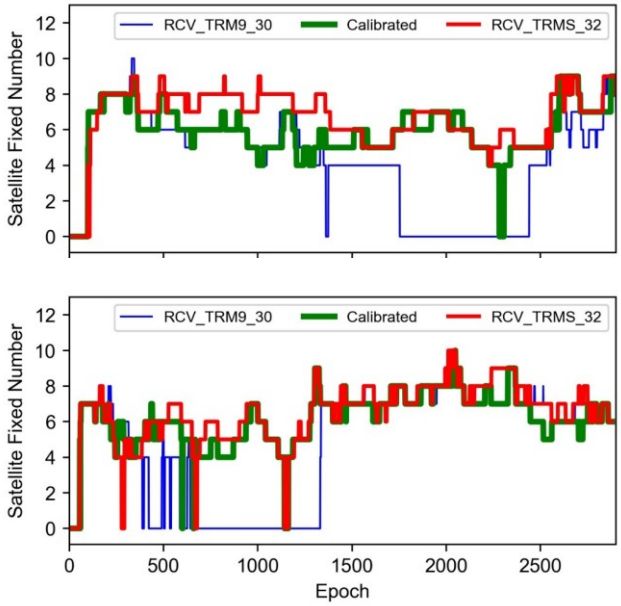

Figure 4-28 The number of fixed satellites for CSST (top) and BSRY (bottom)

From Figure 4-27 the position differences of the PPP-AR solution with RCV_TRM9_30 UPD are rather large up to 10 cm and 20 cm in horizontal for CSST and BSRY, respectively, and even larger in vertical. To investigate the reason, Figure 4-28 shows the number of fixed ambiguities at each epoch for both stations. It can be seen that for the RCV_TRS_32 receivers, the fixing rate using RCV_TRM9_30 UPDs is significantly lower than using the UPD from the same receiver type and the calibrated one. After 2500 epochs, the number of fixed satellites using RCV_TRM9_30 UPD at the BSRY station increased to 7, indicating that the ambiguity fix was again successfully performed. However, it can be seen from Figure 4-27 that there is a significant deviation of almost 15 cm in the positioning bias after 2500 epochs, indicating an incorrect fixing at this stage. The accuracy in terms of the RMS of positioning differences in N, E, and U is improved

from 2.5, 4.1, 5.8 cm to 1.5, 1.3, 4.3 cm, and from 11.2, 4.2, 12.2 cm to 1.5, 1.7, 4.8 cm for CSST, and BRSY stations, respectively, with the calibrated UPDs.

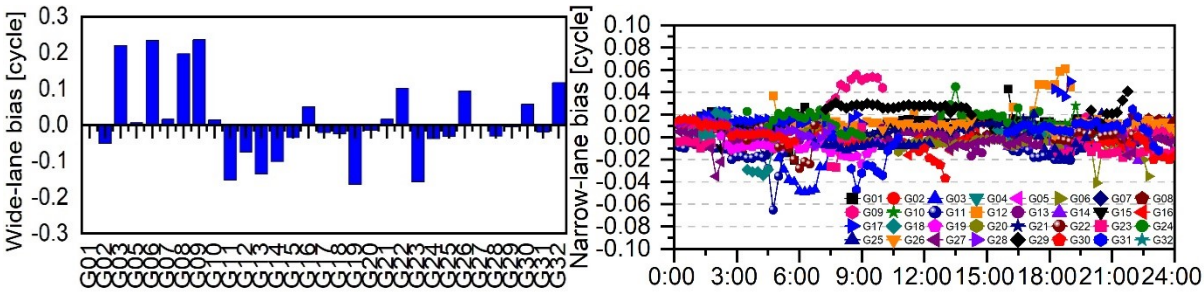

(a) (b)

Figure 4-29 The WL (left) and NL (right) UPDs difference between RCV_TRM9_22 and RCV_TRMS_32

Furthermore, the WL and NL UPDs differences between RCV_TRM9_22 and RCV_TRMS_32 are plotted in Figure 4-29. There are four satellites with deviations larger than 0.2 cycles and seven satellites larger than 0.1 cycles in WL UPDs, whereas the NL UPDs also exist the fluctuations. This might be caused by using the mismatch WL UPDs, which results in degraded WL ambiguity-fixing and consequently different NL ambiguities involved in the NL UPD estimation. Meanwhile, Figure 4-30 gives the differences of carrier and pseudorange residuals of PPP AR using RCV_TRM9_22 and RCV_TRMS_32 UPDs on CSST and BSRY station, respectively.

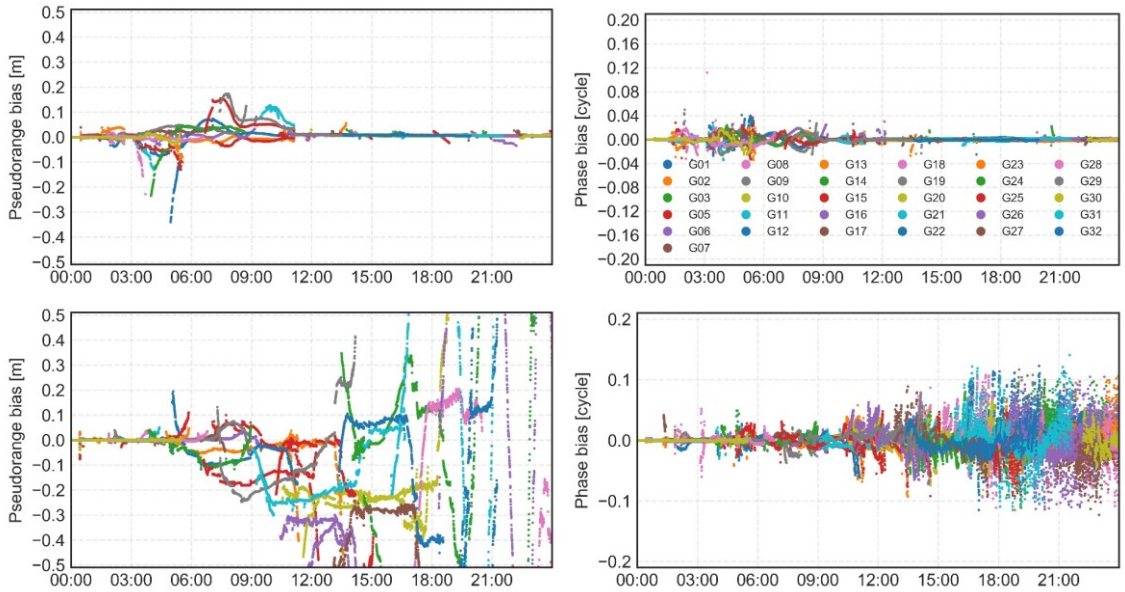

Figure 4-30 Differences of pseudorange (left) and phase (right) residuals between PPP-AR solutions using RCV_TRM9_22 and RCV_TRMS_32 UPD at station CSST (top) and BSRY (bottom)

It can be seen from the residual differences that both the carrier and the pseudorange exhibit diverging characteristics when the number of fixed satellites is decreased. Around 500 and 1500

epochs, at 4:10 and 12:30, the position differences of the solution with uncalibrated UPDs begins to diverge, at CSST and BRSY station, respectively. However, with the calibrated UPDs the convergence and stability of the solution can be retained in this stage. Therefore, using UPDs with a large deviation, the positioning performance could be abnormal, and the effectively calibrated UPDs can significantly improve the positioning accuracy and fixing rate.

4.7 Chapter Summary

To achieve a high ambiguity-fixing rate across all receiver types and available signals in large areas, a calibration method for receiver type-related biases is proposed. In addition, the impact of satellite signal biases on product generation and ambiguity resolution are analyzed. The calibration of pseudo-range biases for ambiguity resolution can be summarized as follows.

Section 4.1 introduces the relationship between GPS pseudo-range classified by codes and signals. The differences between the correction value of DCB and DSB product on the same signals are compared and analyzed. The impact of inter-signal biases on observations data is also described.

Section 4.2 investigates the impact of legacy DCB and new DSB products using different signals settings in POD, PCE, and UPD estimation. Principally, the differences are analyzed.

- The orbit differences between the solutions using DCB and DSB for the mixed-signal setting are within 1 mm without AR, while the values reach 2 to 4 mm with AR. In the fixed-signal solutions, the orbits calculated by DCB and DSB are identical. The orbit differences between using mixed-signal and fixed-signal, are around 3 to 5 mm and 2 to 3 mm using DCB and DSB products, respectively, meanwhile the value reaches up to 10 mm for some satellites.
- The clock difference between using DSB and DCB products can be up to 0.5 and 1.7 ns in mixed-signal and fixed-signal settings, respectively. As for the difference between mixed-signal and fixed-signal settings, the value reaches up to 1.7 ns if DCB is used, whereas it is close to zero if DSB is used. However, the STD values of clock differences in each batch solution are zero, which means different bias products or signal settings only cause a shift in the clock datum.
- The WL UPD differences between using DCB and DSB products reach up to 0.47 cycle, in either mixed-signal or fixed-signal solution, whereas the difference between mixed-signal and fixed-signal is insignificant (less than 0.1 cycle), whether using DCB or DSB products. Additionally, the NL UPDs also have a significant difference up to 0.47 cycle between using DSB and DCB, in both the mixed-signal and fixed-signal solutions. The

difference between mixed-signal and fixed-signal solutions is usually within 0.2 cycle when DSB products are used, but could be 0.4 cycle in the case of using DCB.

Section 4.3 presents the pseudo-range biases and systematic noise in positioning using different signals combination.

- The bias between C, X, S, and L signals cannot be ignored even though they are all classified as C-code, otherwise they can impact the positioning ambiguity fixing rate and convergence time.
- Even though the GNSS community more commonly uses the C and W signals, the X and L signals have much smaller stochastic noise, whereas that of the S signal is the largest, i.e., S, L, W, C, and X in ascending order.
- The systematic noise difference among all satellites is the smallest on S signals, while that of the L signals is the largest, i.e., L, X, W, C, and S in descending order.

Section 4.4 presents a novel method for estimating and calibrating WL UPD caused by satellite-specified range biases at the receiver-end. The data from selected receiver types, which are utilized in UPD estimation, are described. Various types or versions of receivers are considered, and the number of data samples and the usage rate of the FPAs are taken into account.

Section 4.5 illustrates the WL UPD biases that are specific to different receiver types and examines their temporal and spatial stability. The K-means method is applied to accurately estimate these biases, taking into consideration the variations among receiver types. It is found that the group differences could reach up to 0.4 cycles. By applying the estimated group WL UPD differences as corrections, the deviations can be reduced to a precision of about ±0.03 cycles.

Section 4.6 focuses on the application of the estimated corrections to enhance the ambiguity resolution. Neglecting the receiver-dependent UPD deviations can lead to significant positioning errors of up to 20 cm. In addition, by addressing these deviations through correction, the positioning performance can be improved by up to 50%, with a simultaneous enhancement of the fixing rate by 10%. The estimation and calibration of receiver-type-related deviations enable the elimination of pseudo-range biases among all receiver types, thereby achieving a consistent ambiguity fixing rate. These findings highlight the critical importance of considering and addressing receiver-dependent UPD deviations for achieving precise and reliable ambiguity resolution on large-area among all types of receiver.

5 Atmospheric delay model and uncertainty generation

In real-time high-precision positioning applications spanning large areas, achieving a short convergence time is crucial. Rapid AR at a single station heavily relies on accurate atmospheric delay. In the context of large areas with diverse receiver types and signals, precise and stable atmospheric delays can be derived and provided to users through various modes. To generate an accurate model for tropospheric and ionospheric delays, it is essential to ensure that the chosen modeling method aligns with the properties of atmospheric delays. Furthermore, it is necessary to establish proper quality index for the corresponding atmospheric delay model before proceeding with the positioning process.

Firstly, a proper mathematical model should be separately analyzed and delivered based on the properties of tropospheric ZWD and satellite-wise slant ionospheric delay. It is also essential to analyze the relationship between station-spacing, station distribution, and modeling performance. The impact of differences in receiver and satellite hardware should be analyzed for ionospheric delay modeling. On the other hand, accurate real-time atmospheric delay uncertainty for corresponding atmospheric delay correction should be described due to the differences between modeled corrections and estimated delays. To address these issues, the problems of atmospheric delay modeling in large areas are analyzed and investigated in this Chapter. This Chapter ends with a summary of the main conclusions.

5.1 Tropospheric delay fitting model

To decorrelate the ZWD, ambiguity, and station coordinate parameters during the GNSS processing, precise external tropospheric delay products are used as a priori constraint. In this section, by exploiting the water vapor exponential vertical decrease, a modified tropospheric ZWD fitting model is introduced.

5.1.1 Modified optimal fitting model

Normally, the tropospheric ZWD fitting model can be expressed as a second-order polynomial model, e.g., Optimal Fitting Coefficient (OFC) model (Shi et al. 2014).

$$\begin{aligned} ZWD(dB, dL, h) = {} & a_0 + a_1 \cdot dB + a_2 \cdot dL + a_3 \cdot h + a_4 \cdot dB \cdot dL + a_5 \cdot dB \cdot h \\ & + a_6 \cdot h \cdot dL + a_7 \cdot dB^2 + a_8 \cdot dL^2 + a_9 \cdot h^2 \end{aligned} \tag{5.1}$$

where $a_0, \dots, a_9$ are model coefficients; dB, dL are differences between latitude and longitude with respect to a selected reference point, respectively; h is ellipsoid height. However, this model only achieves optimized fitting performance in local areas without significant altitude difference, and large residuals are observed in stations with large height differences to the network average (de Oliveira et al. 2016). Therefore, it is challenging to apply this model effectively in large areas that exhibit significant variations in altitude across their expanse.

To better approximate the altitude-related variations of ZWD, the modified exponential function is combined with the OFC model, i.e., MOFC model (Cui et al. 2022). The new model reduces the model coefficients, i.e., exponential term instead of polynomial terms, while improving the fitting accuracy, especially in regions with significant altitude differences.

$$ZWD(dB, dL) = a_0 + a_1 \cdot dB + a_2 \cdot dL + a_3 \cdot dB \cdot dL + a_4 \cdot dB^2 + a_5 \cdot dL^2 \tag{5.2}$$

$$ZWD_m(dB, dL, h) = ZWD(dB, dL) \cdot \mathrm{e}^{\left(\frac{h}{H}\right)} \tag{5.3}$$

where the second-order polynomial function models the horizontal variation, the function $\mathrm{e}^{\left(\frac{h}{H}\right)}$ describes the change in height, and H is the ZWD scale height which describes the altitude dependence of the ZWD, which needs to be estimated as a model coefficient. The coefficients are calculated by the least-squares adjustment estimation (Dousa & Elias 2014).

During the modeling of tropospheric ZWD, it is crucial to effectively detect and eliminate gross errors in order to achieve a highly accurate model. The quality control in the pre-processing stage is divided into three steps. The first step involves selecting reference stations with a high ambiguity fixing rate for the modeling process. Stations with an ambiguity fixing rate higher than 95% are chosen as suitable candidates. The second step utilizes the median detection method to verify the extracted ZWD values at each station. This helps identify and eliminate any potential outliers. Finally, to ensure accuracy and numerical stability in the estimation process, optimal parameters are obtained through iterative procedures. The model criterion is based on minimizing the RMS of the residuals obtained from fitting the model. In each iteration, the model coefficients in Eq. (5.2) and Eq. (5.4) are updated using a least-squares adjustment, with the ZWD estimates at each station serving as the observations. If the residuals of an observation exceed 3*threshold, it is marked as an outlier. The iteration continues until there are no more outliers and the RMS of the fitting residuals meets the predefined criteria (0.02 m). It is important to note that a maximum of ten iterations is defined. If convergence cannot be achieved within ten iterations, the modeling for that epoch is considered unsuccessful, and the coefficients from the last successful iteration are used for broadcasting.

5.1.2 Data set

To evaluate the proposed method precision and its dependency on the station density of the reference network, the EUREF Permanent GNSS Network (EPN) (Bruyninx et al. 2019), including its densification with about 460 stations in total is used. The station distribution is shown in Figure 5-1. Three reference networks are used to generate the tropospheric delay correction models and defined by selecting stations with an averaged inter-station distance of 100 km, 150 km, and 200 km, marked by blue, green, and red dots, respectively. The number of stations for the three reference networks are 260, 165, and 100, respectively. Additionally, 200 stations, excluding from the server end, served as verification stations marked as purple triangles.

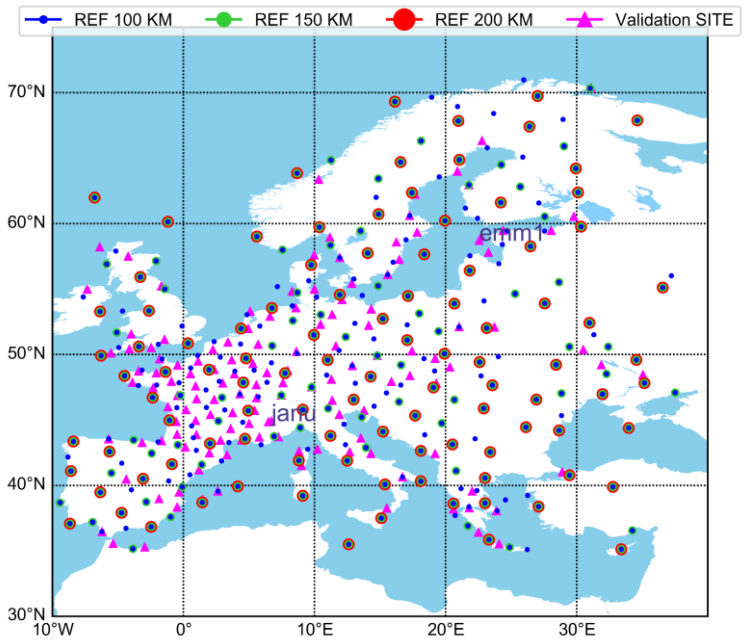

Figure 5-1 EPN network, including its densification with about 460 stations. The blue, green, and red circles denote the reference network with the station-spacing of about 100 km, 150 km, and 200 km, respectively. For external validation 200 stations in purple triangles are used.

The selected three networks separately represent dense, medium, and sparse, and the number of stations of the latter two is reduced by 37% and 62% compared with the dense network. As shown in Figure 5-1, all three networks show an approximate uniform distribution and can cover the region of Europe well.

In addition, due to a strong correlation between the tropospheric ZWD and season, seven weeks of observation data across four seasons, including four weeks in winter (from day 001 to 028) and one week in each of the other seasons (spring from day 090 to 096, summer from day 180 to 186, and autumn from day 270 to 276) are used to fully consider the different water vapor content and validate our method.

Performing the UDUC-PPP-AR on each reference station derives the ZWD and generates the tropospheric delay fitting models. The data processing strategy is presented in Table 3-2.

5.1.3 Tropospheric delay estimated from PPP-AR

The differences in temperature and humidity by inter-seasonal variability can cause ZWD fluctuation. For example, the ZWD delays and inter-epoch difference values on 213, 2020, at three different altitude stations are given in Figure 5-2.

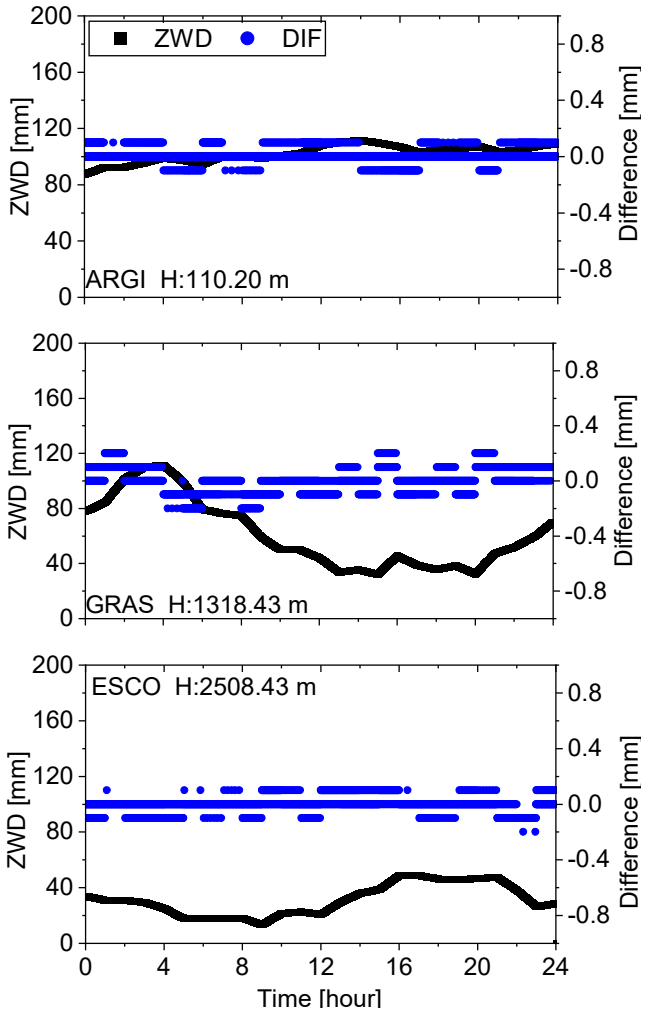

Figure 5-2 ZWD values (in black) and the between-epoch differences (in blue) for three stations with different altitudes on doy 213, 2020. Epoch interval is 30 s.

The tropospheric delay derived from stations located at different areas, namely ARGI (62.0ºN, -06.8ºE, 110.20 m), GRAS (43.8ºN, 06.92ºE, 1318.43 m), and ESCO (42.5ºN, 00.98ºE, 2508.43 m) stations, as shown in Figure 5-1, exhibit significantly differences in altitude. However, they show slight fluctuations and variation (black lines). The inter-epoch (30 s) tropospheric delay variation (blue lines) is very small. With the rapid update of augmentation information from the server, the residual ZWD at the user will not present significant variation in different seasons.

Therefore, the tropospheric delay parameters are updated every five minutes, which is enough to model the temporal variations.

5.1.4 Performance of tropospheric delay modeling

Figure 5-3 shows the residuals of ZWD estimates between PPP-AR derived and OFC and MOFC model calculated at EMM1 (top) and JANU (bottom) stations on doy 1, 2020. Using tropospheric delay model fitting coefficients from the server side, the users can obtain their ZWD values given their coordinates as input. The three types station-spacing network of OFC and MOFC models have comparable residuals at station EMM1 (32 m), but for the station JANU (2584 m) with higher altitude, the OFC models have extremely large residuals up to 15 cm. Hence, the results indicate that the MOFC model can well fit the altitude-dependent tropospheric ZWD variations.

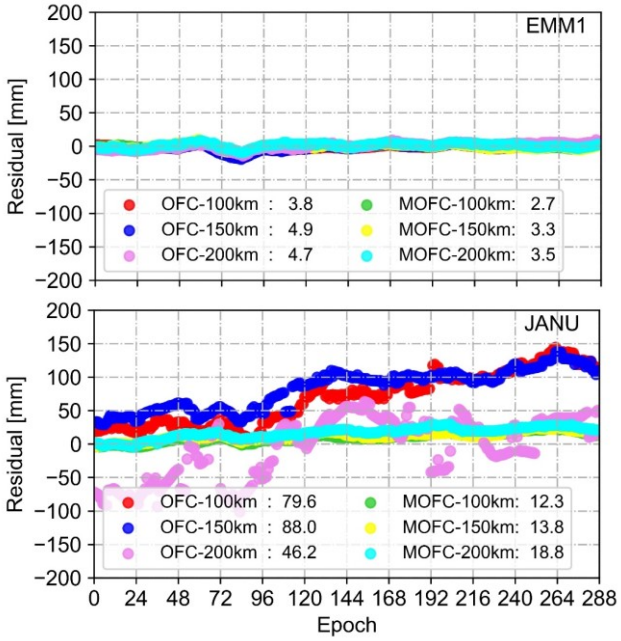

Figure 5-3 The residuals between ZWD modeling values obtained from OFC and MOFC models and PPP-derived on three types of station-spacing.

5.1.5 Analysis of the relationship between modeling precision and altitude

It is well known that the correlation between tropospheric delay and altitude is significant. In this part, among all 460 selected stations, the highest one is PIMI (2923.43 m, located in Bareges La Mongie, France) and the lowest one is VERG (29.99 m, located in Vergi, Estonia), indicating a significant altitude difference of 2893.44 m. The corresponding ZWD differences between PPP-derived and those model fitted from OFC and MOFC models are presented in Figure 5-4.

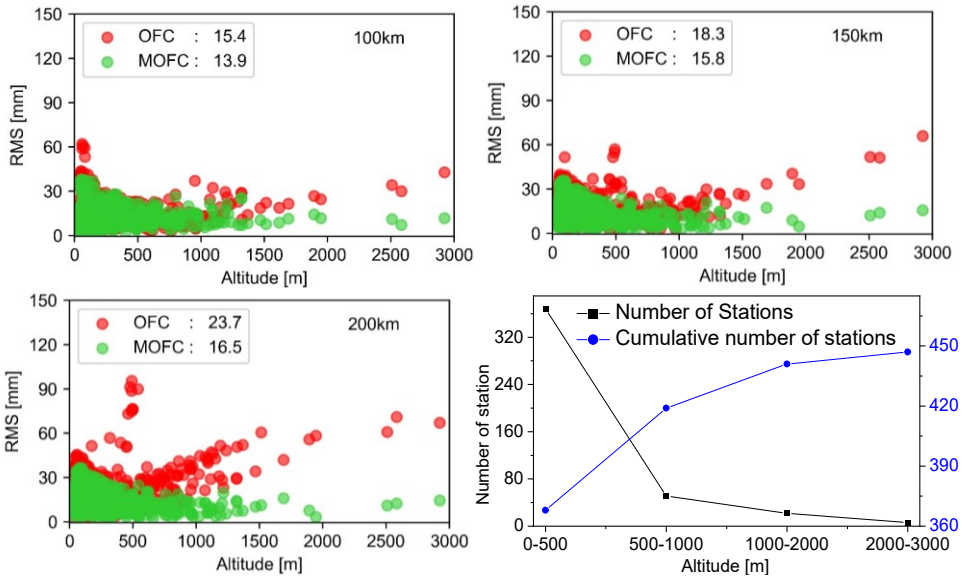

Figure 5-4 Station-specific RMS of the ZWD differences between PPP-derived and that OFC and MOFC modeled using the dense (top left), medium (top right), and sparse (bottom left) station-spacing.

Most stations locate below 500 m. Only 51 stations are between 500–1000 m, 22 within 1000–2000 m, and 3 above 2000 m. It should be noted that the selected reference stations that cover those above 2,000 m are chosen to improve the model precision at high altitudes as the represented station to help the model fit coefficients. The exponential term obeys the relationship between atmosphere pressure and altitude, successfully introducing a link between altitude and tropospheric wet delay. The overall RMSs of ZWD from the OFC model are about 15.4 mm, 18.3 mm, and 23.7 mm for dense, medium, and sparse station-spacing networks, respectively. The RMSs of the OFC model show a significant linear increase with the station-spacing, especially for the sparse network. On the other hand, for the MOFC model, the precisions are improved to about 13.9 mm, 15.8 mm, and 16.5 mm for these three networks, respectively. Additionally, with the MOFC model, the linear trend of the RMS compared to station altitude disappears, and the modeling precision for the medium and sparse networks is almost the same.

In order to further investigate the correlation between fitting accuracy and station altitude, all stations are devided into four groups according to their altitudes. The mean RMS values of the two models for seven weeks in different heights ranging from 0 m to 3000 m are shown in Figure 5-5.

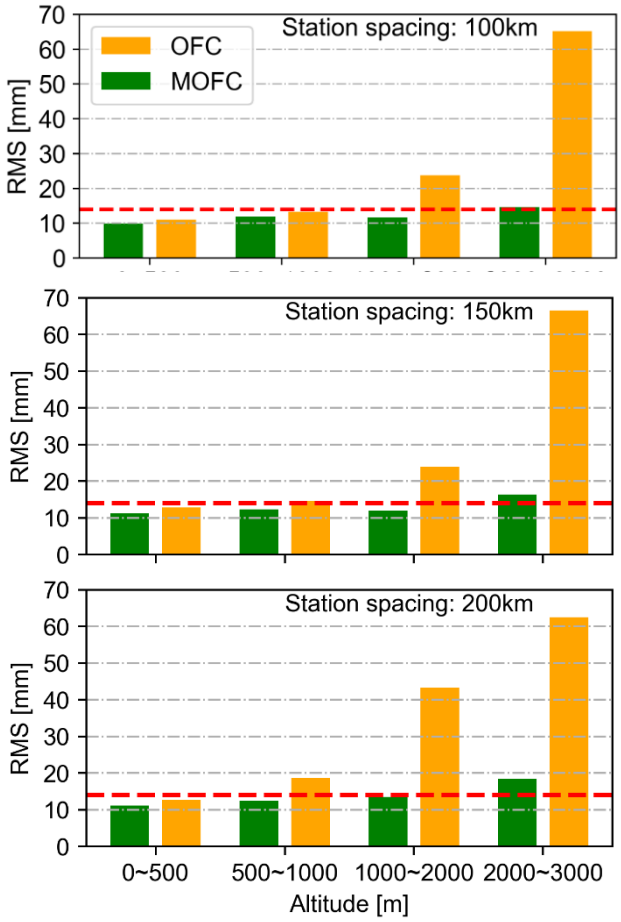

Figure 5-5 Tropospheric ZWD modeling precision of OFC and MOFC at different altitude intervals using 460 stations during seven weeks cross four seasons.

Based on Figure 5-5, the RMS of the OFC and MOFC models show similar for stations located below 500 m altitude, and they increase along with altitude. However, as altitude increases rate, the MOFC model displays a gradual increase in RMS values while the OFC model demonstrates a rapid increase. For stations above 2000 m, the RMS value of OFC exceeds 60 mm, whereas that of MOFC remains consistently below 18 mm across all three reference networks, indicating an improvement of 70%-80%.

These results suggest that OFC cannot provide high-precision tropospheric delay modeling in areas with significant changes in altitude. This is primarily because the OFC model primarily focuses on achieving optimal fit for mathematical components, while not taking into account the inherent altitude correlation. Furthermore, ZWD modeling using MOFC with three different network configurations exhibit similar levels of accuracy. Due to MOFC superior modeling of altitude dependence, it is possible to establish a ZWD correction model with homogeneous accuracy for stations at varying altitudes. Figure 5-6 further illustrates the improvements of the OFC and MOFC models with respect to the PPP-derived values during all periods.

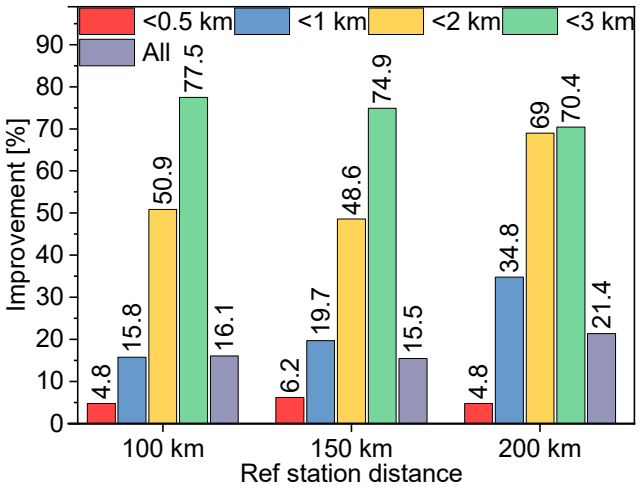

Figure 5-6 Different altitude stations improvements of 100 km (dense), 150 km (medium), and 200 km (sparse) station-spacing network solutions between OFC and MOFC models.

The MOFC model solutions exhibit a slight improvement for stations located below 500 m. However, as altitude increases, the RMS of the OFC model increases significantly faster than that of the MOFC model. It is evident that the significant improvement lies in higher altitude areas. The mean RMS for all assessed periods of the dense, medium, and sparse networks is 16.2, 17.1, and 19.1 mm for the OFC model and 13.5, 14.4, and 15.0 mm for the MOFC model, respectively. Overall, compared to the results of the traditional OFC model, the modeling precision of MOFC improves by 15.6–21.4% in different station-spacing networks, providing basic augmentation information with a uniform precision distribution for large areas, even with significant altitude differences.

5.2 Satellite-wise ionospheric delay fitting model

Instead of using the legacy second-order polynomial model, a new fitting model is introduced to describe satellite-wise slant ionospheric delay for large areas augmentation service. Additionally, the SPR biases from PPP-derived ionospheric delay are estimated and removed to generate the fitting model, resulting in a "clean" ionospheric delay corrections. This section presents and analyzes in detail the ionospheric delay modeling in large areas.

5.2.1 New ionospheric delay fitting model

From Eq. (3.4) and Eq. (3.7), a “clean” slant ionospheric delay $I_{r,1}^{s}$ can be achieved by removing the SPRs.

$$I_{r,1}^{s} = \hat{I}_{r,1}^{s} - \frac{c}{\gamma_2 - 1} * (SPR) \tag{5.4}$$

Generally, for the ionospheric delays modeling, a second-order polynomial function is introduced and described in Eq. (5.5).

$$\tilde{I}_{r,1}^{s} = b_0 + b_1 * d\varphi_i + b_2 * d\lambda_i + b_3 * d\varphi_i * d\lambda_i + b_4 * {d\varphi_i}^2 + b_5 * {d\lambda_i}^2 \quad (5.5)$$

where $\tilde{I}_{r,1}^{s}$ is the STEC model fitted value from model coefficients, $b_0, b_1, b_2, b_3, b_4, b_5$ are the fitting coefficients of the model, $d\varphi_i, d\lambda_i$ are difference latitude and longitude with the reference point, respectively.

Typically, in satellite navigation, a thin-layer assumption is commonly employed to simulate ionospheric delay at all IPPs, with a typical height of 350 km. However, the traditional polynomial model used for fitting the ionospheric delay on a thin-layer plane merely achieves mathematical fitting without adequately capturing the actual characteristics of the slant propagation path. For real-time GNSS service, describing the model on a plane aims to simplify the model complexity where the multi-layer model always takes massive info as the model coefficients. Therefore, in this thesis, a new fitting model is proposed to address the variations in the ionospheric slant delay within large-area modeling, taking into account the actual properties of the ionospheric delay, i.e., the relationship between the propagation length in ionosphere areas and magnitude of ionospheric delay. The new model uses each satellite slant delay to provide the STEC fitting model as a satellite-wise service.

In Figure 5-7, the stations in the modeling areas can receive the signal from the specific satellite, this is, the ionospheric delays from this satellite can be observed by these stations. The satellite signals through the ionosphere start at about 1000 km and extend up to 50 km (blue lines). A path at the center of coverage areas is selected as the reference path (green line). Then, the differences between all slant delays (blue line) and the reference delay (green line) can be calculated using trigonometric functions, with the differences in elevation and azimuth angles as inputs (red line in the right side figure). It is essential to acknowledge that with each update, the selection of the reference path and coverage areas for specific satellites may vary. However, the optimization of coverage and reference path selection is consistently maintained.

$$\hat{I}_{r,dif}^{s} = a_4 * \sin(e - \hat{e}) + a_5 * \cos(z - \hat{z}) \quad (5.6)$$

where $\hat{I}_{r,dif}^{s}$ is the difference between reference path and others; e and z are elevation and azimuth angles of ionospheric delay from each station, respectively; $\hat{e}$ and $\hat{z}$ are elevation and azimuth angles of reference ionospheric delay, respectively.

In addition, the first-order polynomial model is provided as the basic model and the trigonometric model is used to describe the differences between reference path and others. Then, the modeled ionospheric delay $\tilde{I}_{r,m}^{s}$ can be presented as,

$$\tilde{I}^{s}_{r,m} = a_0 + a_1 * d\varphi_{ipp} + a_2 * d\lambda_{ipp} + a_3 * d\varphi_{ipp} * d\lambda_{ipp} + a_4 * \sin(e - \hat{e}) + a_5 * \cos(z - \hat{z}) \quad (5.7)$$

where $d\varphi_{ipp}$ and $d\lambda_{ipp}$ are altitude and longitude coordinates differences between each ionospheric delay slant path (blue line) and the reference path (green line) IPPs.

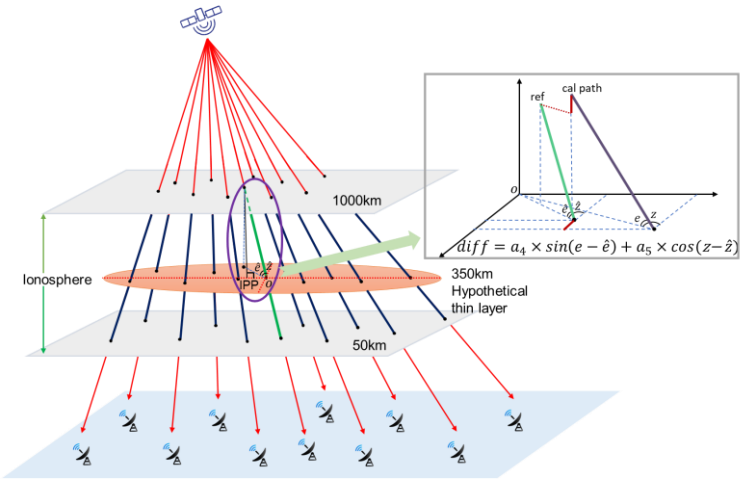

Figure 5-7 Ionospheric delay propagation path simulation, blue lines are ionospheric delays for all stations and the green line is the reference propagation path.

The new model consists of six model coefficients, along with the reference ionospheric delay IPP coordinates, elevation, and azimuth angles. The model is developed on a satellite-wise basis, where specific slant delays for each satellite are derived and collected for modeling purposes. Initially, the reference ionospheric delay is calculated by considering the differences in latitude and longitude range among all slant delays within the modeling areas. This reference ionospheric delay represents the path closest to the center of the coverage areas, and its corresponding latitude and longitude coordinates and elevation and azimuth angles are determined. Subsequently, satellite-specific ionospheric delays from all IPPs are incorporated as input for the modeling process, taking into account their respective differences in latitude, longitude, elevation, and azimuth angles in relation to the reference path. The iterative least-squares adjustment method is then utilized to solve for the model coefficients. It is important to note that outlier detection is conducted in two stages. Firstly, the reference station is selected based on an ambiguity fixing rate of over 95% (Ge et al. 2012). Secondly, during the iteration process, outliers are identified and marked if their values exceed three times the modeling sigma (Cui et al. 2022).

5.2.2 Data set

The ionospheric delay is calculated based on data presented in Figure 5-1 as a 150 km station-

spacing network, and the validation stations are also shown in Figure 5-1, using one-month observations from the period between DOY 270-300, 2022. The observation data interval is set as 30 seconds, and the correction model coefficients are also generated every minute.

Unlike the tropospheric delay, which is derived separately for each station, the ionospheric delay is presented on a per-satellite basis. Only GPS and Galileo satellites have their ionospheric delays derived and modeled because reliable AR can only be performed on these two constellations.

5.2.3 Ionospheric delay estimation

To generate a fitting model, slant ionospheric delays of all satellites should be derived from each reference station. As an example, daily STEC values of all satellites estimated from 0LOV station by UDUC-PPP-AR are presented in Figure 5-8.

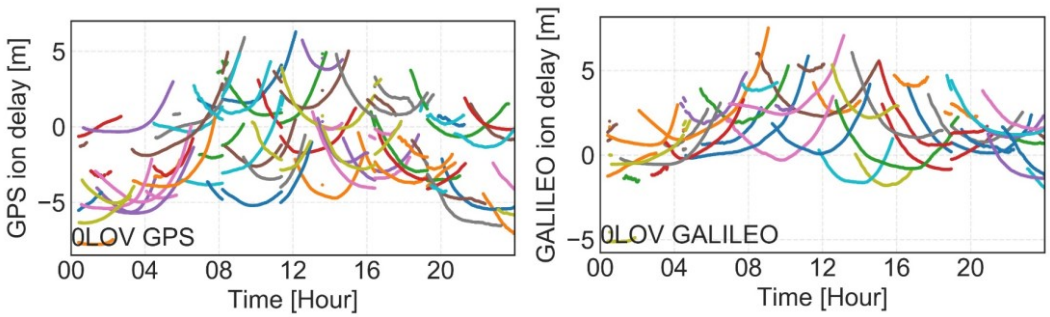

Figure 5-8 GPS and Galileo satellites ionospheric STEC delays derived by UDUC-PPP-AR on 0LOV station.

To ensure the accuracy and stability of the ionospheric delay, only satellites with successfully resolved ambiguities can be used to provide STEC values, as there is a strong correlation between ambiguity and atmospheric delay. As a result, after accurate resolving the ambiguities, the derived ionospheric slant delay exhibits stable and continuous results, which improves the modeling of local VTEC and the estimation of SPRs. Moreover, the outliers also should be handled before modeling, keeping the “clean” ionospheric delay applied.

5.2.4 SPRs estimation

To ensure unbiased modeling of satellite-wise ionospheric delays, it is important to remove the SPRs from all satellites at each station. This results in a "clean" ionospheric delay, without range biases, suitable for large aera modeling. A single-station VTEC model is introduced to model the region ionospheric delay and separates the SPRs from the ionospheric delay derived from UDUC-PPP-AR (Wang et al. 2015). The details of the model are described in Section 3.2.1 (Eqs.

(3.5) and (3.6)). As daily SPRs are considered to be highly stable, examples of their values for GPS and Galileo at the 0LOV and BUTE stations over a period of 30 days are presented in Figure 5-9 and Figure 5-10.

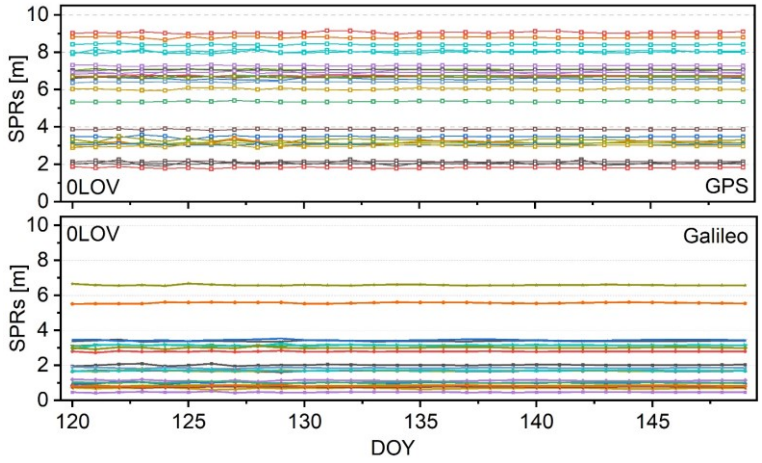

Figure 5-9 Satellite SPR values for GPS (top) and Galileo (bottom) satellites at station 0LOV over 30 days in 2022. Different colors denote different satellites.

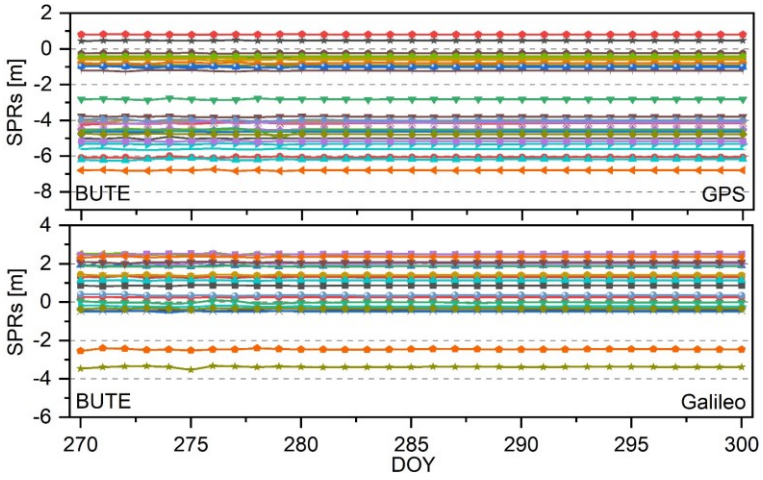

Figure 5-10 Satellite SPR values for GPS (top) and Galileo (bottom) satellites at station BUTE over 30 days in 2021.

It is evident that the SPRs of the 0LOV and BUTE stations remain highly stable over a 30-day period for both GPS and Galileo satellites. The fluctuations typically remain within 5 cm and are well stable. To ensure stable results for ionospheric delay modeling, the SPRs are calculated using a sliding seven-day window. Once the SPR biases are calculated for each reference station, ionospheric delay modeling can be performed.

5.2.5 Ionospheric delay modeling precision

The ionospheric delay model is computed for each satellite. Initially, all satellite ionospheric

delays, relying on reliable AR, are derived from each reference station. Subsequently, model coefficients can be generated for each satellite using their slant delays. Finally, the fitting coefficients are delivered to users, and the modeled value is calculated using the user satellite IPP coordinates and angles as input.

In order to verify the performance of the proposed model in Eq. (5.7), four schemes are presented to compare the proposed ionospheric delay fitting model as described in Table 5-1.

Table 5-1 Four types of ionospheric delay model comparison

Abbr.	Expression	Coefficient number
P1T0	First-order polynomial function	4×N
P2T0	Second-order polynomial function	6×N
P3T0	Third-order polynomial function	11×N
P1T1	First-order polynomial with a trigonometric function	10×N

P and T separately denote the polynomial and trigonometric functions; N is the number of satellite. The numbers in polynomials denote the order level of the fitting model. In contrast, the 1 and 0 in trigonometric functions indicate enabled or not.

The legacy polynomial fitting models are presented as follow,

$$\begin{aligned}
\tilde{I}^{s}_{P1T0} &= a_0 + a_1 * d\varphi_{ipp} + a_2 * d\lambda_{ipp} + a_3 * d\varphi_{ipp} * d\lambda_{ipp} \\
\tilde{I}^{s}_{P2T0} &= a_0 + a_1 * d\varphi_{ipp} + a_2 * d\lambda_{ipp} + a_3 * d\varphi_{ipp} * d\lambda_{ipp} + a_4 * {d\varphi_i}^2 + a_5 * {d\lambda_i}^2 \\
\tilde{I}^{s}_{P3T0} &= a_0 + a_1 * d\varphi_{ipp} + a_2 * d\lambda_{ipp} + a_3 * d\varphi_{ipp} * d\lambda_{ipp} + a_4 * {d\varphi_i}^2 + a_5 * {d\lambda_i}^2 + a_6 * \\
&\quad {d\lambda_i}^2 * d\varphi_i + a_7 * {d\varphi_i}^2 * d\lambda_i + a_8 * {d\lambda_i}^2 * {d\varphi_i}^2 + a_9 * {d\varphi_i}^3 + a_{10} * {d\lambda_i}^3
\end{aligned} \tag{5.8}$$

All satellite slant ionospheric delay differences between modeled and PPP-estimated on all validation stations are presented in Figure 5-11 and Figure 5-12 at each IPP during all test periods.

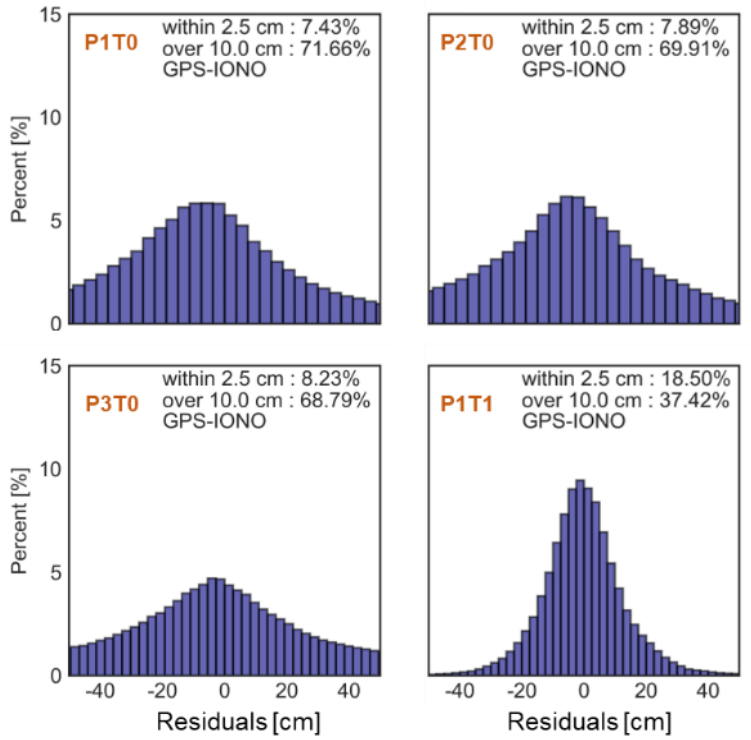

Figure 5-11 GPS satellites slant ionospheric delay differences between modelled and estimated values on all reference stations.

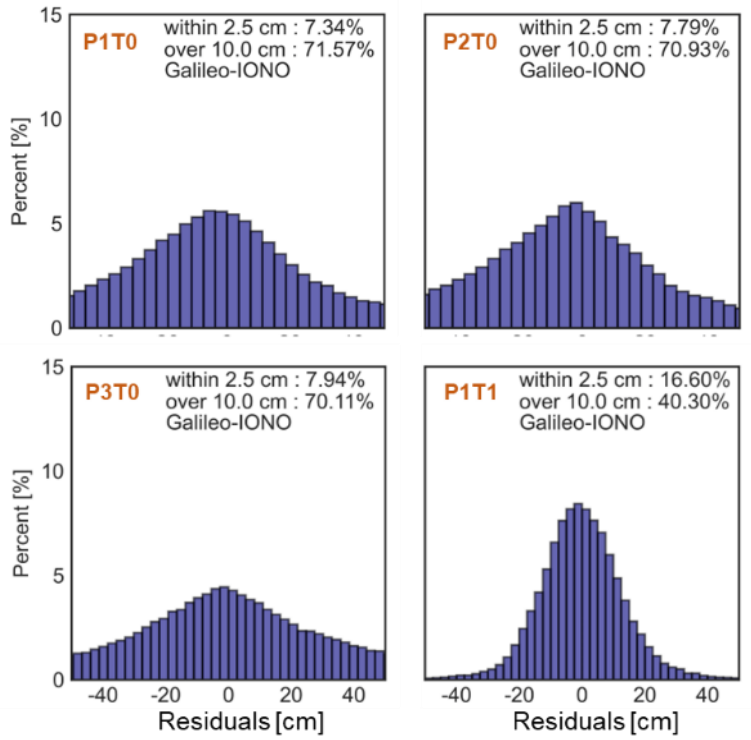

Figure 5-12 Galileo satellites slant ionospheric delay differences between modelled and estimated values on all reference stations.

For GPS satellites, the residuals lower than 2.5 cm achieve 7.4%, 7.9%, 8.2%, and 18.5% for

P1T0, P2T0, P3T0, and P1T1 models, respectively. In contrast, Galileo satellites achieve 7.3%, 7.8%, 7.9%, and 16.6%, respectively. On the other hand, 71.7%, 69.9%, 68.8%, and 37.4% of all GPS satellite modeling residuals are larger than 10 cm for P1T0, P2T0, P3T0, and P1T1 models, respectively. Additionally, 71.7%, 69.9%, 68.8%, and 37.4% of all Galileo satellites have residuals larger than 10 cm, respectively. Compared with the legacy polynomial fitting models, the proposed model significantly improves the modeling performance and reduces the number of larger residuals. There is an improvement of more than 10% in residuals smaller than 2.5 cm, and a reduction of more than 30% in residuals larger than 10 cm. It is mainly because the P1T1 model reasonably describes the relationship arising from differences between different ionospheric delays with propagation path length and magnitudes.

In Figure 5-13, the GPS satellite average modeling precisions are 27.0 cm, 23.9 cm, 20.6 cm, and 9.7 cm, respectively. Galileo satellite average modeling precisions are 27.2 cm, 24.0 cm, 21.0 cm, and 10.0 cm, respectively. Similar modeling precisions are achieved between GPS and Galileo constellations. The proposed ionospheric delay model satisfies a comparatively high accuracy fitting in the large areas.

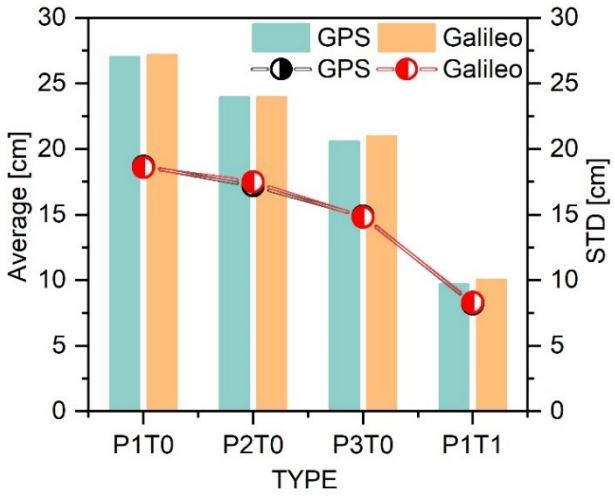

Figure 5-13 The average precision and STD value between PPP-derived and modeled differences for four schemes. The absolute values are applied for calculation. Column bars and dots denote average value (left axis) and modeling STD (right axis), respectively.

In the proposed model, the maximum modeling differences of GPS and Galileo satellites are 14.1 and 13.9 cm, respectively. The ionospheric delay can achieve an precision of approximately 9.0 cm with fewer fitting coefficients in large-area with sparse station networks. The P1T1 model average precision achieves 64.2%, 59.6%, and 53.0% improvements with respect to P1T0, P2T0, and P3T0 models, respectively. The modeling sigma also can be improved 56.1%, 52.3%, and 45.0%, respectively.

The fitting model coefficients can be broadcast via satellite communication, providing

augmentation services with low communication volume in large areas at any time. Conducting the large areas fitting models, the modeled ionospheric and tropospheric delay corrections can serve as essential information even though some regions have significant differences.

5.3 Ionospheric delay modeling among different receiver types

As ionospheric delay and pseudo-range biases are interrelated, it is crucial to properly consider receiver-related biases to ensure accurate satellite-wise ionospheric delay modeling. Failure to account for receiver-related biases can introduce biases into the modeling process, potentially compromising the accuracy of the model and resulting in inconsistencies in corrections for different satellites. Typically, a combination of receiver types is used for modeling, although receivers of the same type often exhibit similar characteristics and performance. In this section, a comprehensive investigation and comparison of the precision of ionospheric delay modeling using various receiver types is conducted.

5.3.1 Receiver type configuration for ionospheric delay modeling

In order to analyze the impact of different receiver types in ionospheric delay modeling, seven receiver types are selected for modeling and comparison, and the distribution of these types are shown in Figure 5-14 with different colors.

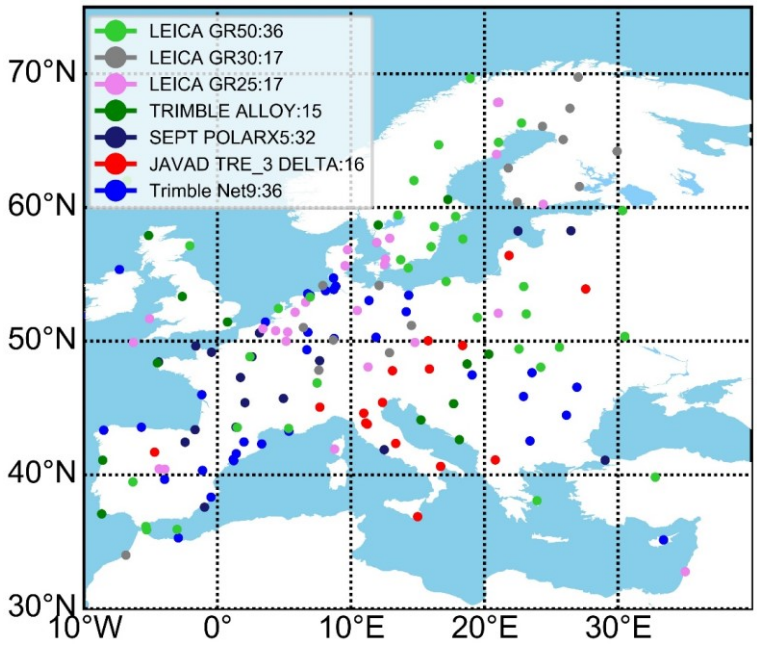

Figure 5-14 Seven types of receiver distribution for ionospheric delay modeling.

The eight schemes are performed in ionospheric delay modeling, including seven fixed-receiver-

type solutions (as in the above figure) and one mixed-receiver-type solution (all seven types). All scheme performances are validated on all reference stations, i.e., the differences between modeled corrections and PPP-derived values. It should be noted that even though some types of receiver numbers are lower than others, they are only concentrated in a small area with a comparable distribution.

Considering the same receiver types only located in the small areas, the large areas is devided into four sub-areas following the latitude of 50°N and longitude of 5°E to analyze the modeling performance. Then, the model is performed in a relative identified size region for each types.

Two sets of solutions, i.e., with and without applying SPRs correction, are performed to analyze the receiver-related biases impacts, relying on fixed receiver types of Trimble NetR9 receivers. The differences between PPP-derived ionospheric delay and modeled delays on 36 stations are presented as examples in Figure 5-15.

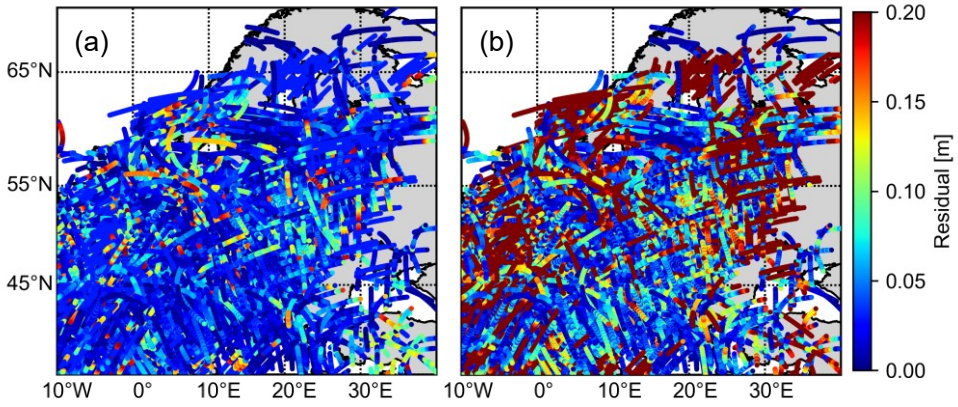

Figure 5-15 Slant ionospheric delay differences between modeled and PPP-derived values on all reference stations using fixed receiver type (Trimble NetR9 receivers) with (a) and without (b) removing SPRs at 14:00-14:05 of DOY 150, 2022. Note that the absolute value of the bias is given.

The schemes without removing the SPRs show a larger RMS than that of with removing the SPRs scheme. In other words, even if the same receiver type is selected, the SPR biases also exist differences, and it could introduce the biases into ionospheric delay and further impact the modeling. The receiver in the same type is selected without distinguishing the version. It also demonstrates that the receiver-type-related satellite-specific deviation exists, and the same type of different versions also have different performances.

5.3.2 Ionospheric delay modeling validation

To perform a comprehensive comparison and analysis of the eight schemes, the RMS of the daily differences in ionospheric delay between PPP-derived values with and without SPRs removed

are calculated, over a period of 90 days. The statistical results are visualized using a box plot, as shown in Figure 5-16. The specific RMS values for the selected seven fixed-type receivers and the mix-type receiver are summarized in Table 5-2.

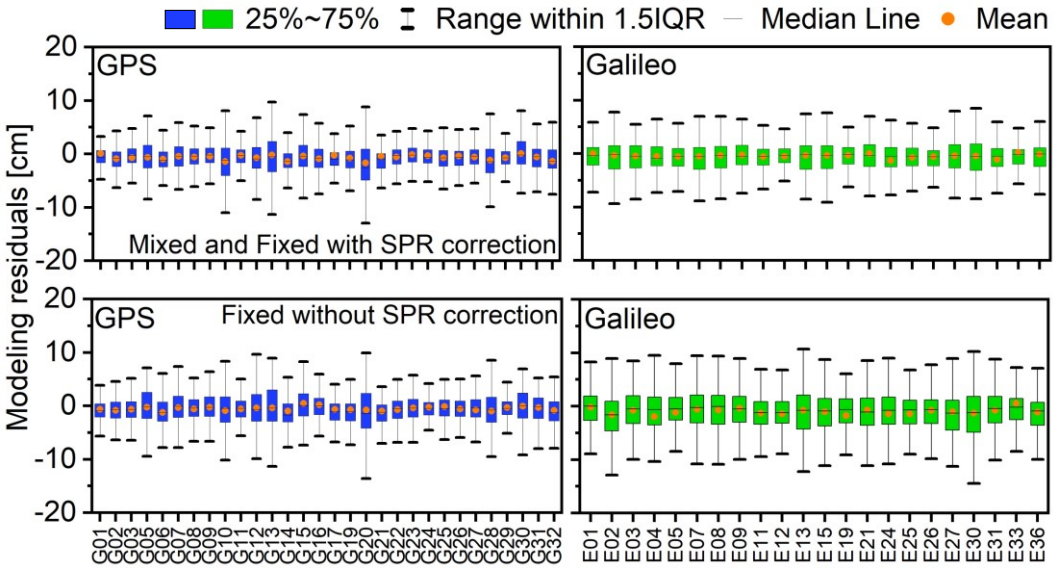

Figure 5-16 GPS (left) and Galileo (right) satellite-wise slant ionospheric delay modeling residuals for with removing SPRs (top) and using the fixed-type without removing SPRs (bottom) during 90 days. For each satellite, the 50.0% and 99% are within the box and upper and bottom lines, respectively. The orange dots and black lines in box denote the average and middle values, respectively.

Table 5-2 Ionospheric delay modeling precision of fixed and mixed receiver types with considering and without considering SPR biases during 90 days.

Receiver types	Station number	Modeling precision (with / without SPR removed) / cm
Trimble NetR9	36	4.2 / 8.7
TRIMBLE ALLOY	15	4.4 / 8.3
SEPT POLARX5	25	4.2 / 9.8
JAVAD TRE_3 DELTA	16	4.3 / 7.4
LEICA GR25	17	4.0 / 6.0
LEICA GR30	17	4.1 / 5.5
LEICA GR50	36	4.2 / 6.3
ALL-Mixed	162	4.2 / --

Considering the SPRs correction, an improvement is shown in the fixed-type and mixed-type solutions, indicating that the receiver-related SPR biases affect the ionosphere model accuracy. The average modeling precision of GPS and Galileo satellites are 4.2 and 3.9 cm when considering the SPRs correction, respectively, indicating that removing the SPR can significantly eliminate the impact of receiver-related biases in large-area ionospheric delay modeling.

On the other hand, the fixed-receiver-type schemes present slightly larger differences without

removing SPRs. Among them, the LEICA GR30 has the best precision, followed by the LEICA GR25, LEICA GR50, JAVAD TRE_3 DELTA, TRIMBLE ALLOY, Trimble NetR9, and the SEPT POLARX5 receiver types. Although we select the same type of receivers, there still have deviations between different versions and sub-types of the same type. It is further demonstrated that the SPRs should be carefully considered in large-area ionosphere modeling, which should not be neglected. However, in some small regions with consistent receiver types, without considering SPR biases also can achieve better performance.

Overall, with considering the SPRs correction, the maximum and minimum modeling RMS of GPS and Galileo satellite ionospheric delays are 9.1 and 8.9, and 1.4 and 1.1 cm, respectively. The Galileo satellites have greater precision and consistent modeling performance among different satellites than that of GPS satellites, which could cause by high-performance hardware equipment. Moreover, the results show that the ionospheric delay modeling with removing SPRs can achieve a homogeneous accuracy.

5.4 The relationship between modeling precision and station-spacing

To determine the appropriate station-spacing for modeling in large areas and regional compensation, and to enhance the performance of atmospheric delay modeling and provide corresponding uncertainty information in large areas augmentation, it is crucial to analyze the relationship between station distances and modeling precision. Consequently, this section focuses on investigating the relationship between station spacing and modeling or interpolation performance.

5.4.1 Station-spacing network setting

The stations selected for this study belong to three different reference networks: the EPN, EPN Densification Network, and EPOS Network. It is important to note that all the selected stations are capable of receiving signals from both GPS and Galileo satellites, while only a few can receive signals from BDS satellites. The modeling is performed exclusively on GPS and Galileo constellations with AR. For modeling, six types of station-spacing networks are implemented, and their distributions are illustrated in Figure 5-17 using different colors. In the left panel, green, purple, and dark dots represent station-spacing networks of 100 km, 300 km, and 500 km, respectively. In the right panel, green, purple, and dark dots denote station-spacing networks of 200 km, 400 km, and 600 km, respectively.

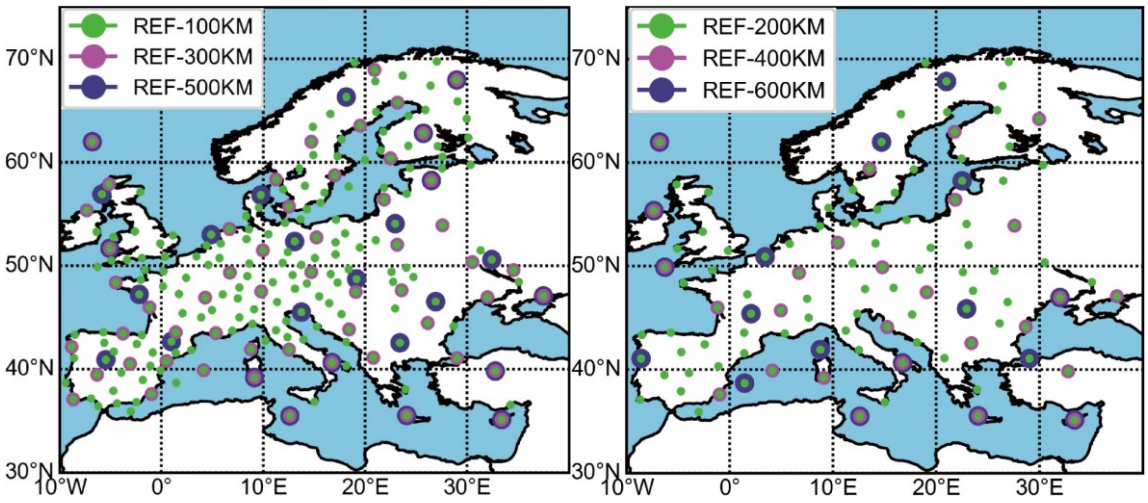

Figure 5-17 The GNSS networks applied to derive atmospheric delay and for modeling or interpolation services.

Figure 5-17, a total of 206 stations on server are used for modeling the atmospheric delays. For the selected six types of networks, the station number are as follows: 206 for 100 km, 103 for 200 km, 62 for 300 km, 41 for 400 km, 32 for 500 km, and 24 for 600 km. All six types are uniformly distributed and completely cover the entire European region. It should be noted that the Europe region also is divided into four sub-region for modeling to keep the consistent configuration with the following positioning mode in Chapter 6. The tropospheric and ionospheric delay models are separately performed in these four sub-regions. The modeling and interpolation performance is assessed over four weeks across four seasons in 2022, i.e., one week of data for each season (DOY 001-007, 091-097, 181-187, and 271-277 of 2022). Because the AR is only performed for GPS and Galileo satellites, the ionospheric delay is also only provided for these satellites. This analysis allows us to assess the modeling performance in relation to different station-spacing configurations. Based on these findings, appropriate station selection criteria can be established for the augmentation server.

5.4.2 Analysis atmospheric delay modeling performance

The following compares and analyzes the fitting and interpolation mode performance using six scale networks. It should be noted that the ionospheric and tropospheric delay modeling use proposed models in section 5.1 and section 5.2.

Ionospheric delay performance under different station-spacing

The ionospheric delay is calculated on a per-satellite basis, and the modeling and interpolation precisions are presented in Figure 5-18. In networks with station-spacing of 100 km, the

interpolation mode (2.7 cm) performs better than that of fitting model (4.3 cm). However, in networks with station-spacing of 200 km, the fitting model (5.1 cm) shows slightly worse performance than that of the interpolation mode (4.6 cm). When the station-spacing network is larger than 200 km, the fitting model exhibits more superior performance. That is, the precision of the interpolation mode decreases faster than that of the fitting model as the station-spacing increases beyond 200 km. This is mainly because the fitting model includes represented stations in specific regions to fit the delay and generate the coefficients. But the interpolation model could overlook this represented stations if the distance is too large.

Overall, the Galileo satellites show superior precision compared to GPS satellites because of their better hardware stability and performance. Although the fitting model can achieve comparable performance with interpolation, larger residuals are observed in specific areas where the modeling approach is used, while the interpolation mode provides more stable performance and uniform accuracy coverage.

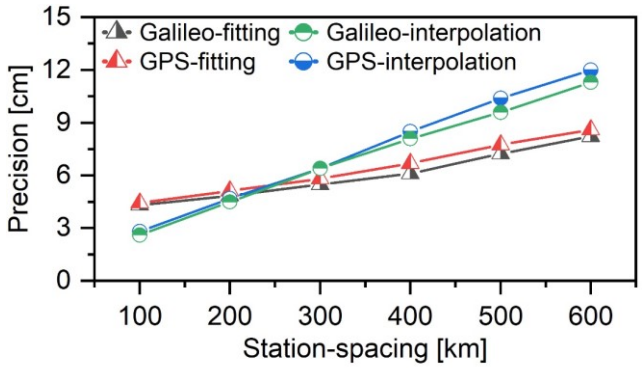

Figure 5-18 GPS and Galileo ionospheric slant delay precision under interpolation mode and fitting modeling.

Tropospheric delay performance under different station-spacing

Unlike the ionospheric delay modeling, the tropospheric delay is derived from each station zenith direction. The interpolation mode and fitting modeling precision are presented in Figure 5-19. The interpolation precision performs better than that of modeling when station-spacing is lower than 300 km. In contrast, the modeling performance increases slowly than that of interpolation from 300 km to 500 km. A superior performance is visible starting at around 400 km station-spacing network. This is because represented stations can provide detailed regional information for fitting models in coverage areas to achieve a satisfactory performance even if the station-spacing is larger.

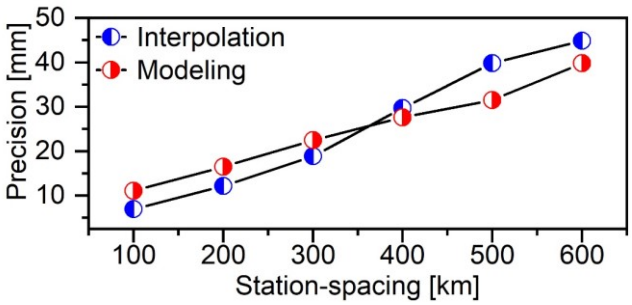

Figure 5-19 Tropospheric delay precision under interpolation and fitting modeling

5.4.3 The large-area network configuration

In large-area augmentation services, conflicts between correction data volume, represented precision, and coverage area size have consistently hindered service performance. Therefore, satellite-based services are the best choice for large areas with limited data transmission volume and precision correction. By utilizing a large area fitting model, precise regional corrections can be interpolated from nearby reference stations to users with high-network capabilities as compensation. Consequently, for large-area applications, a fitting model based on a sparse station network can be developed to provide corrections for augmentation information dissemination. Additionally, the interpolation mode provided by a station network with a density within 200 km can be used as a supplement to deliver high-precision correction information. Based on the analysis of the relationship between station-spacing and modeling performance, a station distance of 200 km is deemed appropriate for large areas reference network. With this setting, the fitting model can achieve an average slant ionospheric delay of 5 cm and tropospheric delay of 1.5 cm.

It is important to note that modeling performance is not solely dependent on station-spacing, but is also influenced by the coverage area size. The fitting model aims to provide an optimized solution for the entire region; however, large meteorological variations in certain areas can introduce discrepancies and impact the overall model performance. When using the same station-spacing networks, smaller regions exhibit better performance compared to larger regions when implementing the modeling method. Conversely, the interpolation mode exhibits consistent performance, irrespective of the area size. The interpolation model in large areas can be considered a region model in each sub-region including a user station and some nearby reference stations. Consequently, the proximity of reference station distances can enhance performance compared to the fitting model. However, the fitting model aims to achieve optimal performance in different-sized areas but may overlook detailed information in specific sub-regions. The performance decreased slowly with the station spacing increasing due to some representation stations ensuring the modeling performance. Because the atmospheric delay

correlation between adjacent stations significantly decreases as the station spacing increases. Therefore, the fitting model performance in large areas is generally lower than interpolation in dense networks but superior in sparse networks.

5.5 Large-area atmospheric delay fitting model uncertainty information generation

The convergence time for positioning is influenced by both the a priori value of atmospheric delay and the constraint value in the positioning model. A constraint is typically introduced to reflect the accuracy of the correction value, which is affected by the disparity between the real-time correction and the actual delay. Therefore, it is crucial to obtain accurate atmospheric delay corrections and proper constraints for rapid AR. The differences between the model-fitted values and those obtained from PPP-derived values provide uncertainty information. Based on the fitting model, the uncertainty grid information can be generated and provided to users along with the model coefficients, making it a quality index. This section presents a method for generating uncertainty information based on the large areas fitting model.

5.5.1 Atmospheric delay uncertainty grid calculation

In order to provide a proper constraint for corrections from a fitting model, two sets of grid error maps are separately generated relying on the fitting model of tropospheric and ionospheric delays. The grid with a 2°×2° grid generated with a fifteen-minute piecewise basis is calculated by the IDW method from the unmodeled values of all reference stations. The resolution setting fully considers the inter-station atmospheric delay correlation. The grid interval distance exceeds the reference station spacing of 150 km and the extent of one degree of European latitude and longitude, which correspond to approximately 110 km and 60 km, respectively. The tropospheric delay grid points are calculated from the absolute fitting residuals of nearby reference stations, while the ionospheric delay grid points are achieved from the absolute fitting residuals of all IPPs.

$$l_{point} = \sum_{i=1}^{n} \widehat{l_i^s}(resi) \times \frac{w_i^s}{\sum_{i=1}^{n}(w_i^s)} \tag{5.9}$$

$$w_i^s = \frac{1}{d_i^{s2}} \tag{5.10}$$

where l_{point} is the uncertainty grid point values; $\widehat{l_i^s}(resi)$ is tropospheric delay modeling residuals; n is the data number applied in uncertainty calculation.

Unlike the tropospheric ZWD modeling, the ionospheric delay is modeled for each satellite. The constraint from one index for all satellites is inaccessible. For large-area services, the uncertainty indexes have to trade off some satellite constraints and correction precision. In grid calculation, all fitting residuals within each grid point 150 km are collected, and 90th percentile (2-sigma) value is selected as the point value. The use end introduce a weight for each satellite to calculate the constraint for each satellite.

Additionally, the constraint value for the user can be determined by utilizing nearby points from the uncertainty grid surrounding the users, using the IDW method. In areas with complete coverage, the user can utilize the surrounding four points. However, in boundary areas, where coverage may be limited, the user can rely on three or two points for constraint determination. It should be noted that tropospheric ZWD directly uses the interpolated value as constraint, while ionospheric delay also combines the grid value with modeling sigma as shown in Eq. (5.11).

$$l_{uncer} = \sum_{i=1}^{m} l_{grid} \times \hat{\sigma}_{sig}^{s} \times \frac{w_i^s}{\sum_{i=1}^{m} w_i^s} \tag{5.11}$$

$$\hat{\sigma}_{sig}^{s} = {\sigma_{sig}^{s}}^2 / \hat{\sigma}_{ave}, \hat{\sigma}_{ave} = \frac{\sum_j^n {\sigma_{sig}^{s}}^2}{n} \tag{5.12}$$

where l_{uncer} is interpolated uncertainty value; m is the grid point used for uncertainty calculation; σ_{sig}^{s} is satellite-wise ionospheric slant delay modeling sigma; $\hat{\sigma}_{sig}^{s}$ is satellite-related factor for each satellite to adjust the uncertainty from grid; $\hat{\sigma}_{ave}^{s}$ is the average value among all satellite modeling sigma.

5.5.2 Atmospheric delay correction generation

The tropospheric and ionospheric delay fitting models are generated based on Sections 5.1 and 5.2 descriptions. Using a 150 km station-spacing network (presented in Figure 5-1) generates the fitting models. The model performance on all reference stations are evaluated and analyzed (as shown in Figure 5-1). The uncertainty information is generated with 15-minute updates, while the differences are calculated every 30 s. This is, each uncertainty grid point uses 15 minutes unmodeled errors to calculate. The interval of 15 minutes is mainly designed for ionospheric delay because of rapid variation and larger magnitude.

Tropospheric delay model

The average residuals between model-fitted and PPP-derived ZWD values on all reference stations between 13:45-14:00 on DOY 270, 2022 are presented in Figure 5-20. On all server end stations, large-area tropospheric delay fitting residuals are less than 1.9 cm for more than 90% stations, and the average difference is 1.3 cm. Several stations located on the boundary areas or with large altitude differences compared to other stations exhibit residuals up to 2.8 cm. Overall, the results show that the large-area ZWD fitting model can obtain good precision in large areas with significant altitude differences.

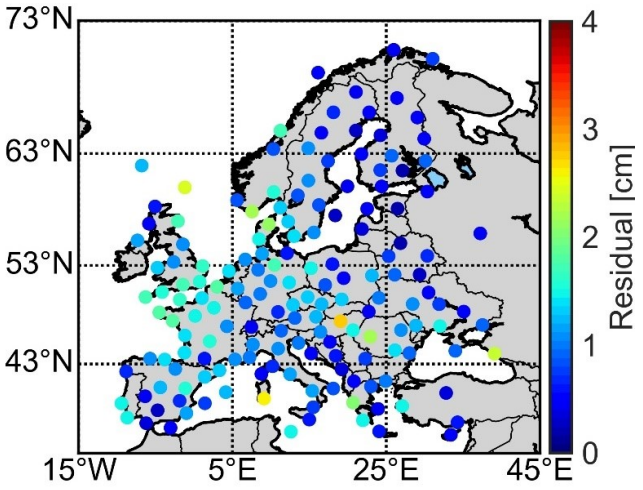

Figure 5-20 Station-wise RMS values of ZWD differences between modelled values and estimated values from PPP-AR solution for all reference stations at 13:45-14:00 on DOY 270, 2022.

Ionospheric delay model performance

The differences between the model-fitted and PPP-derived values for all GPS and Galileo satellites observed at the satellite IPPs of all reference stations between 13:45-14:00 on DOY 270, 2022, are presented in Figure 5-21. Thanks to the stable and high-precision ionospheric delay provided by PPP-AR-derived data, the real-time fitting model can achieve optimal performance. The average residuals of the ionospheric slant delay differences for all satellites is 4.1 cm. By resolving the ambiguity at each reference station, a stable and high-precision ionospheric delay can be derived. Therefore, the precision of the ionospheric delay is mainly affected by latitudinal and meteorological variations. Although different satellites have different coverage areas, the overlapped region shows similar performance, allowing for the generation of a common grid for all satellites. Moreover, satellite-related weighting is introduced into the calculation of grid points.

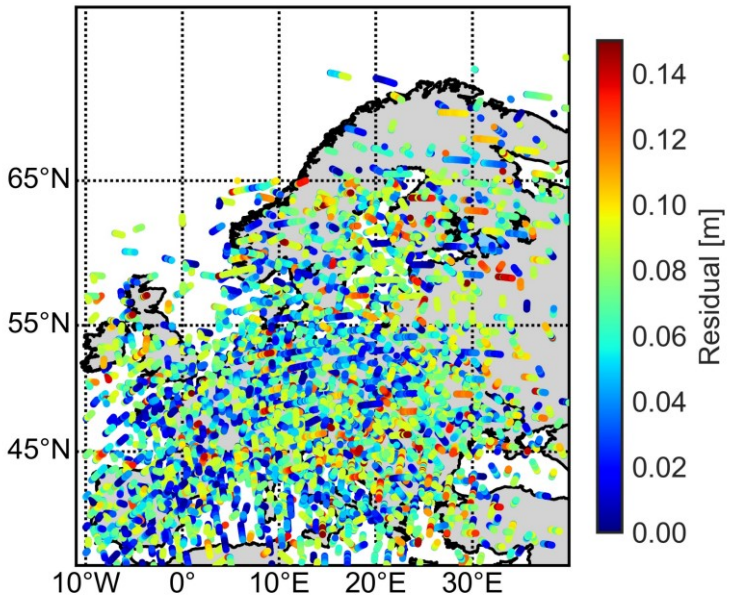

Figure 5-21 Satellite-wise differences of slant ionospheric delay between modelled values and PPP-AR-derived values for all reference stations at 13:45-14:00 on DOY 270, 2022.

5.5.3 Atmospheric delay uncertainty grid generation

After deducting the model-fitted values, the fitting residuals of ZWD at each station or all satellite IPPs are collected to generate wide-area atmosphere uncertainty information. Two sets of 2°×2° grids are created separately for the tropospheric and ionospheric delays, and their generation method is described in detail in Section 3.4.6. The fitting residuals from the above large-area atmospheric delay modeling results show stable and slight differences within 15 minutes. Therefore, the uncertainty information grid with a 15-minute update can provide proper constraints for high-frequency tropospheric and ionospheric delay large-area fitting model corrections. The generated uncertainty information is presented in Figure 5-22 and Figure 5-23.

Tropospheric delay uncertainty information grid

Based on the ZWD unmodeled residuals for each reference station presented in Figure 5-20, an uncertainty information grid is generated. Each point is calculated using nearby station's unmodeled values through interpolation using Eq. (5.9). The tropospheric delay uncertainty in France and surrounding regions exhibits larger values than in other regions, similar to the distribution of the fit residuals presented in Figure 5-20. It should be noted that grid point coverage is dependent on the distribution of the reference station network. As shown by the uncertainty grid, the majority of regions exhibit precision values less than 3 cm, while the largest

residual can reach up to 4.7 cm. Therefore, the grid accuracy map can effectively describe the modeling accuracy of the tropospheric delay fitting model within the coverage area using sparse grid points. Overall, the tropospheric ZWD differences between grid points and unmodeled errors are within one centimeter.

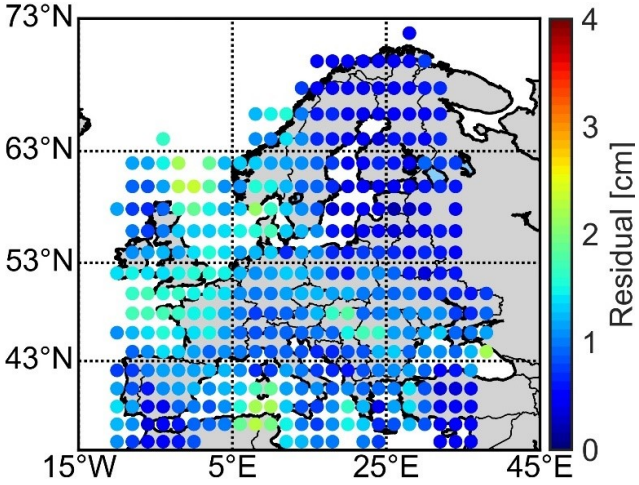

Figure 5-22 Tropospheric delay fitting model uncertainty using fifteen-minute pieces basis between modeled and PPP-AR-derived values between 13:45-14:00 on DOY 270, 2022.

Ionospheric delay uncertainty information grid

The satellite-wise ionospheric slant delay fitting model differs from the tropospheric delay fitting model in that it provides a set of unmodeled residuals for each satellite. Despite the different coverage areas of each satellite, similar performance is observed in the overlapping areas. In addition, the introduced satellite-related weight as a factor can adjust the interpolated uncertainty index according to satellite modeling sigma. Although only one set grid is insufficient to describe the performance of satellite-wise ionospheric delay fitting models precisely, the ionospheric delay uncertainty grid with less data volume approximately represents the corrections for large service areas as the slight loose constraint.

When comparing the unmodeled residuals in Figure 5-21 to the grid points, a similar performance and distribution are observed. Therefore, a single set of grid models is sufficient to represent the performance of the satellite-wise ionospheric delay fitting model. In other words, the overlap area residuals from different satellites will be used for uncertainty grid generation. The uncertainty information of the grid points shows an average value that is close to the ionospheric delay unmodeled residuals, and the range of values is also consistent with the unmodeled residuals. Overall, the ionospheric delay differences between grid points and unmodeled errors are within three centimeter.

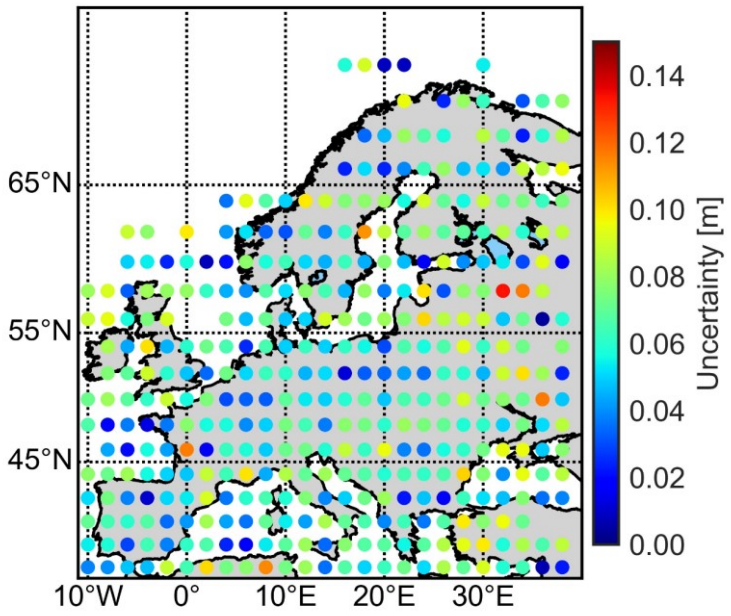

Figure 5-23 Wide-area satellite-wise slant ionospheric delay fitting model uncertainty using fifteen-minute pieces basis between modeled and PPP-AR-derived values between 13:45-14:00 on DOY 270, 2021.

By relying on uncertainty information and large-area fitting model coefficients, the PPP-AR with large-area augmentation can achieve faster convergence and rapid parameter separation. However, it should be noted that the uncertainty information based on fitting models with 2°×2° grid points only represents the large-area fitting model as essential services.

5.6 Regional ionospheric delay uncertainty with inter-cross validation

Relying on fitting models applied in large areas, an essential augmentation can be delivered. However, precise region interpolation requires more accurate uncertainty information to describe the unmodeled errors compensation in regional areas. Unlike the tropospheric ZWD, the ionospheric delay is highly irregular, and thus, the grid uncertainty information as a priori accuracy is limited in the region area (Pi et al. 1997). Therefore, more accurate uncertainty information is required for region correction, especially for ionospheric delay. Moreover, since the ionospheric delay is time- and space-dependent, and the interpolation error varies with different regions, baseline lengths, and time, determining the relationship between ionospheric delay interpolation precision and station distances is crucial. This section describes a precise error function generated by inter-satellite cross-validation for a priori value determination.

5.6.1 Region ionospheric delay uncertainty generation

Regional uncertainty information can be provided according to the inter-station cross-verification among all reference stations with the liner functions. For the regional interpolation mode implemented, the majority of corrections are ionospheric delays due to tropospheric ZWD already achieving better performance using the fitting model. Therefore, the ionospheric delay uncertainty information still needs to optimize and provide. As shown in Figure 5-24, the different range stations are selected, forming a reference network for error function calculation.

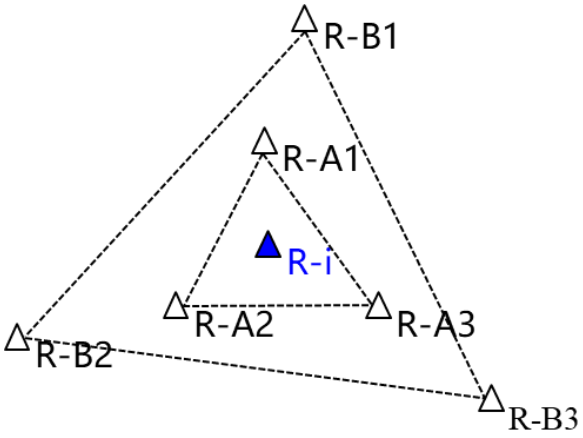

Figure 5-24 different range stations are used forming reference station networks for error function generation.

The regional uncertainty is calculated through inter-station cross-verification and expressed as an error function. For reference station R_i, different reference networks ranging from small-scale R_A to large-scale R_B, formed by three nearby stations, are selected to interpolate ionospheric delays. These networks can be considered to create a virtual reference station derived from each reference network. Two assumptions are made in generating the error function: (1) the average distance between station R_i and the reference network represents the baseline distance between station R_i and the corresponding virtual reference station; (2) the interpolated ionospheric delay is treated as the 'true' value (Psychas & Verhagen 2020). Based on these assumptions, the baseline length D_i and the RMS of the interpolated error R_i for each network can be calculated and used to build a mathematical function $R = f(D)$ for reference station i. Cross-validation is performed at all reference stations to derive their error functions, which can then be used to calculate the ionospheric delay error at any location within the service region. Consequently, the ionospheric delay error map presents the precision at each grid point using a linear error function based on the data from the three nearest reference stations.

$$f(D_i) = a + b \times D_i, \quad D_i = \sum_{j=0}^{n} \frac{D_i^j}{n} \tag{5.13}$$

where a and b are liner model coefficients, respectively; D_i is average distance from reference network j with each station distance D_i^j; n is reference station number.

The error function is generated at each reference station and provided to users. Users can utilize the error functions from selected nearby reference stations to calculate constraints for interpolated ionospheric delays. The constraint index can be considered an average of these calculated values.

5.6.2 Data setting

For region uncertainty information generation, the stations used as shown in Figure 5-1 with 150 km station-spacing network. The stations with low availability of measurements or the solutions with a lower fixing rate (90%) will be filtered out. The GNSS observation data with a sampling rate of 30 seconds in the above-mentioned network from the DOY 270 to 300 in 2022 are used to perform the assessment and the error function are calculated every five-minutes.

5.6.3 Ionospheric delay error map generation

Considering the precision of the ionospheric delay from each reference station and its attenuation or variation along with the baseline direction and length, the RMS of the interpolated ionospheric delay for each reference station is calculated first. The differences can be calculated on each reference station by comparing the interpolated values with PPP-derived ionospheric delays. For example, four stations with 30 km, 90 km, 150 km, and 210 km average distances are presented to demonstrate the correlation between interpolation precision and distance as shown in Figure 5-25.

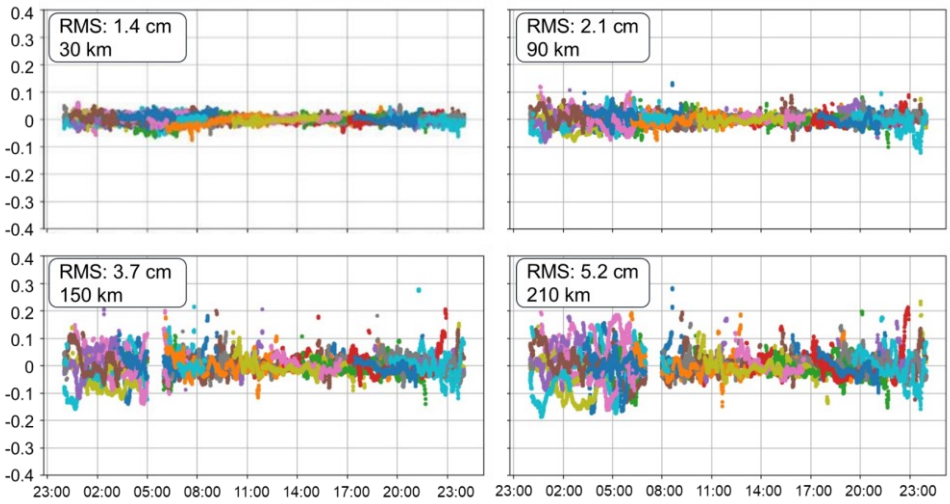

Figure 5-25 The slant single-differenced-between-satellite ionospheric delay interpolation

error for site MALA with limited station distances in Spain, 01 Sept 2022. Different colors represent different satellites.

In Figure 5-25, the SD is used to remove the station end code biases. Initially, the accuracy is lower due to the ionospheric delay accuracy of PPP-derived not being stabilized. This is because the solution is performed daily. When the converged solution is achieved, higher precision interpolation corrections can be directly implemented in nearly station distance solutions. The RMS of interpolation differences presents a decreasing precision and larger fluctuation as the distances increase. In a 30 km distance solution, the interpolation precision can reach up to 1.4 cm, while a large RMS of 5.2 cm is found in 210 km distance solution. Additionally, the station-spacing dependent fitting RMS suggests an error function with similar consideration. Therefore, an error function can be separately generated by analyzing the interpolation precision for each reference station. Figure 5-26 shows the relationship between the inter-station interpolation RMS of all satellites and station distances.

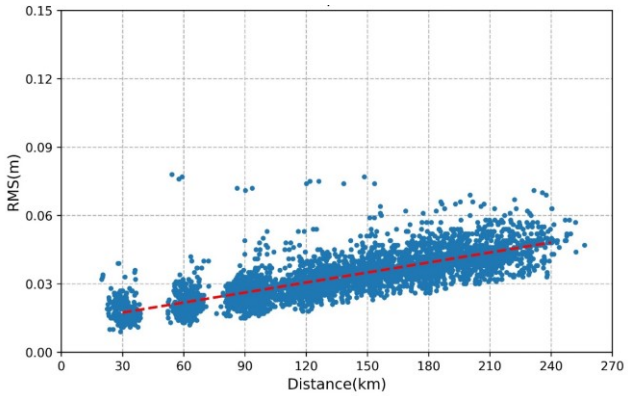

Figure 5-26 The relationship between reference station distances and the RMS of the differences between the interpolated and PPP derived ionospheric delays.

The interpolation distance and the interpolated ionosphere precision present a linear relationship. Following this relation, the high-precision inter-satellite ionospheric delay between each reference station is cross-validated to determine the ionospheric delay interpolating error functions and generate the error map.

5.6.4 Evaluation of ionospheric delay error map

The interpolated RMS on all stations are estimated and the generated ionospheric delay error maps are presented in Figure 5-27 for all satellites.

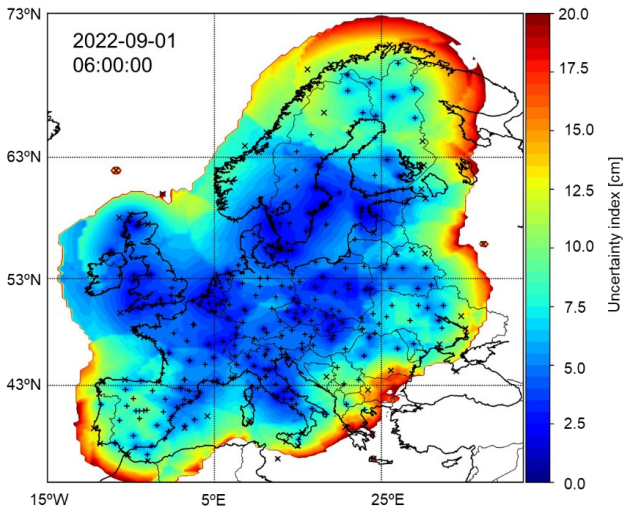

(a)

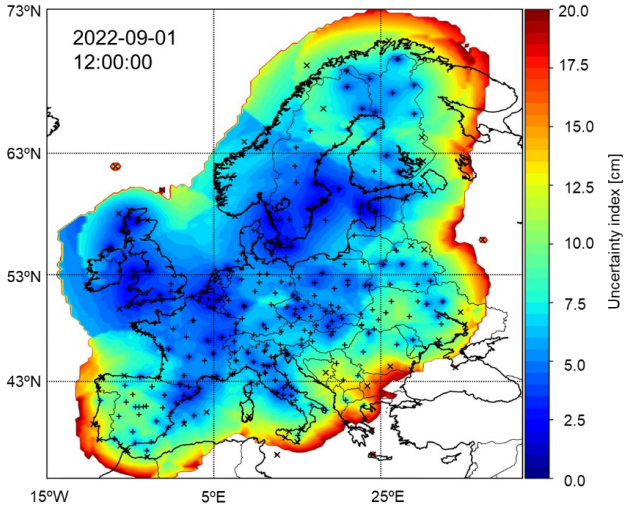

(b)

Figure 5-27 The slant ionospheric delay interpolation error map using five-mins ionospheric delay (in meter) at two epochs, 06:00 (a) and 12:00 (b), 01 Sept, 2022.

The color bar range in Figure 5-27 is between 0 and 0.2 m, and the place without color denotes a precision worse than 0.2 m. In situations where the interpolation accuracy falls worse than 0.2 m, the ionospheric delay enhancement has a significantly minimal impact on PPP. Moreover, for peripheral regions, if the spacing between reference stations exceeds 400 km, atmospheric delay accuracy indicators are no longer provided. This is the reason for the different coverage of these two figures. The 06:00 map shows better precision and a minor difference than the 12:00 map. There is a correlation between this and the activity of the ionospheric delay, which is more active during the daytime, particularly at noon.

In Figure 5-27 (a), the interpolated ionospheric delay error in northern Europe is larger than 20 cm, and that at the Iberian Peninsula is about 10 cm. In such a case, positioning with the

imprecise interpolated ionospheric delay with an unreasonable fixed constraint is problematic. In contrast, in Figure 5-27 (b), the errors in these two areas are more minor, about 2-5 cm, due to stable interpolated precision (Figure 5-25). The interpolated ionospheric delay error in European Central Region, e.g., Germany and its neighbouring countries, is stable and small. This is because the density of the station network is higher in this region than in other areas, this is, at the boundary, and the station density is naturally lower or only one side with stations. It is easy for users in this area to choose three nearby reference stations to provide high-precision ionospheric delay correction.

It is worth noting that the error map reflects the situation of the currently selected station configuration. If the stations are more dense, the precision will be higher. It should be noted that the ionospheric delay activity changes rapidly with time, and thus, the precision RMS function of each station and error map should be calculated and generated piecewise. A five-minute period is set for the precise error map generation to keep the real-time effectiveness, this is, the error map will be recalculated ever five minutes.

5.7 Chapter summary

The large area atmospheric delay model and uncertainty generation are summarized as follow.

Section 5.1 introduces a modified tropospheric delay fitting model with additional exponential functions considering the large altitude differences in large-area using sparse station-spacing network. The proposed model performs better in a sparse network and demonstrates a comparative modeling performance in larger altitude differences areas.

Section 5.2 describes a new satellite-wise ionospheric slant delay modeling method by analyzing ionospheric slant delay characteristics of the path propagation, and a trigonometric model is introduced to describe the path elevation and azimuth angle differences between optimized reference slant path with others. The ionospheric delay modeling can achieve an 53% modeling precision improvement with respect to legacy second-order polynomial model.

Section 5.3 analyzes the ionospheric delay modeling performance implemented on different types of receiver. The modeling precision of specific type with and without applied SPRs correction and all types of receiver with SPRs correction are 4.0 cm, 7.9 cm, and 4.2 cm, respectively. Although the same characteristics are presented in the same type of receiver, the different versions or environments also can impact the PPP-derived ionospheric delay.

Section 5.4 investigate the relationship between station distances and modeling/interpolation precision. Principally, the solutions are analyzed in the following two aspects.

- The precision of interpolation is better under 300 km station-spacing networks, while the opposite performance can be found beginning the 400 km station-spacing networks.
- Both the interpolation and fitting model can achieve a comparative precision in networks with 200 km station-spacing. Interpolation outperforms fitting precision for denser networks, while the opposite performance occurs in sparse networks. The Galileo satellites perform better than that of GPS satellites.

Section 5.5 concisely presents two sets of uncertainty grids by a 2°×2° resolution based on the residuals of fitting model of ionospheric and tropospheric delays. The generated grid can accurately reflect the model-fitted precision in all coverage areas. The users use the generated uncertainty information to calculate the accuracy of the atmospheric delay derived from the fitted model using the nearby grid points.

Section 5.6 proposes a method to determine the precision of the interpolated slant ionospheric delay by cross-validation to consider the high temporal and spatial variation. A distance-dependent function is constructed to represent the stochastic model of the slant ionospheric delay derived from each reference station. At the user-end the ionospheric delay and its precision can be interpolated using the average reference network distance as input to calculate the interpolated precision.

6 Real-time Hierarchical Positioning

This Chapter integrates the atmosphere information and signal bias calibration methods proposed in the previous Chapters. The objective is to address the challenge of achieving large-area coverage and high accuracy while minimizing data transmission volumes. The conflict among data volume, represented precision, and coverage area size is always hindered by the data transmission capability. To overcome these challenges, a hierarchical positioning mode is introduced in this chapter (Cui et al. 2023). This mode incorporates fitting models and compensates for unmodeled residuals based on atmospheric delay uncertainty information. The proposed hierarchical mode integrates PPP, PPP-AR, PPP-WA, and PPP-WRA into a consistent system achieving rapid/instantaneous convergence with minimal data transmission volume in large-area service.

6.1 Hierarchical positioning strategy

The large area fitting model has advantages as it offers a correction service for large areas with minimal coefficients under sparse station networks. These advantages are combined with regional residual delays to create a hierarchical positioning system. The fitting model serves as the essential correction method, covering larger areas, and the residual delays are then interpolated from nearby regional reference stations to enhance atmospheric delay accuracy. If the calculated constraint from the uncertainty grid is larger than the threshold (2.5 cm), four nearby grid points are selected to interpolate the user end index. In this case, further regional residuals are provided from nearby reference stations. This approach reduces the communication burden significantly and mitigates the impact of station distributions and distances.

With different available augmentation information listed in Table 6-1, the hierarchical augmented positioning mode can be divided into three-level, including global PPP and PPP-AR, PPP with wide-area augmentation (PPP-WA), and PPP-WA with region compensation (PPP-WRA). Moreover, Figure 6-1 describes the real-time large areas hierarchical system structure. In the first level, i.e., globally PPP and PPP-AR, orbit, clock, and UPD are directly provided for global users. The second level, i.e., PPP-WA, includes first-level and tropospheric and ionospheric delay fitting models. The third level, i.e., PPP-WRA, is based on the first- and second-levels and combine three reference stations residual delays interpolation.

Fitting model coefficients can be broadcasted through satellite communication links to provide real-time augmentation information for users in large areas. Due to variations in topography,

changes in meteorology, etc., the fitting performance in some areas is affected, leading to the existence of unmodeled delays at reference stations. Upon subtracting the ionospheric and tropospheric modeled values, the unmodeled values are complementarily provided to the user from nearby stations using the IDW interpolation model. Corresponding uncertainty is generated separately through the fitting residuals and inter-satellite cross-verification.

Table 6-1 Required corrections for different augmented level positioning

Correction	PPP	PPP-AR	PPP-WA	PPP-WRA
Orbit and clock	✓	✓	✓	✓
UPD		✓	✓	✓
Wide-area fitting model			✓	✓
Unmodeled errors				✓
Coverage-area	Global		Wide-area	
Augmented method	SSR broadcast		Fitting model	Interpolation

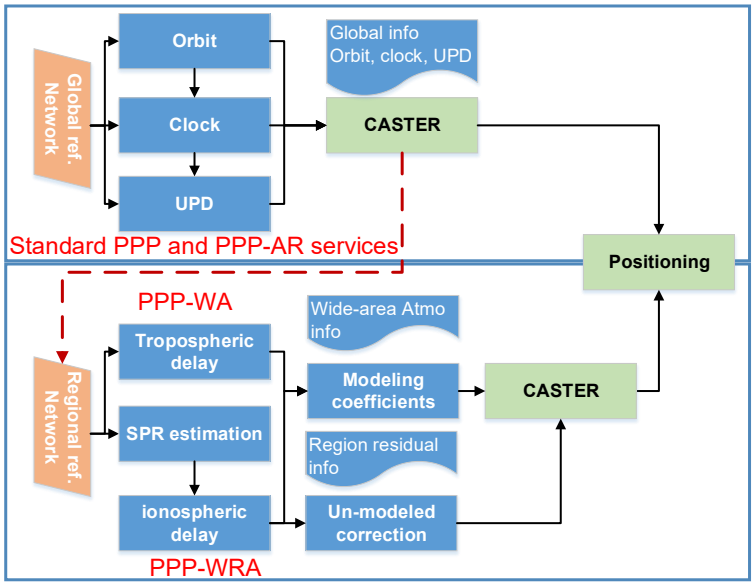

Figure 6-1 System structure of the real-time precise positioning service with different level augmentation. The upper panel is the PPP and PPP-AR, where real-time orbits, clocks, and UPD are estimated from GFZ AC real-time stream. The bottom panel shows the wide-area PPP-WA and regional PPP-WRA where atmospheric delay model and unmodeled errors are generated from all reference stations.

In the user end, atmospheric delays from the fitting model or interpolation model can be used as virtual observations with an a priori constraint. Usually, user should impose a constraint on the corresponding parameters with the following equations,

$$x_{est} - x_{ref} = 0 \quad P = \frac{1}{\sigma_{ref}^2} \tag{6.1}$$

where x_{est} and x_{ref} are real estimated and external correction values, including ionospheric delay and tropospheric ZWD, respectively; σ_{ref}^2 is the a priori variance factor from the uncertainty information, which serves as the constraint. For PPP-WA solution, the grids are provided as the constraints, while the precise uncertainty is achieve by the error function for PPP-WRA.

6.2 Dataset

Three months (DOY 120-300, 2022) of Multi-GNSS dual-frequency data from 83 globally distributed MGEX permanent stations (Figure 6-2) and 187 distributed EPN stations (Figure 6-3) are processed. The real-time precise orbits and clocks are from GFZ real-time product stream[12]. The global stations are used for UPD estimation. In addition, 103 EPN stations (all have GE observations) are used as large-area reference stations to perform static UDUC-PPP-AR to derive atmospheric delays, and the remaining 84 stations (all with GREC observations) are selected as positioning performance verification stations.

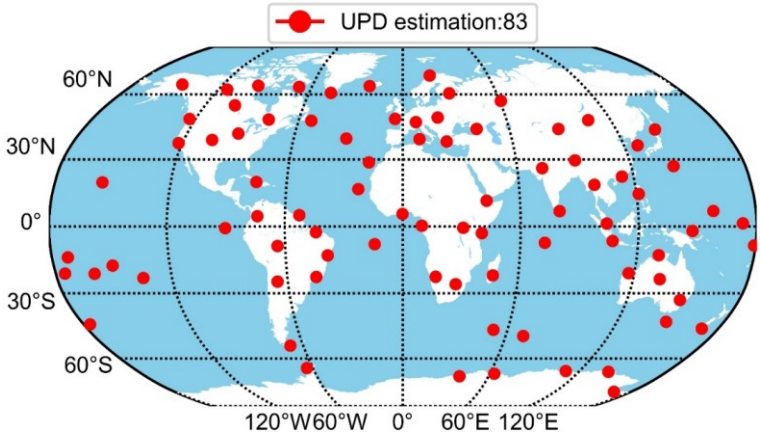

Figure 6-2 Station distribution of 83 MGEX stations used for real-time UPD estimation

[12] 139.17.3.115:2101/SSRA00GFZ0

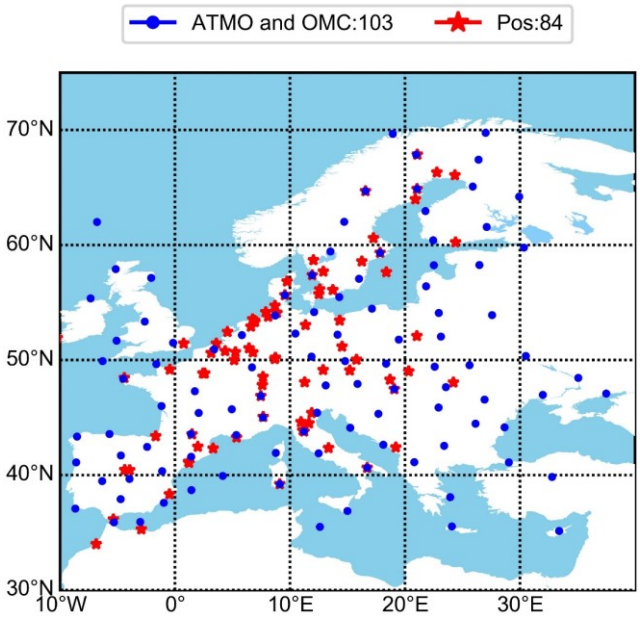

Figure 6-3 Station distribution with 187 EPN stations. Blue dots denote 103 stations used for atmosphere augmentation generation and 84 red pentagrams are used for positioning verification.

As shown in Figure 6-3, the 103 server stations with 200 km station-spacing enable uniform coverage of the Europe region. For large-area service, the fitting model performance is impact by coverage areas size. To ensure a higher precision of the fitting model applied in large-area with less data transmission volume, the Europe region is divided into four sub-areas following the 50°N altitude and 15°E longitude lines.

6.3 Real-Time correction product precision analysis

The atmosphere augmentation correction generation strategy applied in this section is described in Chapter 3, including tropospheric and ionospheric delays modeling, UPD estimation, and uncertainty information generation, which is already demonstrated in Chapter 4 and Chapter 5. To perform and verify the real-time positioning with augmentation information, the real-time products and generated atmospheric delay correction precision are assessed in this section.

6.3.1 UPD performance evaluation

AR is only performed on GPS and Galileo constellations, because the majority EPN stations still only can receive these two constellations. The BDS satellite only can be observed around 100 station in EPN, which is mainly included in the user end positioning verification. The GLONASS is only performed as a float solution due to FDMA mode, even though enough station numbers are

satisfied. Therefore, the atmospheric delay modeling and uncertainty is only performed for GPS and Galileo satellites.

Figure 6-4 provides the WL and NL UPDs time series for all observed GPS and Galileo satellites on DOY 150, 2022. The temporal resolution is 30 s. As expected, WL UPDs for all satellites are quite stable over time, with the maximum STD below 0.05 and 0.03 cycle for GPS and Galileo satellites, respectively. Temporal stability of NL UPDs shows slightly worse temporal stability than that of WL due to the significantly shorter wavelength. In particular, some NL UPDs present clearly large fluctuations up to 0.2 cycle, while the mean STDs over the experiment periods are all within 0.1 cycles for both GPS and Galileo satellites. Moreover, NL UPDs can still be accurately estimated and predicted over tens of minutes to a few hours, and the predicted values facilitate AR for real-time PPP users.

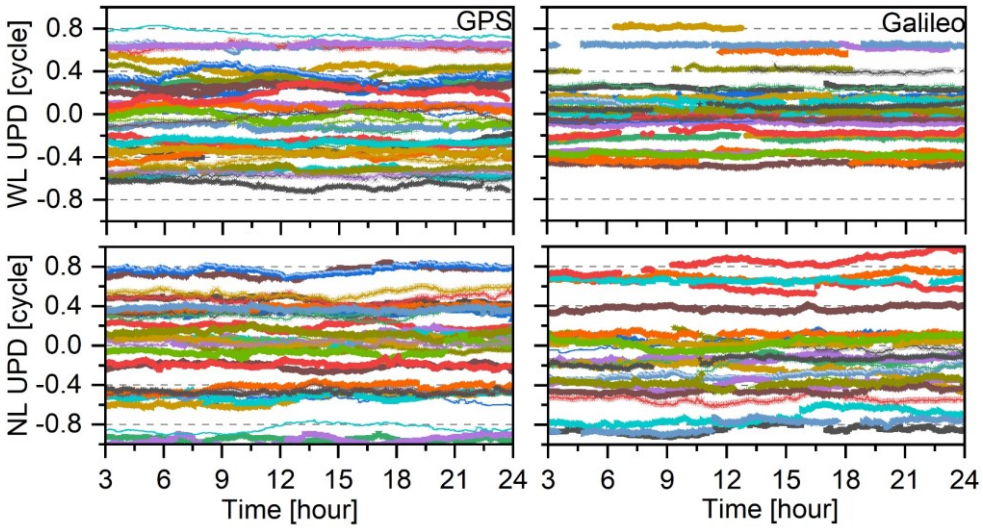

Figure 6-4 WL (upper) and NL (lower) UPDs for GPS (left) and Galileo (right) satellites on DOY 150, 2022.

In addition, the STD of AR residuals in WL and NL UPDs estimation are presented in Figure 6-5. The 90-day UPD calculation residuals in all epochs are collected. The residuals are calculated as the float ambiguity minus UPDs of the corresponding satellite and station, which should be an integer value. And the fractional part can thus be considered as residuals to evaluate the precision of the UPD. The average STDs of GPS and Galileo are around 0.02 cycle, and the Galileo satellites have slightly smaller residuals. Both GPS and Galileo satellites show very concentrated and smaller STD.

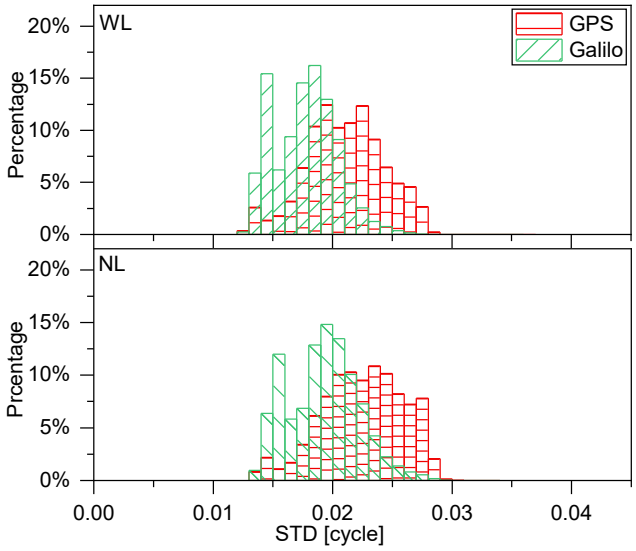

Figure 6-5 The residuals STD of WL (top) and NL (bottom) in UPD calculation.

6.3.2 Analysis atmosphere modeling precision

The precision of large-area atmospheric delay fitting model is evaluated in this section.

Tropospheric delay modeling

The dots with different colors on each station, including all reference and verification stations, denote the RMS of the fitting model performed in Europe. The worst station has a large residuals of up to 4.6 cm, and the average fitting value is 1.3 cm. The fitting precision of stations located in marginal areas and the areas with significant altitude differences are lower than that of average fitting precision. As a result, the fitting model can achieve relatively uniform precision in large-area with few model coefficients.

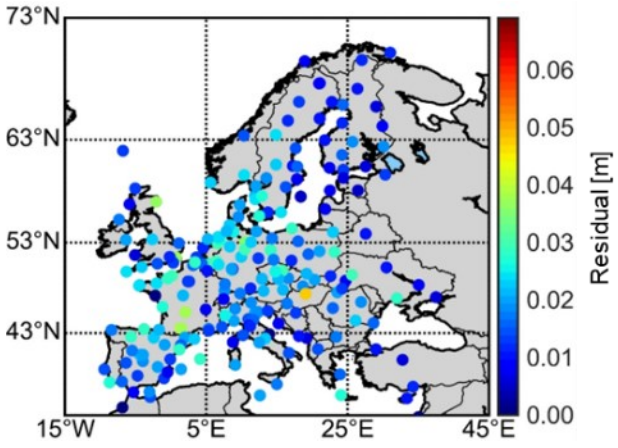

Figure 6-6 Fitting precision of large-area tropospheric ZWD fitting model

Ionospheric delay modeling

Compared with the tropospheric ZWD, ionospheric delay usually presents stronger variation trends and more active characteristics. A thirty-minute residual arc segment (14:00-14:30 of DOY 150, 2022) is presented, and the point with different colors denote the magnitude of residuals for each epoch between modeled value and the PPP-derived value for all satellites. The average modeling precision is 4.1 cm. Additionally, the maximum residuals can reach up to 17.1 cm. Overall, more than 90% of residuals are within 7.9 cm of each other.

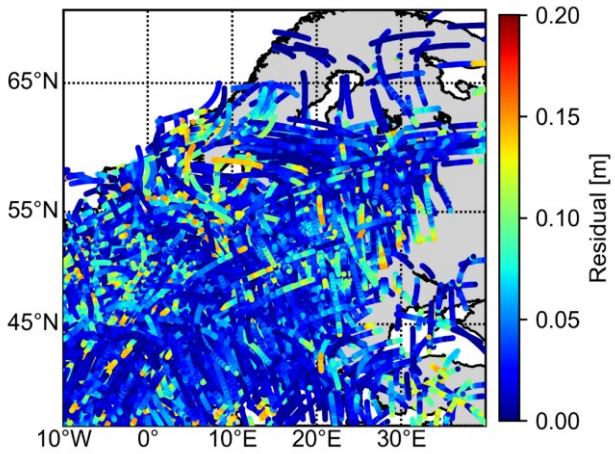

Figure 6-7 Slant ionospheric delay differences between modeled and PPP-derived values on all reference stations.

6.4 Unmodeled correction generation

For large-area service, both the fitting model coefficients and their uncertainty information are crucial. This ensures that model values can contribute to user-end positioning with proper weight or constraint, as detailed in Section 5.5. The provision of unmodeled errors depends on the magnitude of the large-area uncertainty grids, providing optional compensation instead of the traditional high-frequency continuous transfer. This section elucidates the process of generating unmodeled errors.

6.4.1 Station setting

For a comprehensive evaluation of the unmodeled errors, the results of using 0LOV, BUTE, EUSK, and ZIM3 stations as an example are presented in Figure 6-8. The distances with respect to corresponding reference stations vary between 70 and 350 km, and the average distance is 150 km for EUSK and 0LOV stations and 270 km for the other two stations.

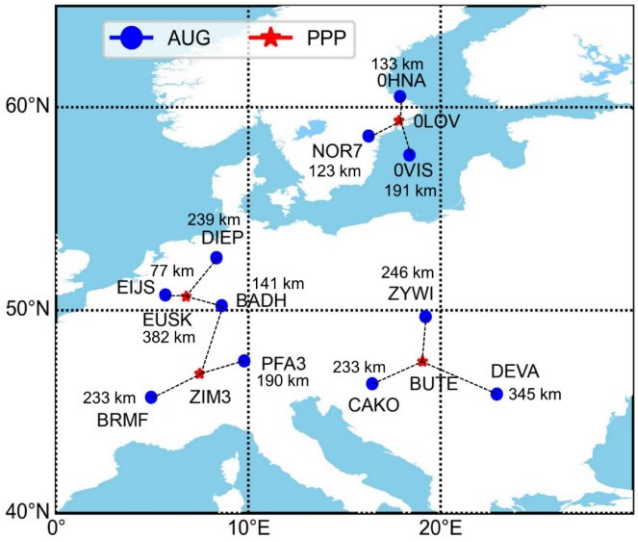

Figure 6-8 Selected stations for the demonstration of different positioning modes (red star) and the corresponding server stations used for the unmodeled correction calculation (blue dot). The distances between user stations and reference stations are given.

6.4.2 Atmospheric delay unmodeled errors

After receiving the large-area fitting model coefficients, the obtained modeled corrections are compared with those PPP-derived from user stations to evaluate the accuracy of the models on these four stations. The differences of tropospheric and ionospheric delay on these stations are presented in Figure 6-9 and Figure 6-10.

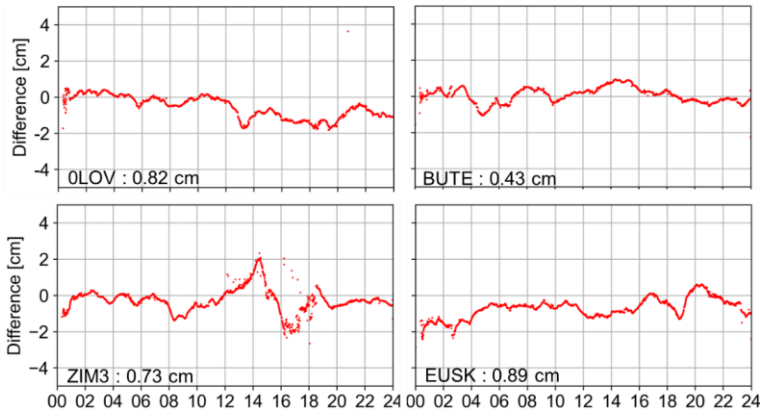

Figure 6-9 Differences between the modeled and estimated ZWD at 0LOV, BUTE, ZIM3, and EUSK stations, on DOY 120, 2022.

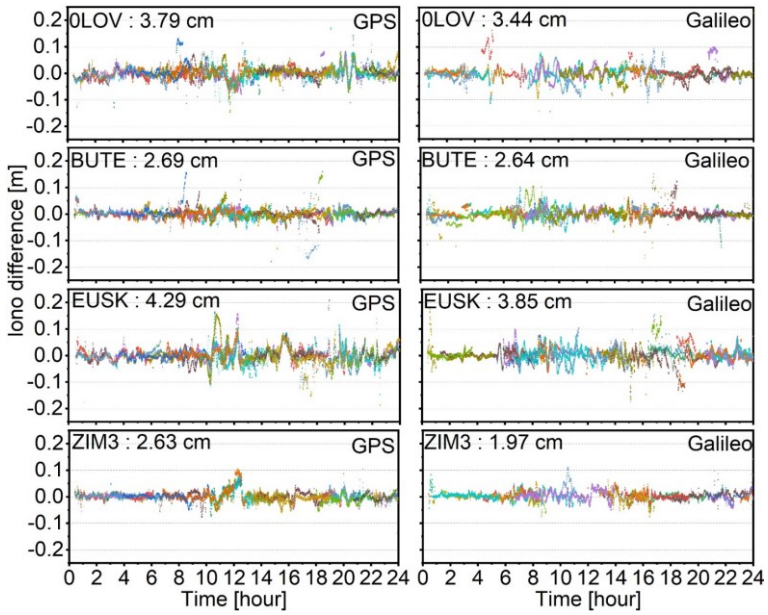

Figure 6-10 Differences between the modeled and estimated slant ionospheric delays of all GPS satellites (left) and all Galileo satellites (right) on DOY 120, 2022.

From Figure 6-9 and Figure 6-10, the differences between the tropospheric and ionospheric delay modeled and PPP-derived values in these stations are presented. 0LOV, BUTE, ZIM3, and EUSK stations have RMS of ZWD differences between modeled and estimated values of 0.82, 0.43, 0.73, and 0.89 cm, respectively. In contrast, the variation of ionospheric delays is more significant than that of tropospheric delays, which makes worse model precision. Unlike the tropospheric ZWD modeling, the ionospheric delay model is generated for each satellite, which strongly relates to the hardware. For these four stations, the RMS of ionospheric delay differences between modeled and PPP-derived values for Galileo are 3.44, 2.64, 3.85, and 1.99 cm and that for GPS are 3.79, 2.69, 4.29, and 2.63 cm. The performance of ionospheric delay modeling for Galileo satellites is better than that of GPS satellites, which can attribute to the more stable SPR biases estimation and related to the Galileo satellite hardware performance.

6.4.3 Residual unmodeled error analysis

Since the large-area fitting model aims to achieve optimal performance over the whole coverage area, the atmospheric delay fitting accuracy is not consistent in some specific areas, especially the areas with considerable altitude or meteorological condition changes. As a result, the interpolation model is applied to compensate for further residual unmodeled errors. The unmodeled errors are divided into troposphere and ionosphere components. However, compared with tropospheric ZWD modeling, the ionospheric delay is still the major error component of the residuals.

The compensation determination is based on the magnitude of fitting residuals, this is, the region interpolation correction is enabled if the values from nearby reference stations model fitting residuals are larger than the thresholds or large-area uncertainty grid calculated index is larger than the threshold. In this thesis, the threshold is set as 2.5 cm, which is less than a quarter of one cycle NL wavelength (Psychas et al. 2019b). This threshold is primarily set for unmodeled ionospheric delays to ensure that ambiguity fixing is not significantly affected in terms of possibility and correctness.

After combining the unmodeled errors from nearby stations, the majority errors can be removed. From Figure 6-9 and Figure 6-10, some epochs' unmodeled errors are within the threshold, that is, the large-area fitting model already provides accurate corrections, sometimes without region compensation required. Therefore, the region compensation of the hierarchical augmentation mode has optional implementation according to the magnitude of the unmodeled errors. Figure 6-11 presents the residual unmodeled errors distribution of tropospheric delay on all station ZWDs and satellite-wise slant ionospheric delays for GPS and Galileo satellites.

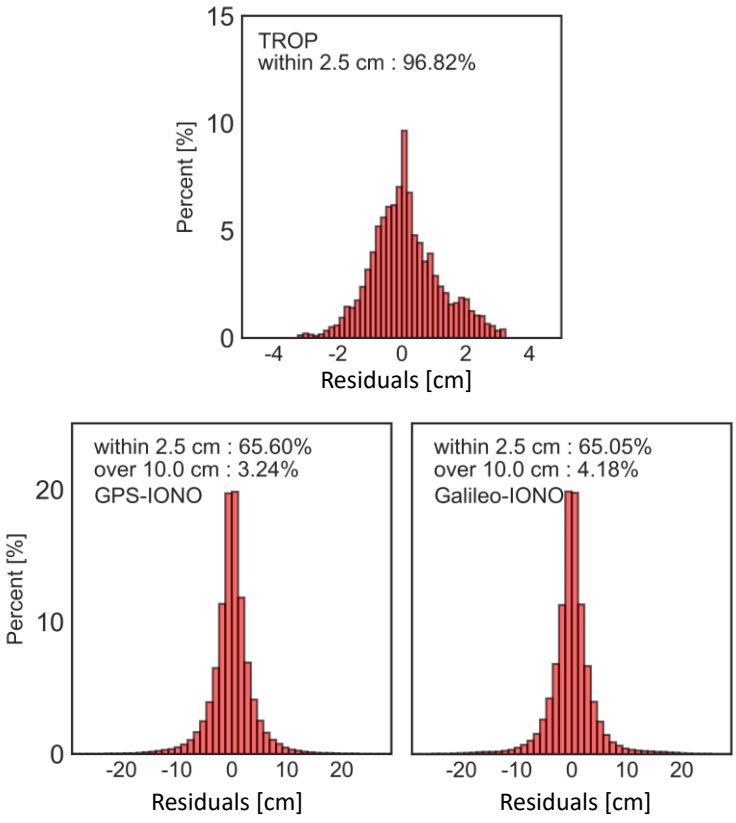

Figure 6-11 Tropospheric delay (top) of all stations and satellite-wise ionospheric slant delay (bottom) unmodeled corrections distribution for GPS and Galileo satellites on all stations.

From Figure 6-11, the majority of unmodeled values are within 2.5 cm for the tropospheric and ionospheric delays. Compared with legacy interpolation mode, corrections of tropospheric and

ionospheric delays can achieve 96.8% and 65.3% bandwidth savings.

For tropospheric delay, approximately 82% of the unmodeled residuals are within 1.5 cm, and about 15% of the residuals fall between 1.5 cm and 2.5 cm. These larger residuals mainly occur in higher altitude areas, where there are larger deviations from the mean level. Additionally, iterative data processing is employed to detect outliers and continuously de-weight them, reducing their impact on the solution. Consequently, the effect of applying the same threshold for both tropospheric and ionospheric delays on positioning can be mitigated.

Compared with the legacy augmentation mode, the hierarchical mode not only achieves lower data communication volume than the interpolation-only mode but also enables instantaneous AR with respect to the fitting-only mode in the large-area, which integrates both advantages. Different modes of data communication volume are presented in Table 6-2.

Table 6-2 Different positioning mode data communication volume using S satellites and N stations from the networks for each epoch.

Mode	Data volume	Convergence
Only-fitting (PPP-WA)	Trop: 7 Iono: $10 \times S$	Rapidly
Only-interpolation (Atmosphere)	Trop: N Iono: $S \times N$	Instantaneous
Only-interpolation (OMC)	$N \times S \times F$ (F: frequency number)	Instantaneous
Hierarchical augmentation (PPP-WRA)	Trop: 7+N ×3.2% Iono: $10 \times S$+$S \times N \times 34.7\%$	Instantaneous

Compared to the legacy interpolation mode, the hierarchical augmentation mode significantly reduces the burden of data communication volume. The fitting model, which already corrects the majority of tropospheric and ionospheric delays in large areas, eliminates the need to broadcast all unmodeled errors for every epoch.

In real-time augmentation services, the RTCM (Radio Technical Commission for Maritime Services) service can offer various corrections through satellite communication (for large areas) and internet communication (for specific regions). To ensure smooth utilization of the models, the description of tropospheric and ionospheric delay fitting models and interpolated corrections information should be proactively informed to users in advance, including the respective number of parameters for each model and how to use these parameters. Additionally, users will be provided with advance communication about the latitude and longitude coverage range, along with reference center coordinates for each region. This proactive information aims

to assist users in better understanding and effectively applying the models. Ultimately, users have the option to directly apply the received parameters for fitting, enabling a seamless integration of correction data into their real-time augmentation processes.

In the context of four sub-region segmentations within European regions, the correction data transmission volume is 28 for tropospheric ZWD and 40×N (N represents the number of satellites) for ionospheric delay, respectively. The uncertainty for large-area services is represented in the form of grids, with 475 grid points sharing the same data volume for both the troposphere and ionosphere. Under sub-region service conditions, this data volume remains within the satellite-link 2400bps communication capability. The model coefficients are updated every one minute and broadcast by the satellite every ten seconds, resulting in six repetitions every minute. This means that users can receive all model coefficients within ten seconds. Additionally, all uncertainty grid points are updated every fifteen minutes with repetitions in one minute.

It should be noted that when further compensation is not enabled, the constraints of the tropospheric and ionospheric delay are calculated by the atmospheric delay uncertainty grid points (Section 5.5) which is generated by the large-area fitting model on all reference stations. Otherwise, the constraints are determined by the inter-satellite across-validation functions on three nearby reference stations (Section 5.6). When regional compensation is enabled, three nearby stations provide ionospheric delay corrections for all satellites, and tropospheric delay corrections for users, amounting to approximately 3×S and 3 corrections at each epoch, respectively (where S is the satellite number).

6.5 Integrated large-area hierarchical positioning

Based on the real-time orbits, clocks, and calibrated UPDs products, as well as additional atmospheric delay and its uncertainty information, PPP-AR can be performed to validate the performance of integrated hierarchical augmentation positioning. The hierarchical positioning mode is used to implement the rapid/instantaneous-AR at the user end, and the results are analyzed in this section.

6.5.1 Positioning performance verification

Using four stations as an example (shown in Figure 6-8), the results of PPP, PPP-AR, PPP-WA, and PPP-WRA are presented. In order to calculate the convergence performance and TTFF of positioning, daily observation is divided into 24 sub-sessions, i.e., one hour per sub-session, resulting in a total of 362880 sub-sessions in 180 days. More details about data processing

strategies are presented in Table 3-3. The positioning is set as kinematic mode and the coordinates are estimated as white noise. The tropospheric ZWD is estimated as random work noise with a variation of 0.1 $mm/\sqrt{s}$. The ionospheric delay is also estimated as random work noise with a large variation of 3 $m/\sqrt{s}$ due to its rapid variation and delay magnitude.

Figure 6-12 shows the positioning time series of PPP, PPP-AR, PPP-WA, and PPP-WRA on four selected stations on the first hour of DOY 120, 2022. In the float PPP scheme, convergence takes approximately 13 mins, but positioning performance is poor, with 1.8 and 3.5 cm for horizontal and vertical components. As a result of the PPP-AR solution, which uses UPD products, the convergence time can be shortened by up to 5 mins, while the precision also can be improved slightly. In contrast, the PPP-WA can further reduce the convergence time and TTFF to 2.5 mins, and the positioning precision is improved to 0.7 and 1.2 cm on the horizontal and vertical components, respectively. The AR can be achieved at 0LOV and EUSK stations at the first epoch when unmodeled information is enabled from nearby reference stations, that is, when the PPP-WRA mode is used. At ZIM3 and BUTE stations, ambiguity fixing can be achieved at the second epoch, mainly due to the larger distance of ~270 km of these two stations against ~150 km of EUSK and 0LOV stations. Overall, a positioning precision of centimeter-level can be achieved from the single epoch solution with additional atmospheric unmodeled errors enabled.

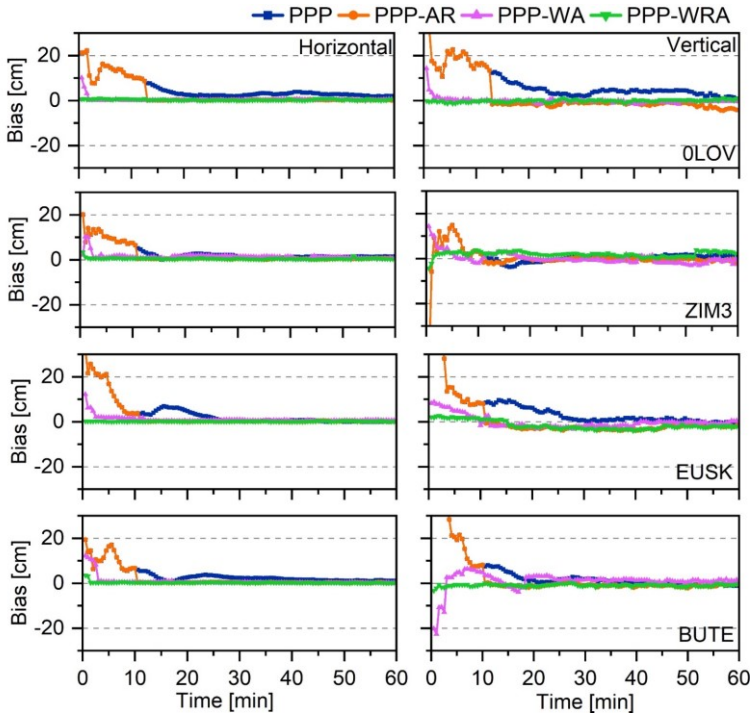

Figure 6-12 Positioning time series for 0LOV, ZIM3, EUSK, and BUTE stations of PPP, PPP-AR, PPP-WA, and PPP-WRA in the horizontal (left) and vertical (right) components.

In addition, the number of tracked satellites and those with ambiguity fixed states in different modes are inspected and presented in Figure 6-13. Half of the satellites can achieve ambiguity

fixing, corresponding to the tracked number of GPS and Galileo satellites, as the AR is not performed on the GLONASS and BDS satellites. The major impact caused by using large-area or region augmentation information is during the convergence period, where more satellites are fixed with the aid of this information.

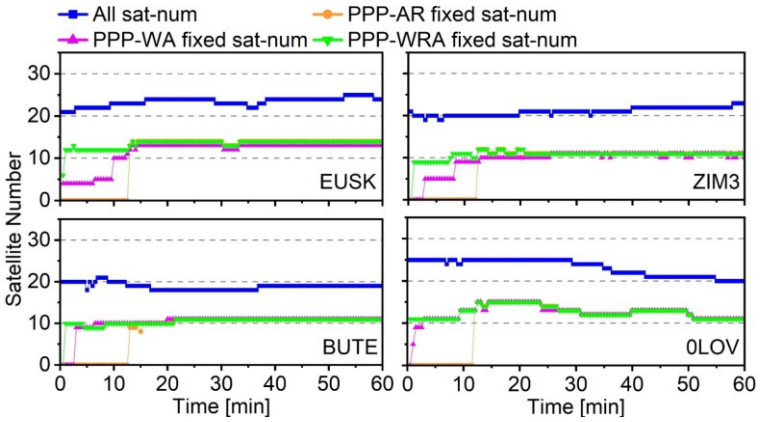

Figure 6-13 Number of satellites available and with ambiguity fixed for EUSK, ZIM3, BUTE, and 0LOV stations.

6.5.2 Positioning performance evaluation

Finally, all station positioning results are performed and analyzed, and the 68th (good) and 90th (poor) percentile positioning results, convergence time, and the TTFF are statistically presented in Figure 6-14, and Table 6-3 presents the average results. Positioning precision of 68th percentile improve 17% and 20% for PPP-WA compare to PPP-AR and PPP-WRA compare to PPP-WA, and that of 90th percentile are 7% and 6%, respectively. Convergence times of 68th percentile are improved by 87% and 64% for PPP-AR and PPP-WA, and that of 90th percentile are 55% and 57%, respectively. The 68th percentile TTFF of PPP-WA and PPP-WRA are 2.0 and 0.5 mins, and that of 90th percentile are 7.5 and 4.0 mins, respectively. Compared with the PPP-AR and PPP-WA, the performance of PPP-WRA is greatly improved. The instantaneous AR can be achieved in the station with average reference station distances of less than 200 km in case the unmodeled errors are available. Overall, 85.3% of all solutions can be implemented instantaneous-AR, and all results are within 1 min.

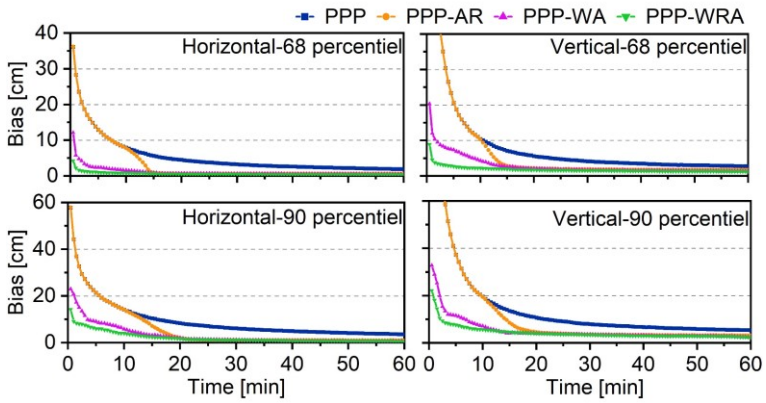

Figure 6-14 Four schemes positioning statistics results with every 1-hour reset.

Table 6-3 The average results of positioning precision, convergence time, and TTFF under different augmented methods

Item	Precision (cm)		Convergence (min)		TTFF (min)
	Horizontal	Vertical	Horizontal	Vertical	
PPP	2.8	3.6	8.3	12.5	
PPP-AR	1.2	1.9	7.6	10.9	11.2
PPP-WA	0.8	1.6	1.6	3.2	2.1
PPP-WRA	0.7	1.3	0.5	0.5	0.5

6.6 Chapter summary

This Chapter presents a hierarchical positioning strategy with the integrated large-area tropospheric ZWD and satellite-wise ionospheric slant delay fitting models, supplementary unmodeled residuals, and atmospheric delay uncertainty information to provide a new augmentation mode.

Section 6.1 describes the data processing strategy of the hierarchical positioning mode.

Section 6.2 gives the observation and stations used in atmospheric delay modeling. A 200 km sparse station-sparing station network can be applied to generate the models.

Section 6.3 describes the precision and performance of real-time products, with the following conclusions.

- GFZ real-time orbit and clock products are implemented.
- Real-time GPS and Galileo satellite estimated WL and NL UPDs are quite stable over time with STD of less than 0.02 and 0.03 cycle, respectively.
- The wide-area tropospheric fitting model achieves an average precision of 1.3 cm in Europe.
- Ionospheric delay fitting models average precision are 4.4 and 4.0 cm for GPS and Galileo

satellites, respectively.

- Two sets of atmosphere uncertainty grids and the regional inter-satellite cross-validation functions are introduced to provide index for unmodeled error compensation and proper atmosphere correction constraints.

Section 6.4 analyzes the residual unmodeled errors among all reference stations. The data communication bandwidth can be separately saved at 96.8% and 65.5% according to the uncertainty grids of the troposphere and ionosphere.

Section 6.5 presents the multi-GNSS positioning results with augmentation information. It is clearly shown that the fusion of multi-level augmentation can significantly improve positioning accuracy, continuity, and reliability as well as reduce the convergence time and reduce data communication volume. Moreover, the hierarchical mode can satisfy different level augmentation demands, and even the instantaneous-AR can be achieved by supplemented PPP-WRA mode. The following conclusions are drawn.

- PPP-AR requires 12.6 mins to achieve ambiguity fixing with calibrated UPD and real-time products.
- PPP-WA can reach rapid convergence in by sparse station-spacing with fewer model coefficients. Positioning accuracy can reach 0.8 and 1.6 cm for the horizontal and vertical components, respectively, and it needs 2.4 mins to achieve ambiguity resolution.
- PPP-WRA can achieve instantaneous-AR for 85.3% of all solutions, and the overall mean initialization time is within 1.0 min under the condition of the reference station-spacing network within 200 km.

7 Conclusion and outlooks

PPP technology, which incorporates AR and atmosphere augmentation information, contributes comprehensively to the core of geodesy applications, such as disaster monitoring and early warning, autopilot, precision agriculture, etc. As GNSS receivers and constellations continue to expand worldwide, boosting the observation signal data volume, the potential applications of PPP continue to grow. In this thesis, a complete large areas augmentation system that incorporates different types of receiver and signal biases correction, as well as proper atmosphere information augmentation strategies, is essential for PPP-AR to be applied effectively. The main contributions and conclusions of this research, as well as the outlooks, are presented in this Chapter.

7.1 Conclusions and recommendations

This thesis presents a new positioning strategy for large areas that integrates signal bias calibration, atmosphere fitting and interpolation models, and associated uncertainty information into an augmentation system. The proposed system leverages the strengths of both fitting and interpolation models and incorporates optional unmodeled correction compensation and atmospheric uncertainty information to enable rapid and accurate positioning across large areas while minimizing data transfer requirements and utilizing all available signals and receivers.

Pseudo-range observations serve as the fundamental basis for GNSS signals, and inconsistent signals arising from different receiver types, signal modulation modes, or parallel used DCB/DSB corrections can pose potential challenges to precise data processing and ambiguity resolution. In the context of large-area services, achieving stable and accurate ambiguity resolution is crucial and serves as a prerequisite for atmosphere augmentation. To ensure a reliable AR across diverse areas encompassing different satellite signals and receiver types, deviation calibration is divided into two aspects: satellite-end and receiver-end.

Currently, the mixed-signal setting and parallel used DCB and DSB products introduce the biases into precise data processing and jeopardize the ambiguity resolution, which is investigated in detail on precise GNSS data processing. The imprecise pseudo-range signals and inconsistent corrections have an impact on the orbit, resulting in differences of up to 5 mm with ambiguity resolution. In some cases, the impact can be as much as 10 mm for certain satellites. The biases in the clock estimation affect the RMS of up to 1.7 ns, while the STD is zero, meaning the precision is determined by phase, and the pseudo-range only changes the datum. The biases lead to large biases in WL UPD of up to 0.46 cycle in either Mixed-signal or Fixed-signal solutions.

Meanwhile, the NL UPDs also have a significant difference up to 0.47 cycle.

On the other hand, the biases between C, X, S, and L signals cannot be ignored, even though they are all classified as C-code. The stochastic noise in descending order is S, L, C, X, and W signals, and the stochastic noise difference among different satellites is in descending order X, C, W, L, and S signals. The investigation of satellite signal biases presents a comprehensive analysis for signal biases correction in precise data processing and ambiguity resolution, especially pointing out the noise characteristics of each signal and the differences between each satellite on a certain signal.

On the receiver end, a new data processing strategy based on the temporal and spatial stability of WL UPD is developed to investigate the inconsistency of WL UPDs estimated from different types of receiver caused by the satellite-specific biases. The large biases of up to 0.4 cycles can be found in WL UPDs among different receiver types, which impacts the UPD estimation and hinders ambiguity resolution. By using the K-means clustering method to calculate the deviations and calibrate UPDs with a precision of 0.03 cycle, the correct ambiguity fixing rate can be improved by up to 10%.

Relying on the pseudo-range biases calibration for different satellite signals and various types of receiver resolves ambiguity to correct integers in large-area services, which derives precise atmospheric delay for the real-time atmosphere modeling. The atmosphere model is separately studied for ionospheric and tropospheric delays. In addition, the associated uncertainty information for large areas and regional unmodeled errors are established.

In large area augmentation, the new atmospheric delay fitting model is proposed by considering the physical properties of the tropospheric and ionospheric delay propagation paths. By exploiting the exponential decrease in water vapor with altitude, a modified exponential function is adopted to model the altitude dependence of tropospheric delay, generating a tropospheric delay correction model to augment PPP-AR over large areas with high altitude variations. This is especially true in regions with significant altitude differences, where it can improve accuracy by up to 78%. For the ionosphere, analysis of the satellite-wise ionospheric slant delay characteristics of the path propagation, a trigonometric model is introduced to describe the path elevation and azimuth angle differences between optimized reference slant paths with others. The new model reduces the large biases by up to 30% and improves the modeling precision by up to 53% with respect to the legacy second-order polynomial fitting model, achieving an average precision of 8.9 cm in Europe. Besides the precise modeling of ionospheric delay, the different types of receiver set impact on ionospheric delay modeling performance is further analyzed due to the correlation between hardware biases and ionospheric delay.

On the one hand, the unmodeled residuals generated by the large-area fitting model provide grid-based uncertainty information for both tropospheric ZWD and ionospheric delay. This information offers more accurate insights into atmospheric uncertainty compared to the modeling sigma alone. The tropospheric delay uncertainty grid use IDW to calculate each point. The ionospheric delay uncertainty at each grid point is adopted 90^{th} percentile by sorting all residuals within 150km, and satellite-wise modeling precision-related weight is accounted for each satellite constraint. Moreover, by examining the relationship between modeling precision and station distances, the inter-station cross-validation method is implemented to further characterize the interpolation precision of ionospheric delay. This is achieved by utilizing accurate error functions that are distance-dependent, enabling region compensation. Consequently, a hierarchical atmospheric augmentation mode is employed in large areas relying on the proper station-spacing networks, determined by the relationship between modeling performance and station distances, employing two models: the fitting model + uncertainty grid as the fundamental service, and the residual delay + ionosphere error function as the upgraded service. These two modes work in tandem to describe the atmosphere correction and uncertainty information.

Finally, the hierarchical augmentation positioning mode integrated biases calibration, atmosphere fitting model and residual delays compensation, and atmosphere uncertainty information, are proposed. The integration of the hierarchical augmentation mode enables consistent and optimized AR for both the generating atmosphere information at the server and positioning at the user. Using the optional unmodeled correction compensation determined by the fitting residuals magnitude, the data transmission volume can be significantly reduced, up to 96.8% and 65.6% for tropospheric and ionospheric delays, respectively, compared to the legacy mode. This approach simultaneously reduces the achieved instantaneous AR of 85.3% of all solutions.

In conclusion, the integrated solution presented in this study offers a comprehensive approach that incorporates crucial corrections, including receiver and signal deviation calibration, as well as atmosphere correction, leveraging all available observations from diverse receiver types and signal modulation methods. By combining the strengths of fitting models and interpolation modes, it achieves enhanced accuracy in large-area atmosphere augmentation while minimizing data requirements and overcoming the conflict among data transmission volume, represented precision, and coverage area size. Furthermore, this solution significantly reduces convergence time through precise atmospheric delay corrections and provides reliable uncertainty information, ensuring stability and applicability in large-area applications.

The integrated solution presented herein demonstrates its potential for rapid and accurate

positioning in large areas. Its effectiveness in applications paves the way for improved positioning capabilities, benefiting various sectors such as transportation, geodesy, and remote sensing. By leveraging the synergy between fitting models, interpolation modes, and uncertainty estimation, this integrated approach opens up new avenues for enhancing the precision and robustness of satellite-based positioning systems.

7.2 Future work

The research presented in this thesis provides a new approach for accurate large area augmentation for rapid/instantaneous positioning. This work motivates further research on several aspects.

In the context of real-time PPP applications, such as disaster monitoring, early warning systems, and autopilot, the integration of low-cost receivers becomes crucial. As these receivers may introduce various deviations during data processing, it is essential to estimate receiver-end deviations and signal biases as meaningful corrections. Future research should focus on these deviations, enabling real-time high-precision positioning with arbitrary low-cost receivers and all available satellite signals.

The growing number of satellites and frequency bands in satellite navigation systems presents both opportunities and challenges. Future work should expand the scope of multi-frequency and multi-GNSS rapid/instantaneous positioning from large regional areas to global coverage. The construction of atmosphere augmentation models should consider the number of satellites and frequencies available in the region, integrating optional augmentation techniques. A comprehensive evaluation and application of appropriate augmentation modes and strategies are necessary for multi-GNSS and multi-frequency positioning.

Moreover, exploring the synergies between multi-GNSS PPP-AR and other technologies can enhance positioning capabilities and reduce dependence on external information sources. Investigating the integration of GNSS with complementary technologies can lead to improved accuracy, robustness, and reliability in positioning systems. Future research should leverage the advantages of different technologies and develop integrated approaches that harness the strengths of each component.

Last but not least, future research in satellite navigation should focus on estimating and compensating for deviations in low-cost receivers and multi-sensors, expanding accurate service to a global scale and exploring synergies with other technologies. These advancements will contribute to the realization of real-time high-precision positioning systems and further enhance the performance and applicability of satellite navigation in various domains.

Bibliography

Agency, E. G. N. S. s. (2019). *PPP-RTK market and technology report*.

Aggrey, J., & Bisnath, S. (2019). Improving GNSS PPP Convergence: The Case of Atmospheric-Constrained, Multi-GNSS PPP-AR. *Sensors (Basel), 19*(3). doi:10.3390/s19030587

Alber, C., Ware, R., Rocken, C., & Solheim, F. (1997). GPS surveying with 1 mm precision using corrections for atmospheric slant path delay. *Geophysical Research Letters, 24*(15), 1859-1862. doi:10.1029/97gl01877

Andrei, C.-O., & Chen, R. (2008). Assessment of time-series of troposphere zenith delays derived from the Global Data Assimilation System numerical weather model. *GPS Solutions, 13*(2), 109-117. doi:10.1007/s10291-008-0104-1

Arikan, F., Nayir, H., Sezen, U., & Arikan, O. (2008). Estimation of single station interfrequency receiver bias using GPS-TEC. *Radio Science, 43*(4), n/a-n/a. doi:10.1029/2007rs003785

Ashby, N. (2003). Relativity in the Global Positioning System. *Living Rev. Relativity, 6*(1).

Ashby, N. (2004). The Sagnac Effect in the Global Positioning System. In G. Rizzi, M. L. Ruggiero, & (eds) (Eds.), *Relativity in Rotating Frames. Fundamental Theories of Physics* (Vol. vol 135). Dordrecht: Springer.

Banville, S., Hassen, E., Walker, M., & Bond, J. (2022). Wide-Area Grid-Based Slant Ionospheric Delay Corrections for Precise Point Positioning. *Remote Sensing, 14*(5). doi:10.3390/rs14051073

Bevis, M., Businger, S., Herring, T. A., Rocken, C., Anthes, R. A., & Ware, R. H. (1992). GPS meteorology: Remote sensing of atmospheric water vapor using the global positioning system. *Journal of Geophysical Research, 97*(D14). doi:10.1029/92jd01517

Bilitza, D. (2018). IRI the International Standard for the Ionosphere. *Advances in Radio Science, 16*, 1-11. doi:10.5194/ars-16-1-2018

Blewitt, G. (1989). Carrier phase ambiguity resolution for the Global Positioning System applied to geodetic baselines up to 2000 km. *Journal of Geophysical Research: Solid Earth, 94*(B8), 10187-10203. doi:10.1029/JB094iB08p10187

Bock, O., Tarniewicz, J., Thom, C., Pelon, J., & Kasser, M. (2001). Study of external path delay correction techniques for high accuracy height determination with GPS. *Physics and Chemistry of the Earth, Part A: Solid Earth and Geodesy, 26*(3), 165-171. doi:10.1016/s1464-1895(01)00041-2

Boehm, J., Werl, B., & Schuh, H. (2006). Troposphere mapping functions for GPS and very long baseline interferometry from European Centre for Medium-Range Weather Forecasts operational analysis data. *Journal of Geophysical Research: Solid Earth, 111*(B2), n/a-n/a. doi:10.1029/2005jb003629

Böhm, J., Möller, G., Schindelegger, M., Pain, G., & Weber, R. (2014). Development of an improved empirical model for slant delays in the troposphere (GPT2w). *GPS Solutions, 19*(3), 433-441. doi:10.1007/s10291-014-0403-7

Boisits, J., Glaner, M., & Weber, R. (2020). Regiomontan: A Regional High Precision Ionosphere Delay Model and Its Application in Precise Point Positioning. *Sensors (Basel), 20*(10). doi:10.3390/s20102845

Bosser, P., Bock, O., Thom, C., Pelon, J., & Willis, P. (2009). A case study of using Raman lidar measurements in high-accuracy GPS applications. *Journal of Geodesy, 84*(4), 251-265. doi:10.1007/s00190-009-0362-x

Bruyninx, C., Legrand, J., Fabian, A., & Pottiaux, E. (2019). GNSS metadata and data validation in the EUREF Permanent Network. *GPS Solutions, 23*(4). doi:10.1007/s10291-019-0880-9

Chen, G., & Herring, T. A. (1997). Effects of atmospheric azimuthal asymmetry on the analysis of space geodetic data. *Journal of Geophysical Research-Solid Earth, 102*(B9), 20489-20502. doi:Doi 10.1029/97jb01739

Chen, J., Wang, J., Wang, A., Ding, J., & Zhang, Y. (2020). SHAtropE—A Regional Gridded ZTD Model for China and the Surrounding Areas. *Remote Sensing, 12*(1).

doi:10.3390/rs12010165

Cherniak, I., Krankowski, A., & Zakharenkova, I. (2018). ROTI Maps: a new IGS ionospheric product characterizing the ionospheric irregularities occurrence. *GPS Solutions, 22*(3). doi:10.1007/s10291-018-0730-1

Coïsson, P., Radicella, S. M., Leitinger, R., & Nava, B. (2006). Topside electron density in IRI and NeQuick: Features and limitations. *Advances in Space Research, 37*(5), 937-942. doi:10.1016/j.asr.2005.09.015

Collins, P. (2008). *Isolating and Estimating Undifferenced GPS Integer Ambiguities.* Paper presented at the ION, San Diego, CA.

Counselman, C. C. (1999). Multipath-rejecting GPS antennas. *Proceedings of the IEEE, 87*(1), 86-91. doi:10.1109/5.736343

Cui, B., Jiang, X., Wang, J., Li, P., Ge, M., & Schuh, H. (2023). A new large-area hierarchical PPP-RTK service strategy. *GPS Solutions, 27*(134). doi:10.1007/s10291-023-01476-8

Cui, B., Li, P., Wang, J., Ge, M., & Schuh, H. (2021). Calibrating receiver-type-dependent wide-lane uncalibrated phase delay biases for PPP integer ambiguity resolution. *Journal of Geodesy, 95*(7). doi:10.1007/s00190-021-01524-6

Cui, B., Wang, J., Li, P., Ge, M., & Schuh, H. (2022). Modeling wide-area tropospheric delay corrections for fast PPP ambiguity resolution. *GPS Solutions, 26*(2). doi:10.1007/s10291-022-01243-1

Davis, J. L., Herring, T. A., Shapiro, I. I., Rogers, A. E. E., & Elgered, G. (1985). Geodesy by radio interferometry: Effects of atmospheric modeling errors on estimates of baseline length. *Radio Science, 20*(6), 1593-1607. doi:10.1029/RS020i006p01593

Dong, D.-N., & Bock, Y. (1989). Global Positioning System Network analysis with phase ambiguity resolution applied to crustal deformation studies in California. *Journal of Geophysical Research: Solid Earth, 94*(B4), 3949-3966. doi:10.1029/JB094iB04p03949

Dong, D., Wang, M., Chen, W., Zeng, Z., Song, L., Zhang, Q., Cai, M., Cheng, Y., & Lv, J. (2015). Mitigation of multipath effect in GNSS short baseline positioning by the multipath hemispherical map. *Journal of Geodesy, 90*(3), 255-262. doi:10.1007/s00190-015-0870-9

Dousa, J., & Elias, M. (2014). An improved model for calculating tropospheric wet delay. *Geophysical Research Letters, 41*(12), 4389-4397. doi:10.1002/2014gl060271

Du, Z., Chai, H., Xiao, G., Wang, M., Yin, X., & Chong, Y. (2020). A method for undifferenced and uncombined PPP ambiguity resolution based on IF FCB. *Advances in Space Research, 66*(12), 2888-2899. doi:10.1016/j.asr.2020.04.027

Duong, V., Harima, K., Choy, S., Laurichesse, D., & Rizos, C. (2019). An optimal linear combination model to accelerate PPP convergence using multi-frequency multi-GNSS measurements. *GPS Solutions, 23*(2). doi:10.1007/s10291-019-0842-2

Fan, J., & Ma, G. (2014). Characteristics of GPS positioning error with non-uniform pseudorange error. *GPS Solutions, 18*(4), 615-623. doi:10.1007/s10291-013-0359-z

Farebrother, R. W. (2001). Adrien-Marie Legendre. In C. C. Heyde, E. Seneta, P. Crépel, S. E. Fienberg, & J. Gani (Eds.), *Statisticians of the Centuries* (pp. 101-104). New York, NY: Springer New York.

Feltens, J. (2003). The activities of the Ionosphere Working Group of the International GPS Service (IGS). *GPS Solutions, 7*(1), 41-46. doi:10.1007/s10291-003-0051-9

Feng, Y., & Wang, J. (2008). GPS RTK Performance Characteristics and Analysis. *Journal of Global Positioning Systems, 7*(1), 1-8. doi:10.5081/jgps.7.1.1

Fotopoulos, G., & Cannon, M. E. (2001). An Overview of Multi-Reference Station Methods for cm-Level Positionin. *GPS Solutions, 4*(3), 1-10.

Frei, E., & Beutler, G. (1990). *Rapid static positioning based on the fast ambiguity resolution approach*.

Fund, F., Morel, L., Mocquet, A., & Boehm, J. (2010). Assessment of ECMWF-derived tropospheric delay models within the EUREF Permanent Network. *GPS Solutions, 15*(1), 39-48. doi:10.1007/s10291-010-0166-8

Gao, J. A. Y. (1997). Resolution and accuracy of terrain representation by grid DEMs at a micro-scale. *International Journal of Geographical Information Science, 11*(2), 199-212. doi:10.1080/136588197242464

Gabor, M. J., & Nerem, R. S. (1999). GPS Carrier phase Ambiguity Resolution Using Satellite-Satellite Single Differences. Paper presented at the Proceedings of the 12th International Technical Meeting of the Satellite Division of The Institute of Navigation (ION GPS 1999), Nashville, TN.

Ge, M., Gendt, G., Dick, G., & Zhang, F. P. (2005). Improving carrier-phase ambiguity resolution in global GPS network solutions. *Journal of Geodesy, 79*(1-3), 103-110. doi:10.1007/s00190-005-0447-0

Ge, M., Gendt, G., Dick, G., Zhang, F. P., & Rothacher, M. (2006). A New Data Processing Strategy for Huge GNSS Global Networks. *Journal of Geodesy, 80*(4), 199-203. doi:10.1007/s00190-006-0044-x

Ge, M., Gendt, G., Rothacher, M., Shi, C., & Liu, J. (2007). Resolution of GPS carrier-phase ambiguities in Precise Point Positioning (PPP) with daily observations. *Journal of Geodesy, 82*(7), 389-399. doi:10.1007/s00190-007-0187-4

Gratton, S., Lawless, A. S., & Nichols, N. K. (2007). Approximate Gauss–Newton Methods for Nonlinear Least Squares Problems. *SIAM Journal on Optimization, 18*(1), 106-132. doi:10.1137/050624935

Guo, F., & Zhang, X. (2013). Real-time clock jump compensation for precise point positioning. GPS Solutions, 18(1), 41-50. doi:10.1007/s10291-012-0307-3

Gu, S., Shi, C., Lou, Y., & Liu, J. (2015). Ionospheric effects in uncalibrated phase delay estimation and ambiguity-fixed PPP based on raw observable model. *Journal of Geodesy, 89*(5), 447-457. doi:10.1007/s00190-015-0789-1

Hadas, T., Kaplon, J., Bosy, J., Sierny, J., & Wilgan, K. (2013). Near-real-time regional troposphere models for the GNSS precise point positioning technique. *Measurement Science and Technology, 24*(5). doi:10.1088/0957-0233/24/5/055003

Hadas, T., Teferle, F. N., Kazmierski, K., Hordyniec, P., & Bosy, J. (2016). Optimum stochastic modeling for GNSS tropospheric delay estimation in real-time. *GPS Solutions, 21*(3), 1069-1081. doi:10.1007/s10291-016-0595-0

Hansen, P., Ngai, E., Cheung, B. K., & Mladenovic, N. (2005). Analysis of Global k-Means, an Incremental Heuristic for Minimum Sum-of-Squares Clustering. *Journal of Classification, 22*(2), 287-310. doi:10.1007/s00357-005-0018-3

Hauschild, A., & Montenbruck, O. (2014). A study on the dependency of GNSS pseudorange biases on correlator spacing. *GPS Solutions, 20*(2), 159-171. doi:10.1007/s10291-014-0426-0

Hirokawa, R., Fernández-Hernández, I., & Reynolds, S. (2021). PPP/PPP-RTK open formats: Overview, comparison, and proposal for an interoperable message. *Navigation, 68*(4), 759-778. doi:10.1002/navi.452

Hobiger, T., Ichikawa, R., Koyama, Y., & Kondo, T. (2008). Fast and accurate ray-tracing algorithms for real-time space geodetic applications using numerical weather models. *Journal of Geophysical Research, 113*(D20). doi:10.1029/2008jd010503

Irsigler, M. (2008). *Multipath Propagation, Mitigation and Monitoring in the Light of Galileo and the Modernized GPS.* (PhD). Universität der Bundeswehr München, München.

Irsigler, M. (2010). Characterization of multipath phase rates in different multipath environments. *GPS Solutions, 14*(4), 305-317. doi:10.1007/s10291-009-0155-y

Jefferson, D. C., Heflin, M. B., & Muellerschoen, R. J. (2001). Examining the C1-P1 Pseudorange Bias. *GPS Solutions, 4*, 25-30. doi:https://doi.org/10.1007/PL00012862

Ji, S., Chen, W., Ding, X., Chen, Y., Zhao, C., & Hu, C. (2010). Ambiguity validation with combined ratio test and ellipsoidal integer aperture estimator. *Journal of Geodesy, 84*(10), 597-604. doi:10.1007/s00190-010-0400-8

Kalinnikov, V. V., Khutorova, O. G., & Teptin, G. M. (2012). Determination of troposphere characteristics using signals of satellite navigation systems. *Izvestiya, Atmospheric and Oceanic Physics, 48*(6), 631-638. doi:10.1134/s0001433812060060

Kalman, R. E. (1960). A New Approach to Linear Filtering and Prediction Problems. *Journal of Basic Engineering, 82*(1), 35-45. doi:10.1115/1.3662552

Kalman, R. E., & Bucy, R. S. (1961). New Results in Linear Filtering and Prediction Theory. *Journal of Basic Engineering, 83*(1), 95-108. doi:10.1115/1.3658902

Keshin, M. (2012). A new algorithm for single receiver DCB estimation using IGS TEC maps. *GPS Solutions, 16*, 283–292.

Khodabandeh, A., & Teunissen, P. J. G. (2016). PPP-RTK and inter-system biases: the ISB look-up table as a means to support multi-system PPP-RTK. *Journal of Geodesy, 90*(9), 837-851. doi:10.1007/s00190-016-0914-9

Khodabandeh, A., & Teunissen, P. J. G. (2019). Integer estimability in GNSS networks. *Journal of Geodesy, 93*(9), 1805-1819. doi:10.1007/s00190-019-01282-6

Klobuchar, J. (1987). Ionospheric Time-Delay Algorithm for Single-Frequency GPS Users. *IEEE TRANSACTIONS ON AEROSPACE AND ELECTRONIC SYSTEMS, AES-23*(3), 325-331. doi:10.1109/taes.1987.310829

Kouba, J., & Héroux, P. (2000). GPS Precise Point Positioning Using IGS Orbit Products.

Kouba, J., & Héroux, P. (2001). Precise Point Positioning Using IGS Orbit and Clock Products. *GPS Solutions, 5*(2), 12-28. doi:10.1007/pl00012883

Krishna, K., & Narasimha Murty, M. (1999). Genetic K-means algorithm. *IEEE Trans Syst Man Cybern B Cybern, 29*(3), 433-439. doi:10.1109/3477.764879

Langley, R. B. (1998). GPS Receivers and the Observables. In P. J. G. Teunissen & A. Kleusberg (Eds.), *GPS for Geodesy* (pp. 151-185). Berlin, Heidelberg: Springer Berlin Heidelberg.

Laurichesse, D., Mercier, F., BERTHIAS, J.-P., BROCA, P., & CERRI, L. (2009). Integer Ambiguity Resolution on Undifferenced GPS Phase Measurements and Its Application to PPP and Satellite Precise Orbit Determination. *NAVIGATION: Journal of The Institute of Navigation, 56*(2).

Laurichesse, D., Mercier, F., & Berthias, J. P. (2010). Real-time PPP with undifferenced integer ambiguity resolution, experimental results. *Proceedings of the 23rd International Technical Meeting of the Satellite Division of the Institute of Navigation (Ion Gnss 2010)*, 2534-2544.

Li, P., Cui, B., Hu, J., Liu, X., Zhang, X., Ge, M., & Schuh, H. (2022). PPP-RTK considering the ionosphere uncertainty with cross-validation. *Satellite Navigation, 3*(1). doi:10.1186/s43020-022-00071-5

Li, P., Zhang, X., & Guo, F. (2016). Ambiguity resolved precise point positioning with GPS and BeiDou. *Journal of Geodesy, 91*(1), 25-40. doi:10.1007/s00190-016-0935-4

Li, P., Zhang, X., Ren, X., Zuo, X., & Pan, Y. (2015). Generating GPS satellite fractional cycle bias for ambiguity-fixed precise point positioning. *GPS Solutions, 20*(4), 771-782. doi:10.1007/s10291-015-0483-z

Li, X., Huang, J., Li, X., Lyu, H., Wang, B., Xiong, Y., & Xie, W. (2021). Multi-constellation GNSS PPP instantaneous ambiguity resolution with precise atmospheric corrections augmentation. *GPS Solutions, 25*(3). doi:10.1007/s10291-021-01123-0

Li, X., Li, X., Liu, G., Feng, G., Guo, F., Yuan, Y., & Zhang, K. (2018). Spatial–temporal characteristic of BDS phase delays and PPP ambiguity resolution with GEO/IGSO/MEO satellites. *GPS Solutions, 22*(4). doi:10.1007/s10291-018-0790-2

Li, X., Li, X., Yuan, Y., Zhang, K., Zhang, X., & Wickert, J. (2017). Multi-GNSS phase delay estimation and PPP ambiguity resolution: GPS, BDS, GLONASS, Galileo. *Journal of Geodesy, 92*(6), 579-608. doi:10.1007/s00190-017-1081-3

Li, X., Zhang, X., & Ge, M. (2010). Regional reference network augmented precise point positioning for instantaneous ambiguity resolution. *Journal of Geodesy, 85*(3), 151-158. doi:10.1007/s00190-010-0424-0

Li, Z., Wang, N., Wang, L., Liu, A., Yuan, H., & Zhang, K. (2019). Regional ionospheric TEC modeling based on a two-layer spherical harmonic approximation for real-time single-frequency PPP. *Journal of Geodesy, 93*(9), 1659-1671. doi:10.1007/s00190-019-01275-5

Li, Z., Yuan, Y., Li, H., Ou, J., & Huo, X. (2012). Two-step method for the determination of the differential code biases of COMPASS satellites. *Journal of Geodesy, 86*(11), 1059-1076. doi:10.1007/s00190-012-0565-4

Li, Z., Yuan, Y., Wang, N., Hernandez-Pajares, M., & Huo, X. (2014). SHPTS: towards a new method for generating precise global ionospheric TEC map based on spherical harmonic and generalized trigonometric series functions. *Journal of Geodesy, 89*(4), 331-345. doi:10.1007/s00190-014-0778-9

Likas, A., Vlassis, N., & J. Verbeek, J. (2003). The global k-means clustering algorithm. *Pattern Recognition, 36*(2), 451-461. doi:10.1016/s0031-3203(02)00060-2

Likasa, A., Vlassisb, N., & Verbeek, J. (2003). Pattern Recognition-The global k-means clustering algorithm. *Pattern Recognition Society, 36*, 451-461.

Liu, J., Gu, D., Ju, B., Shen, Z., Lai, Y., & Yi, D. (2016a). A new empirical solar radiation pressure model for BeiDou GEO satellites. *Advances in Space Research, 57*(1), 234-244. doi:10.1016/j.asr.2015.10.043

Liu, Q., Hernández-Pajares, M., Yang, H., Monte-Moreno, E., Roma-Dollase, D., García-Rigo, A., Li, Z., Wang, N., Laurichesse, D., Blot, A., Zhao, Q., Zhang, Q., Hauschild, A., Agrotis, L., Schmitz, M., Wübbena, G., Stürze, A., Krankowski, A., Schaer, S., Feltens, J., Komjathy, A., & Ghoddousi-Fard, R. (2021). The cooperative IGS RT-GIMs: a reliable estimation of the global ionospheric electron content distribution in real time. *Earth System Science Data, 13*(9), 4567-4582. doi:10.5194/essd-13-4567-2021

Liu, T., & Zhang, B. (2021). Estimation of code observation-specific biases (OSBs) for the modernized multi-frequency and multi-GNSS signals: an undifferenced and uncombined approach. *Journal of Geodesy, 95*(8). doi:10.1007/s00190-021-01549-x

Liu, T., Zhang, B., Yuan, Y., & Zhang, X. (2019). On the application of the raw-observation-based PPP to global ionosphere VTEC modeling: an advantage demonstration in the multi-frequency and multi-GNSS context. *Journal of Geodesy, 94*(1). doi:10.1007/s00190-019-01332-z

Liu, Y., Song, W., Lou, Y., Ye, S., & Zhang, R. (2016b). GLONASS phase bias estimation and its PPP ambiguity resolution using homogeneous receivers. *GPS Solutions, 21*(2), 427-437. doi:10.1007/s10291-016-0529-x

Lu, C., Li, X., Zus, F., Heinkelmann, R., Dick, G., Ge, M., Wickert, J., & Schuh, H. (2017). Improving BeiDou real-time precise point positioning with numerical weather models. *Journal of Geodesy, 91*(9), 1019-1029. doi:10.1007/s00190-017-1005-2

Malys, S., & Jensen, P. A. (1990). Geodetic point positioning with GPS carrier beat phase data from the CASA UNO Experiment. *Geophysical Research Letters, 17*(5), 651-654. doi:10.1029/GL017i005p00651

Mannucci, A. J., Wilson, B. D., Yuan, D. N., Ho, C. H., Lindqwister, U. J., & Runge, T. F. (1998). A global mapping technique for GPS-derived ionospheric total electron content measurements. *Radio Science, 33*(3), 565-582. doi:10.1029/97rs02707

Melbourne, W. (1985). *The case for ranging in GPS based geodetic systems.* Paper presented at the In: Proceedings of the First International Symposium on Precise Positioning with the Global Positioning System, Rockville, MD, USA, 15–19 April.

Montenbruck, O., Hauschild, A., & Steigenberger, P. (2014a). Differential Code Bias Estimation using Multi-GNSS Observations and Global Ionosphere Maps. *Navigation: Journal ofThe Institute of Navigation, 61*(3), 191-201.

Montenbruck, O., Steigenberger, P., & Hauschild, A. (2014b). Broadcast versus precise ephemerides: a multi-GNSS perspective. *GPS Solutions, 19*(2), 321-333. doi:10.1007/s10291-014-0390-8

Moradi, R., Schuster, W., Feng, S., Jokinen, A., & Ochieng, W. (2014). The carrier-multipath observable: a new carrier-phase multipath mitigation technique. *GPS Solutions, 19*(1), 73-82. doi:10.1007/s10291-014-0366-8

Mylnikova, A. A., Yasyukevich, Y. V., Kunitsyn, V. E., & Padokhin, A. M. (2015). Variability of GPS/GLONASS differential code biases. *Results in Physics, 5*, 9-10. doi:10.1016/j.rinp.2014.11.002

Nadarajah, N., Khodabandeh, A., Wang, K., Choudhury, M., & Teunissen, P. J. G. (2018). Multi-GNSS PPP-RTK: From Large- to Small-Scale Networks. *Sensors (Basel), 18*(4). doi:10.3390/s18041078

Nischan, T. (2016). GFZRNX - RINEX GNSS Data Conversion and Manipulation Toolbox. *GFZ Data Services*. doi:https://doi.org/10.5880/GFZ.1.1.2016.002

Odijk, D., & Teunissen, P. J. G. (2008). ADOP in closed form for a hierarchy of multi-frequency single-baseline GNSS models. *Journal of Geodesy, 82*(8), 473-492. doi:10.1007/s00190-007-0197-2

Parkinson, B. W., Morton, Y. T. J., van Diggelen, F., & Spilker Jr., J. J. (2020). Introduction, Early History, and Assuring PNT (PTA). In *Position, Navigation, and Timing Technologies in the 21st Century* (pp. 1-42).

Paul, C. (2008). Precise Point Positioning with Ambiguity Resolution using the Decoupled Clock Model. *ION GNSS*.

Pena, J. M., Lozano, J. A., & Larranaga, P. (1999). An empirical comparison of four initialization methods for the K-Means algorithm. *Pattern Recognition Letters, 20*(10), 1027-1040. doi:Doi 10.1016/S0167-8655(99)00069-0

IERS Conventions (2010). Retrieved from Frankfurt am Main:

Pi, X., Mannucci, A. J., Lindqwister, U. J., & Ho, C. M. (1997). Monitoring of global ionospheric irregularities using the Worldwide GPS Network. *Geophysical Research Letters, 24*(18), 2283-2286. doi:10.1029/97gl02273

Psychas, D., Khodabandeh, A., & Teunissen, P. J. G. (2021). Impact and mitigation of neglecting PPP-RTK correctional uncertainty. *GPS Solutions, 26*(1). doi:10.1007/s10291-021-01214-y

Psychas, D., & Verhagen, S. (2020). Real-Time PPP-RTK Performance Analysis Using Ionospheric Corrections from Multi-Scale Network Configurations. *Sensors (Basel), 20*(11). doi:10.3390/s20113012

Psychas, D., Verhagen, S., & Liu, X. (2019a). Preliminary analysis of the ionosphere-corrected PPP-RTK user performance. *Geophysical Research Abstracts, 21*.

Psychas, D., Verhagen, S., Liu, X., Memarzadeh, Y., & Visser, H. (2019b). Assessment of ionospheric corrections for PPP-RTK using regional ionosphere modelling. *Measurement Science and Technology, 30*(1). doi:10.1088/1361-6501/aaefe5

Pugliano, G., Robustelli, U., Rossi, F., & Santamaria, R. (2015). A new method for specular and diffuse pseudorange multipath error extraction using wavelet analysis. *GPS Solutions, 20*(3), 499-508. doi:10.1007/s10291-015-0458-0

Ren, X., Chen, J., Li, X., Zhang, X., & Freeshah, M. (2019). Performance evaluation of real-time global ionospheric maps provided by different IGS analysis centers. *GPS Solutions, 23*(4). doi:10.1007/s10291-019-0904-5

Rodriguez-Solano, C. J., Hugentobler, U., & Steigenberger, P. (2012). Adjustable box-wing model for solar radiation pressure impacting GPS satellites. *Advances in Space Research, 49*(7), 1113-1128. doi:10.1016/j.asr.2012.01.016

Rózsa, S., Ambrus, B., Juni, I., Ober, P. B., & Mile, M. (2020). An advanced residual error model for tropospheric delay estimation. *GPS Solutions, 24*(4). doi:10.1007/s10291-020-01017-7

Saastamoinen, J. (1972). Contributions to the theory of atmospheric refraction. *Bull. Geodesique, 105*, 279-298. doi:https://doi.org/10.1007/BF02521844

Schaer, S. (2012). *Overview of GNSS biases*. Retrieved from Workshop on GNSS Biases, Uni Bern:

Schmid, R., Rothacher, M., Thaller, D., & Steigenberger, P. (2005). Absolute phase center corrections of satellite and receiver antennas. *GPS Solutions, 9*(4), 283-293. doi:10.1007/s10291-005-0134-x

Seepersad, G., & Bisnath, S. (2014). Reduction of PPP convergence period through pseudorange multipath and noise mitigation. *GPS Solutions, 19*(3), 369-379. doi:10.1007/s10291-014-0395-3

Segment, N. G. S. (2012). Global Positioning Systems Directorate Systems Engineering & Integration Interface Specification IS-GPS-200. In *Navigation user interface*.

Shi, J., Xu, C., Guo, J., & Gao, Y. (2014). Local troposphere augmentation for real-time precise point positioning. *Earth, Planets and Space, 66*(1). doi:10.1186/1880-5981-66-30

Steigenberger, P., Thoelert, S., & Montenbruck, O. (2017). GNSS satellite transmit power and its impact on orbit determination. *Journal of Geodesy, 92*(6), 609-624. doi:10.1007/s00190-017-1082-2

Takeichi, N., Sakai, T., Fukushima, S., & Ito, K. (2009). Tropospheric delay correction with dense GPS network in L1-SAIF augmentation. *GPS Solutions, 14*(2), 185-192. doi:10.1007/s10291-009-0133-4

Tatarnikov, D. V., Stepanenko, A. P., & Astakhov, A. V. (2016). Moderately compact helix antennas with cutoff patterns for millimeter RTK positioning. *GPS Solutions, 20*(3), 587-594.

doi:10.1007/s10291-016-0534-0
Teunissen, P. J. G. (1994). A New Method for Fast Carrier Phase Ambiguity Estimation. *IEEE*, 562-573.
Teunissen, P. J. G. (1998). Success probability of integer GPS ambiguity rounding and bootstrapping. *Journal of Geodesy, 72*(10), 606-612. doi:10.1007/s001900050199
Teunissen, P. J. G., & Khodabandeh, A. (2014). Review and principles of PPP-RTK methods. *Journal of Geodesy, 89*(3), 217-240. doi:10.1007/s00190-014-0771-3
Teunissen, P. J. G., Odijk, D., & Zhang, B. (2010). PPP-RTK: results of CORS network-based PPP with integer ambiguity resolution. *Journal of Aeronautics, Astronautics and Aviation, 42*(4), 223-230.
Teunissen, P. J. G., & Verhagen, S. (2013). The GNSS ambiguity ratio-test revisited: a better way of using it. *Survey Review, 41*(312), 138-151. doi:10.1179/003962609x390058
Verhagen, S. (2004). Integer ambiguity validation: an open problem? *GPS Solutions, 8*(1), 36-43. doi:10.1007/s10291-004-0087-5
Verhagen, S., & Teunissen, P. J. G. (2012). The ratio test for future GNSS ambiguity resolution. *GPS Solutions, 17*(4), 535-548. doi:10.1007/s10291-012-0299-z
Vuković, J., & Kos, T. (2017). Locally adapted NeQuick 2 model performance in European middle latitude ionosphere under different solar, geomagnetic and seasonal conditions. *Advances in Space Research, 60*(8), 1739-1750. doi:10.1016/j.asr.2017.05.007
Wang, C., Fan, L., Wang, Z., & Shi, C. (2019). Assessment of global ionospheric maps over continental areas using precise point positioning technique. *Journal of Spatial Science, 65*(1), 25-39. doi:10.1080/14498596.2019.1654943
Wang, J., & Feng, Y. (2012). Reliability of partial ambiguity fixing with multiple GNSS constellations. *Journal of Geodesy, 87*(1), 1-14. doi:10.1007/s00190-012-0573-4
Wang, N., Li, Z., Duan, B., Hugentobler, U., & Wang, L. (2020). GPS and GLONASS observable-specific code bias estimation: comparison of solutions from the IGS and MGEX networks. *Journal of Geodesy, 94*(8). doi:10.1007/s00190-020-01404-5
Wang, N., & Yuan, Y. (2016). *Multi-GNSS differential code biases (DCBs) estimation within MGEX*. Retrieved from
Wang, N., Yuan, Y., Li, Z., Montenbruck, O., & Tan, B. (2015). Determination of differential code biases with multi-GNSS observations. *Journal of Geodesy, 90*(3), 209-228. doi:10.1007/s00190-015-0867-4
Wang, S., Li, B., Li, X., & Zang, N. (2018). Performance analysis of PPP ambiguity resolution with UPD products estimated from different scales of reference station networks. *Advances in Space Research, 61*(1), 385-401. doi:10.1016/j.asr.2017.09.005
Ware, R., Rocken, C., Solheim, F., Van Hove, T., Alber, C., & Johnson, J. (1993). Pointed water vapor radiometer corrections for accurate global positioning system surveying. *Geophysical Research Letters, 20*(23), 2635-2638. doi:10.1029/93gl02936
Wickert, J., Dick, G., Schmidt, T., Asgarimehr, M., Antonoglou, N., Arras, C., Brack, A., Ge, M., Kepkar, A., Männel, B., Nguyen, C., Oluwadare, T. S., Schuh, H., Semmling, M., Simeonov, T., Vey, S., Wilgan, K., & Zus, F. (2020). GNSS Remote Sensing at GFZ: Overview and Recent Results. *zfv – Zeitschrift für Geodäsie, Geoinformation und Landmanagement*. doi:10.12902/zfv-0320-2020
Wieser, A., & Brunner, F. K. (2014). An extended weight model for GPS phase observations. *Earth, Planets and Space, 52*(10), 777-782. doi:10.1186/bf03352281
Wilgan, K., Hadas, T., Hordyniec, P., & Bosy, J. (2017). Real-time precise point positioning augmented with high-resolution numerical weather prediction model. *GPS Solutions, 21*(3), 1341-1353. doi:10.1007/s10291-017-0617-6
Wu, J., Wu, S., Hajj, G., Bertiguer, W., & Lichten, S. (1993). Effects of Antenna Orientation on GPS Carrier Phase Measurements. *Manuscripta Geodaetica, 18*, 91-98.
Wübbena, G. (1985). *Software Development for Geodetic Positioning with GPS Using TI 4100 Code and Carrier Measurements*. Paper presented at the Proceedings of First Int. Symposium on Precise Position with GPS, Rockville, Maryland.
Wübbena, G., Schmitz, M., & Bagge, A. (2005). *PPP-RTK: Precise Point Positioning Using State-Space Representation in RTK Networks*. Paper presented at the 18th International

Technical Meeting, ION GNSS-05, September 13-16, 2005, Long Beach, California.

Xiao, G., Li, P., Gao, Y., & Heck, B. (2019). A Unified Model for Multi-Frequency PPP Ambiguity Resolution and Test Results with Galileo and BeiDou Triple-Frequency Observations. *Remote Sensing, 11*(2). doi:10.3390/rs11020116

Yao, Y., Hu, Y., Yu, C., Zhang, B., & Guo, J. (2016). An improved global zenith tropospheric delay model GZTD2 considering diurnal variations. *Nonlinear Processes in Geophysics, 23*(3), 127-136. doi:10.5194/npg-23-127-2016

Zha, J., Zhang, B., Liu, T., & Hou, P. (2021). Ionosphere-weighted undifferenced and uncombined PPP-RTK: theoretical models and experimental results. *GPS Solutions, 25*(4). doi:10.1007/s10291-021-01169-0

Zhang, B., Teunissen, P. J. G., & Odijk, D. (2011). A Novel Un-differenced PPP-RTK Concept. *Journal of Navigation, 64*(S1), S180-S191. doi:10.1017/s0373463311000361

Zhang, X., Zhang, Y., & Zhu, F. (2020). A method of improving ambiguity fixing rate for post-processing kinematic GNSS data. *Satellite Navigation, 1*(1). doi:10.1186/s43020-020-00022-y

Zhao, J., Hernández-Pajares, M., Li, Z., Wang, N., & Yuan, H. (2021). Integrity investigation of global ionospheric TEC maps for high-precision positioning. *Journal of Geodesy, 95*(3). doi:10.1007/s00190-021-01487-8

Zhou, P., Wang, J., Nie, Z., & Gao, Y. (2019). Estimation and representation of regional atmospheric corrections for augmenting real-time single-frequency PPP. *GPS Solutions, 24*(1). doi:10.1007/s10291-019-0920-5

Zou, X., Wang, Y., Deng, C., Tang, W., Li, Z., Cui, J., Wang, C., & Shi, C. (2017). Instantaneous BDS + GPS undifferenced NRTK positioning with dynamic atmospheric constraints. *GPS Solutions, 22*(1). doi:10.1007/s10291-017-0668-8

Zumberge, J. F., Heflin, M. B., Jefferson, D. C., Watkins, M. M., & Webb, F. H. (1997). Precise point positioning for the efficient and robust analysis of GPS data from large networks. *Journal of Geophysical Research: Solid Earth, 102*(B3), 5005-5017. doi:10.1029/96jb03860

List of Abbreviations

AC	Analysis Center
ADOP	ambiguity dilution of precision
ANTEX	Antenna Exchange Format
APC	Antenna Phase Center
AR	Ambiguity Resolution
ARP	Antenna Reference Point
BDS	BeiDou Navigation Satellite System
BDT	BDS Time
CDMA	Code Division Multiple Access
DCB	Differential Code Biases
DD	Double-Difference
DOP	Dilution Of Precision
DOY	Day of Year
DSB	Differential Signal Biases
FDMA	Frequency Division Multiple Access
FOC	Full Operational Capability
FPA	fractional part of the float ambiguity
GBM	GPS BDS and multi-GNSS
GEO	geostationary orbit
GFZ	GeoForschungsZentrum
GIM	Global Ionosphere Map
GLONASS	Global Navigation Satellite System
GMF	Global Mapping Function
GNSS	Global Navigation Satellite System
GPS	Global Positioning System
GPT2w	Global Pressure and Temperature 2
GTS	generalized trigonometric series
GZTD	Global Zenith Tropospheric Delay
IAT	International Atomic Time
IF	Ionosphere-Free
IDW	Inverse Distance Weighting
iGMAS	international GNSS continuous Monitoring and Assessment System
IGS	International GNSS Service

IGSO	inclined geostationary orbit
IONEX	IONosphere Map EXchange
IOV	In-Orbit Validation
IPP	Ionospheric Pierce Point
IRI	International reference ionosphere
IRNSS	Indian Regional Navigation Satellite System
ISB	Inter-system bias
LSQ	Least-Squares
MEO	medium circular orbit
MGEX	Multi-GNSS Experiment
MW	Melbourne-Wübbena
NL	Narrow-Lane
NWM	Numerical Weather Model
OCS	Operational Control Segment
OFC	Optimal Fitting Coefficient
OMC	Observed-Mines-Computed
OSB	Observable-specific Signal Biases
OSR	Observation Space Representation
PCE	Precise Clock Estimation
POD	Precise Orbit Determination
PCO	Phase Center Offset
PCV	Phase Center Variation
PNT	Positioning, Navigation, and Timing
PPP	Precise Point Positioning
PPP-WA	PPP with wide-area augmentation
PPP-WRA	PPP-WA with region compensation
QZSS	Quasi-Zenith Satellite System
RINEX	Receiver Independent Exchange Format
RTK	Real-time Kinematic
SBAS	Space Based Augmentation Systems
SD	Single-Difference
SNR	Signal-to-Noise Ratio
SPR	Satellite Plus Receiver
SSR	State Space Representation
STEC	Slant Total Electron Content
TECU	Total Electron Content Unite

TTFF	Time To First Fix
UDUC	Un-Differenced and Un-Combined
UPD	uncalibrated phase delay
UTC	Coordinated Universal Time
VMF	Vienna Mapping Function
VTEC	Vertical Total Electron Content
WL	Wide-Lane
ZHD	Zenith Hydrostatic Delay
ZTD	Zenith Tropospheric Delay
ZWD	Zenith Wet Delay

List of Figures

List of Tables